MASTER THESIS

Thesis submitted in partial fulfillment of the requirements
for the degree of Master of Science in Engineering at the
University of Applied Sciences Technikum Vienna
Degree Program Renewable Urban Energy Systems

Evaluation of photovoltaic modeling algorithms for various weather conditions based on granular intra-array module and weather measurements taken at NIST – Validation of IEC 61853-3 committee draft sub-models and spatial PV array analysis

By: Peter Illich, BSc
Student Number: 1510578023

Supervisor 1: FH-Prof. DI Hubert Fechner, MSc, MAS; UAS, Vienna, Austria
Supervisor 2: Brian Dougherty, M.S., B.S.; NIST, Gaithersburg, USA
Supervisor 3: Matthew Boyd, M.S., B.S.; NIST, Gaithersburg, USA

Gaithersburg/Vienna, August 2017

FH University of Applied Sciences
TECHNIKUM WIEN

Declaration of Authenticity

“As author and creator of this work to hand, I confirm with my signature knowledge of the relevant copyright regulations governed by higher education acts (for example see §§ 21, 46 and 57 UrhG (Austrian copyright law) as amended as well as § 14 of the Statute on Studies Act Provisions / Examination Regulations of the UAS Technikum Wien).

I hereby declare that I completed the present work independently and that any ideas, whether written by others or by myself, have been fully sourced and referenced. I am aware of any consequences I may face on the part of the degree program director if there should be evidence of missing autonomy and independence or evidence of any intent to fraudulently achieve a pass mark for this work (see § 14 para. 1 Statute on Studies Act Provisions / Examination Regulations of the UAS Technikum Wien).

I further declare that up to this date I have not published the work to hand nor have I presented it to another examination board in the same or similar form. I affirm that the version submitted matches the version in the upload tool.”

Place, Date	Signature

Abstract

As the globally installed PV capacity is growing rapidly, quantification of PV system operation reliability under outdoor conditions merits increased attention. In this regard, the understanding of the PV performance dependence on different climatic weather conditions is of crucial importance. This research focuses on the evaluation of sub-models, applied by the international standard IEC 61853-3 committee draft, for the prediction of PV module temperature and power at various weather conditions – binned into ranges of irradiance, ambient temperature, wind speed and angle of incidence. The evaluation is based on minutely averages of weather parameter measurements that serve as inputs for the IEC standard's sub-models, as well as granular intra-array PV operational parameter measurements for the validation of the IEC standard's predictions. Both, weather and PV operational parameters are measured at a ground mounted PV array at NIST in Gaithersburg, Maryland (USA). PV operational parameters are monitored via wireless IV-tracers mounted at one PV module within each of the 96 series strings of the observed PV array – measuring operational current and voltage, along with periodically conducting IV-curve traces. These distributed tracer measurements also permit a granular spatial analysis of PV module performance prediction variability across the PV array, providing crucial information for performance modeling and rating of entire PV arrays.

Results show modeling errors between 1 and 9 °C RMSE for the PV module temperature prediction, and between 2 and 33 W RMSE for the PV module power prediction. Highest prediction errors occur at low irradiances between 100 and 300 W/m² and low ambient and PV module temperatures below 10 °C and 15 °C, respectively – represented as strong overpredictions in PV module power. These errors appear to be independent of wind speed, occur mainly at AOI between 30 and 50° and are most probably caused by magnified errors through linear extrapolation of the performance matrix to lower PV module temperature ranges, as well as non-linearities of PV module performance at lower irradiances and/or module temperatures – not taken into account by the linear inter-/extrapolation. Also, neglecting natural convection cooling at high irradiances and low wind speeds, as well as radiation cooling at low irradiances leads to visible irregularities of residuals and increased errors for the temperature and power prediction.

The spatial analysis of power prediction error and IV-curve parameter variability across the PV array shows a significant pattern of inconsistencies at certain weather conditions, most probably related to temperature differences between the affected PV module positions. These inconsistencies are strongly pronounced at high irradiances and/or ambient temperatures and especially noticeable at high wind speeds. At these weather conditions, the difference in median power prediction error across the observed 96 PV modules within the PV array reaches values between 2 and 4 W, with evident corresponding differences in median measured Voc and Isc between 0.2 and 1 V and up to 0.5 A, respectively.

Keywords: photovoltaic array, monitoring, modeling, weather conditions, spatial analysis

Acknowledgements

I want to thank all people who strongly supported me with writing this thesis, especially my supervisors from NIST, Brian Dougherty and Matthew Boyd, for their helpful guidance and assistance during my time in the USA, as well as my supervisor from the UAS Technikum Vienna, Hubert Fechner, for his constant encouragement and valuable support.
I also want to thank Karl Berger from the AIT, for his critical comments and suggestions during initial phases of this work.
I also acknowledge the University of Applied Sciences Technikum Vienna, the National Institute of Standards and Technology, as well as the Austrian Marshall Plan Foundation for providing me with the opportunity of this immensely valuable professional experience.
Finally, I want to express my deepest gratitude to my wife, Aline, for her immeasurable and continuous love, support and understanding. I also want thank my closest family and friends for their perpetual enthusiasm and pride for me.

Table of contents

1 Introduction

The worldwide installed photovoltaic (PV) capacity has been growing significantly in the last several years to a point that it now joins hydro and wind energy as one of the main renewable energy sources. (IEA, 2017a) Especially over the last two years, the total installed PV capacity worldwide has increased remarkably, showing a market growth rate of 25 % for 2015 and 50 % for 2016, which account to about 50 and 75 gigawatts peak (GWp) of yearly installation in these years. (IEA, 2017a) Given this growth, the total globally installed PV capacity at the end of 2016 surpassed 300 GWp, leading to a contribution to the world's electricity generation of about 1.8 %. (IEA, 2017a) In the upcoming years PV is expected to exceed an installed capacity of 400 GWp worldwide by 2020 – which will surpass the globally installed capacity of nuclear power as of 2015.[1] (IEA, 2015) The most commonly used and commercially available PV technology is based on monocrystalline (m-Si) and polycrystalline (p-Si) silicon (Si) cells, sharing about 90% of the global PV market. The other 10% mainly consist of thin film technologies based on materials like cadmium telluride (CdTe), copper indium gallium [di-] selenide (CIGS), amorphous silicon (a-Si) and other technologies (CPV, multi-junction solar cells, etc.). (IEA, 2016) The significant recent growth of PV worldwide can partly be attributed to the rapid cost reduction of PV modules and PV balance-of-system (BOS) components. This growth has contributed to PV generated energy now being competitive with conventional electricity prices in several countries when comparing levelized costs of electricity (LCOE). Also, favorable policies have considerably influenced the PV market development over the last few years. (IEA, 2016)

Even as these market drivers eventually saturate, system operation costs and system operation reliability will remain crucial to PV's continued growth and improvement – as these factors strongly influence the confidence of investors in the technology. In this context, quantifying the performance of PV systems – especially PV modules – under outdoor conditions merits high attention. Whereas installed PV modules operate under a wide range of ambient conditions, PV modules usually are rated at Standard Test Conditions (STC) following the methods and specifications in the international standards IEC 60904-1 and IEC 61215. These standard test conditions include an irradiance of 1000 W/m² in plane of the PV module, at a specific spectral irradiance distribution (AM 1.5) and a module temperature of 25°C. (IEC, 2016b) These test conditions define the so-called rated or nominal power of a PV module. However, the output power and finally the energy conversion efficiency of a PV module in outdoor operation conditions depends on a range of different external influences that cause the module efficiency or output power to deviate from its nominal performance at STC. (Huld and Amillo, 2015) Among these influences are:

[1] Nuclear power plants have 6 to 8 times higher capacity factors than solar PV systems - i.e. the amount of energy produced per year by PV systems is still less.

- The reflectivity of the PV module top outer surface, which depends on the angle of the incoming light (angle of incidence).
- The wavelength and the intensity of the incoming light.
- The temperature of the PV modules, which depends on the temperature of the surrounding ambient air, the light intensity and the local wind speed.

In addition to the above-mentioned effects, the PV module efficiency is influenced by the installation conditions (e.g. orientation of the module), the available solar irradiance at the installation site as well as the chance of shadows, dust and/or snow covering the module's surface. (Spataru et al., 2015) Next to these effects some PV module technologies show variation in module efficiency caused by long-term exposure to light and/or high temperature ranges. (Huld and Amillo, 2015) Also, degradation or failures of components of the PV module (e.g., encapsulation materials, solar cells, grid fingers) and/or BOS components (e.g., connectors, fuses, cables, junction boxes) through moisture ingress, corrosion, mechanical or thermal stress can lead to the occurrence of power loss and potential hazards in PV modules or systems. (Spataru et al., 2015)
All of these factors need to be considered when observing the performance of a PV module in outdoor operating conditions as they can lead to deviations from its nominal performance at STC. Ultimately, considering several PV modules connected to an array, inherent performance differences between the modules within the array (e.g. manufacturing differences) or one or more of the above mentioned effects can cause non-ideal operation of the individual modules mounted within a PV array – which is referred to as mismatch behavior. These non-ideal performance behaviors leads to power losses on the one hand, but also increases the risk of potential hazards and problems associated with the long-term operation and reliability of a PV system. (Spataru et al., 2015)

In this regard, PV array diagnostic methods are necessary to reveal these fault behaviors and degradation modes and consequently minimize power losses and hazards by preventative or reparative measures. This will in turn reduce the total lifetime costs of the PV array. Common existing PV diagnostic methods usually apply certain PV system models that allow the estimation of system parameters such as the output power of the PV system or the energy yield over a specific time. The model's estimated parameters are compared to measured parameters in order to detect faults or system anomalies. (Spataru et al., 2015) Commonly used PV system models can for example be based on analytical, empirical, statistical or generic models. Another approach for diagnosing PV systems is the measurement and subsequent analysis of current-voltage (IV) characteristic curves of the PV generators, i.e. the PV modules, strings or arrays, by IV curve tracers. (Spataru et al., 2015) As described in the work of Spataru et al. (2015), IV curve tracers – in comparison to other PV diagnostic methods – can deliver significant information concerning the condition and electrical characteristics of the observed PV generator. These include: short-circuit

current (Isc), open-circuit voltage (Voc), maximum power (Pmp), current at maximum power (Imp) and voltage at maximum power (Vmp) and fill factor (FF) as well as operational power (Pop), current (Iop) and voltage (Vop). (Daliento et al., 2017) These electrical properties of PV modules allow the indication and diagnosis of fault behavior as well as degradation modes.

1.1 Subject of research

One focus of the research is to evaluate how well existing PV performance modeling algorithms predict installed performance. Installed performance, in this particular case, corresponds to measurements made at the PV module level. These particular PV modules are distributed throughout a conventional, grid-connected PV array. The PV array is a ground-mounted system that is located at the facilities of the National Institute of Standards and Technology (NIST)[2] in Gaithersburg, Maryland (USA). Novel monitoring units were used to measure the DC current and differential voltage of individual modules, along with periodically conducting an IV curve trace while the module was briefly bypassed. In addition to the module-level measurements, detailed weather-related parameters and module backside temperatures are also locally measured. A subset of these measured ambient and operating conditions serve as inputs to the modeling algorithms.

The modeling algorithms currently appearing in the draft version of the international standard IEC 61853-3 version 82/1066/CD were selected for evaluation. These algorithms appear in the third part of the four-part standard; this part 3 document is at this time (August 2017) under development and exists as an online available committee draft (CD) version. (IEC, 2016b) Parts 1 and 2 of the IEC standard 61853 specify detailed testing requirements, rating a PV module over a range of irradiance and temperatures, varying angle of incidence and sunlight spectra. These standards also specify the methods for estimating the module temperature from the irradiance, ambient temperature and wind speed. (IEC, 2011, IEC, 2016a) IEC 61853 parts 3 and 4 are based on these first two parts and will specify the procedure for using the test results to calculate the energy rating of the particular PV module when deployed in specified representative climates. (IEC, 2016b, IEC, 2016c) The calculation of the module's output power within part 3 is based on first principles mathematical models and findings from relevant research studies. Climatic data in this project that is required as inputs to the mathematical models, is provided by on-site instantaneous weather and module temperature measurements. Three modules, one new and two that had been aged outdoors for nearly the same interval as the modules mounted in the ground array, were tested in accordance with the above described part 1 and 2 of the

[2] Certain commercial equipment, instruments, or materials are identified in this work to foster understanding. Such identification does not imply recommendation or endorsement by the National Institute of Standards and Technology, nor does it imply that the materials or equipment identified are necessarily the best available for the purpose.

IEC 61853 standard. A more detailed description of this standard draft and its calculation procedure can be found in section 2 of this work.
The observed ground mounted PV array was commissioned in August 2012 and consists of 1152 m-Si modules[3], having a total rated DC power of 271 kilowatt peak (kWp). (Boyd, 2015) Since May 2016, one module within each of the 96 series strings in the PV ground array has been monitored using wireless IV-tracers[4]. Each tracer monitors the module (and subsequently the string) current along with the voltage increase across the particular module on a continuous basis, with the measured values being saved every second. In addition, the tracers perform an IV curve sweep of each individual module within the array every five minutes. An IV curve sweep requires approximately 300 ms to complete. During a sweep, the module is bypassed within its series string. The traces are not synced with one another. In addition to facilitating the evaluation of the algorithms used in IEC 61853-3, the distributed tracer measurements also allow a granular spatial analysis of modules within the array and thus a comparison of their existing performance variability within the observed PV ground array. Details on the electrical layout of the PV array, deployed IV-tracers, as well as measurement locations of measurement equipment can be found in section 7 of this work.

1.2 Project Goals

The first project goal is to provide a comprehensive overview of the factors that need to be considered when analyzing outdoor PV array measurements. In this regard, for example, DC array losses, optical and thermal effects, as well as known degradation modes will be described in section 4 of this work. Secondly, this work aims to provide an overview of essential PV modeling algorithms and standards that are relevant to the scope of this work. Therefore, section 5 will point out relevant modeling algorithms and standards for this research.
The experimental, applied part of this work begins in section 6, which provides more detailed information about the observed PV array on NIST's campus. The electrical layout of the PV array, as well as information about measurement positions and the functional principles of the IV-tracers are described. It is important to note that a quantitative analysis of pertinent system and model uncertainties is beyond the scope of this project. However, component uncertainties and a qualitative description of the system components is provided in section 6 as well as in the Appendix A of this work.
Section 7 of the thesis covers the evaluation of the performance modeling algorithms used in the IEC 61853-3 committee draft version 82/1066/CD. The evaluation is carried out by assessing the goodness of fit of modelled to measured operational DC output power and module temperature for a data set having 24 days with a range of 8 characteristic weather

[3] Sharp NU-U235F2, monocrystalline-front-contact PV module
[4] Stratasense Wireless PV tracers, (acc. to STRATASENSE, L. 2013. Stratasense Wireless IV Curve Tracer - Brochure.)

conditions. These characteristic weather conditions are based on irradiance, wind speed and ambient temperature ranges. The inputs to the IEC draft algorithm are the measured, instantaneous climatic data recorded at or very near the ground array. Measured weather data from days covering as wide a range as available were selected. This selection permits investigating the sensitivity of the model to irradiance, wind speed, ambient temperature and angle of incidence through the binning of the available data set, as well as the model's behavior at specific days with characteristic weather conditions. An understanding of these sensitivities is of high interest, as the finalized version of this standard intends to provide a set of standard reference climatic profiles for the prediction of the PV module performance in these different climates. (IEC, 2016b, IEC, 2016c)

Comparing the modelled with the measured PV performance data requires a better understanding of effects occurring within the observed ground array. Therefore, section 8 covers the analysis of the individually traced PV modules within the PV array. In order to provide a comprehensive overview of differences in performance within the array, the modules are grouped and compared according to their position within the array. This way inconsistencies and possible performance differences between the modules can be related to their position within the array. The array analysis will be performed on the same data set of 24 days with characteristic weather conditions, allowing the assessment of the array for the chosen ranges of irradiance, ambient temperature, wind speed and angle of incidences. Consequently, observed differences between the module positions within the array can be analyzed using parameters retrieved from the measured IV characteristic curves, such as the open circuit voltage (Voc) and the short circuit current (Isc).

Ultimately, this work's goal is to combine the findings of the model evaluation and the spatial array analysis in order to evaluate how well the observed modeling algorithms for stand-alone PV modules can be applied to estimate the performance of the observed PV array at certain weather conditions. Thus, the aim is to provide crucial information which can be used for the development of modeling algorithms and rating standards dealing with entire PV arrays.

To conclude, the project goals of this work are to:

- Provide a comprehensive overview of factors affecting outdoor PV array measurements and performance.
- Provide an overview of existing PV modeling algorithms and standards that are relevant to this work.
- Describe the electrical layout of the PV array, as well as give information about measurement positions and the functional principles of the deployed IV-tracers.
- Evaluate the goodness of fit of the modeling algorithms of IEC 61853-3 draft version 82/1066/CD using the on-site, instantaneous measured climatic data at NIST's facilities for different irradiances, wind speeds, ambient temperatures and angles of incidence as well as for different days with characteristic weather conditions.

- Analyze differences between the array's modules according to their position at various irradiances, ambient temperatures, wind speeds and angles of incidence, as well as on specific days with characteristic weather conditions, by using measured IV curve parameters, such as Voc and Isc.

1.3 Scientific Questions

Concluding the above described project goals, the following four main scientific questions for this work are:

- How well do the modeling algorithms suggested by the IEC 61853-3 committee draft version 82/1066/CD predict the operating power and backside temperature of field-deployed PV modules?
- Does the agreement between modelled and measured performance change for different types of days having characteristic weather conditions and/or different ranges of irradiance, wind speed, ambient temperature and angles of incidence?
- Do the comparisons have any dependence on where a particular module is located within the ground mounted PV array?
- What are possible reasons for observed inconsistencies between the in-array mounted PV modules when comparing them according to their position within the array row (top, middle, bottom position) and their position within the whole array itself (middle of array, edge of array) and how can these differences be explained by using IV curve characteristic parameters (Voc and Isc) measured by IV tracers at the granular module level?

1.4 Scope of work and limitations of research

The following chapters describe the scope and limitations of the above mentioned project goals and scientific questions.

1.4.1 Observed PV module characteristics

This project focuses on individual PV modules within the ground mounted PV array at NIST's campus in Gaithersburg, Maryland (USA). Observations concentrate on direct current (DC) measurements taken by IV curve tracers mounted on the rack framing structure of individual modules of each of the 96 strings in the PV array. Measured electrical PV module data includes the module/string operational current (Iop) and module differential voltage (Vop) at every 1-second time interval as well as IV curve sweeps of each individual module every 5-minutes. This work's effort does not include any investigation regarding module or system component degradation. A more detailed description of electrical measurements taken by IV curve tracers can be found in section 3 and section 6 of this work.

1.4.2 Modeling algorithm compromises

Performance modeling of the PV output power and energy yield estimations are calculated by the modeling algorithms used in the international standard IEC 61853-3 which currently exists as committee draft version 82/1066/CD. The mathematical algorithms of this standard take into account (1) angle of incidence (AOI) effects, (2) spectral sensitivity correction, (3) the dependence of the module temperature on irradiance, ambient temperature and wind speed as well as (4) the dependence of the module efficiency and output power on ranges of irradiance and module temperature. (IEC, 2016b) For the scope of this work, the evaluation of the algorithms suggested by the IEC 61853-3 draft focus on the (1), (3) and (4), while the spectral correction (2) is considered through a different approach in this work, namely that developed by Lee and Panchula (2016) and suggested by the Photovoltaic Performance Modeling Collaborative (PVPMC). (PVPMC, 2017) This is on the one hand due to limited data availability, on the other hand it is because the current draft version of IEC 61853-3 does not provide a complete definition of the spectral correction calculation procedure. Furthermore, the spectral correction is shown to be significantly smaller than the AOI correction. Thus, the evaluation of the algorithms suggested by the IEC 61853-3 draft focuses on the correction procedure for angle of incidence (1) based on the model presented by Martin and Ruiz (2000), the spectral correction (2) based on the model of Lee and Panchula (2016), the prediction of the module temperature (3) based on the model from Faiman (2008), and the interpolation method (4) using the performance matrix of IEC 61853-1 that ultimately provides the instantaneous predicted power values. The following table gives an overview of modeling algorithms used in IEC 61853-3 and the alternative model used in this work for spectral correction.

	AOI correction (1)	**Spectral correction (2)**	**Module temperature (3)**	**DC module output power (4)**
Model used for evaluation	**IEC 61853-3:** Martin and Ruiz (2000)	**Alternative model to IEC 61853-3:** Lee and Panchula (2016)	**IEC 61853-3:** Faiman (2008)	**IEC 61853-3:** Interpolation method, IEC (2016b)

Table 1 Overview of models involved in the evaluation of IEC 61853-3 of this work (own table)

In addition, it is important to mention that this work focuses on the use of on-site, instantaneous measurements taken by the installed equipment at NIST's ground mounted PV array in Gaithersburg, rather than using representative and averaged standard climate profiles as suggested by the IEC standard draft. The use of the calculation algorithms described in the draft version of IEC 61853-3 requires a relatively small number of tests in

order to determine key parameters for the estimation of power, and subsequently energy values of individual PV modules. These preliminary required test procedures are described in the first two parts of the standard (IEC 61853-1 and IEC 61853-2) and have already been performed for NIST's ground array module types. Three PV modules of the same type as those in the observed PV array were tested at an independent test laboratory – CFV solar test laboratory in Albuquerque, NM (USA) – in October 2016. (CFV, 2016) For the scope of this thesis, it is assumed that these three tested modules can be treated as equivalent to the modules within the PV array, as two of them had been aged outside for nearly the same time interval as the modules within the ground array (although in open-circuit condition). Differences in aging are assumed to be negligible; however, studies of Jordan (2012) show that crystalline silicon modules left in open-circuit conditions show slightly lower degradation rates than maximum power tracked modules, with a difference of < 1 %/year. Furthermore, the modeling algorithms used in this project do not consider any degradation modes. A detailed description of the applied modeling algorithms and test procedures performed by CFV Solar Test Laboratory in this work can be found in section 3 of this work.

1.4.3 Measurement position compromises

Measurement data required for the modeling algorithms, such as ambient temperature (T_{amb}), wind speed (v), global horizontal irradiance (GHI) and the global in-plane irradiance (G_{poa}), are taken directly at the ground mounted PV array location. Additionally, the PV module temperature ($T_{mod,meas}$) is measured at the backside of a module in the middle of the PV array, located in the middle row of the third shed of the array, column 24 (indicators: row 13, column 24). This temperature measurement consists of the measurement of 4 RTD sensors positioned according to the international standard IEC 60891. (IEC, 2009) For the scope of this project it is assumed that the mean of these 4 RTD sensors measured on this particular module can be seen as representative for all modules in the array. The direct normal irradiance (DNI), required for the calculation of the direct horizontal irradiance (DHI) and the direct in-plane irradiance (B_p) is measured at a weather station about 740 m from the array at NIST's campus. For the scope of this project it is assumed that differences in sky conditions between instantaneously measured data at the weather station and data measured directly at the ground mounted PV array can be neglected. A closer description of the deployed measurement equipment and its positions can be found in section 6 of this work.

1.4.4 Observed weather conditions and characteristic days

The data used in this research was measured between August 2016 and April 2017. Comparisons in the project focus on a set of 8 characteristic weather conditions, each of them represented by 24 days of measurements, with 3 days per characteristic weather condition. All observations referred to in this work are therefore limited to these specific 24 days. This permits the evaluation modeling algorithms for certain ranges of irradiance, wind

speed, ambient temperature as well as angle of incidence on actual measured days. A detailed description of the selection criteria for the chosen days (data set population) can be found in section 3 of this work. The 8 characteristic weather conditions are categorized according to their daily average irradiance, wind speed and ambient temperature during daylight times (sun zenith angle < 90) and periods without shadowing or deposition of snow on the array's modules. It is assumed that any dust deposition happens uniformly across the entire array. To ensure these conditions, weather data, as well as images of the array and sky have been assessed.

1.4.5 Uncertainty and calibration of equipment

The scope of this work does not consider quantitative evaluations of uncertainty introduced by the measurement equipment, although it intends to provide a qualitative description of the system components. However, all deployed measurement equipment in this project is verified to be accurately calibrated according to standard procedures. The last recalibration of the pyranometers at the ground array happened in May 2016. The last recalibration of the pyrheliometers measuring the direct normal irradiance (DNI) happened in November 2016. The last recalibration of the ambient temperature sensor happened in April 2013. The last recalibration of the wind speed sensor happened in July 2016. Silicon sensors were calibrated at the factory and verified to be within their specifications. Additionally, the radiometers are cleaned three times a week in order to avoid deviation of measurements from dust deposition.

2 Definition of terms

This chapter deals with the description and definition of terms and expressions used throughout the elaboration of this thesis. In the following paragraphs, terminology related to the observed PV ground array, data monitoring, data analysis and weather data is explained.

2.1 PV ground array terminology

The terminology of the PV ground array's module positions finds use in the comparison of differences within the 96 traced PV modules at certain positions of the array within this thesis. Figure 1 shows the observed PV ground array at the campus of NIST mounted on coarse gray granite stone (#57 stone) and surrounded by grass and bio retention area. It consists of five sheds, of which four of them contain five rows of PV modules. The northern-most fifth shed consists of only four rows. In total, there are 48 columns and 24 rows of PV modules within the array.

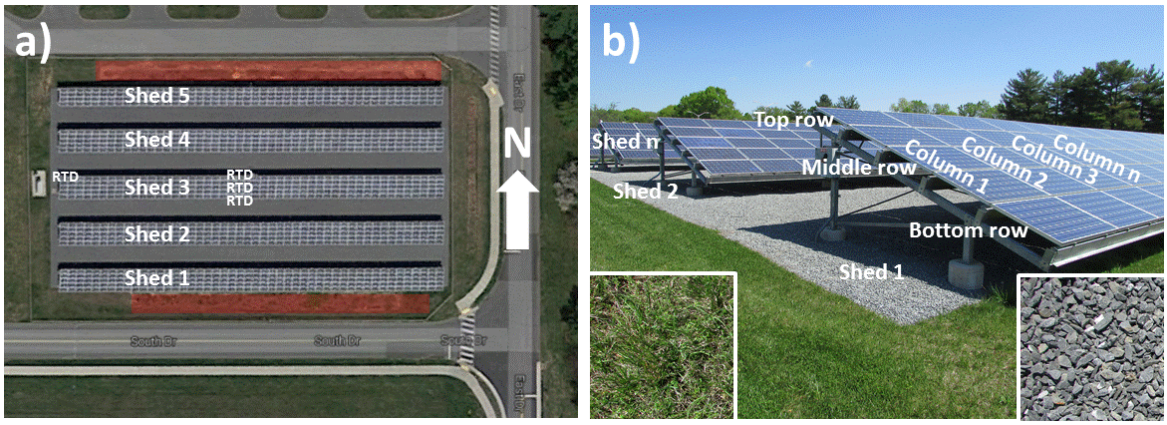

Figure 1 Terminology of positions of PV ground array at campus of NIST, Gaithersburg, a) satellite picture for the definition of sheds, b) picture of shed 1 for the definition of rows and columns within a shed (Fairbrother, 2017)

This work focuses – next to the evaluation of IEC 61853-3 calculation procedures – on the comparison of PV module positions – also explained in section 0 of this work – such as top, middle, bottom of each shed of the array. Furthermore, it brings traced modules mounted at the middle of the array and traced modules mounted at the edge of the array into comparison – see section 0 of this work.

2.2 Data processing terminology

For better understanding of topics related to monitoring data processing, this chapter defines the following terms used in this thesis:

2.2.1 Weather data

Weather data refers to on-site measured weather parameters that are required for the evaluation of IEC 61853-3 calculation procedures, such as: ambient temperature (T_{amb}), wind speed (v), global horizontal irradiance (GHI), direct normal irradiance (DNI) and global in-plane irradiance (G_{poa}). Solar zenith angle (θ_z) and solar azimuth angle (θ_A) are calculated. Weather data is available as minutely averages. For further explanation see section 0.

2.2.2 Operational data

Operational data refers to PV module DC parameters measured by deployed IV tracers at one module of each string within the observed array (in total 96 tracers/modules). It includes operational, instantaneous voltage (Vop) and current (Iop) as well as frequently taken IV curve sweeps. Vop and Iop are available in 1-second intervals. IV curve sweeps are available in 5-minutes intervals. For further explanation see section 0.

2.2.3 IV curve sweep

IV curve sweeps or traces are measurements performed by 'sweeping', i.e. varying, the load on a PV source over a range of voltages (between 0V and Voc) and currents (depending on the irradiance). Many performance characteristics of the observed PV module/cell can be determined through IV curves – as described in section 0. An IV curve sweep typically takes less than a second, in the case of this work about 300ms. For further explanation related to IV curve tracers and IV curve parameters see section 0.

2.2.4 Minutely averages of weather and operational data

This work focuses on the comparison of minutely averages of weather data, used as input for the calculation procedure of IEC 61853-3, compared to minutely averages of operational voltage (Vop) and current (Iop). Averages contain available data measured in secondly intervals, starting with the first second of a minute (e.g. 13:10:01) up to the last second of a minute (e.g. 13:11:00). For further explanation related to monitoring data timing see section 0.

2.2.5 Time stamp

Time stamp refers to the corresponding time of a monitored data point. The time reference in this work is provided by the weather data. Data points of operational data close to this

time stamp are used for further data processing and analysis. For further explanation related to monitoring data timing see chapter 0.

2.2.6 Data anomaly

Data anomaly refers to data that is identified as an obvious outlier in, or is missing from an observed data set. This data is either filtered and not considered in further data processing and analysis or is added through mathematical approaches (e.g. linear interpolation between data points of a data set). For further explanation related to data anomaly processing see section 0.

2.3 Weather data terminology

The following chapters provide definitions of weather data used for the purposes of this work.

2.3.1 Ambient temperature (T_{amb})

The ambient temperature refers to the outdoor measured ambient air temperature at the observed PV ground array at the campus of NIST provided in degrees Celsius (°C). The temperature is measured via resistance temperature detector (RTD) probe on-site at the array's location – not shading the modules and not in stagnant air – mounted in radiation shield to prevent the probe to be influenced by radiative heat exchange from the sun and surroundings, while still allowing ambient air flow around the probe. (Boyd, 2015) For further explanation related to measurement position and equipment see section 6 of this work.

2.3.2 Module temperature (T_{mod})

The term 'module temperature' refers to the measured PV module back sheet surface temperature ($T_{mod,meas}$) measured via 4 mounted RTDs at the back of one module deployed in the middle of the observed PV array – measured in degrees Celsius (°C). RTDs are positioned according to IEC 60891. (IEC, 2009) For further explanation related to measurement position and equipment see section 6 of this work.
The modeled module temperature ($T_{mod,IEC}$) through the procedures of IEC 61853-3 refers to the estimation formula developed by Faiman (2008). For further explanation related to the module temperature calculation see section 0 of this work.

2.3.3 Wind speed (v)

Wind speed refers to measurements taken by an ultrasonic wind sensor at the north of the entire observed PV ground array, located in horizontal orientation next to the array about 56 cm above the array and 83 cm to the north of the modules. Measurement data is provided

in meters per second (m/s). For further explanation related to measurement position and equipment see section 6 of this work.

2.3.4 Sun elevation (θ_{el}), zenith (θ_z), azimuth (θ_a)

The sun elevation angle is defined as the angle between the horizon and the sun, i.e. the altitude of the sun. The sun zenith angle is defined as the angle complementary to the sun elevation angle, i.e. the angle between the zenith and the sun. The sun azimuth angle is the horizontal angle of the sun, measured clockwise from north (e.g. north = 0, east = 90, west = 270). The figure below shows the above described sun position angles.

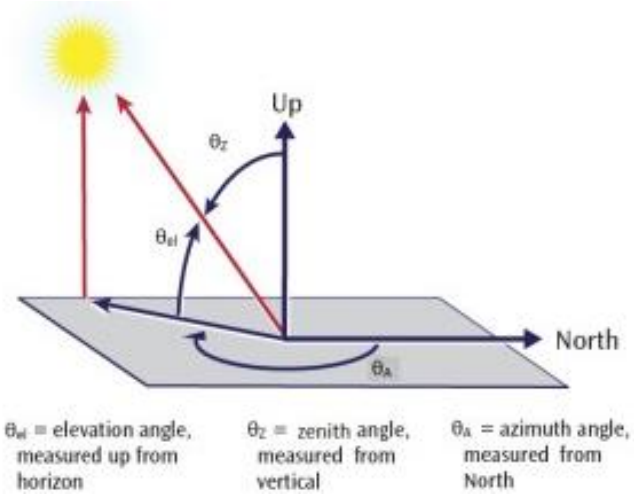

Figure 2 Sun position and relevant angles for calculation procedures (PVPMC, 2017)

The above described angles, used in this work, are provided via calculations through the SOLPOS sun position algorithms of NREL (2000).

2.3.5 Sun angle of incidence (AOI)

The angle of incidence (AOI) is defined as the angle between the sun's rays and the observed surface hit by the sun rays, e.g. the surface of the PV array/module. It can be determined as:

$$AOI = \cos^{-1}\left[\cos(\theta_z) * \cos(\theta_T) + \sin(\theta_z) * \sin(\theta_T) * \cos\left(\theta_A - \theta_{A,array}\right)\right]$$

Equation 1 Formula for calculation of angle of incidence (PVPMC, 2017)

Where θ_z is the sun zenith angle, θ_T the tilt angle of the PV array/module, θ_A the solar azimuth angle and $\theta_{A,array}$ the azimuth angle of the observed array/module. (PVPMC, 2017)

2.3.6 Air mass (AM)

The air mass (AM) describes the path length of solar radiation beams through the atmosphere before reaching the earth, relative to its overhead path length (shortest possible path length). (Molina, 2016)

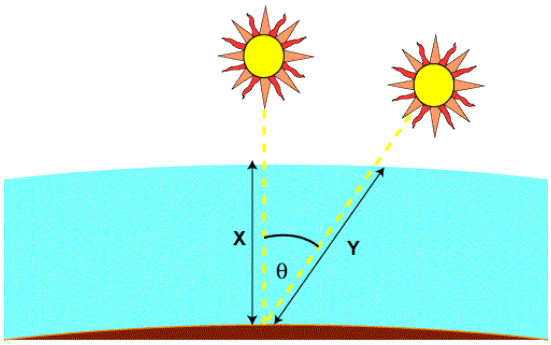

Figure 3 Air mass definition (pveducation, 2017a)

Thus, it is an indicator that quantifies the reduction in power of light that passes through the atmosphere and is absorbed by air and dust – usually used for spectral corrections – and is defined as:

$$AM = \frac{1}{\cos(\theta_z)}$$

Equation 2 Formula for calculation of GHI (pveducation, 2017a)

Where θ_z is the zenith angle. Thus, AM is a function of time and equals 1 when the sun is exactly in overhead position. AM furthermore serves the purpose of definition of standard spectra that facilitate the accurate comparison between solar cells – as mentioned in section 0 of this work. The defined standard spectrum is called AM 1.5 (or AM 1.5G, with G indicating global radiation including direct and diffuse components). (pveducation, 2017a) In order to obtain values of AM related to the corresponding altitude of the observed location, it is required to correct the values of AM. This is done via correction through air pressure. (PVPMC, 2017) AM used in this work for spectral correction therefore refers to the absolute, pressure corrected air mass AM_a at the location of interest related to the standard pressure at sea level (in the unit of Pascal).

$$AM_a = \frac{AM * pressure}{101325}$$

Equation 3 Formula for calculation of pressure corrected AM, AMa (PVPMC, 2017)

AM in this work is provided via calculations through the SOLPOS sun position algorithms of NREL (2000).

2.3.7 Air pressure (p)

Changes in the ambient air pressure can lead to changes in the atmosphere and therefore lead to systematic changes in the solar spectrum. Air pressure can be measured with a barometer. (PVPMC, 2017) In this work it is measured via capacitive silicone pressure sensors and given in the unit of kilopascal (kPa). (Boyd, 2016b)

2.3.8 Relative humidity (RH)

Changes in relative humidity can also significantly influence changes in the solar spectrum. The relative humidity given in percent (%) is a measure of how saturated a gas is with water vapor. It can be measured with hygrometers. In this work the relative humidity is measured via capacitive thin film polymer humidity sensors in 1-second averages. (Boyd, 2016b)

2.3.9 Precipitable water (P_{wat})

Precipitable water (P_{wat}) describes the total amount of water in a vertical column of the atmosphere and is specified through centimeters of liquid water (atm cm). P_{wat} is an important indicator, as water causes heavy spectral absorption. Typical values for P_{wat} range from 1-3 cm in temperate climates and reach values up to 5 cm in tropical locations. Accurate definitions of P_{wat} usually requires measurements via radiosonde balloon soundings. However, it is possible to estimate P_{wat} with sufficient accuracy by using ground-level relative humidity and ambient temperature – as done in this work using the method suggested by Keogh and Blakers (2004). P_{wat}, together with AM, is used for spectral correction in this work.

2.3.10 Turbidity (β)

Turbidity is not used in further observations of this work, but shall be mentioned for completeness – as it is also part of the work done by Keogh and Blakers (2004) and considered to be one of the major influences for spectral losses. It describes the scattering and absorption of light by small particles in the atmosphere (e.g., dust, water, ice, hygroscopic salt particles). High values of turbidity correspond to higher spectral mismatch. (Keogh and Blakers, 2004)

2.3.11 Direct normal irradiance (DNI)

Is defined as the amount of solar radiation per square meters received by a surface that is always normal to the sun's rays. It is given in watts per square meter (W/m^2). The direct normal irradiance (DNI) typically is measured via small aperture instruments called pyrheliometers with thermopile sensors – or other photosensitive sensors. The construction of this instruments limits its measurement to the direct beam and circumsolar radiation normal to the sun. If not measured, DNI can be calculated via co-planar measurements of diffuse and total radiation by devices with a view of 180° and with known incident angle

between measurement plane and the sun. (PVPMC, 2017) In this work, DNI is measured via thermopile pyrheliometers. (Boyd, 2015)

2.3.12 Global horizontal irradiance (GHI)

The global horizontal irradiance (GHI) is defined as the amount of terrestrial irradiance on a surface horizontal to the surface of the earth in watts per square meter (W/m^2). It can be measured with a range of measurement instruments. (PVPMC, 2017) In the case of this work it is measured by a field deployed pyranometer. (Boyd, 2015) If it is not measured, GHI can be calculated using the direct normal irradiance (DNI) and the diffuse horizontal irradiance (DHI) as follows:

$$GHI = DHI + DNI * \cos(\theta_z)$$

Equation 4 Formula for calculation of GHI (PVPMC, 2017)

2.3.13 Diffuse horizontal irradiance (DHI)

The diffuse horizontal irradiance (DHI) is defined as the terrestrial irradiance received by a horizontal surface and scattered or diffused by the atmosphere – given in watts per square meter (W/m^2). It is – as explained above – part of the GHI that is not coming from the sun beam. Typically, DHI is measured also via pyranometers that block the direct beam component of the radiation, in order to measure only the diffuse part of the radiation. If not measured, DHI can be calculated in a similar way as GHI – see above. (PVPMC, 2017)

2.3.14 Direct horizontal and in-plane irradiance

The direct horizontal irradiance is defined as the direct normal irradiance (DNI) on a horizontal plane and the direct in-plane irradiance is defined as the DNI on a tilted plane – both in watts per square meter (W/m^2) – and can be calculated as follows using the angle of incidence to horizontal and tilted surfaces:

$$DirHI = DNI * \cos(AOI_{horizontal})$$

Equation 5 Formula for calculation of the direct horizontal irradiance (PVPMC, 2017)

$$DirII = DNI * \cos(AOI_{tilted})$$

Equation 6 Formula for calculation of the direct in-plane irradiance (PVPMC, 2017)

2.3.15 Global in-plane irradiance (G_{poa})

The global in-plane irradiance (G_{poa}) – or plane of array irradiance – in this work is defined according to IEC 61853-3 draft as the sum of the direct in-plane irradiance and the diffuse in-plane irradiance. (IEC, 2016b) G_{poa} can be measured using reference cells, pyranometers or reference modules mounted in the same orientation of the array/module. (Boyd, 2015) In this work, G_{poa} measured data is available from silicone reference cell measurements,

thermopile pyranometer measurements and silicone photodiode pyranometer measurements – available in watts per square meter (W/m^2). Used measurements for the observations of this work refer to measurements taken by a thermopile pyranometer. G_{poa} can be used to calculate the diffuse in-plane irradiance through the difference of G_{poa} and direct in-plane irradiance as follows:

$$Diff.II = G_{poa} - DirII$$

Equation 7 Formula for calculation of the diffuse in-plane irradiance (IEC, 2016b)

3 Methodology

Based on the above described project goals and scientific questions, the methodological approach of this work is divided into 4 steps: (1) a comprehensive summary of the state of the art of outdoor PV array measurements and performance as well as PV modeling methods, (2) the organization and processing of monitoring data, (3) the evaluation of the goodness of fit of the modeling algorithms applied by the IEC 61853-3 draft, (4) the analysis of inconsistencies of PV modules mounted at different positions within the PV array.

3.1 State of the art research

Section 4 and 5 of this work cover the overview of factors affecting outdoor PV array measurements and performance as well as pertinent existing PV modeling algorithms and standards. Section 6 of the thesis describes the electrical layout of the PV array as well as measurement positions and function principles of applied equipment. Findings related to these topics are based on literature research and work done at NIST, Gaithersburg, and will be referred to accordingly in the respective section of this work.

3.2 Organization and processing of monitoring data

All data analyzed in this work is processed off-line using the commercial software package of MATLAB R2015b (The MathWorks, Inc.). For processing, data was first imported into MATLAB from the database via SQL database queries and import functions for comma separated values files before further including the measured data into the calculation procedures.

3.2.1 Monitoring data and timing

The available monitoring data consists of (1) recorded weather data (ambient temperature, wind speed, global horizontal irradiance, direct normal irradiance, global in-plane irradiance) at or close to the ground-mounted PV array and of (2) operational data of modules mounted within the array (module backside surface temperature, operational current, operational voltage, IV curve measurements). Monitored weather data, including measurements of the module backside surface temperature, is being recorded in 1-second intervals and available as minutely averages as comma separated value (.csv) files accessible via SQL database queries. Operational data of PV modules within the array is being recorded in 1-second intervals, except for the IV-curve traces which are being recorded every 5 minutes – both also available as .csv-files. Each IV curve sweep lasts up to 300 ms, in this time the particular PV module is bypassed from its string. This means that during IV-curve sweeps operational voltage (Vop) and current (Iop) are not being monitored. Next to the weather data and operational PV module data, (3) network cameras are installed around the PV array, taking pictures of the array at certain positions within the array in 5-minute intervals. A sky camera

equipped with a fisheye lens takes horizon to horizon sky images in 5-10-second intervals. An overview of monitored data, parameter abbreviations, measurement intervals and equipment locations is shown in Table 1. Closer information to the corresponding measurement equipment and equipment models can be found in section 6 of this work as well as in Appendix A.

Monitoring data set	Parameter	Abbreviation	Measurement interval	Measurement location
Weather data	ambient temperature	T_{amb}	1 minute averages of 1 second measurements	ground array
	wind speed	v	1 minute averages of 1 second measurements	ground array
	global horizontal irradiance	GHI	1 minute averages of 1 second measurements	ground array
	direct normal irradiance	DNI	1 minute averages of 1 second measurements	rooftop weather station
	global in-plane irradiance	G_{poa}	1 minute averages of 1 second measurements	ground array
PV module operational data	module backside temperature	$T_{mod,meas}$	1 minute averages of 1 second measurement	ground array
	operational current	Iop	1 minute averages of 1 second measurement	ground array
	operational voltage	Vop	1 minute averages of 1 second measurement	ground array
	IV curve traces	-	5 minutes	ground array
Camera pictures	array camera	-	5 minutes	ground array
	sky camera	-	5 - 10 seconds	rooftop weather station

Table 1 Overview of available monitoring data, data abbreviations, measurement intervals and measurement locations (own table)

All measurements are synced once a day to an internet time server and are accurate to within a second. The weather data – including the module backside temperature – is being recorded in 1-second intervals and available as minutely integrated values. The operational data from the 96 IV tracers – that are mounted at 1 module per string within the array – is being recorded in 1-second intervals (operational voltage Vop, operational current Iop) and 5-minute intervals for IV curve sweeps – both sequentially logged according to the corresponding tracer network processing procedure. There are 4 sets of wireless tracer networks in use, each of them containing a certain number of tracers adding up to a total of

96 tracers for the whole array. Tracing Vop and Iop at each module happens at each tracer network separately and unsynchronized, but at similar time steps close to each other. The approximate time difference between the tracer networks at each time step for operational voltage and current ranges from less than 1 second to maximum about 2 minutes[5]. IV sweeps are taken every 5 minutes also unsynchronized and separately within each tracer network. Although not synchronized, the IV sweeps of each tracer network are taken at similar times close to each other with an approximate time difference at each time step between the tracer networks of about maximum 5 minutes. The approximate sweep time for one IV sweep is up to 300 ms. The number of operational 1 second data missing caused through bypassing the modules for IV sweeps is 1 to 2 seconds, with an average of 1.5 seconds. The following figure shows a schematic diagram that visualizes the described behavior of traced data at certain time intervals.

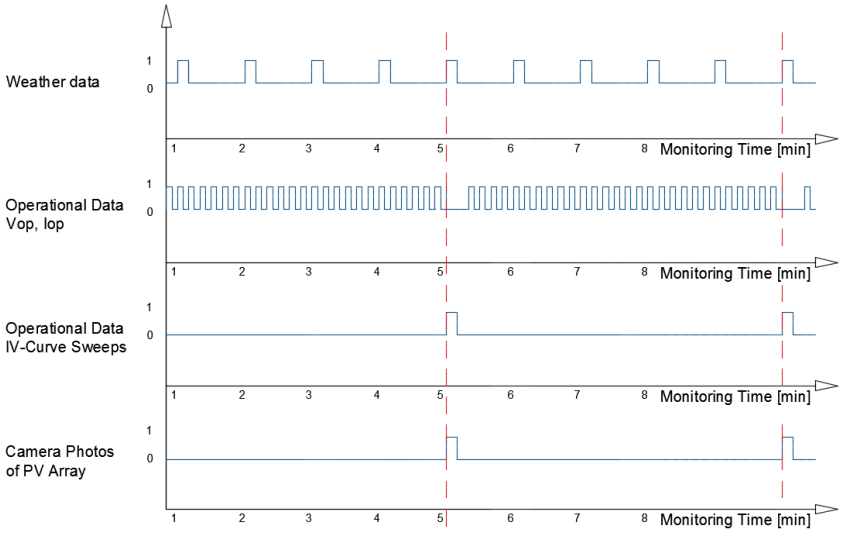

Figure 4 Schematic graph for visualization of weather data, operational data and camera picture timing (own figure)

The data resolution applied in this research focuses on instantaneously monitored, minutely averages of weather and operational data. The available minutely averages of the weather data serve as a time reference. Averages of monitored PV operational data are calculated by averaging all existing 1 second measured data within 1 minute of the time reference. This way, the issue of non-synchronized data monitoring between the 4 tracer networks and the weather data monitoring can be overcome by picking only data that corresponds to the observed minutely time point of the weather data time reference. The operational data being processed to minutely averages starts with the one at the time point closest to time reference time point – i.e. the closest 1 second data point in case of Iop and Vop and the closest 5 minute data point set in case of the IV curve sweeps. For missing data points or data points that are slightly off the corresponding reference minute, a maximum offset to the timing

[5] Based on a sufficient number of self-conducted random sample tests.

reference is implemented. This maximum offset to the minutely timing reference for the 1 second operational data points is set to up to 1 minute and up to 5 minutes for the every 5 minutes measured IV curve sweep data point sets. This means that the maximum allowed difference between modeled and measured data points for comparison is 1 minute for secondly and 5 minutes for 5-minutely monitored data. Thus, data points that do not meet this requirement are not considered for further evaluations. The following figure shows a schematic draft table to better visualize the timing reference and chosen offsets.

Time	Weather data	Operational data	IV sweeps
-	(every 1 minute)	(every 1 second)	(every 5 minutes)
13:09:59		data point 1	
13:10:00	data point 1		data point 1
13:10:01			
13:10:02		data point 2	
.		.	
.		.	
.		.	
13:12:57		data point 175	
13:12:58		data point 176	
13:12:59		data point 177	
13:13:00	data point 2	data point 178	
13:13:01		data point 179	
13:13:02		data point 180	
13:13:03		data point 181	
.		.	
.		.	
.		.	
13:13:59		data point 237	
13:14:00	data point 3	data point 238	
13:14:01		data point 239	
.		.	
.		.	
.		.	
13:14:59		data point 297	
13:15:00	data point 3		data point 2
13:15:01			
13:15:02		data point 298	
13:15:03		data point 299	

Table 2 Schematic visualization of weather data as timing reference: crossed out cells represent data points that are not available, cause through temporarily bypassing the module for IV curve sweeps; grey filled cells represent available data points closest to the timing reference

The choice of processing minutely averaged data is related to the availability of the monitored weather data, which is available as minutely averages through SQL data base queries. This leads to the effect that possible changes of weather within a 1 minute time interval are smoothed by the average calculation. It must be considered that especially the irradiance – that directly affects the PV modules photocurrent generation – could suffer from uncertainties introduced by this smoothing through the average calculation. Ambient temperature, as well as wind speed – indirectly influencing the PV modules open circuit voltage (Voc) and thus the fill factor and efficiency of the PV module – are expected to be less sensitive to this smoothing effect, as it involves also a certain degree of thermal inertia of the PV modules. On the other hand, the minutely averaging of the available weather and operational data leads to the advantage that data anomalies, such as sudden peaks, variation or missing irradiance or wind speed data as well as sudden peaks, variations or missing operational data are smoothed, allowing easier comparison of the monitored data – given the fact that module traces are not happening at the exact same time.

3.2.2 Monitoring data anomalies

Before further processing the accessed monitoring data it is important to identify potential data anomalies and outliers. Those data can be caused by incorrect measurements or measurement noise, which is important to be filtered out or corrected before further analyzing the monitored data. To not lose scientifically interesting data points, it is at the same time crucial to be careful when dealing with samples containing such data. In the current work four types of data anomalies could be identified and corrected or filtered to allow better assessment of data, those are:

- **Missing, not existing data points:**
  These data anomaly relates to data points that do not appear at all in the data sets (also not as time steps), meaning that one or more time steps are not monitored and therefore can not be considered. This type of data anomaly could be detected for the secondly available operational voltage (Vop) and current (Iop), which are not monitored for short time intervals when IV curve sweeps are taken (every 5 minutes) – as mentioned above.
- **Empty values in data samples:**
  Such data points indicate that the measurement at the particular time point was not monitored for unknown reasons, but exists as a time point in the sample. Those data usually are represented as ‘not-a-number’ (NaN) values or a sequence of zeros ‘0’ (for SQL queries), when processing data in MATLAB, and were detected for minutely available irradiance and secondly available operational voltage (Vop) and current (Iop) measurements.

- **Negative values in data samples:**
  Negative values of data that seems unlikely to reach values below zero were identified. This data anomaly could indicate faulty measurement or measurement noise. Affected are mainly irradiance and wind speed measurements (available for every minute), but to some extent also secondly measurements of operational voltage (Vop) and current (Iop). In the case of operational data this could indicate local mismatch behavior within the array, caused by partial shading or inherent differences between the modules. In the case of irradiance measurements, this can be related to the thermopile sensor radiating more outward than receiving – which is usual to happen to thermopile pyranometers at night times. The exact source of this anomaly was not detected within the scope of this work.
- **Sudden peaks or variation:**
  Sudden peaks in data that seem unlikely to reach values above certain limits were identified. This data anomalies could be related to faulty measurement or measurement noise, it occurs mainly for wind speed measurements. The actual source of this anomaly was not detected within the scope of this work.

Missing, not existing secondly available time points of operational data are corrected by minutely averaging the available data points, also explained in section 3.2.1.
In the calculation of minutely averages of the secondly available operational data points within one minute time interval 'NaN' data points are omitted. In the case of irradiance data which is available in minutely time intervals, 'NaN' values are corrected by linear interpolation between the previous and next existing 'faultless' data points.
Negative, unlikely values and sudden peaks in minutely available irradiance and wind speed data sets also are corrected through linear interpolation using the same method. The uppermost acceptable limit of wind speed is set to 20 m/s.
Correction of anomalies of minutely data through linear interpolation is done for anomalies occurring for more than 1 minute period by using the following one-dimensional linear interpolation formula:

$$y = y_0 + \left[\frac{(y_1 - y_0)}{(x_1 - x_0)} * (x - x_0)\right]$$

Equation 8 1D linear interpolation correction of data anomalies (own formula)

3.3 Evaluation of PV modeling algorithms

This chapter describes the methodological approach of this work related to the evaluation of the PV module modeling algorithms suggested by the IEC 61853-3 committee draft. The algorithms of the evaluated standard draft are based on first principles mathematical models and depend on a set of climatic data that serve as input data for its calculation procedure. The aim of the evaluation in this work is to find out about how well the modeling algorithms

of the IEC 61853-3 estimate the operating power and backside surface temperature of field-deployed PV modules at various ranges of weather conditions measured at or close to the ground mounted PV array at NIST.
Besides the climatic weather data as input, the modeling algorithms of IEC 61853-3 require a relatively small number of test results delivered by part 1 and part 2 of the standard. As described in section 0 of this work, the tests of IEC 61853-1 and 2 have been performed at an independent test laboratory for three modules of the same type as deployed in the observed PV array. As for the climatic data set, instead of using climatic reference profiles – as suggested by the IEC 61583-3 – on-site measurements at or close to the observed ground array serve as input for the algorithms of IEC 61853-3.
In total, this work focuses its observations on a set of 24 days of measurement, consisting of 8 characteristic weather conditions. This way it is aimed to cover a range of climatic conditions as wide as possible to allow comprehensive feedback about the behavior of the model's algorithms at various weather conditions – referred to as days with characteristic weather conditions – as well as ranges of irradiance, ambient temperature, wind speed and angles of incidence – referred to as binning of weather data (data bins/data samples). This is of high interest, as the developed standard aims to provide the ability of module power and energy rating at different climatic profiles for different locations.
The following sections of this chapter cover a detailed description of methods applied by the modeling algorithms and calculation procedures of IEC 61853-3, the selection approach of days with characteristic weather conditions (data population), the selection approach of bins (data samples) of relevant weather data as well as the statistical evaluation approaches through exploratory data analysis (EDA).

3.3.1 IEC 61853-3 modeling algorithms

The aim of the international standard IEC 61853 is to establish a method for determining and rating the PV module performance concerning energy and the antecedent power for a set of selected reference climatic profiles, also provided by the IEC standard. Part 3 of the standard contains – next to necessary calculation of correction factors for angle of incidence and spectral response – the procedures for the calculation of the module backside temperature as well as the module output power and, integrated over its time steps, ultimately the energy output of the modelled PV module. This work focuses on the evaluation of module temperature prediction as well as the prediction of the module output power, as these factors ultimately influence the energy output of the PV module according to the suggested calculation procedure. To predict the module temperature as well as the module output power it is required to provide the calculations of IEC 61853-3 with a set of measured input data, based on climatic data sets as well as on preliminary tests done by applying the test procedures of IEC 61853-1 and 2. Figure 1 shows a summary of steps involved in calculation procedure of IEC 61853-3.

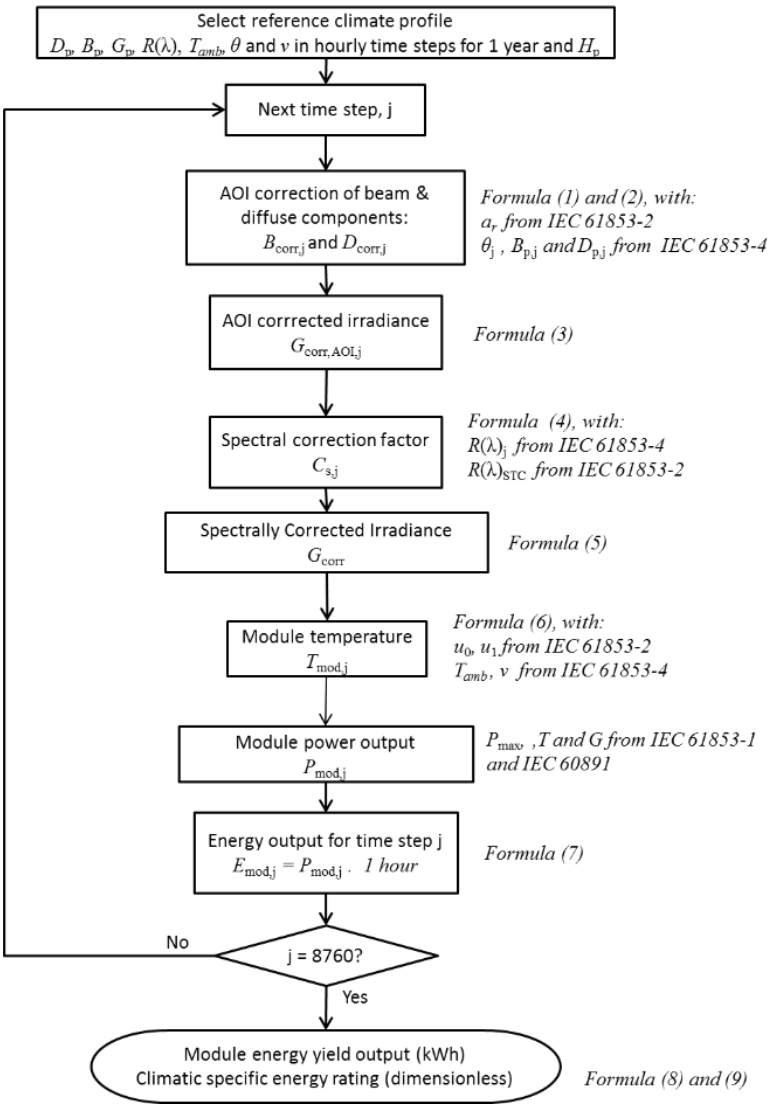

Figure 5 Flow chart of calculation procedure applied by IEC 61853-3 (IEC, 2016b)

More precisely, power prediction in the IEC 61853-3 ultimately is defined by the interpolation of PV module output power between measured points at ranges of irradiance and module temperature. The performance matrix used for interpolation is delivered by the tests of part 1 of the standard. (IEC, 2011) In the following, each of the steps in Figure 5 – until the module output power prediction – is described in detail regarding the approach of this project.

3.3.2 Weather data inputs

The climatic data that serve as input for the above shown modeling algorithms are based on on-site measurements at or close to the PV ground array at NIST – available as minutely averages. A data set of 24 days in total is observed, containing a range of weather conditions as wide as available – as mentioned in section 1.4. The data set focuses on times at which the PV array is not shadowed and/or snow is deposited on top of the deployed PV modules.

Required data include ambient temperature (T_{amb}), wind speed (v), global horizontal irradiance (GHI) and the global in-plane irradiance (G_{poa}). G_{poa} is measured via calibrated thermopile pyranometer[6]. The measurement of the direct normal irradiance (DNI), which is required for the calculation of the direct horizontal irradiance (DHI), the global horizontal irradiance (GHI) and the direct in-plane irradiance (B_p), is taken at a different location close to the array at the installed weather station on the rooftop of Building 226 at NIST's campus – measured via calibrated thermopile pyrheliometer[7]. As mentioned in section 1.4 of this work, the spectral correction of the measured irradiance is considered through the approach of Lee and Panchula (2016) – described in section 3.3.1. Thus, the calculation procedure of IEC 61853-3 regarding spectral correction is not evaluated within the scope of this work. The measured PV module temperature ($T_{mod,meas}$) referred to in this work is the mean of the measured module temperature of 4 RTD probes, positioned according to IEC 60891 at the backside of the PV module deployed in the middle of the observed array. For further information related to measurement position compromises and deployed equipment see section 1.4 and section 6 of this work.

3.3.3 IEC 61853-1 and IEC 61853-2

Part 1 of the standard describes the evaluation procedure of the PV module performance in terms of power over a range of irradiances and temperatures. The main result of part 1 is a performance matrix, containing measured module power for different irradiance and module temperature ranges. (IEC, 2011) This matrix serves as basis for the determination of module power at certain measured module temperature and irradiance ranges. Part 2 of the standard describes the evaluation procedure of the PV module performance in terms of power over a range of angle of incidences and sunlight spectra as well as the estimation of module temperature. The result of part 2 are a set of characteristic parameters, required for the calculation procedures in IEC 61853-3. (IEC, 2016a) Procedures of part 1 and 2 of the IEC standard have been performed by an independent laboratory, CFV Solar Test Laboratory, for three PV modules of the same type as deployed in the observed PV array – as described in section 1.4 of this work. (CFV, 2016)

Regarding the performance matrix measurements performed at the test laboratory, test points for the multi-irradiance and multi-temperature measurements cover irradiances from 100 to 1100 W/m^2 and module temperatures from 15 to 75°C, measured by using an A+A+A+ solar simulator and an integrated thermal chamber for the test module, applying laminar air flow and continuously monitoring of the module temperature at 4 points at the module's backside through calibrated RTD sensors. (CFV, 2016) The following table

[6, 7] Calibrated to the response (µV/(W/m^2)) at 45° incident angle with an uncertainty of about 3 % over the entire incident angle range (0-90°), BOYD, M. T. 2016a. Broadband Outdoor Radiometer Calibration Shortwave. Gaithersburg, MD, USA: NIST.

illustrates the available multi-irradiance and multi-temperature measurements of the performance matrix, measured at CFV Solar Test Laboratory.

Irradiance (W/m^2)	Temperature			
	15°C	25°C	50°C	75°C
1100		⊙	⊙	⊙
1000	⊙	⊙	⊙	⊙
800	⊙	⊙	⊙	⊙
600	⊙	⊙	⊙	⊙
400	⊙	⊙	⊙	⊗
200	⊙	⊙	⊗	⊗
100	⊙	⊙	⊗	⊗

⊙ Measured and required by the IEC 61853-1 standard
⊗ Additional test points; Measured but not required by the IEC 61853-1 standard

Table 3 Available measurement points of performance matrix (CFV, 2016)

Results of part 2 of the standard deliver coefficients necessary for the modeling of the module temperature. Those are 'u_0', being the constant heat transfer coefficient given in [$W/m^2°C$], and 'u_1', being the convective heat transfer coefficient given in [$Ws/m^3°Cs$]. (IEC, 2016a) The required angular loss coefficient, 'a_r', is not delivered by the preliminary tests. Therefore the applied coefficient a_r in this work refers to research done by Martin and Ruiz (2000), relating to typical crystalline silicone modules. A similar approach can be found in the work done by Huld and Amillo (2015).

3.3.4 AOI correction – Model of Martin and Ruiz (2000)

The correction for effects related to angle of incidence (AOI) refer to optical losses of PV modules working in field conditions. This is, because for most of the existing PV applications angles of incidence of the solar radiation vary from the normal incidence at standard test conditions (STC). Thus, solar radiation that hits the PV module's surface at angles that deviate from the normal to the surface suffer from increased reflection off the module and therefore do not contribute to the photocurrent. (Huld and Amillo, 2015) The figure below gives a schematic overview of angular losses of deployed PV modules and measurement equipment.

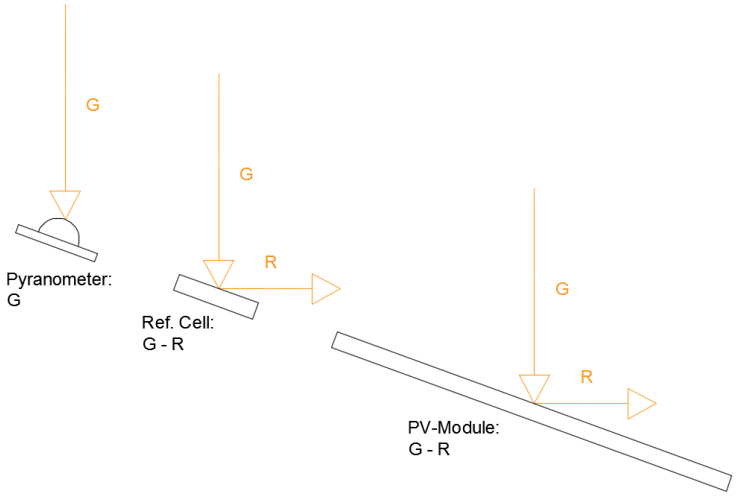

Figure 6 Schematic figure of PV module, pyranometer and reference cell and optical losses through reflection (own figure)

In the present work, angular loss corrections apply to the measurements taken by the thermopile pyranometer (G_{poa}) as well as the thermopile pyrheliometer (DNI) – as they are measuring in-plane irradiance with (almost) no reflective losses and, after AOI and spectral correction are ultimately used for further prediction of module temperature and module output power through the calculation procedure of IEC 61853-3. The AOI corrected in-plane irradiance $G_{corr,AOI}$ is calculated according to the procedure suggested by Martin and Ruiz (2000), as follows:

$$G_{corr,AOI} = B_{corr,AOI} + D_{corr,AOI}$$

Equation 9 Corrected in-plane global irradiance $G_{corr,AOI}$ (IEC, 2016b)

With $B_{corr,AOI}$ being the AOI corrected in-plane direct irradiance and $D_{corr,AOI}$ the AOI corrected diffuse irradiance, calculated as follows:

$$B_{corr,AOI} = DNI * \cos\left(AOI_{tilt,module}\right) * \left[\frac{1 - \exp(-\frac{\cos\left(AOI_{tilt,module}\right)}{a_r})}{1 - \exp(-\frac{1}{a_r})}\right]$$

Equation 10 Corrected in-plane direct irradiance $B_{corr,AOI}$ (IEC, 2016b)

$$D_{corr,AOI} = \left[G_{poa} - DNI * \cos\left(AOI_{tilt,module}\right)\right] * \left\{1 - exp\left[-\frac{1}{a_r} * \left(\frac{4}{3\pi} * \left(\sin\beta + \frac{\pi-\beta-\sin\beta}{1+\cos\beta}\right) + (0.5 * a_r - 0.154) * \left(\sin\beta + \frac{\pi-\beta-\sin\beta}{1+\cos\beta}\right)\right)\right]\right\}$$

Equation 11 Corrected in-plane global irradiance $D_{corr,AOI}$ (IEC, 2016b)

With a_r being the above mentioned dimensionless, empirically determined angular loss coefficient and β being the PV module surface tilt. The angular loss coefficient a_r suggested by Martin and Ruiz (2000) is applied, which is typically 0.169 for crystalline silicone technologies, with higher values corresponding to higher angular losses.

$a_{r,c\text{-}Si}$ [-]
0.169

Table 4 Typical value for angular loss coefficient for c-Si PV modules (Martin and Ruiz, 2000)

This empirical parameter is mainly influenced through the optical transmittance of the PV module – being strongly dependent on the degree of dust deposition, but as a second-order effect as well influenced by the type of technology in use. (Martin and Ruiz, 2000) According to Martin and Ruiz (2000), typical values for m-Si of 0.169 modules become 0.20 or 0.27 if a moderate or thick dust layer is deposited on its surface, leading to a minimum possible annual performance loss of about 3 % for the investigated ranges of latitudes and tilt angles in their study. For this work, a value of 0.169 is chosen, assuming insignificant and uniform dust deposition across the observed PV array at the chosen weather data set of 24 days. Thus, the time since the last rain fall – i.e. cleaning of dust – is not considered in this data set. The dependence of the optical transmittance of the PV module on a_r can also be illustrated through the following figure, showing the angular factor (relative reflectance) of a module as a function of AOI and a_r.

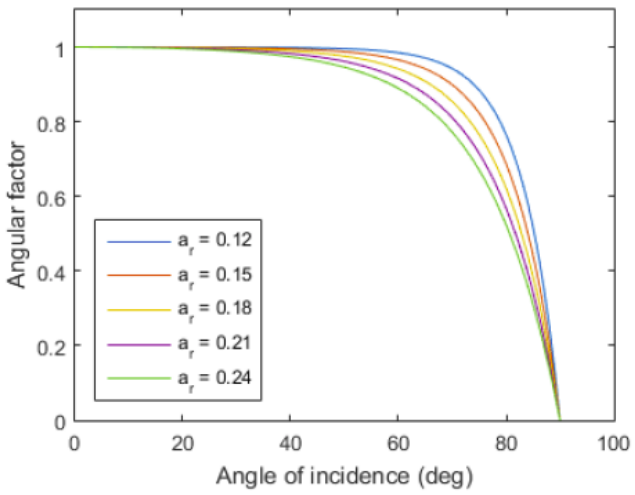

Figure 7 Relative reflectance of a PV module as a function of AOI and a_r (IEA, 2017c)

Angles of incidence are calculated according to the above described formula using the MATLAB function ‘pvl_getaoi’, which is part of the online for free available MATLAB toolbox provided by the PVPMC platform and requires as input the following data. (PVPMC, 2017) The function ‘pvl_getaoi’ refers to the work done by King et al. (1997).

3.3.5 Spectral correction – Model of IEC 61853-3 and Lee and Panchula (2016)

As mentioned in the introduction, the energy conversion efficiency of PV cells depends also on the wavelength of the incoming light – which is referred to as spectral response. Spectral responsivity depends on the used technology, meaning that depending on the properties of the used PV technology, photons with specific energy (wavelength) can excite electrons in the PV material or not. (pveducation, 2017c) The spectral response (SR) of a PV module is defined as the fraction of available irradiance that is converted into current, given in units of A/W. SR is a function of wavelength and related to the quantum efficiency (QE, unitless), as follows:

$$SR_\lambda = QE_\lambda * \lambda * \frac{e}{h * c}$$

Equation 12 Spectral response (SR) as a function of the wavelength and the quantum efficiency (pveducation, 2017c)

Where λ is the wavelength of the light, e is the electron charge (1.602176565*10^-19 Coulomb), h is Plank's constant (6.62606957*10^-34 J*s), and c is the speed of light (2.99792458*10^8 m/s). (PVPMC, 2017) The quantum efficiency (QE) refers to the measurement of the ratio of the number of carriers collected by the PV module/cell to the number of photons of energy incident onto the PV module/cell. (PVPMC, 2017) The figure below shows example of typical spectral response curves from a variety of PV technologies.

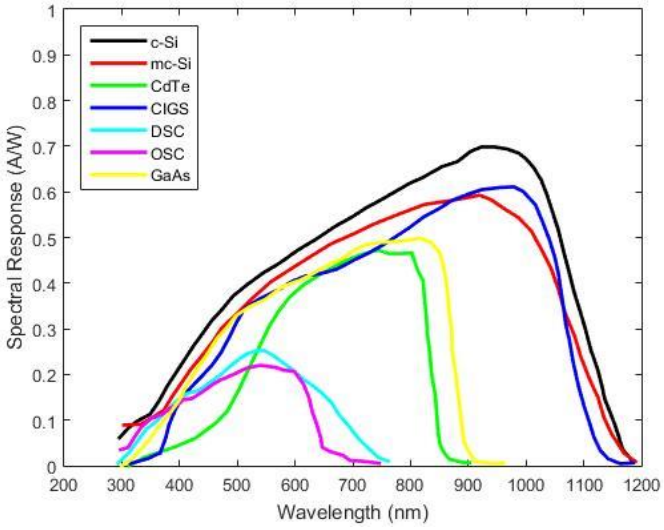

Figure 8 Typical spectral responses of different PV technologies (PVPMC, 2017)

As the spectrum of the light – and thus also the wavelength and energy of photons – reaching the PV module varies with time, the PV module output power – next to the total in-plane irradiance – also depends on the spectrum of the light at each instantaneous time step. (Huld et al., 2015) To consider this effect, spectral correction in the IEC 61853-3 draft's calculation

procedure is considered by using a correction factor C_s to calculate the spectrally corrected global in-plane irradiance ($G_{corr,AOI,spectral,1}$) as follows (IEC, 2016b):

$$G_{corr,AOI,spectral,1} = G_{corr,AOI} * C_s = G_{corr,AOI} * \left[\frac{1000 * \int_{\lambda_s}^{\lambda_e}(S(\lambda) * R_{corr,AOI}(\lambda) * d\lambda)}{G_{corr,AOI} * \int_{\lambda_s}^{\lambda_e}(S(\lambda) * R_{STC}(\lambda) * d\lambda)}\right]$$

Equation 13 Corrected in-plane direct irradiance Gcorr,AOI,spectral,1 (IEC, 2016b)

With S(λ) being the spectral response, $R_{corr,AOI}$ (λ) the spectrally resolved in-plane irradiance and R_{STC} (λ) being the corresponding spectral intensity for the standard test condition (STC) spectrum AM 1.5 according to IEC 60904-3 – using the integration limits from 300nm to 4000nm. (IEC, 2016b)

As mentioned in section 1.4 of this work, the spectral correction according to procedures in IEC 61853-3 is not evaluated within the scope of this work due to lack of data availability on the one hand, as well as due to an up to this time not fully defined approach of the IEC 61853-3 calculation procedures regarding spectral correction. To consider the spectral correction in this work – and thus make predicted temperature and power values fully comparable – the approach of Lee and Panchula (2016) is used to calculate a dimensionless spectral mismatch factor to correct the measured global in-plane irradiance. This approach – also suggested by PVPMC (2017)– calculates a correction factor for the irradiance from atmospheric precipitable water (P_{wat}) and the absolute air mass (AM_a) for certain PV technologies with characteristic QE curve profiles. The spectrum considered in this approach ranges from 280nm to 2800nm and does not cover the entire required spectral range from 300nm to 4000nm according to IEC 61853-3 procedure. (IEC, 2016b) The therefore used functions are part of the PV library that is online available at the PVPMC platform: 'pvl_FSspeccorr', 'pvl_calcPwat', 'pvl_absoluteairmass'. (PVPMC, 2017) Using the calculated relative air mass (AM_r) and measured site pressure (p_s), the function 'pvl_absoluteairmass' provides the absolute air mass (AM_a) for locations not at sea level (i.e. not at standard pressure) – as described in section 2. The precipitable water (P_{wat}) in the atmosphere is calculated by using the function 'pvl_calcPwat' with the measured ambient temperature (T_{amb}) as well as the measured relative humidity (φ_r) as input values – as described in section 2 through the approach of Keogh and Blakers (2004). The function 'pvl_FSspeccorr' ultimately allows to calculate the spectral mismatch factor using the calculated precipitable water (P_{wat}) and absolute air mass (AM_a). (PVPMC, 2017)

$$G_{corr,AOI,spectral,2} = G_{corr,AOI} * C_s(AM_a, P_{wat})$$

Equation 14 Corrected in-plane direct irradiance Gcorr,AOI,spectral,2 (PVPMC, 2017)

3.3.6 PV module temperature calculation – Model of Faiman (2008)

The module temperature measured at instantaneous time steps is mainly influenced by the incoming solar irradiance, the module's optical, electrical and thermal properties as well as its (convective) heat exchange with the environment it is mounted in. (Koehl et al., 2011) There are several approaches that aim to model the temperature of PV modules. An overview of existing proposals for the simulation of the module temperature can be found in the survey done by Skoplaki and Palyvos (2009). The model to estimate the PV module temperature suggested by the IEC 61853-3 draft is derived from the energy balance of solar thermal collectors (Hottel–Whillier–Bliss equations[8]), developed and validated by Faiman (2008). The module temperature in this model, also used in the draft of IEC 61853-3, is calculated using the following formula:

$$T_{mod,IEC} = T_{amb} + \frac{G_{corr,AOI}}{u_0 + u_1 * \nu}$$

Equation 15 Estimated module temperature according to model of Faiman (2008)

Where T_{amb} is the ambient temperature, $G_{corr,AOI}$ is the in-plane irradiance, corrected for angle of incidence effects (see above) and ν is the wind speed at the height of the module. The parameters u_0 and u_1 are results from the test procedures in IEC 61853-2 and describe the effect of constant heat transfer and convection on the module. Those are constants and are retrieved through a least-squares linear fit of measured data with u_0 being the intercept value and u_1 being the slope value. According to the test results of the IEC 61853-2 tests performed at CFV Solar Test Laboratory, the coefficients for u_0 and u_1 are:

u_0 [W/m²°C]	**u_1 [W/m³Cs]**
29.9	5.586

Table 5 Thermal model coefficients from IEC 61853-2 (CFV, 2016)

The approach of Faiman (2008) is based on the assumption that the thermal mass of conventional PV modules – glass front side, polymer encapsulant back side – has a negligible effect on the heat exchange with its environment. This way, it is possible to predict the temperature of the PV module based on ambient temperature, incident irradiance and wind speed by using only two numerical constants that can be derived by relatively simple experiments performed with the procedures of IEC 61853-2. (IEC, 2016a) Faiman (2008) validated his model for different module types, evaluating temperature data for 5 minute averages. Results of the validation showed RMS errors ranging from 1.86 to 2.13 °C – meaning the module power to be determinable to a precision of about ±1 %, considering

[8] Hottel HC, Whillier A. Evaluation of flat plate collector performance. Transactions of the Conference on the Use of Solar Energy, Vol. 2, Part 1, University of Arizona Press, 1958; p. 74.

typical temperature coefficients of power ratings of conventional PV modules of about 0.5 % per K under stable weather conditions. (Faiman, 2008)
Like in the work done by Faiman (2008) conventional m-Si cell PV modules observed in this work are mounted on an open rack, being exposed to convective cooling and radiation exchange with its environment. Unlike in the work done by Faiman (2008), the evaluation of the calculation procedures of IEC 61853-3 in this work is done for 1 minute averages of monitored data instead of 5 minute averages – as mentioned in section 3.2.
Furthermore, Koehl et al. (2011) investigated the model of Faiman (2008), pointing out that the influence of infrared irradiation exchange with the cold sky and the natural convection at low wind speeds and low irradiation are neglected in this model. However, the investigations of Koehl et al. (2011) showed that the impact of radiation cooling and natural convection can be neglected for wind speeds above 2 m/s – showing main effects of radiation cooling during night times which are not relevant for the solar energy generation.

3.3.7 PV module output power calculation – Interpolation method

As mentioned above, the method used to determine the PV module output power is based on the interpolation between measured module power at ranges of irradiance and module temperature. The procedure of IEC 61853-3 suggests to use calculated parameters for irradiance as well as module temperature to be used for the determination of the PV module output power by using the performance matrix provided by IEC 61853-1 – shown in section 3.3.3 of this work. (IEC, 2016b) This approach is referred to as ‘interpolation method’ and requires two-dimensional, bilinear interpolation between existing points within the performance matrix. The interpolation method already has been analyzed by Whitaker and Newmiller (1998), NREL, and lead to the following observation:

“The most notable behavior of the Interpolation model is its error at low irradiance. […] The weakness of the interpolation model is that you must actually extrapolate to obtain points beyond its measurement range. At the low irradiance end, linear extrapolation is used where the performance is becoming non linear. Any error in the four points used for extrapolation will be magnified for large extrapolation. Thus, a requirement for use of the Interpolation model is the to have measurements covering the entire range of expected weather conditions.” (Whitaker and Newmiller, 1998)

This means that the approach through linear interpolation brings about the compromise with the known non-linear behavior of PV modules, especially at low irradiances or at ranges that are not included in the performance matrix. (Whitaker and Newmiller, 1998)
Interpolation is done via two dimensional bilinear interpolation of power through the two variables irradiance ($G_{corr,AOI,spectral,2}$) and module temperature ($T_{mod,IEC}$) – as suggested in the IEC 61853-3 standard draft. (IEC, 2016b) Conventional 2D-bilinear interpolation of power

values of the performance matrix has been performed using the following formula (own formula):

$$P(G,T) = \frac{(P_{11} * (G_2 - G) * (T_2 - T) + P_{21} * (G - G_1) * (T_2 - T) + P_{12} * (G_2 - G) * (T - T_1) + P_{22} * (G - G_1) * (T - T_1)}{(G_2 - G_1) * (T_2 - T_1)}$$

Equation 16 2D bilinear interpolation of power through the performance matrix depending on irradiance and module temperature (own formula)

With P, G and T being the interpolated points within the grid square defined by four given points P_{11}, P_{21}, P_{12}, P_{22} at each time step – as also shown in the following figure.

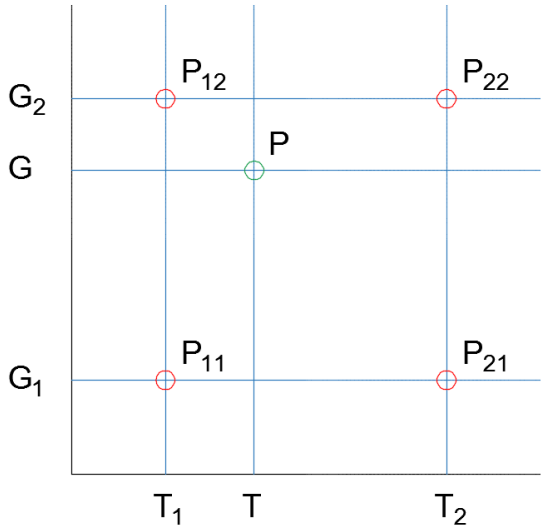

Figure 9 Schematic figure of grid square for the 2D bilinear interpolation method of the performance matrix (own figure)

However, in some cases the module temperature and/or irradiance values might be outside the range covered by the performance matrix of IEC 61853-1, as also mentioned in the research done by Whitaker and Newmiller (1998). To also consider these values, it is necessary to extend the matrix's points to the desired irradiance and module temperature range to also consider these values during the interpolation procedure explained above. This is done through one-dimensional linear extrapolation – as suggested by the IEC 61853-3 draft. Extrapolation of the matrix parameters is done using the following formula:

$$y(x) = y_1 + \left[\frac{(x - x_1)}{(x_2 - x_1)} * (y_2 - y_1)\right]$$

Equation 17 1D linear extrapolation of performance matrix (own formula)

The figure below schematically illustrates the linear extrapolation of performance matrix parameters.

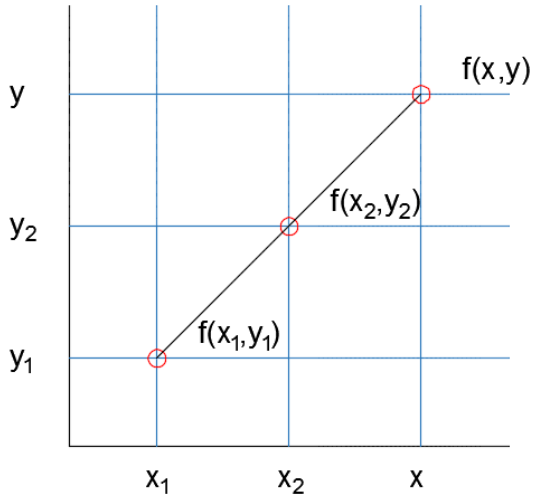

Figure 10 Schematic figure of linear extrapolation of performance matrix parameters (own figure)

The extrapolated performance matrix can be found in the Appendix B of this work – together with the not extrapolated performance matrix. To cover the majority of irradiances and module temperatures of the observed data set population, the performance matrix especially requires extrapolating to lower ranges of module temperature and irradiance. This also increases the chance of magnifying errors in the performance matrix and can lead to difficulties for the prediction of module output power, further analyzed in section 7 of this work – as also mentioned above and discussed in Whitaker and Newmiller (1998).

The suggested approach through linear inter-/extrapolation determines the module output power through the two dimensional available performance matrix describing the module output power as a function of $G_{corr,AOI,spectral,2}$ and T_{mod}. However, this approach neglects possible cross-dependencies to other influences (e.g. temperature dependence of spectral response) which would require a multidimensional test matrix – as also discussed in Whitaker and Newmiller (1998). Within the scope of this work it is intended to discuss possible cross-dependencies regarding irradiance, ambient temperature, wind speed and angle of incidence.

3.4 Spatial PV array performance analysis

To find out about whether the above explained comparisons related to the IEC 61853-3 modeling algorithms have any dependence on where a particular module is located inside the PV array, this work also analyzes the 96 measured and traced PV modules according to their positions within the array. The aim is to analyze differences between positions of individual and groups of modules for specific days with characteristic weather conditions as well as ranges (data samples) of weather parameters.

3.4.1 Differences in local irradiance and module temperature

Differences between the PV module positions are – besides comparing operational power (Pop) – also analyzed using IV curve parameters. Specifically, the open circuit voltage (Voc) and short circuit current (Isc), as determined from each IV curve, serve as indirect measurements of the module's temperature and its absorbed irradiance, respectively. These two parameters can thus be used to help identify and explain performance differences among the spatially distributed, 96 monitored modules within the 1152-module array. The translation into actual module temperature and irradiance values can for example be accomplished by following procedures described in IEC 60891, via using the available performance matrix. (IEC, 2009)

Increased PV module/cell temperatures affect the PV output power negatively. This effect is mainly caused by the inability of the PV junction to separate charges – as the increased lattice vibration at higher temperatures interferes with the movement the charge carriers. This interference leads to a decreased band gap which causes more electrons to jump in the conduction band and therefore decreases the open-circuit voltage (Voc) significantly – notably this same temperature effect (decreased band gap) causes the short-circuit current (Isc) to increase very minimally. (Yahyaoui and Segatto, 2017) The following figure shows the effect of temperature on the IV characteristic curve parameters Voc and Isc.

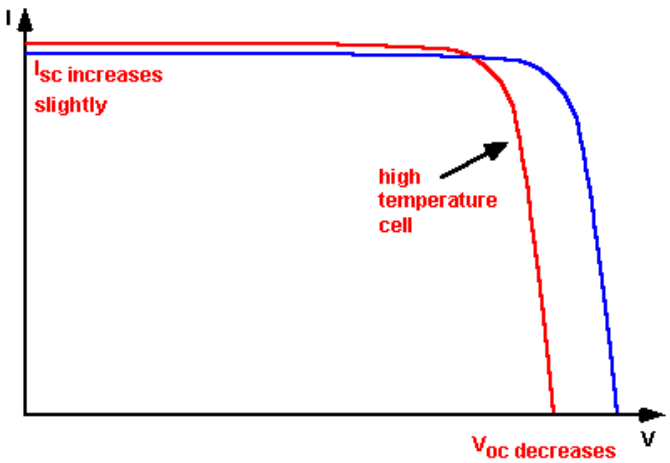

Figure 11 Effect of temperature on IV curve characteristic shape (pveducation, 2017b)

Furthermore, while Isc depends linearly on light intensity, Voc depends logarithmically on changes in the light intensity. This non-linear dependence is pronounced at lower light intensities and especially becomes of high importance for example with PV modules/cells that have lower shunt resistances. (pveducation, 2017a) However, for the scope of this work it is assumed that possible inherent differences and degradation are negligible for the observed PV array – as mentioned initially and described in section 4.4. Other possible mismatch effects are explained in section 4 of this work. Nevertheless, a first step to identify the mentioned effects is through the analysis of IV curve parameters such as Voc and Isc.

3.4.2 Observed PV module positions

The analysis of the module performance at different positions within the array aids the work of Fairbrother (2017), who is investigating differences in PV back sheet degradation and gradient exposure effects among modules within an operating array. According to Fairbrother (2017) differential exposure conditions caused by the surroundings (e.g. different ground covers, buildings, trees, etc.) influence the amount of UV light that strikes the back of the modules. The different exposures lead to unique patterns of back sheet degradation in which modules at certain positions in the array show more signs of degradation. (Fairbrother, 2017) Despite these findings after four years of exposure, no clear relationship was identified between the level of back sheet degradation and the PV modules' electrical performance. Regardless of this (current) lack of correlation, the position grouping suggested by Fairbrother (2017) should serves as a reference case.

The following positions of traced PV modules within the ground array are grouped together and analyzed collectively (numbers between parentheses show amounts of PV modules within the group):

- Modules in top rows (12)
- Modules in middle rows (36)
- Modules in bottom rows (12)
- Modules in the middle of the array (28)
- Modules at the edge of the array (42)
- All modules including shed 1 and shed 5 (96)

The figure below shows the five sheds of the observed ground array. The colored cells inside each shed represent the 96 monitored PV modules, one within each array series string. Red lines indicate all modules mounted at the edge as well as all modules mounted in the middle of the PV array. The labels top, middle and bottom refer to all modules mounted in top, middle and bottom rows of all observed sheds.

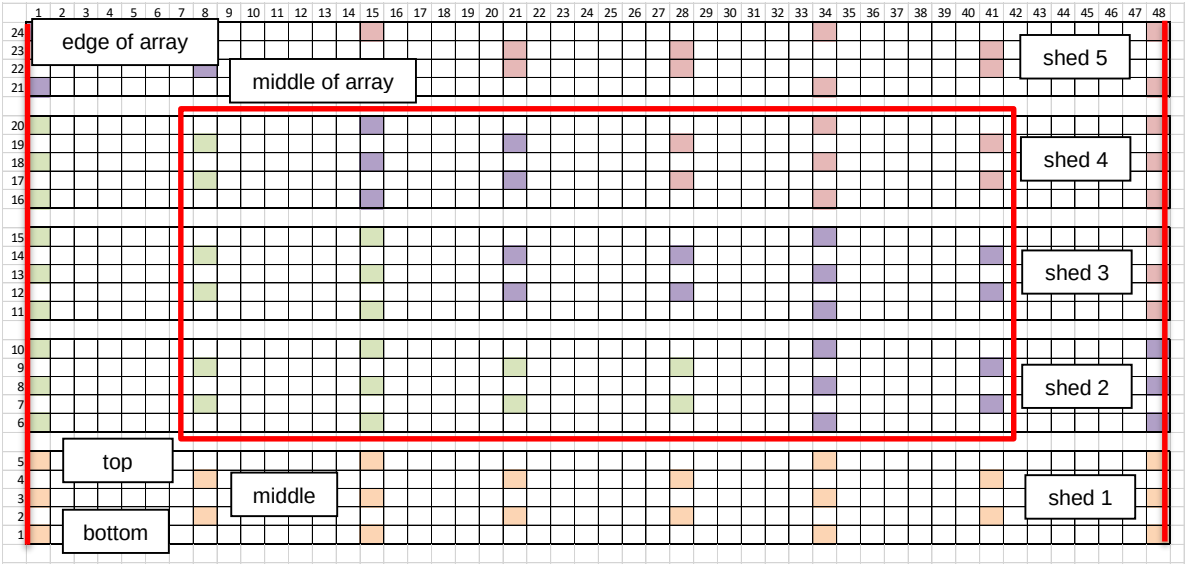

Figure 12 Observed position groups within the PV array

Modules in top, middle and bottom row positions do not include modules deployed at the edge of the PV array. Furthermore, shed 5 contains only 4 rows of PV modules – as mentioned in section 2.1.

3.5 Days with characteristic weather conditions

The above described calculation procedures, suggested by the IEC 61853-3, are evaluated for a data set of 24 days, containing in total 8 characteristic weather conditions (i.e. 3 days per weather condition). This approach permits evaluating the model for as wide a range of weather conditions as possible, while keeping the data processing effort reasonable. This allows a better understanding of inconsistencies within the ground array at certain weather conditions and helps understanding deviations between measurements and modelled data using the algorithms of IEC 61853-3. The 8 characteristic weather conditions are distinguished by their daily averages for irradiance, ambient temperature and wind speed. The data used to calculate these averages are determined from measurements made during the daylight period (sun zenith angle < 90) when the array is completely unshaded and clear of any snow accumulation. This fully illuminated condition is verified using photos of the entire array which are available approximately every 5 minutes for each of the observed days – as shown in the following example:

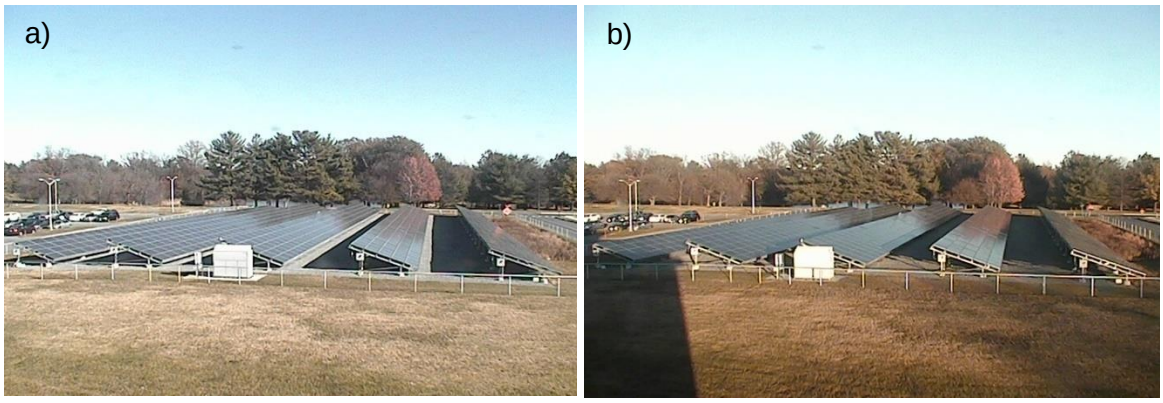

Figure 13 Verification of occurrence of no shading on the array, a) no shading: 11/21/2016 at 13:00, b) interrow shading: 11/21/2016 at 16:00

A table with an overview of the examined daytimes for each of the observed days can be found in the Appendix C. The mentioned 8 characteristic weather conditions are categorized into values of high or low daily averages of irradiance, ambient temperature and wind speed. Table 6 gives an overview of this categorization into 8 characteristic weather conditions of high/low irradiance, ambient temperature and wind speed ranges.

Category	Irradiance	Ambient temperature	Wind speed
1	High	High	High
2	High	High	Low
3	High	Low	High
4	High	Low	Low

5	Low	Low	Low
6	Low	Low	High
7	Low	High	Low
8	Low	High	High

Table 6 Categorization of 8 characteristic weather conditions

In order to increase the amount of data points for each of the characteristic weather conditions, 3 days per category are selected. The following table shows the days observed in this work (data population), indicating high and low values by conditional formatting through cell colors.

irradiance/tamb/wind	day	Irradiance [W/m²]	Ambient temperature [°C]	Wind speed [m/s]
H/H/H	9/11/2016	540	26	3
H/H/H	10/10/2016	606	14	2.5
H/H/H	10/9/2016	526	16	4.2
H/H/L	8/28/2016	552	30	1
H/H/L	9/12/2016	590	25.3	1
H/H/L	4/10/2017	554	22.36	1.97
H/L/H	11/21/2016	540	3.9	4.1
H/L/H	2/13/2017	592	3.8	5
H/L/H	11/22/2016	525	5.5	2.9
H/L/L	12/20/2016	500	1	1
H/L/L	12/25/2016	480	7	1.4
H/L/L	12/19/2016	438	-0.4	1.6
L/L/L	1/5/2017	93	-0.5	1.4
L/L/L	1/9/2017	300	-5	1.7
L/L/L	12/16/2016	130	-6	1.65
L/L/H	2/16/2017	366	1.2	4
L/L/H	2/9/2017	270	-0.1	5
L/L/H	1/24/2017	240	6	4
L/H/L	8/9/2016	184	25.5	1.2
L/H/L	11/25/2016	130	12	1
L/H/L	8/1/2016	390	28.3	1.2
L/H/H	12/27/2016	265	16	2.5
L/H/H	11/11/2016	400	15	3.3
L/H/H	12/18/2016	44	12	3

Table 7 Observed days (data population) with characteristic weather conditions (own table, H = high, L = low, color code: high = green to low = red)

3.6 Data binning to various ranges of weather conditions

To facilitate the evaluation of the modeling algorithms used by IEC 61853-3, irradiance, ambient temperature, wind speed as well as angles of incidence values of the above mentioned data set population are separated into bins (data samples). Binning data also provides helpful information when analyzing inconsistencies among the PV modules within the array field. Selecting bin widths is aided by plotting histograms for each parameter, as shown in the following figures.

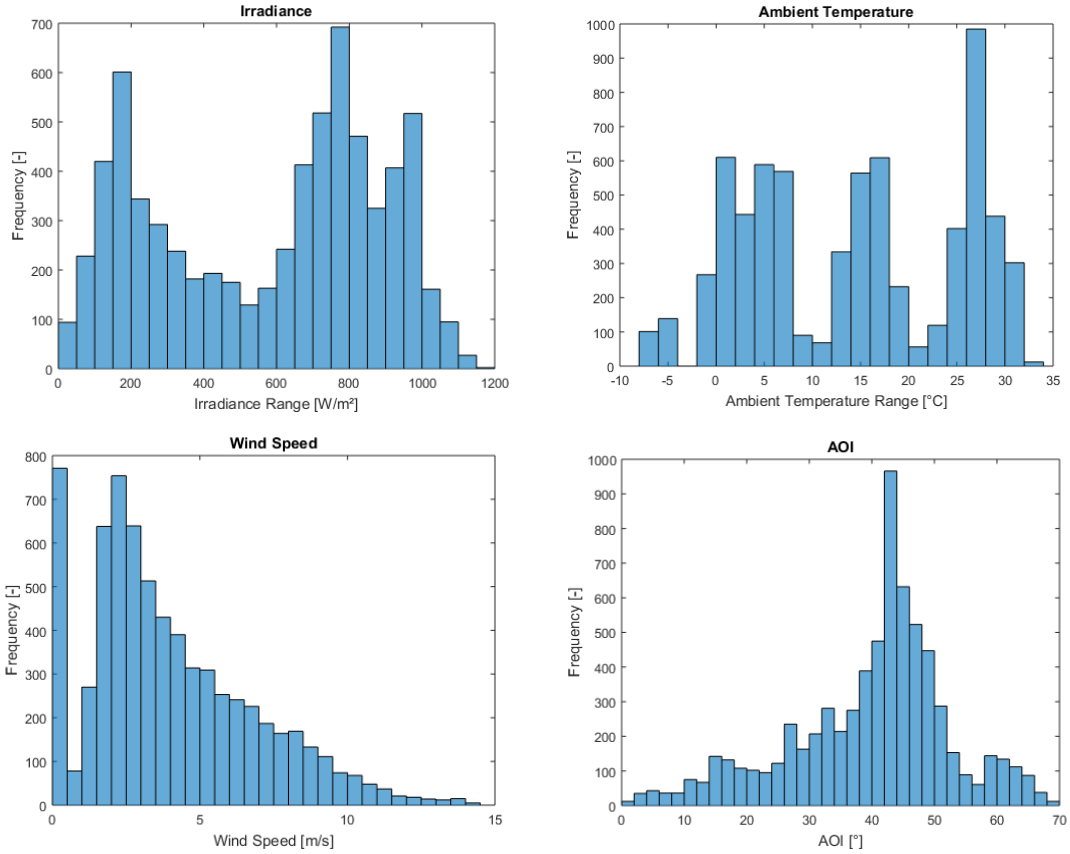

Figure 14 Frequency-range histograms for irradiance, ambient temperature, wind speed and angles of incidence in the observed data set of 24 days

The histograms summarize the distribution of the available data set graphically and thus are a useful tool for choosing bin ranges (data samples). Based on the histograms in Figure 14, the following upper and lower bin limits are examined in this work:

Parameter	Range 1	Range 2	Range 3
Irradiance	0 – 400 W/m²	400 – 800 W/m²	800 – 1200 W/m²
Ambient temperature	-10 – +13 °C	+13 – +36 °C	-
Wind speed	0 – 3 m/s	3 – 6 m/s	6 – 9 m/s
Angle of incidence	0 – 45°	45 – 60°	60 – 70°

Table 8 Evaluated binning ranges for irradiance, ambient temperature (tamb), wind speed and angles of incidence (AOI)

The goal with using binned data samples is to evaluate the sensitivity of the IEC 61853-3 algorithms to irradiance, ambient temperature, wind speed and angles of incidence. Identifying if the IEC algorithms predict better or worse for a given set of weather conditions is of high interest because the current draft of the standard aims to provide a few sets of reference climatic profiles. (IEC, 2016c) Insight into the accuracy of the IEC predicted energy yields for each of these reference climates will be gained from documenting how the accuracy of the IEC predictions change with the weather conditions.

The above mentioned 11 ranges of irradiance, ambient temperature, wind speed and angles of incidence allow the evaluation of IEC predictions for the independent variation of each bin individually, as well as the cross-dependent variation of each bin – allowing in total 54 combinations of bins (3*2*3*3). A table of all combinations possible can be found in the Appendix D.

3.7 Exploratory data analysis (EDA)

The results from exercising the modeling algorithms of the IEC 61853-3 committee draft are evaluated using an exploratory data analysis (EDA) approach. EDA covers a variety of techniques for the statistical evaluation of data sets. (NIST/SEMATECH, 2012)
The main focus is on how well the modeled values agree with the measured data. In order to correctly evaluate the goodness of fit of the modeling algorithms applied by IEC 61853-3, the following table parameters and graphical techniques are applied. Differences between traced module positions within the ground array are also investigated. The following chapters also describe methods used for comparing modules based on their positions within the PV array.

3.7.1 Linear regression model approach

A common approach for the comparison of a range of monitoring parameters being related to each other is to plot and linearly fit measured and modeled parameters. This approach is recommended by the IEA (2014a) in a report on good practices for the analysis of PV array monitoring data. Using a linear regression is justified if the measured and modeled data show a linear relationship, the residuals are independent and normally distributed and show constant variance (homoscedasticity). Thus, identifying significant changes in the statistical linearity makes it possible to identify anomalies among the monitored versus modeled data. (IEA, 2014a)
The linear regression model in this work is obtained by using the MATLAB function ‘fitlm’, which is able to return a linear model fit to the measured data. (MathWorks, 2017b) As modelled data in this work is obtained by following the procedures described in IEC 61853-3, the function is used to provide characteristic parameters retrieved by comparing modelled versus measured data – dependent and independent variables. This way it is possible to perform graphical analysis of residuals via normal probability plots or other graphical analysis tools as well as the calculation of the coefficient of determination (R^2) with the help of the built-in function of MATLAB. Some of the observed parameters are explained in the following chapters.

3.7.2 Statistical diagnostic parameters

Statistical diagnostic parameters used in this work serve as indicators that should describe the characteristics of the observed data sets and thus allow a better interpretation of the measured versus modeled data.

Coefficient of variation (c_v): standard deviation (S) and mean (μ)

The standard deviation – i.e. the square root of the variance – describes the variance or dispersion of a data set relative to its mean, is expressed in the same unit as the observed data, and is mathematically defined as follows (NIST/SEMATECH, 2012)

$$S = \sqrt{\frac{1}{N-1} * \sum_{i=1}^{N} |A_i - \mu|^2}$$

Equation 18 Standard deviation (NIST/SEMATECH, 2012)

With A being a variable vector that contains N scalar observations. μ is the arithmetic mean of A and is defined as:

$$\mu = \frac{1}{N} * \sum_{i=1}^{N} A_i$$

Equation 19 Arithmetic mean (NIST/SEMATECH, 2012)

The coefficient of variation (c_v) is defined as the ratio between the standard deviation and the mean of a data set. It indicates how strongly the standard deviation varies from the mean and is therefore useful for comparing different data sets. (NIST/SEMATECH, 2012)

$$c_v = \frac{S}{\mu}$$

Equation 20 Coefficient of variance (NIST/SEMATECH, 2012)

The coefficient of variance is mentioned by means of completeness in this thesis and not further used for the analysis of the observed data sets.

Root mean square error (RMSE), mean bias error (MBE) and unbiased root mean square error ($RMSE_{no\ bias}$)

The root mean square error is a measure for quantifying the difference between predicted and observed values and therefore a useful statistical indicator for the purposes of this research. It is defined as the square root of the mean square error and calculated as follows (NIST/SEMATECH, 2012)

$$RMSE = \sqrt{\frac{1}{N} * \sum_{i=1}^{N} |y_i - x_i|^2}$$

Equation 21 Root mean square error (NIST/SEMATECH, 2012)

Where y_i refers to modelled values and x_i to measured values. In order to obtain values for RMSE that are not biased it is necessary to calculate the mean of the error between predicted and measured values, also referred to as mean bias error. This is done as follows:

$$MBE = \left[\frac{1}{N} * \sum_{i=1}^{N} (y_i - x_i)\right]$$

Equation 22 Mean bias error (Boyd, 2013)

Therefore, the unbiased values for RMSE can be calculated as follows:

$$RMSE_{no\ bias} = \sqrt{\frac{1}{N} * \sum_{i=1}^{N} (y_i - x_i - MBE)^2}$$

Equation 23 Unbiased root mean square error (Boyd, 2013)

In this thesis, RMSE is used in combination with MAD to quantify differences in errors between modeled and measured PV module temperature and power. The unbiased RMSE is mentioned by means of completeness and not further used in this work.

Median absolute deviation (MAD)

The median absolute deviation (MAD) is a measure of how spread out an observed data set is. In the case of observed residuals (differences between modeled and measured data points), it presents a more robust way to extremes in a data set than the RMSE, as it is not as sensitive to extremely high or extremely low outliers. (NIST/SEMATECH, 2012) MAD therefore presents another useful way to quantify differences between modeled and measured values and is defined as follows:

$$MAD = median(|(y_i - x_i) - median(y_i - x_i))|)$$

Equation 24 Median absolute deviation (NIST/SEMATECH, 2012)

Where y_i refers to modelled and x_i to measured values. 'Median' refers to the data points separating the 'higher half' from the 'lower half' of an observed data set. (NIST/SEMATECH, 2012) In this thesis, MAD and RMSE are used as a measure of quantifying the error between modeled and measured PV module temperature and power.

Coefficient of determination (R^2 or $R_{squared}$)

The coefficient of determination is a common indicator used for the evaluation of modeling algorithms. It measures the fraction of the total variability in the response that is accounted for by the model. (MathWorks, 2017a) In other words, it provides information about how well a model can describe the variability of observed data and is calculated as follows:

$$R^2 = 1 - \frac{SSE}{SST}$$

Equation 25 $R_{squared}$ (MathWorks, 2017a)

With SSE being the residual sum of squares defined as the sum of squared errors between the observed measured values x_i and the modelled or predicted values y_i:

$$SSE = \sum (x_i - y_i)^2$$

Equation 26 Sum of squared errors SSE (MathWorks, 2017a)

And SST being the total sum of squares, i.e. the sum of measured values x_i minus the mean of the measured data x_i, and is calculated as follows:

$$SST = \sum (x_i - \bar{x_i})^2$$

Equation 27 Sum of squared total SSE (MathWorks, 2017a)

Values for R^2 in this work are retrieved from linear fit model results of the built-in MATLAB function 'fitlm' using the dot notation '.Rsquared.Adjusted'. (MathWorks, 2017a)

Pearson correlation coefficient ($R_{pearson}$)

The Pearson correlation coefficient is a measure that aims to indicate how well sets of data correlate with each other. The full name of the Pearson correlation coefficient is the Pearson Product Moment Correlation or PPMC. The coefficient shows the linear relationship between two sets of data with values between -1 and 1. Depending on the type of correlation – either positive, negative or no correlation – different coefficient values between these values can be achieved. The closer the coefficient value gets to zero, the lower the correlation, i.e. the greater the differences in the observed data points. (NIST/SEMATECH, 2012) $R_{pearson}$ serves as an additional statistical indicator for the evaluation of modeled versus measured data in this work.

Spearman correlation coefficient ($R_{spearman}$)

The Spearman correlation coefficient is a nonparametric version of the Pearson correlation coefficient, also returning values between -1 and 1 – values close to zero indicate less correlation. It is based on ranked values of variables, which means that while the Pearson correlation assesses the linear relationship, Spearman correlation assesses relationships whether linear or not. (NIST/SEMATECH, 2012) In this thesis, $R_{spearman}$ and $R_{pearson}$ are used as additional statistical indicators to R^2, informing about how well the evaluated modeling algorithms fit and correlate to measured PV module temperature and power.

Sample size (n) and confidence level

Data samples are parts of the total observed data population and can be used to draw conclusions about a population as a whole. However, sample parameters – such as the above mentioned statistical parameters – may vary significantly between different samples as well as between samples and the whole population. (NIST/SEMATECH, 2012) The maximum difference between the population's parameter and the sample's parameter in comparison is defined as the margin of error (MOE) and is defined as:

$$MOE = z_{\alpha/2} * \frac{S}{\sqrt{n}}$$

Equation 28 Margin of error MOE (NIST/SEMATECH, 2012)

Where $z_{\alpha/2}$ is known as the critical z-score value of a normal distribution, S is the standard deviation of the population and n is the sample size. The critical value for the z-score describes in general the cut-off values of a distribution that defines regions where data points are unlikely to lie. It is defined to be the amount of standard deviations below and above the mean of a population and usually can be found in tables. For a confidence level of 95%, $z_{\alpha/2}$ is defined to be 1.96. For a confidence level of 90%, $z_{\alpha/2}$ is 1.645. (NIST/SEMATECH, 2012) In order to quantify the accuracy and reliability of the investigated results and comparisons of data samples in this work, the minimum required sample size to meet the desired confidence level needs to be determined. Given a maximum allowed value of MOE, the therefore required sample size (n) can be calculated through the following formula:

$$n = \left(\frac{z_{\alpha/2} * S}{MOE}\right)^2$$

Equation 29 Required sample size n (NIST/SEMATECH, 2012)

This formula can be applied when the population's standard deviation S is known – which is the case in this work. The resulting sample size n determines the minimum required size of a data sample for its mean to differ from the data population's mean by ± the value of MOE at a certain defined confidence level. (NIST/SEMATECH, 2012)

3.7.3 Graphical analysis of residuals

It is important to point out that the mentioned indicators alone do not allow a full illustration of the observed data set characteristics. To complement the above described indicators, graphical analysis of the observed data is necessary. To evaluate the IEC 61853-3 draft's calculation procedures, the difference between the modelled and measured data sets are illustrated graphically. This evaluation is done via analysis of the residuals. Residuals are differences between the observed measured data and the predicted or modelled data. The examination of residuals counts as key method of statistical model evaluations. (NIST/SEMATECH, 2012) A clear definition of residuals, provided by NIST/SEMATECH (2012) is as follows:

"Residuals can be thought of as elements of variation unexplained by the fitted model. Since this is a form of error, the same general assumptions apply to the group of residuals that we typically use for errors in general: one expects them to be (roughly) normal and (approximately) independently distributed with a mean of 0 and some constant variance."

This means that the overall pattern of plotted residuals of a data set should be similar to the bell-shaped pattern of plotted data that is normally distributed. Departures from this distribution pattern lead to structured residuals and indicates parameters not accounted for in the model. By identifying such structures, terms can be added to the prediction algorithms and thus improve the model. (NIST/SEMATECH, 2012) The following graphical analysis methods help identify the behavior of the observed residuals and thus the goodness of fit of the calculation procedures suggested in IEC 61853-3 draft to measured data. There are three common types of plots that are suitable to graphically illustrate the distribution of a set of residuals, which are:

- Frequency (or probability) range histograms of residuals,
- Normal probability plots of residuals and
- Plots of residuals over time and over predicted values.

Frequency range histogram of residuals

The histogram graphically summarizes the distribution of a data set by giving information about the center of the observed data, the spread of it, skewness and presence of outliers and presence of multiple modes within the data. (NIST/SEMATECH, 2012)

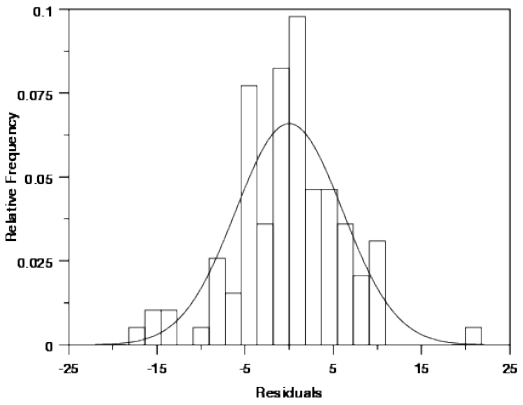

Figure 15 Example of frequency range histogram (NIST/SEMATECH, 2012)

Normal probability plot

A more sensitive graph to reveal information about the distribution of observed residuals is the normal probability plot. These plots show the calculated probability of each residual versus the residual value, by using the formula:

$$P_{i-th\ residual} = \frac{i}{(N+1)}$$

Equation 30 Cumulative probability of a residual point (NIST/SEMATECH, 2012)

With i being the residual point (order of value in the observed list of values) and N the number of entries in the list. If the residual points come from a normal distribution, the points P in the normal probability plot should form a straight line.

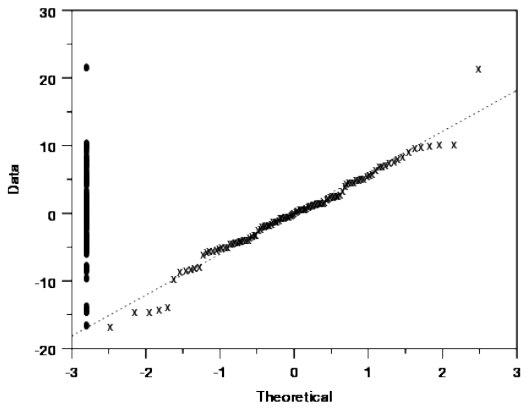

Figure 16 Example of normal probability plot of residual values (NIST/SEMATECH, 2012)

Additionally it is possible to also plot the values of residuals within a normal probability plot to indicate the distribution of residuals – as it is done in Figure 16 along the y-axis at the

left side of the graph. Usually, small departures of the straight line are common. Nevertheless, clear s-shaped curves in this plot suggest a bimodal distribution of the residuals. Breaks in the middle of the graph indicate anomalies in the residual distribution. (NIST/SEMATECH, 2012)

Residuals plots

In order to test the time dependence of the observed data set, plotting the residuals over the time is a helpful method. The following figure shows an example of plotted residuals over time that present a clear time trend. (NIST/SEMATECH, 2012)

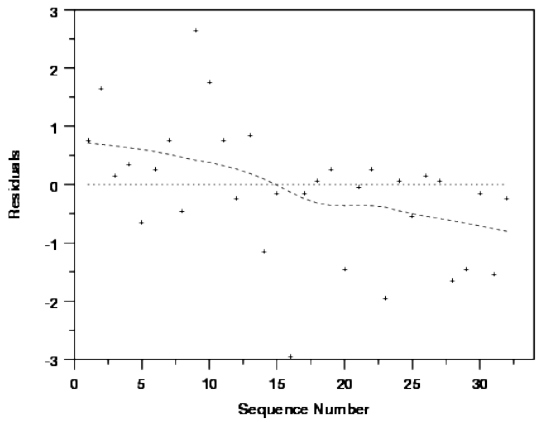

Figure 17 Example 1 of plotted residuals over time – Clear time trend (NIST/SEMATECH, 2012)

While the example shown in Figure 17 shows a clear time trend, the residuals in Figure 18 do not show a clear tendency. The example in Figure 17 shows residuals that are drifting to lower values as the investigation continues. Extreme cases of such drift of residuals will also indicate a poor ability to account for the variability in the data, represented by low values of R^2 – see above. In this context, the term of so-called 'homoscedasticity' is used, which refers to the constant of variance of the observed data (residuals) over time – whereas 'heteroscedasticity' refers to inconstant variance of the observed data (residuals) over time. (NIST/SEMATECH, 2012)

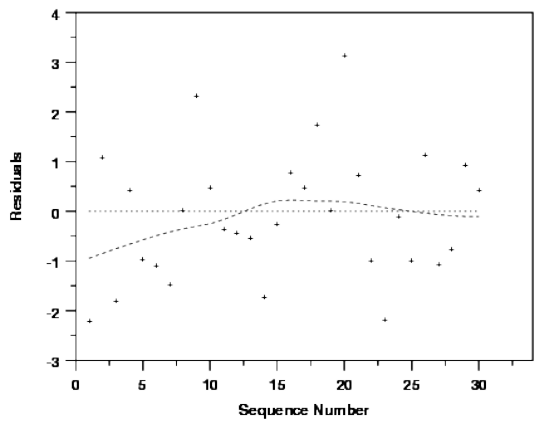

Figure 18 Example 2 of plotted residuals over time – No clear time trend (NIST/SEMATECH, 2012)

Plotting the residuals versus the predicted, fitted values should show a distribution of points scattered randomly around 0. Any tendency of the residuals to deviate with increasing or decreasing values of predicted values indicate that the residuals have growing or decreasing scatter as the response, i.e. the predicted values, are changing. The following figure shows the plot of absolute values of residuals over the predicted values, which cleary shows an increasing value of residuals with growing values of response data, also indicating heteroscedasticity (no constant variance). (NIST/SEMATECH, 2012)

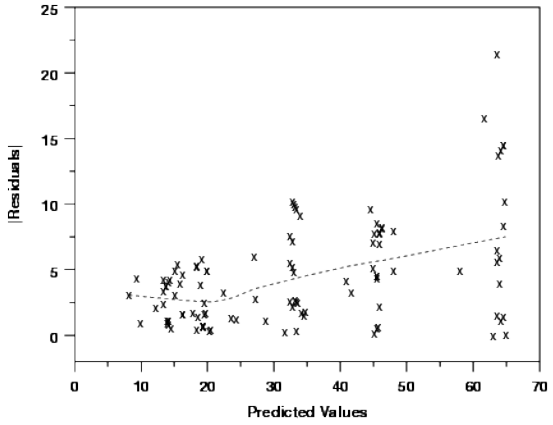

Figure 19 Example of plotted residuals over predicted values (NIST/SEMATECH, 2012)

This work uses residual plots to identify the behavior of residuals (difference between modeled and measured PV module parameters) over the observed bin ranges.

3.7.4 Graphical analysis of location effects

A useful tool to get information about the effect of location and variation changes of different groups of data is by plotting clustered data as so-called 'boxplots', illustrated in the following figure. (NIST/SEMATECH, 2012) In this work, boxplots are used to graphically show difference between the traced module position groups – mentioned in section 0 - within the observed ground array's data.

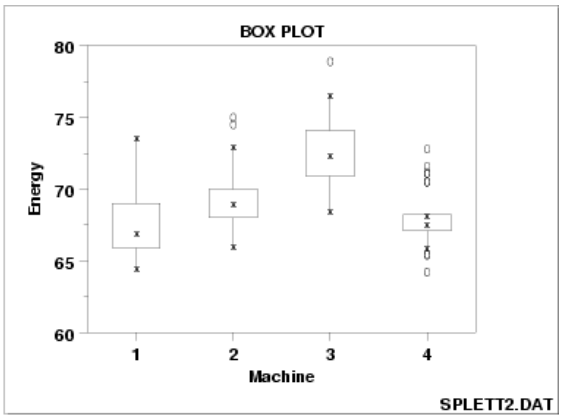

Figure 20 Example of boxplot (NIST/SEMATECH, 2012)

Boxplots show the response variable plotted on the vertical axis versus the variation of interest clustered on the horizontal axis (clustered position groups). Boxes inside the graph give information about the variation of the observed response data, showing the median of an observed data set, the lower quartile (25^{th} percentile) and the upper quartile (75^{th} percentile) of the data. I.e. the box in this plot represents the middle 50% of the observed data. Furthermore, boxplots give information about minimum and maximum points of a data set and identify outliers of the observed data. Outliers are data points that lie an abnormal distance from the minimum and maximum data point. (NIST/SEMATECH, 2012)

3.8 Overview of research steps

The following flow chart sums up the main research steps of this work:

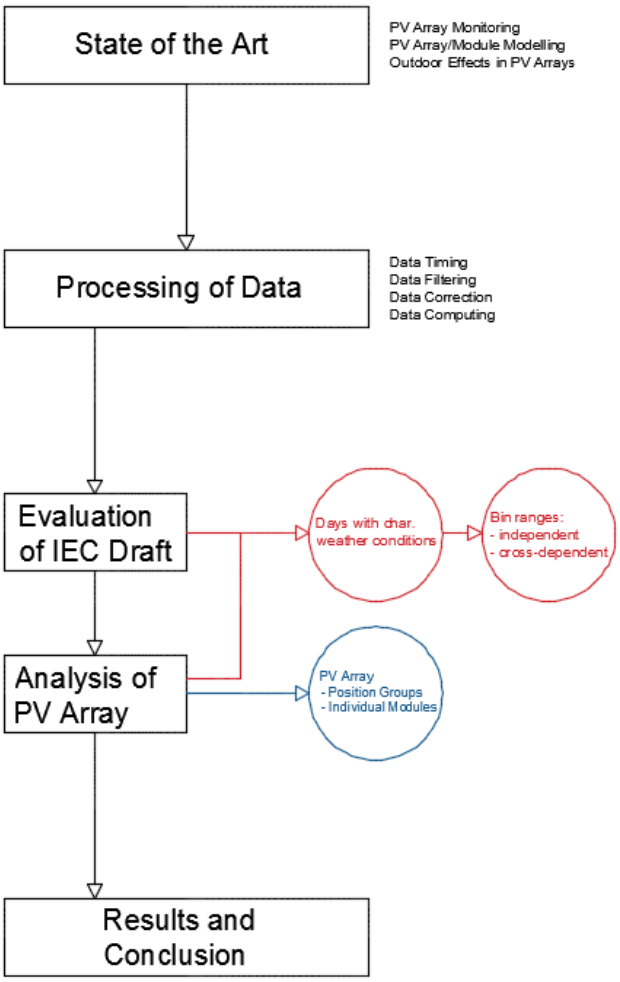

Figure 21 Flow chart overview of research steps (own figure)

4 Effects and influences in outdoor PV arrays

This chapter provides a comprehensive overview of effects that need to be considered when dealing with PV modules mounted in outdoor PV arrays and being exposed to environmental conditions. The effects discussed are not analyzed individually in this thesis, as they should serve the purpose of completeness and understanding and will be referred to if necessary.

4.1 DC performance array losses

Typically, PV modules mounted in a PV array are connected in series to strings which then are connected in parallel to source circuits. Within the same string, all modules in series must transport the same current. Within the same source circuit, all parallel strings must operate at the same voltage. This means that inherent performance differences between individual modules, non-uniform available irradiance, inhomogeneous temperatures across the PV array and/or wiring (system component) losses across the array can cause the performance of the PV array to operate at non-ideal conditions, which means that operation at the maximum power point (MPP) cannot be realized. (PVPMC, 2017)

4.1.1 Quantification of mismatch losses

The above explained effects causes individual circuits of the PV array to perform outside their maximum power point (MPP), forcing them to compromise values of performance. One way to quantify the impact of mismatch losses can be calculated as follows:

$$MM_{loss} = 1 - \frac{P_{DC,array,output}}{\sum P_{MPP,module} - \sum P_{DC,wiring\ losses}}$$

Equation 31 DC Mismatch losses (PVPMC, 2017)

Mismatch caused by inhomogeneities of irradiance or module temperature across the PV array are usually quantified separately as they are co-dependent with each other and strongly influence the electrical characteristics of PV modules. (PVPMC, 2017)

4.1.2 PV array system component losses

System component losses refer to failures and/or degradation of DC components such as cells, modules, connectors, fuses, cables, combiner boxes and other system components. Such types of losses can lead to declines in performance as well as local heating in the module – referred to as localized hot spots. (PVPMC, 2017) Complete damage of one or more of these components can result in several ways with different complexity, depending on the type and location of the failure. Changes in component health typically also can be detected through an increase in the PV module's series resistance R_s. (Spataru et al., 2015)

4.1.3 DC wiring losses

This type of loss is mainly caused by changes in the ohmic resistance of the cabling that connects PV array components. (PVPMC, 2017) Power loss over such components varies as a function of the current squared:

$$P_{DC,loss,wiring} = I^2 * R_{component}$$

Equation 32 DC wiring power loss (PVPMC, 2017)

Differences in cable length or size between parallel strings can also lead to voltage drops – as also do series protection diodes – and can be considered as follows:

$$V_{DC,loss,wiring} = I * R_{component}$$

Equation 33 DC wiring voltage drop (PVPMC, 2017)

A closer examination of DC wiring losses of the observed array is outside the scope of this work and therefore not part of the array evaluation and analysis.

4.2 Optical effects

In the following, outdoor effects that optically influence the PV performance are described – those listed below refer to the effect of soiling and shading, angle of incidence effects as well as the effect of the spectrum of the incoming light on the PV array performance.

4.2.1 Soiling and shading

PV module front glass soiling describes the effect of the accumulation of dust and pollution which causes limited light transmittance, increased relative angular losses or shading to the PV solar cells. (Spataru et al., 2015) According to Martin and Ruiz (2000) the annual losses caused through soiling or dust deposition is depending on the latitude and the tilt angle of the observed PV system. In their study, Martin and Ruiz (2000) found a minimum annual loss value of about 3% for all the considered sites in their research, while maxima of between 5 to 7% of annual losses were shown. This range of soiling losses can be confirmed in the work of Laukamp et al. (2002), in which annual energy losses due to soiling up to 6% are shown. Thus, soiling can represent a significant performance loss factor for PV systems. As mentioned in section 1.4 of this work, for the scope of this work it is assumed that soiling and dust deposition occurs uniformly across the observed ground array. Furthermore, the observed data set consists of days that are considered to present a rather minimal occurrence of dust deposition – involving only one day of a month with known high dust deposition caused through pollen dust.

Shading, and in particular partial shading, can cause significant performance losses of the PV system mostly depending on the position of the shadow and the bypass diode configuration of the PV modules within the array. Specifically localized – or partial – shading or front glass soiling (as explained above) can lead to irreversible hot-spot damage through reverse biasing of the affected solar cells – whereas uniform shading across the whole array itself does not present that high of a risk, as it happens equally over the entire array. (Spataru et al., 2015)

4.2.2 Reflectivity and AOI

In case the PV array is not mounted on a two-axis tracker system, the direct component of the solar radiation will not be normal to the PV array plane for the entire observation time. Thus, angles of incidence greater than zero (normal to the plane of array) lead to optical losses due to increased reflections from the module surface – and ultimately from the module materials. (PVPMC, 2017) A typical way to define the loss due to angle of incidence effects is through the incidence angle modifier (IAM) as follows:

$$IAM = \frac{\tau(\theta)}{\tau(0)} = \frac{R(\theta) - A(\theta)}{R(0) - A(0)}$$

Equation 34 Incidence angle modifier (IAM) for the beam component of the incident irradiance (PVPMC, 2017)

With τ being the spectrally weighted transmittance, R the spectrally weighted reflectance and A the spectrally weighted absorptance of the observed PV modules as a function of the incidence angle θ. (PVPMC, 2017) Reflectivity and angular loss effects in this work are considered through the approach developed by Martin and Ruiz (2000) as a function involving an empirically determined, dimensionless parameter a_r (angular loss coefficient) – as described in section 0 of this work.

4.2.3 Spectral responsivity

Furthermore, the conversion efficiency of PV cells/modules depends on the wavelength of the incoming light and is referred to as spectral response – which depends on the PV technology used, as mentioned in section 0 of this work. Spectral changes of light and thus deviation in measured and predicted performance values in this work are considered through the approach of Lee and Panchula (2016) – as described in section 0 of this work.

4.3 Thermal effects

The PV module temperature depends on a number of factors, such as the air temperature, irradiance, wind speed and PV module materials – as described in section 2.3.2 of this work. Thus, the actual operating temperature of a PV module is the equilibrium between generated heat and heat losses of the module to its surroundings. The main three mechanisms of heat loss are: heat conduction, convection and radiation. (pveducation, 2017a) These mechanisms are schematically illustrated in the following figure:

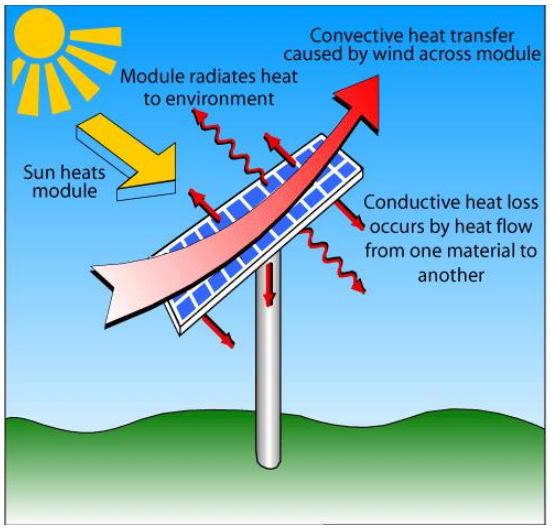

Figure 22 Heat loss mechanisms of PV modules (pveducation, 2017a)

Conductive heat transfer is caused through thermal gradients between the PV module and its surroundings in contact to the material and is characterized by the thermal resistance of the PV module – in units of W/m°C. Convective heat transfer describes the effect of heat transfer caused through thermal gradients between surrounding material (air) moving across the surface of the PV module and is characterized by the convection heat transfer coefficient – in units of W/m²°C. Radiation is the effect of emitting heat based on the temperature of an object and its thermal gradient to its surroundings and is characterized by the object's degree of emissivity ε - unitless. (pveducation, 2017a)

There exists a number of models that aim to estimate the PV module temperature under certain ambient conditions for specific types of PV technologies. The model used in this work and applied by the IEC 61853-3 draft is developed by Faiman (2008), while an alternative way to estimate the module temperature is suggested by the Sandia Module Temperature Model – which will not be further analyzed within the scope of this thesis. (PVPMC, 2017)

In this regard, also the dependence of the short circuit current (Isc) and the open circuit voltage (Voc) on the PV module temperature should be mentioned with reference to section 3.4.1 of this work. Local temperature (and irradiance) differences within the observed PV array of this work will be analyzed according to the position of the modules within the array.

4.4 Degradation and failure modes

The present work does not take into consideration any PV failure or degradation within the analysis of the observed PV array data sets and the evaluation of the modeling algorithms of IEC 61853-3. This is on the one hand due to the fact that the installed PV array is still relatively new, assuming that possible infant failures have not influenced the PV performance significantly yet. On the other hand – as mentioned initially – modeling algorithms use a performance matrix which is based on the same type of PV modules, aged outside nearly for the same time as the modules mounted inside the array. However, it should be mentioned that about 3% of the PV modules installed in the observed ground array are affected by hot spot back sheet burn marks, which also includes 3 traced PV modules that are part of the observed dataset in this work. Exemplary hot spot burn marks of modules within the ground array can be seen in Figure 23. Also, the study of Fairbrother (2017) has shown different degrees of back sheet yellowing and glazing depending on the position of the PV modules in the array – as explained in section 0 of this work.

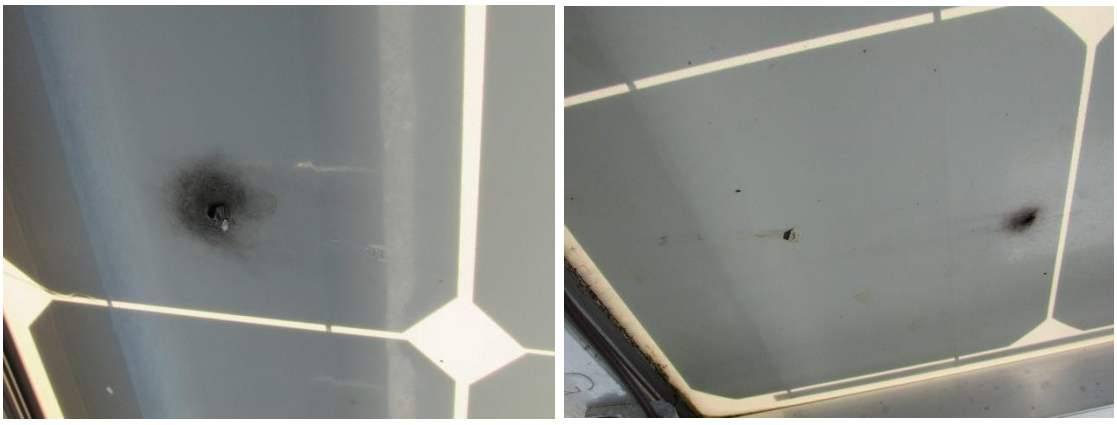

Figure 23 Hot spot burn marks at the back sheet of PV modules within the ground array at NIST (own figures)

While the origin of the observed hot spot burn marks – as a typical midlife failure mode – is not completely clear up to this date, it could be shown that at the time of investigation there is no significant difference in performance when comparing to PV modules without burn marks – which most probably can be related to the relatively young age of the PV array of about 4 years since installation. Furthermore, a lack of availability and accessibility of (‘fresh’) PV module measurements before their installment at NIST does not allow a reliable investigation of performance degradation behavior at this point. Thus, degradation and failure modes are not considered within the scope of this work and assumed to be negligible. Nevertheless, common degradation and failure modes shall be mentioned in the following and serve further discussion and possible conclusions of this research.

A typical categorization of failures and degradation modes of wafer based crystalline PV modules and system components can be divided into infant failures, midlife failures and wear-out failures (IEA, 2014b) – as shown in the following figure:

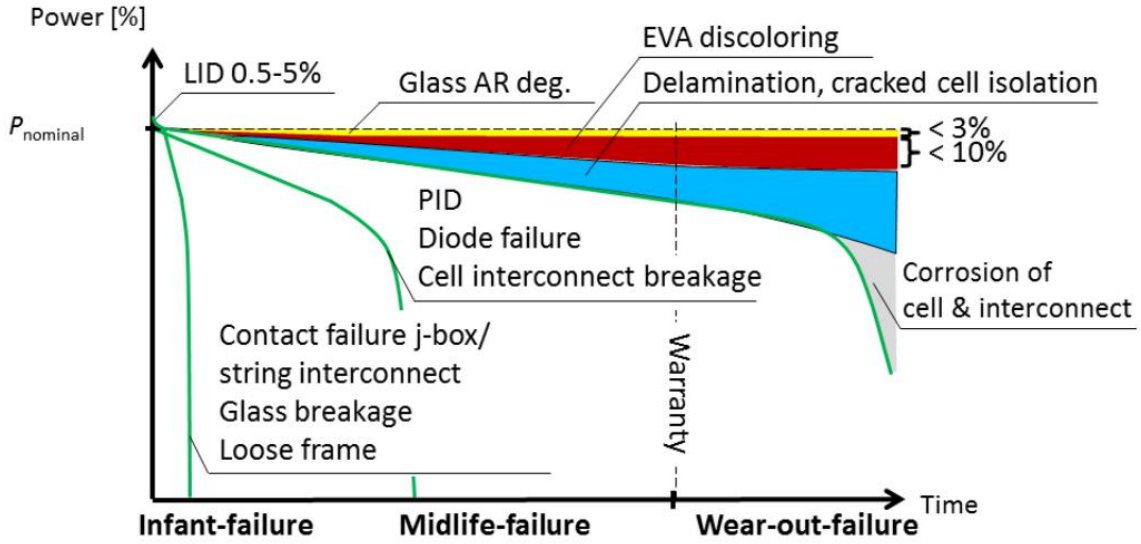

Figure 24 Typical failure scenarios for wafer-based c-Si PV modules and system components (IEA, 2014b)

LID refers to light induced power degradation[9] and occurs right after the installation of the PV modules. It is considered to be an expected and predictable power loss after the installed PV modules are installed and exposed to light. While LID is not fully considered to be an infant-mortality failure (as it is predictable), failures related to PV system components such as contact failures, glass breakages, defective cell interconnects or loose frames and delamination are common infant failures. (IEA, 2014b)

Common midlife failures are considered to be related to interconnection defects, diode failures and failures due to glass breakage or potential induced degradation (PID)[10] effects, but also encapsulant failures or burn marks on the cells are common failures occurring at this stage of lifetime of PV modules and system components. (IEA, 2014b)

[9] LID is related to the quality of the wafer manufacturing and in most literature refers to traces of Oxygen defects included in the semiconductor material of the PV module's cells - according to: NREL 2012. Understanding Light-Induced Degradation of c-Si Solar Cells. NREL/CP-5200-54200 ed. 2012 IEEE Photovoltaic Specialists Conference Austin, Texas.

[10] PID is mainly influenced by the (in most c-Si) negative voltage of the individual PV module to the ground and is enhanced by high system voltages, high temperatures and high humidity and influences the active layer of the PV module's cells, according to: NREL 2011. System Voltage Potential-Induced Degradation Mechanisms in PV Modules and Methods for Test. NREL/CP-5200-50716 ed. 37th IEEE Photovoltaic Specialists Conference (PVSC 37) Seattle, Washington.

Wear out failures are failure modes that occur at the end of the lifetime of PV modules and system components and are usually defined as failures that lead to safety problems or to a performance drop under a certain level – typically defined as 80 % or 70 % of the initial power rating. Main end of life failures are delamination, cell cracks or discoloring of the laminate. (IEA, 2014b)

There exists a range of standardized test procedures that aims to provide information about the behavior of PV modules and components throughout its lifetime. Most critical tests for c-Si PV modules that aim to provide knowledge and indicators about their lifetime and degradation behavior of a module and provide a basis for certification of PV modules and materials are for example: standardized temperature cycle tests, damp heat tests, initial ('fresh') performance measurements, humidity freeze tests, hot spot endurance tests and mechanical load tests. (IEA, 2014b)

5 State of the art – PV performance modeling approaches

This chapter summarizes existing efforts and developments towards PV performance modeling algorithms. Alternative modeling algorithms to the ones used in this thesis are given in Table 9 and shall only be mentioned for completeness and are not further analyzed within the scope of this work.

	AOI correction (1)	**Spectral correction (2)**	**Module temperature (3)**	**DC module output power (4)**
Modeling algorithms used for evaluation	**IEC 61853-3:** Martin and Ruiz (2000)	**Alternative model to IEC 61853-3:** Lee and Panchula (2016)	**IEC 61853-3:** Faiman (2008)	**IEC 61853-3:** Interpolation method, IEC (2016b)
Alternative modeling algorithms	**Physical IAM Model:** De Soto et al. (2006) **ASHRAE IAM Model:** ASHRAE (1977) **Sandia IAM Model:** King et al. (2004)	**IEC 61853-3 CD approach, discussed in:** IEC (2016b), Huld et al. (2015), Alonso-Abella et al. (2014), Dirnberger et al. (2015) **AM Model, adapted by:** De Soto et al. (2006) **SMARTS2 Model:** Gueymard (1995)	**Sandia Module Temperature Model:** King et al. (2004) **Overview of other PV module temperature models:** Skoplaki and Palyvos (2009)	**Model of Huld et al.:** Huld et al. (2011) **Sandia PV Array Performance Model:** King et al. (2004) **De Soto Five Parameter Module Model:** De Soto et al. (2006)

Table 9 Overview of existing PV module and array modeling algorithms (own table)

Furthermore, there exists a range of worldwide efforts that aim to improve and develop PV performance modeling in a comprehensive and publically available manner. One of these efforts happens through the PV Performance and Modeling Collaborative (PVPMC) platform, established by the Sandia National Laboratories, US Department of Energy. The aim of this platform is to improve the accuracy of PV performance models and analyses. It therefore provides a variety of existing studies and tools in the field of PV modeling. (PVPMC, 2017)

As for other international developments and efforts towards the understanding of the behavior of PV modules and arrays (including system components) exposed to environmental conditions throughout their lifetime, the efforts of the IEA PVPS Task 13 shall also be mentioned. This task deals with the performance and reliability analysis of PV systems in an international consortium. (IEA, 2017b) A comprehensive overview of PV performance modeling methods and practices – some of them included above – was developed at the 4th modeling collaborative workshop lead and organized by IEA PVPS Task 13 members. (IEA, 2017c)

Another project that partly can be related to this thesis' efforts is the Austrian national project Infinity. Infinity is a national Austrian lead project subsided by the Austrian Climate and Energy Fund, dealing with climate sensitivity of photovoltaics. It therefore also strongly deals with monitoring and modeling of performance behavior of PV systems. (CTR, 2017)

6 Monitoring of NIST's ground mounted PV array

This chapter contains a description of the observed PV ground array, located at the campus of NIST. Furthermore it describes the electrical layout of the array and provides information about measurement equipment and positions. It is intended to cover the description of relevant ground array and measurement components involved in this work.

A more detailed description of the entire array and monitoring system may be consulted via the NIST Technical Note 1896 done by Boyd (2015), publically available from: http://dx.doi.org/10.6028/NIST.TN.1896

6.1 Surroundings and location

The observed ground array is located at the campus of NIST in Gaithersburg, with the coordinates 39° 07' 54.7'' N; 77° 12' 50.8'' W and an altitude of 136 m. Prevailing climate conditions at this location can be described as humid continental climate, characterized by a hot summer and no dry season. (Fairbrother, 2017) The array is situated on coarse, gray granite stone (#57 stone) and surrounded by grass and bio retention zones as can be seen in the figure below.

Figure 25 Ground array at NIST (Boyd, 2015)

The array consists of five tilted sheds running east-west. All sheds are tilted at nominally 20° due south. As mentioned in section 2, the four southernmost sheds consist of five module rows, while the northernmost (fifth) shed consists of 4 rows. Local shading is periodically caused by inter-row shading, a research building that is located directly west of the array, shading coming from the bio retention area south of the array as well as a 1.2 m high cable rail fence surrounding the array. (Boyd, 2015)

6.2 Electrical layout and measurement positions

Each PV module string of the array contains 12 modules and runs from east to west in each of the five sheds. The strings combine in parallel at seven combiner boxes and form seven output circuits that run to the inverter. Strings combined in parallel are called source circuits (SC) and are illustrated in the figure below, combined to seven combiner boxes shown as numbered squares. Furthermore, the figure below shows positions of the deployed measurement equipment.

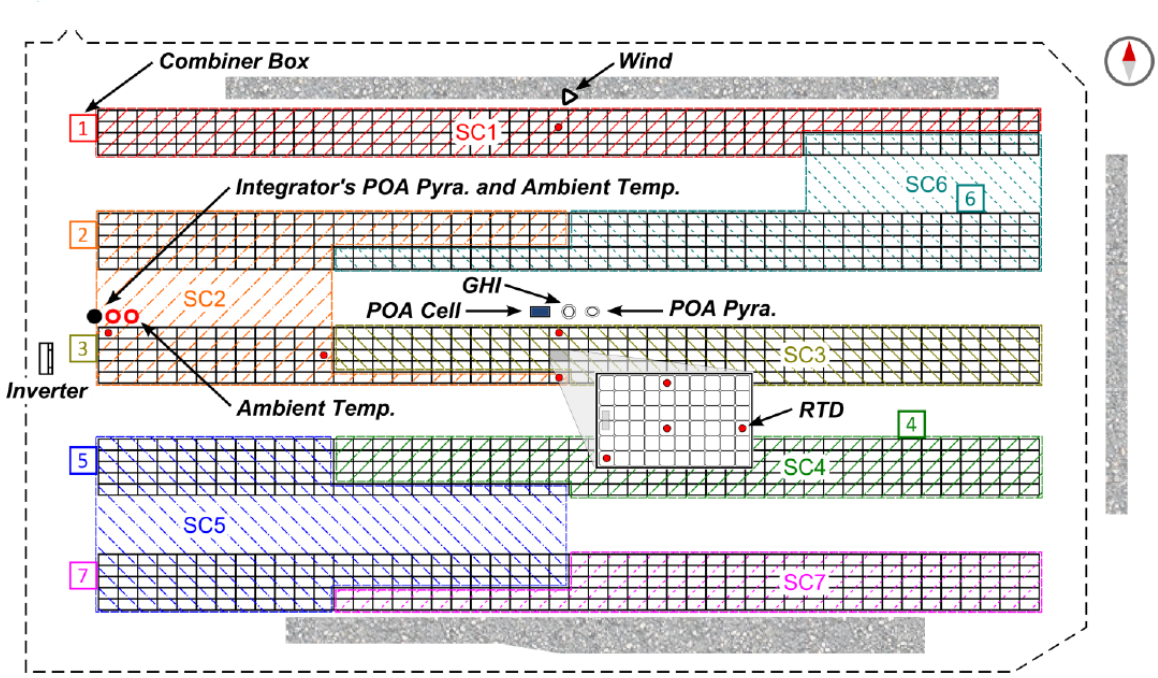

Figure 26 Ground array electrical layout and measurement positions (Boyd, 2015)

'POA Pyra' stands for the thermopile pyranometer in the plane of the array, which measures the global in-plane irradiance (G_{poa}) used for this work. 'POA Cell' refers to a silicon reference cell that also measures the global in-plane irradiance (G_{poa}). 'GHI' stands for the thermopile pyranometer measuring the global horizontal irradiance (GHI). 'RTD' stands for the resistance temperature detectors that are mounted according to IEC (2009) on the backsides of the respective modules indicated as red dots. 'Ambient Temp.' refers to the measurement of the ambient temperature via an RTD probe in a passively ventilated radiation shield. 'Wind' stands for the measurement position of the wind speed via heated ultrasonic wind sensor. (Boyd, 2015) Furthermore the integrator of the PV array mounted a Silicone photodiode pyranometer and a sensor measuring the ambient temperature.

The following figure shows the irradiance sensors at the ground array, mounted by NIST.

Figure 27 Irradiance sensors at the ground array measuring G_{poa} and GHI (Boyd, 2015)

The figure below shows the installed temperature probe and radiation shield used to measure the outdoor ambient temperature at the ground array.

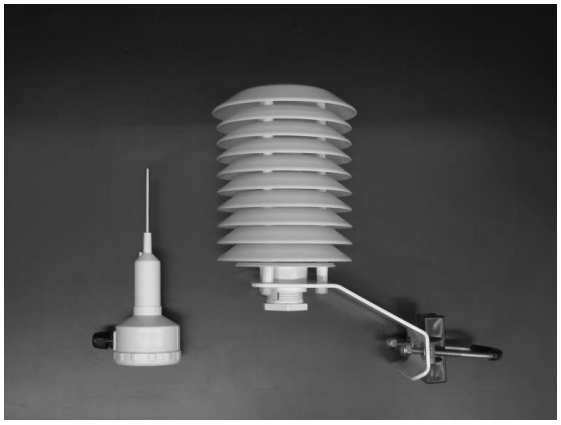

Figure 28 RTD temperature probe and radiation shield for ambient temperature measurement (Boyd, 2015)

The following figure shows an RTD mounted on the backside of a PV module for the measurement of the PV module backside surface temperature, using thermally conductive epoxy and adhesive film overlay.

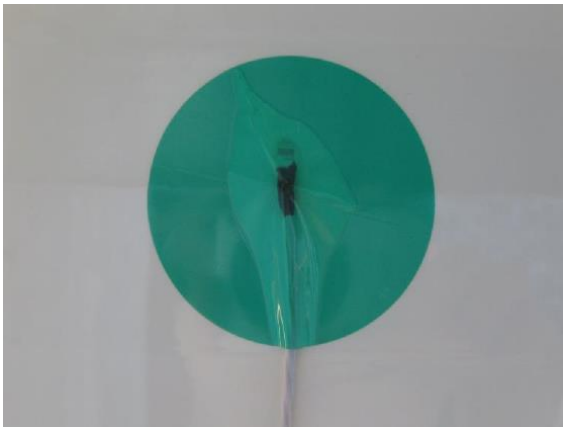

Figure 29 RTD mounted on the backside of a PV module (Boyd, 2015)

The following figure shows the deployed ultrasonic wind sensor at the ground array.

Figure 30 Wind sensor at the ground array (Boyd, 2015)

The direct normal irradiance is measured at a different location, at the rooftop weather station of a nearby research building on the NIST campus via a thermopile pyrheliometer. The following figure shows the deployed pyranometers at the rooftop weather station at NIST.

Figure 31 Pyrheliometers mounted on the side of the solar tracker also showing the diffuse measuring pyranometers (left and right) and the IR measuring pyrgeometer (center) (Boyd, 2015)

6.3 IV curve tracers

The deployed IV curve tracers from the company Stratasense (2013) are taking measurements at one module of each string of the ground array, i.e. in total 96 IV curve tracers. As can be seen in the following figure, the tracers are mounted on the mounting structure for the PV modules in order to not influence the thermal behavior of the PV modules' backside.

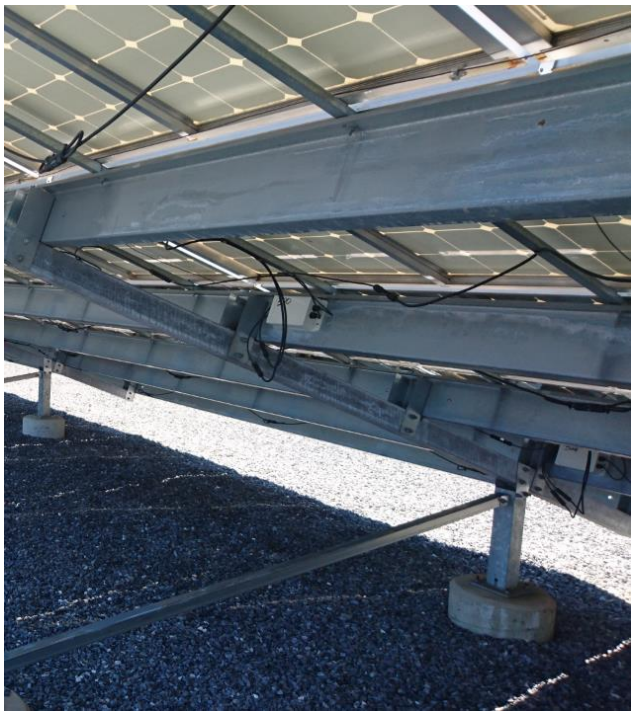

Figure 32 IV curve tracers on the mounting structure (own picture)

The tracers perform periodic IV curve sweeps in five minute intervals. Sweeps of different tracers happen sequentially according to the tracers' network addresses, i.e. IV curve sweeps are not happening at the exact same times. One sweep takes approximately 300 ms. During that time, the PV module is bypassed from its string, i.e. operational data is not monitored. The tracers transmit data wirelessly and do not require any additional grid connection or wiring as they charge from the PV modules – containing also backup batteries. Stratasense wireless PV tracers are verified within 1% accuracy. (Stratasense, 2013)

6.4 Summary of PV ground array characteristics

The table below summarizes characteristic data of the observed PV ground array:

Parameter	**Value**
Array rated DC power [kW]	271
Latitude [°N]	39.1319
Longitude [°E]	-77.2141
Elevation above sea level [m]	138
Height above ground [m]	0.67
Tilt [°]	20
Azimuth from North [°]	180
Number of modules	1152
Module manufacturer	Sharp
Module model	NU/U235F2
Module technology	Monocrystalline silicon – front contact
Module rated power	235
Modules per string	12
Number of combiner boxes	7
Inverter manufacturer	PV Powered (now Advanced Energy)
Inverter model	PVP260kW
Inverter rated power [kW]	260

Table 10 Summary of ground array data (modified according to Boyd, 2015)

The following table summarizes the for this work relevant installed measurement equipment at the ground array at NIST.

Monitoring data set	Parameter	Abbreviation	Measurement equipment	Model of equipment
Weather data	ambient temperature	T_{amb}	RTD probe in a multi-plate passively ventilated radiation shield	R.M. Young 41342LC in an R.M. Young 41003
	wind speed	v	ultrasonic wind sensor	Vaisala WMT52
	global horizontal irradiance	GHI	thermopile pyranometer	Eppley PSP
	direct normal irradiance	DNI	thermopile pyrheliometer	Kipp & Zonen CHP 1
	global in-plane irradiance	G_{poa}	thermopile pyranometer	Kipp & Zonen CMP 11
PV module operational data	module backside temperature	$T_{mod,meas}$	RTD	Unknown, Pt1000
	operational current	I_{op}	wireless IV curve tracer	Stratasense
	operational voltage	V_{op}	wireless IV curve tracer	Stratasense
	IV curve traces	-	wireless IV curve tracer	Stratasense
Camera pictures	entire array	-	network camera	Axis Q6032-E PTZ
	middle third	-	network camera	Axis Q6032-E PTZ
	north third	-	network camera	Axis Q6032-E PTZ
	south third	-	network camera	Axis Q6032-E PTZ
	sky camera	-	fisheye lens network camera	Axis M3027-PVE with a Fujinon FE185C046HA-1
	sky camera	-	fisheye lens network camera	Alcor System OMEA-2.0M-HCA with a Fujinon FE185C046HA-1

Table 11 Measurement equipment deployed at the ground array and used in this work (modified according to Boyd, 2015)

7 Evaluation of PV modeling algorithms

In this chapter, results related to the evaluation of the IEC 61853-3 draft's calculation procedures are summarized, described and interpreted. Results related to the correction procedures, as well as modeled PV module temperature and power are illustrated as time series plots with regard to the entire observed data set population of days with characteristic weather conditions – as mentioned in section 3.5. Moreover, effects of each days with characteristic weather conditions, each observed bin range individually and the interaction between each of the observed bin ranges are evaluated regarding modeled and measured PV module temperature and power.

In total, the observed data set contains about 7000 data points (i.e. minutely averages) out of in total 21 of the 24 listed days with characteristic weather conditions – mentioned in section 3.5 of this work. This reduction is due to irregularities and faults in measurement data for 3 of the observed days: 01/09/2017 a day with low daily averages of irradiance, ambient temperature and wind speed (L/L/L), 02/09/2017 a day with low daily averages of irradiance and ambient temperature and high daily average wind speed (L/L/H), 08/28/2016 a day with high daily averages of irradiance and ambient temperature and low daily average wind speed (H/H/L). In order to avoid the distortion of results, these days are not considered in the following evaluation.

7.1 Angle of incidence correction

The correction for angle of incidence effects through the model of Martin and Ruiz (2000) – described in section 0 – is schematically illustrated in the following figure. Figure 33 shows the measured global in-plane irradiance (black full line – top graph) compared to the AOI-corrected global in-plane irradiance (red dashed line – top graph). Residuals between measured and corrected irradiance values are plotted in the bottom graph of Figure 33 (yellow dots). The mean difference between the measured and the corrected values is about 46 W/m², the median difference is about 54 W/m² for the entire observed data set population of 6929 data points.

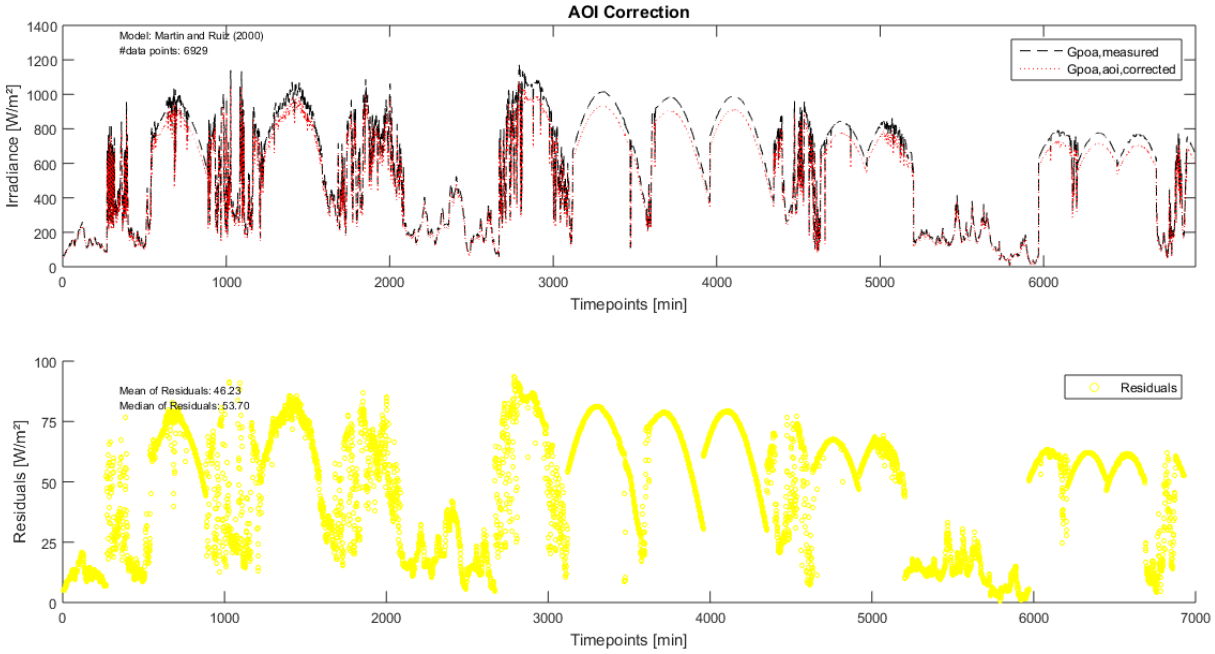

Figure 33 AOI correction of global in-plane irradiance (own figure)

7.2 Spectral correction

The spectral correction through the model of Lee and Panchula (2016) – described in section 0 – is schematically illustrated in the following figure. Figure 34 shows the measured and AOI-corrected global in-plane irradiance (black full line – top graph) compared to the spectrally and AOI-corrected global in-plane irradiance (red dashed line – top graph). Residuals between AOI-corrected and spectrally (and AOI) corrected irradiance values are plotted in the bottom graph of Figure 34 (yellow dots). The mean difference between the AOI-corrected and the spectrally and AOI-corrected irradiance is significantly smaller compared to the mean difference caused through correction of AOI effects and results to about 0.7W/m², the median difference to about -0.1 W/m² for the entire observed data set population of 6929 data points. I.e. that spectral correction leads to relatively small changes in global in-plane irradiance values.

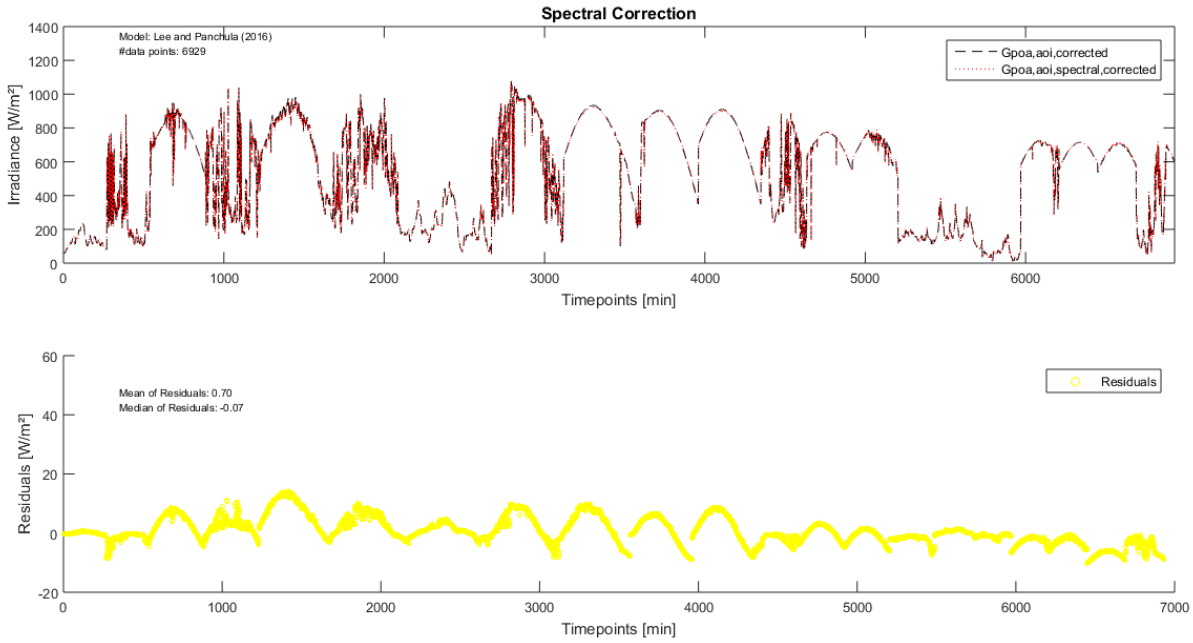

Figure 34 Spectral correction of AOI corrected global in-plane irradiance (own figure)

7.3 Module temperature calculation

The PV module temperature calculation according to the model of Faiman (2008) – described in section 3.3.6 – is schematically illustrated in the following figure. Figure 35 shows the measured PV module temperature (black full line – top graph) compared to the estimated/calculated PV module temperature (red dashed line – top graph). Residuals between measured and modeled PV module temperature values are plotted in the bottom graph of Figure 34 (yellow dots). The mean difference between the measured and the estimated PV module temperature is about 1.54°C and the median difference 1.53°C for the entire observed data set population of 6929 data points – with RMSE of about 3.7°C and MAD of about 1.4°C.

Temperature Modeling Error – Entire Data Set			
RMSE [°C]	MAD [°C]	μ [°C]	Median diff. [°C]
3.7	1.4	1.5	1.5

Table 12 Temperature modeling error indicators for the entire data set population (own table)

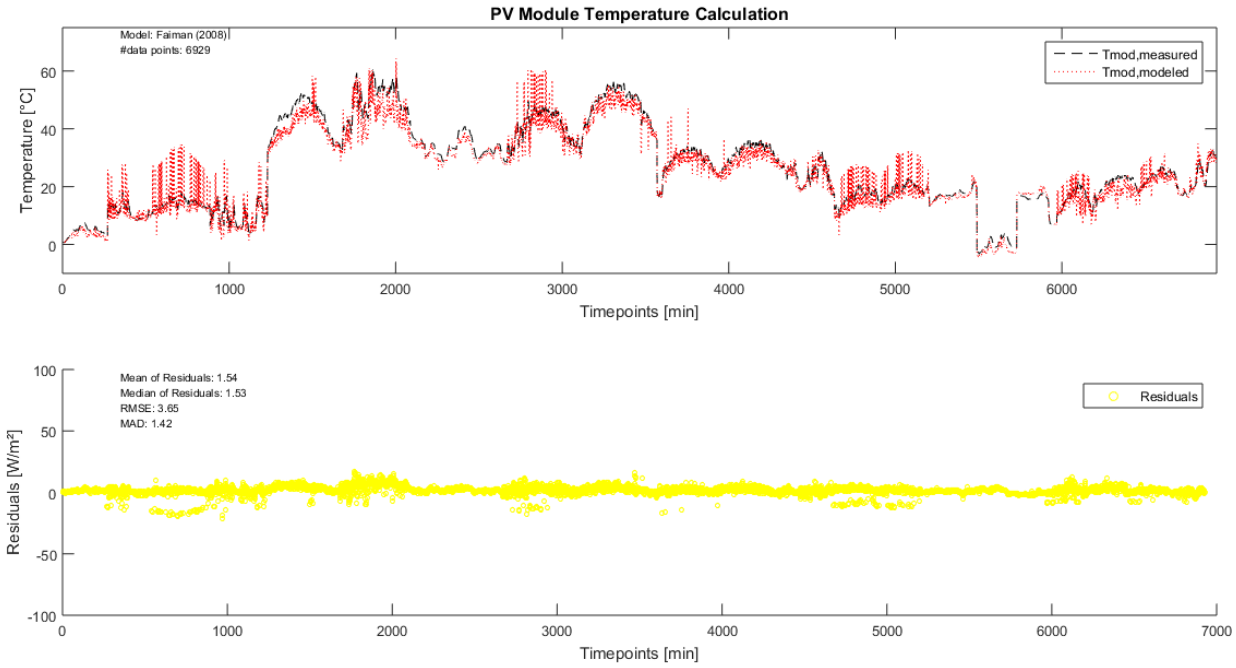

Figure 35 PV module temperature calculation (own figure)

7.3.1 Distribution of residuals and sample size - Temperature

Furthermore, the observed residuals of modeled and measured PV module temperature show a normal distribution with the population center close to zero and very little positive outliers on the right side of the center – representing also a slightly larger skew to the left as shown in the figure below. The left skew indicates the tendency of the model to underpredict the PV module temperature, leading to more negative residuals for the observed entire data set population. As can also be seen in the plot of residuals over time in Figure 35.

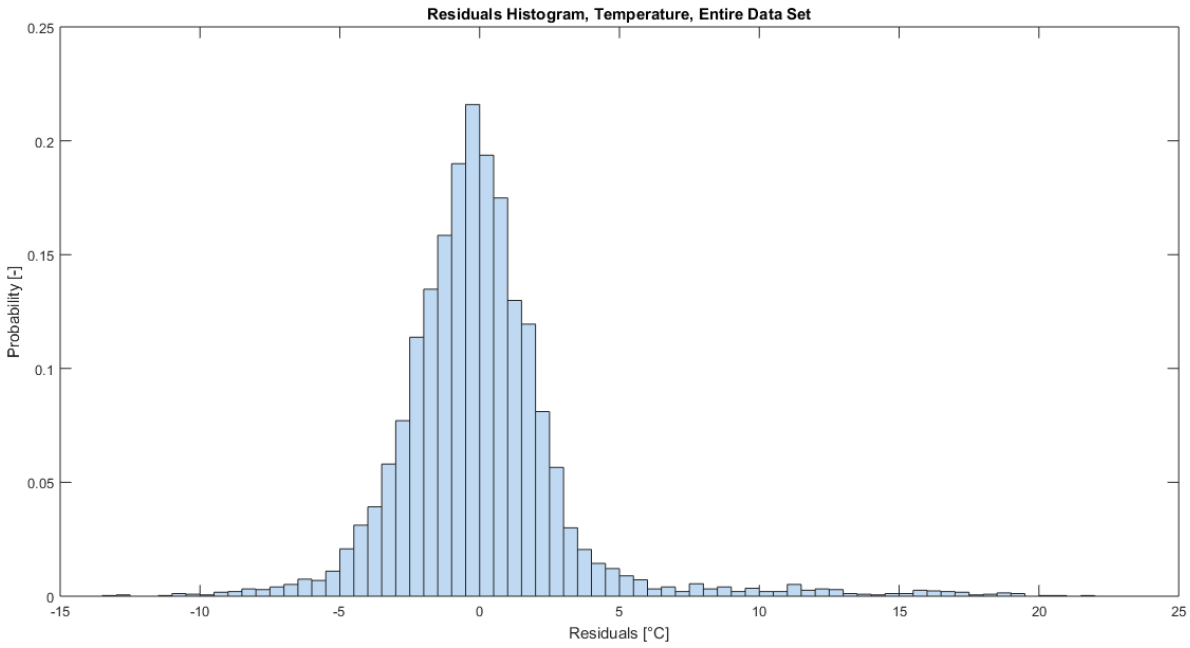

Figure 36 Frequency range histogram of PV module temperature residuals of entire data set population (own figure)

The standard deviation S of the temperature residuals of the entire data set population is 3.3°C. For a desired MOE of 1°C and a confidence level of 95% (i.e. a value of $z_{\alpha/2}$ of 1.96), a minimum sample size n of about 42 data points is required for further comparisons of PV module temperature data samples (bin ranges).

7.4 Module power calculation

The PV module power calculation according to the interpolation method suggested by the IEC 61853-3 committee draft – described in section 3.3.7 – is schematically illustrated in the following figure. In order to allow power modeling over the entire observed data set population, the given performance matrix had to be extrapolated to cover also lower irradiance and temperature ranges – as explained in section 3.3.7. Figure 37 shows the measured PV output power (black full line – top graph) compared to the estimated/calculated PV module output power (red dashed line – top graph). Residuals between measured and modeled PV module power values are plotted in the bottom graph of Figure 34 (yellow dots). The mean difference between the measured and the estimated PV module output power is about -4.2 W and the median difference –1 W for the entire observed data set population of 6929 data points – with RMSE of about 12.7 W and MAD of about 2.6 W.

Power Modeling Error – Entire Data Set			
RMSE [W]	MAD [W]	μ [W]	Median diff. [W]
12.7	2.6	-4.2	-1

Table 13 Power modeling error indicators for the entire data set population (own table)

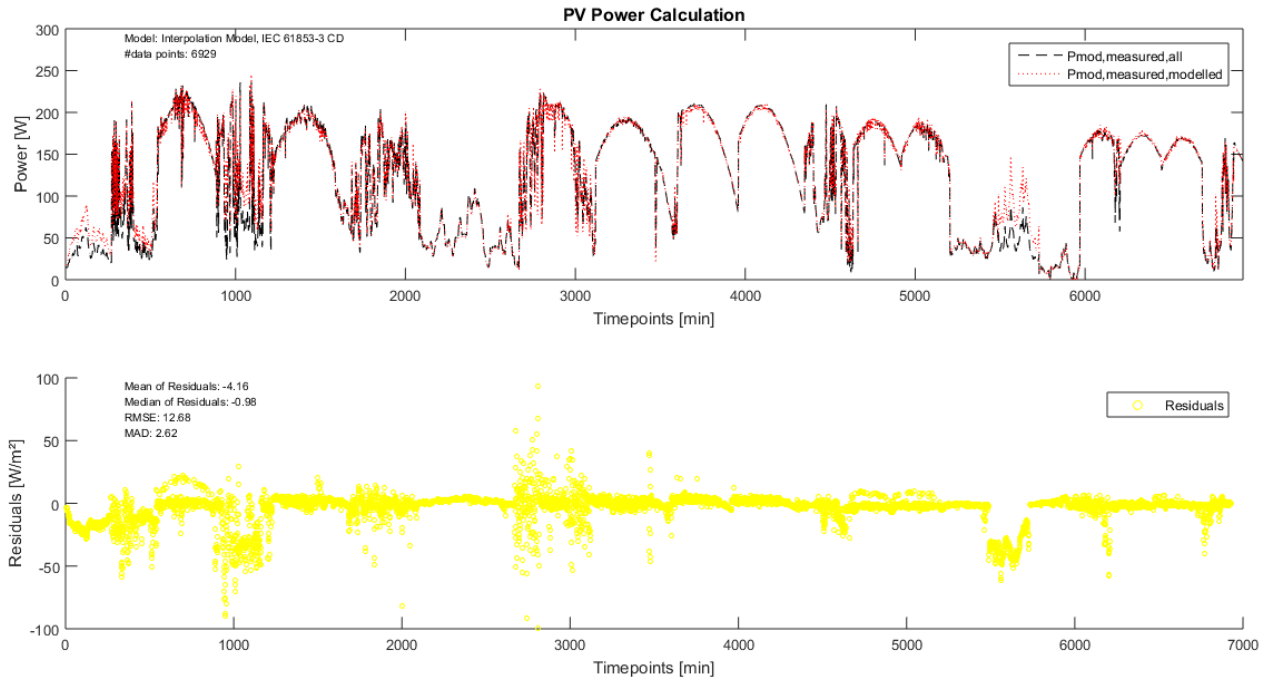

Figure 37 PV module power calculation (own figure)

7.4.1 Distribution of residuals and sample size - Power

The observed residuals of modeled and measured PV module power show a more narrow distribution and the presence of one significant peak close to zero. The distribution of the residuals roughly follows a normal distribution with the center being close to zero and a light skew to the left (negative residuals). The slightly visible left skew indicates the tendency of the model to underpredict the PV module power, leading to more negative residuals for the observed entire data set population. As can also be seen in the plot of residuals over time in Figure 37Figure 35.

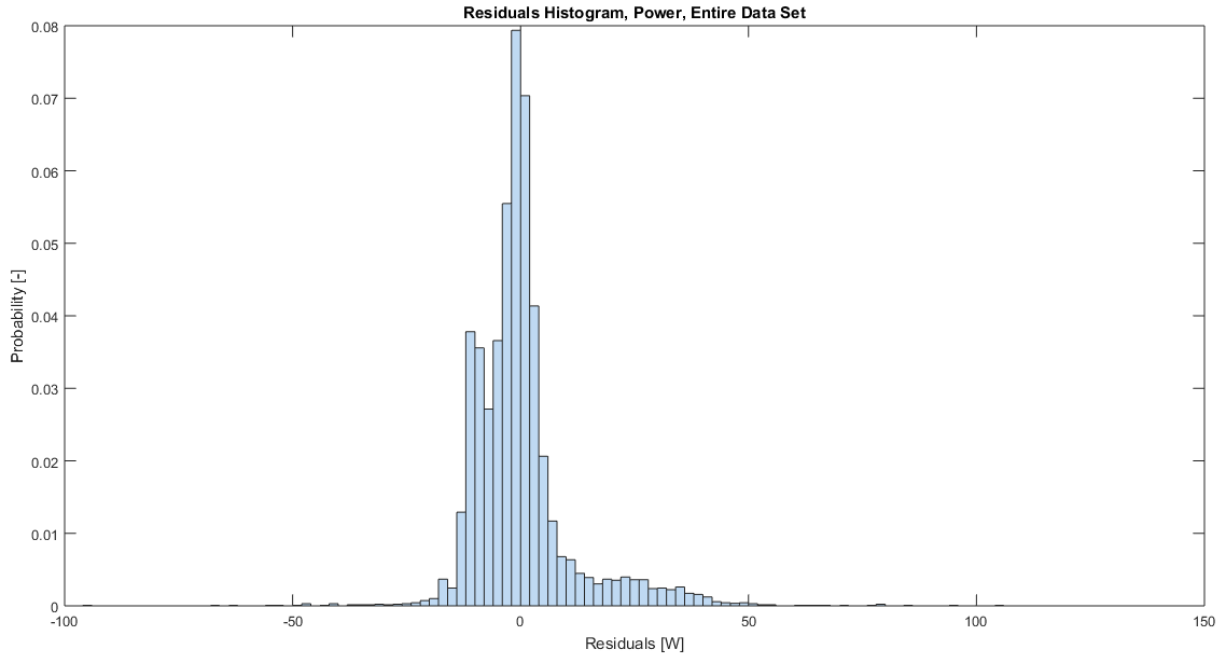

Figure 38 Frequency range histogram of PV module power residuals of entire data set population (own figure)

The standard deviation S of the power residuals of the entire data set population is about 12 W. For a desired MOE of 2 W and a confidence level of 95% (i.e. a value of $z_{\alpha/2}$ of 1.96), a minimum sample size n of about 138 data points is required for further comparisons of PV module power data samples (bin ranges).

7.5 Analysis of days with characteristic weather conditions

This chapter summarizes statistical indicators for each of the observed days with characteristic weather conditions – as mentioned in section 3.5 – such as RMSE, MAD, R^2, $R_{pearson}$ and $R_{spearman}$. The combination of these indicators should provide information about how well the IEC 61853-3 draft calculation procedures can estimate PV module temperature and power for each of the observed days and serve as a first evaluation of the standard's modeling algorithms.

The following table shows the statistical indicator values for the comparison of the modeled and measured PV module temperature.

Temperature: Modelled versus measured

irradiance/temperature/wind speed	RMSE [°C]	MAD [°C]	R^2 [-]	$R_{pearson}$ [-]	$R_{spearman}$ [-]
H/H/H	4,34	2,05	0,57	0,75	0,83
H/H/H	2,61	1,13	0,73	0,86	0,84
H/H/H	2,89	1,25	0,63	0,80	0,81
H/H/L	3,74	1,28	0,81	0,90	0,88
H/H/L	4,24	1,41	0,84	0,92	0,95
H/L/H	4,30	0,94	0,21	0,46	0,70
H/L/H	5,62	0,95	0,02	0,15	0,45
H/L/H	3,78	1,20	0,12	0,35	0,51
H/L/L	3,77	1,37	0,35	0,59	0,60
H/L/L	2,43	1,07	0,34	0,58	0,69
H/L/L	3,85	1,54	0,20	0,45	0,48
L/L/L	1,58	0,59	0,77	0,88	0,83
L/L/L	2,24	0,66	0,71	0,84	0,84
L/L/H	3,70	1,55	0,44	0,66	0,73
L/L/H	2,79	0,74	0,39	0,63	0,74
L/H/L	2,14	0,85	0,87	0,93	0,91
L/H/L	1,05	0,49	0,81	0,90	0,84
L/H/L	6,50	2,82	0,67	0,82	0,83
L/H/H	1,82	0,88	0,89	0,94	0,94
L/H/H	2,25	1,27	0,69	0,83	0,83
L/H/H	1,42	0,46	0,98	0,99	0,85

Table 14 Statistical parameters for days with characteristic weather conditions, temperature – low values of RMSE and MAD indicate better predictions while high values of R^2, $R_{pearson}$ and $R_{spearman}$ indicate better correlation and determination of predictions (own table)

Table 14 clearly shows, that for days with lower average irradiance, the PV module temperature estimation errors – represented by RMSE and MAD – are significantly lower than for days with higher average irradiance. The best model fit – represented by R^2, $R_{pearson}$ and $R_{spearman}$ – can be achieved at days with high average ambient temperature, independent of daily average irradiance and wind speed.

The highest prediction error according to values of RMSE and MAD occurs on a day with low average irradiance and wind speed values and high average ambient temperature (LHL, 08/01/2016), showing a clear difference to the other two days of the same type. The affected day shows significant fluctuation in measured irradiance – see figure below.

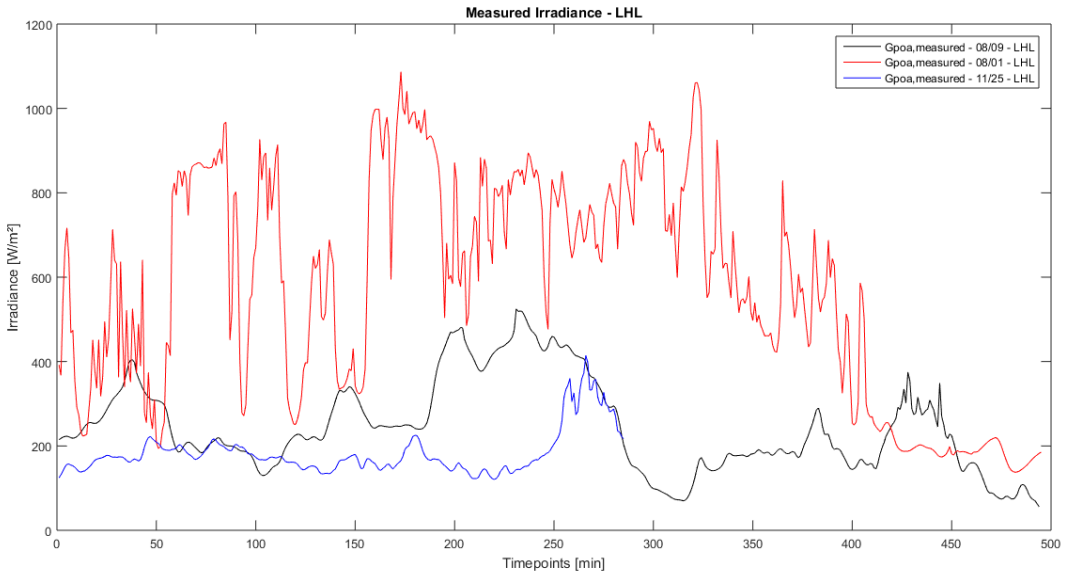

Figure 39 Irradiance differences on LHL days (own figure)

These strong fluctuations typically indicate measurements taken on a cloudy day. The modeling approach of Faiman (2008), used to predict PV module temperatures, directly translates these fluctuations into fluctuations in PV module temperature – as can be seen in the figure below (red line, 08/01 LHL). The error between measured and modeled PV module temperature appears due to neglecting of thermal mass of the PV module in the applied modeling approach – using 1-minute averages of measured data. Thus, smaller fluctuation in measurements and/or the increase of the averaging interval of measurements possibly leads to a more accurate prediction for days with strong fluctuation in irradiance (and wind speed). Furthermore, the consideration of thermal mass and/or longer averaging periods of data in comparison can also improve the prediction error.

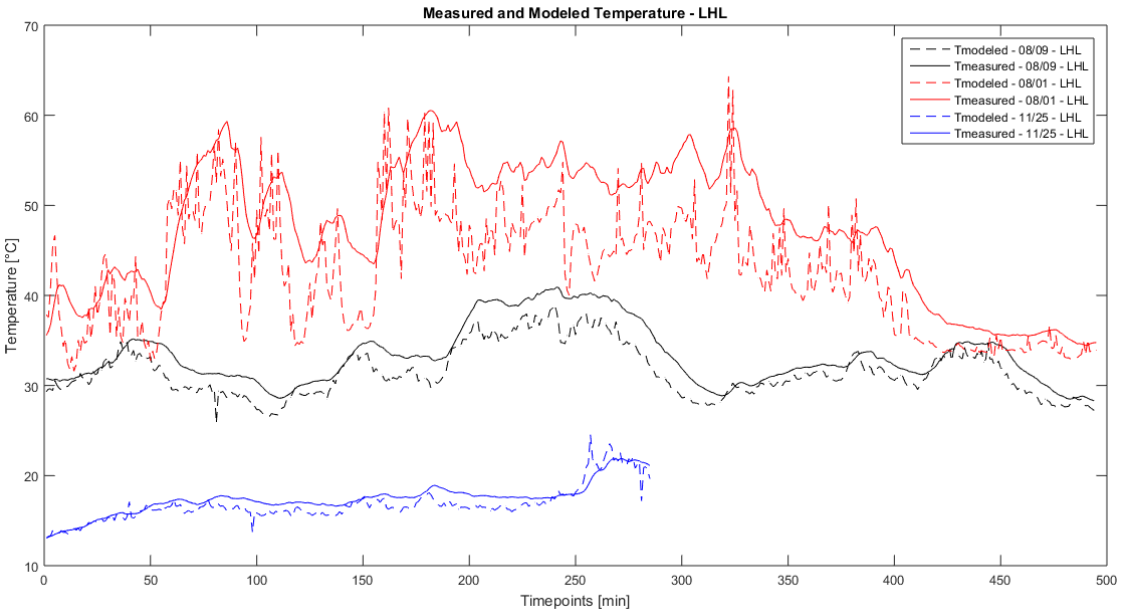

Figure 40 Measured versus modeled temperature on LHL days (own figure)

The following table shows the statistical indicator values for the comparison of the modeled and measured PV module temperature.

Power: Modelled versus measured

irradiance/temperature/wind speed	RMSE [W]	MAD [W]	R^2 [-]	$R_{pearson}$ [-]	$R_{spearman}$ [-]
H/H/H	18,78	5,59	0,89	0,94	0,93
H/H/H	4,18	1,70	1,00	1,00	0,99
H/H/H	2,57	1,21	1,00	1,00	0,99
H/H/L	5,54	1,97	0,97	0,99	0,98
H/H/L	3,37	1,92	1,00	1,00	0,99
H/L/H	4,75	1,03	0,95	0,97	0,95
H/L/H	5,94	1,75	0,95	0,97	0,96
H/L/H	3,25	0,82	0,96	0,98	0,97
H/L/L	2,28	1,00	0,98	0,99	0,99
H/L/L	1,78	0,76	0,97	0,99	0,98
H/L/L	10,24	2,17	0,89	0,94	0,91
L/L/L	17,45	1,97	0,98	0,99	0,99
L/L/L	35,77	6,29	0,98	0,99	1,00
L/L/H	30,40	17,07	0,93	0,96	0,97
L/L/H	19,84	5,18	0,93	0,96	0,96
L/H/L	2,53	0,99	1,00	1,00	1,00
L/H/L	3,03	0,45	0,96	0,98	0,99
L/H/L	8,03	2,24	0,98	0,99	0,99

L/H/H	6,61	1,59	0,99	0,99	0,99
L/H/H	7,32	1,55	0,99	0,99	0,99
L/H/H	1,71	0,62	0,97	0,99	0,99

Table 15 Statistical parameters for days with characteristic weather conditions, power (own table) – low values of RMSE and MAD indicate better predictions while high values of R^2, $R_{pearson}$ and $R_{spearman}$ indicate better correlation and determination of predictions (own table)

The results in Table 15 show the tendency to lower estimation errors for days with higher average irradiance. However, tendencies are not as clearly visible as with the temperature modeling.

The highest prediction errors according to values of RMSE and MAD occur on a days with low average irradiance, ambient temperature and wind speed (LLL) as well as for days with low average irradiance, ambient temperature and high average wind speed (LLH). Modeled (dashed lines) and measured (full lines) power for these days is illustrated in the figure below.

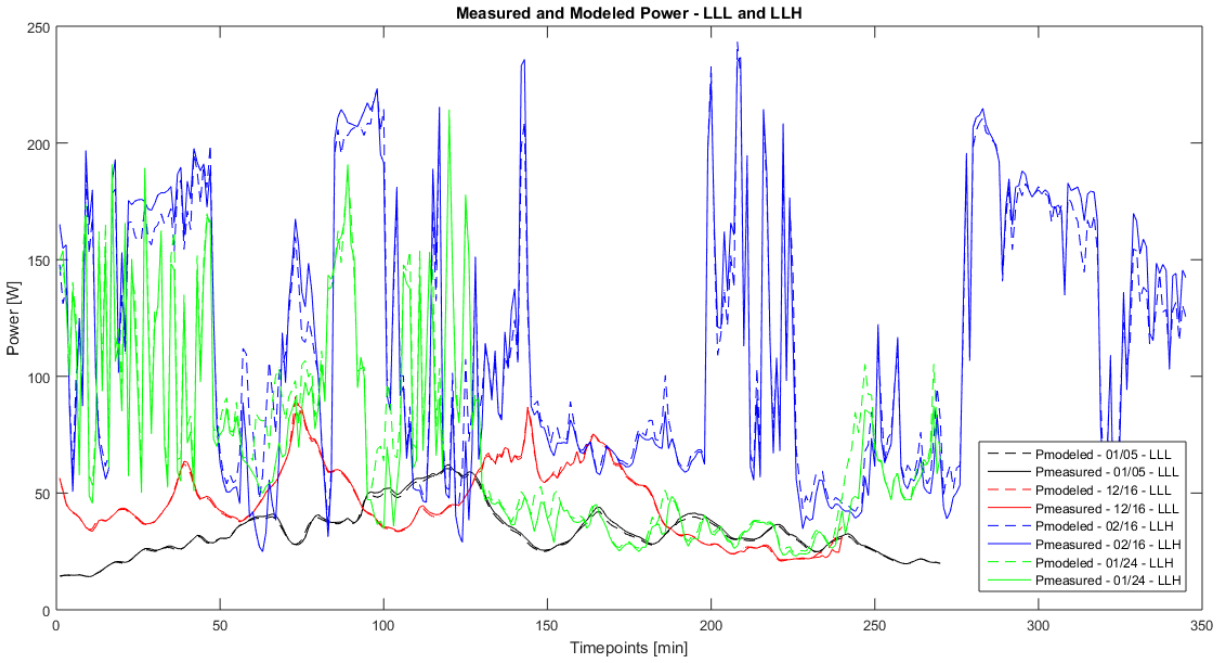

Figure 41 Measured versus modeled temperature on LLL and LLH days (own figure)

The comparison of power estimation error for different days with characteristic weather conditions shows no fully conclusive pattern. Thus, for better understanding and in order to study and evaluate the IEC modeling algorithms for specific weather conditions at various ranges of irradiance, ambient temperature, wind speed and angle of incidence, it is necessary to divide the described data set of all days with characteristic weather conditions into bins – as explained in section 0. This is done through the analysis of effects of individual bin range variation as well as the analysis of the bin ranges interaction with each other.

7.6 Analysis of effects of independent variation of bin ranges

Prior to the analysis of interactions and cross-dependencies between the observed bin ranges, this analysis focuses on effects caused by the individual variation of each of the above mentioned parameters irradiance, ambient temperature, wind speed and angle of incidence for the entire data set population. Effects are analyzed via residual analysis. Therefore, residuals – differences between modeled and measured values – are plotted over the corresponding parameters of interest. Furthermore, plots include information about RMSE and R^2 values related to the corresponding ranges.

In the following, at first effects on the temperature model of Faiman (2008) and then effects on the modeled PV module output power according to IEC 61853-3 calculation procedures are analyzed.

Temperature - Modeled versus measured

The following figure illustrates the variation analysis of PV module temperature residuals, depending on the independent variation of irradiance (black, top left), ambient temperature (red, top right), wind speed (blue, bottom left) and angle of incidence (green, bottom right). It includes information about RMSE variation for each observed range (red axis on the right and red dashed line inside the graphs) as well as information about the coefficient of determination R^2 (listed along the x-axis for each range).

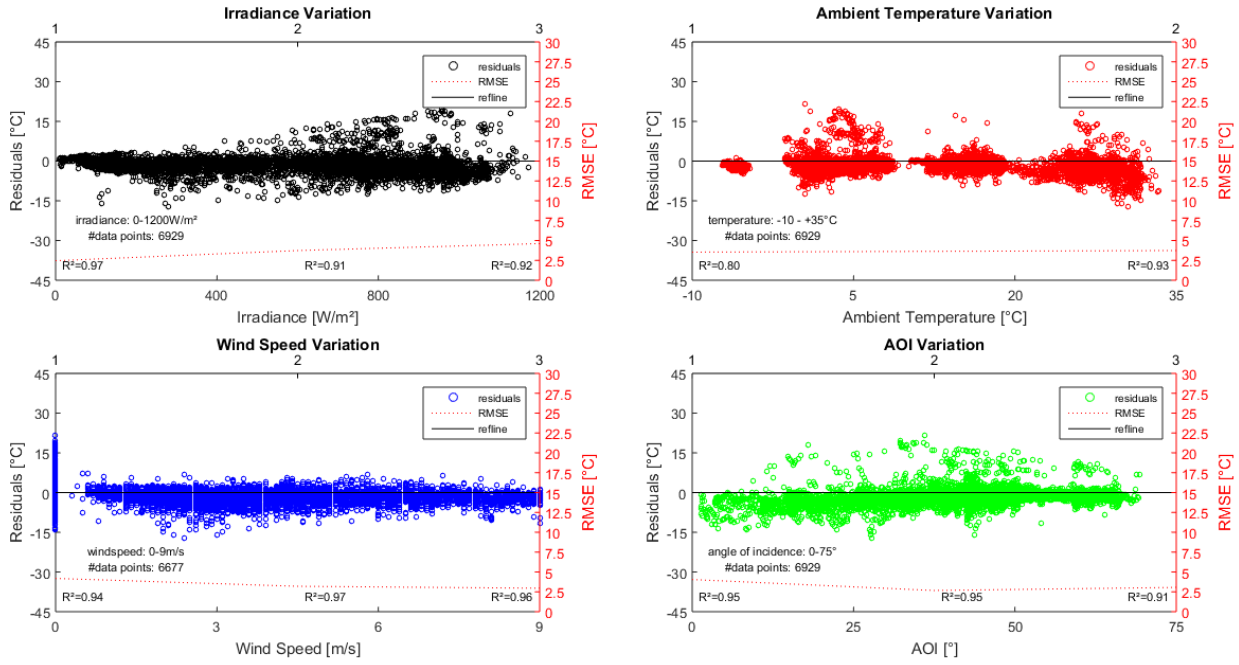

Figure 42 Independent parameter variation analysis of residuals for the modeled temperature (own figure)

Figure 42 shows that for increasing irradiance values, RMSE increases from about 2.5 °C to about 4.6°C. It is visible that with increasing irradiance values, also the variance of the residuals changes (heteroscedasticity) – more pronounced to positive values, i.e. overprediction of the module temperature. This behavior is also reflected in a slight decrease of the coefficient of determination R^2, which indicates difficulties of the model in the estimation of PV module temperature for higher irradiance ranges, confirming also the findings of the analysis of days with characteristic weather conditions. There seems to be no significant effect of the ambient temperature increase on values of RMSE for the temperature prediction. Nevertheless, residuals show a slight trend to more negative values with increasing ambient temperature. Also, the variance of the residuals with increasing temperature values seems to get more constant (homoscedasticity) – also leading to better values in R^2. An increase in wind speed leads to a slight decrease in RMSE ranging from 4 °C to 3 °C. It can also be seen that an increase in wind speed causes a more narrow distribution of the residuals, with no significant changes in values of R^2. The variation of the angle of incidence (AOI) between 0° and 70° leads to more significant changes for angles between 0° and 45°. An increase in AOI shows a decrease in RMSE, also reflected in the change of distribution of residuals around zero – leading to lower errors. Negative residuals reduce further for AOI between 45° and 70°, leading to no significant change in RMSE and/or R^2.

Lowest errors and best correlation could be achieved at low irradiance values ranging from 0 to 400 W/m² measured global in-plane irradiance – with RMSE of about 2.5 °C – as well as for angles of incidences between 45° and 60° - with RMSE of about 2.7 °C.

Variations in modeling error and correlation can also be illustrated with the median absolute deviation (MAD), the Pearson coefficient of correlation ($R_{pearson}$) and the Spearman coefficient of correlation ($R_{spearman}$). These parameters follow the above described behavior and are shown in the following table:

Independent Variation	RMSE [°C]	MAD [°C]	R^2 [-]	$R_{pearson}$ [-]	$R_{spearman}$ [-]
Irradiance 1 **(0-400W/m²)**	2.46	0.94	0.97	0.99	0.98
Irradiance 2 **(400-800W/m²)**	3.74	1.52	0.91	0.96	0.94
Irradiance 3 **(800-1200W/m²)**	4.61	1.52	0.92	0.96	0.95
Ambient Temperature 1 **(-10-+13°C)**	3.54	1.13	0.80	0.90	0.90
Ambient Temperature 2 **(+13-+36°C)**	3.74	1.70	0.93	0.96	0.97
Wind Speed 1 **(0-3m/s)**	4.19	1.35	0.94	0.97	0.96
Wind Speed 2 **(3-6m/s)**	3.20	1.57	0.97	0.98	0.98
Wind Speed 3 **(6-9m/s)**	2.95	1.37	0.96	0.98	0.97
AOI 1 **(0-45°)**	4.05	1.52	0.95	0.97	0.97

AOI 2 (45-60°)	2.67	1.04	0.95	0.97	0.96
AOI 3 (60-70°)	3.06	1.25	0.91	0.96	0.95

Table 16 Independent parameter variation analysis for whole array, temperature: RMSE, MAD, R^2, $R_{pearson}$, $R_{spearman}$ (own table)

Power - Modeled versus measured

The following figure also illustrates the variation analysis of PV module power residuals, depending on the independent variation of irradiance (black, top left), ambient temperature (red, top right), wind speed (blue, bottom left) and angle of incidence (green, bottom right). It includes information about RMSE variation for each observed range (red axis on the right and red dashed line inside the graphs) as well as information about the coefficient of determination R^2 (listed along the x-axis for each range).

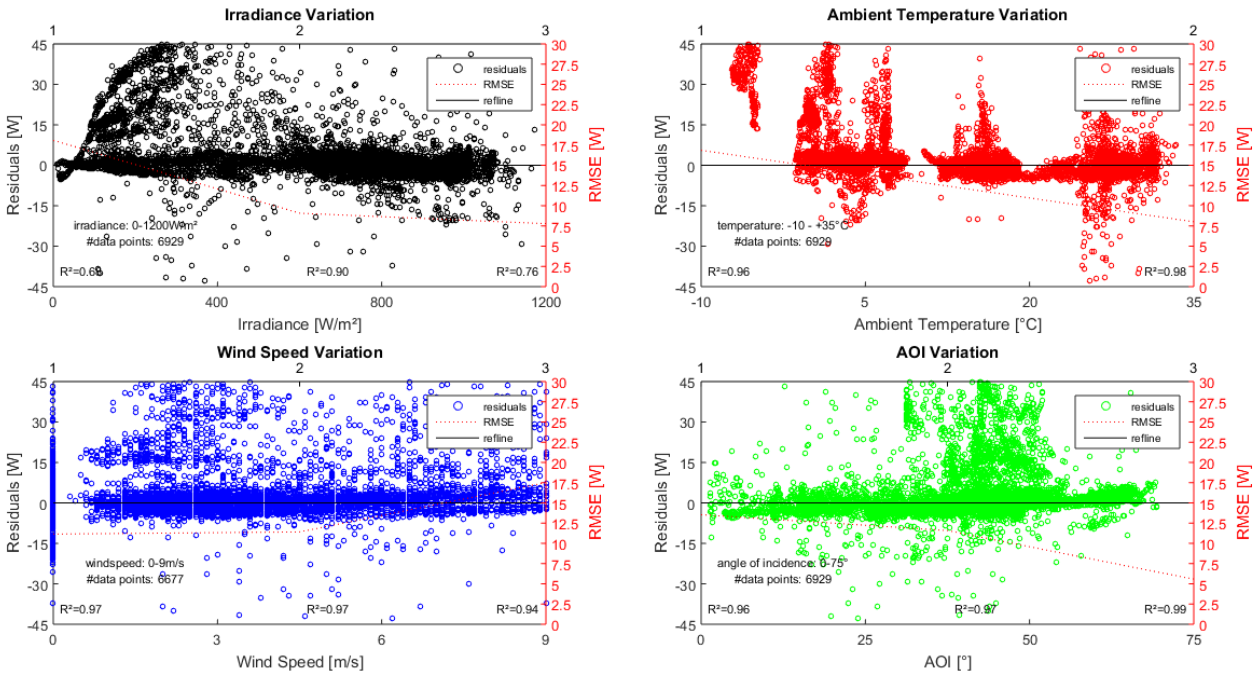

Figure 43 Independent parameter variation analysis of residuals for the modeled power (own figure)

Figure 43 clearly shows a tendency to higher values in RMSE and significantly increased variance of residuals, shown as a strong overprediction at low irradiance ranges between 0 and 400 W/m² – with RMSE of about 18 W and R^2 of about 0.7. An increase of irradiance leads to better estimations, with RMSE of about 9 W for irradiances between 400 and 800 W/m² and 8 W for irradiances between 800 and 1200 W/m², showing also improvement in R^2. An increase of ambient temperature shows positive effect on the modeling error, leading to RMSE values of about 17 W for low and 8 W for high ambient temperature ranges. High values in RMSE at low ambient temperatures between -10 and +13 °C are represented

as strong overprediction of power. Increasing ranges of wind speed show strong effect on modeling error for ranges above 6 m/s, leading to values of RMSE of about 18 W. Lower wind speeds between 0 and 6 m/s show slightly lower RMSE of about 11 W. Increasing ranges of AOI show a significant reduction of the modeling error from about 14 W for low values of AOI to about 6 W for high ranges of AOI. However, residuals show a stronger visible overprediction of power between AOI of 30 to 50°.

Lowest errors and best correlation could be achieved for high irradiances ranging from 800 to 1200 W/m² measured global in-plane irradiance, as well as for AOI between 60° and 70° and high ambient temperatures – with RMSE between about 6 and 8 W.

Variations in modeling error and correlation can again be illustrated with the median absolute deviation (MAD), the Pearson coefficient of correlation ($R_{pearson}$) and the Spearman coefficient of correlation ($R_{spearman}$). These parameters follow the above described behavior and are shown in the following table:

Independent Variation	RMSE [W]	MAD [W]	R^2 [-]	$R_{pearson}$ [-]	$R_{spearman}$ [-]
Irradiance 1 (0-400W/m²)	18.09	4.21	0.68	0.83	0.86
Irradiance 2 (400-800W/m²)	9.08	1.99	0.90	0.95	0.97
Irradiance 3 (800-1200W/m²)	7.78	2.37	0.76	0.87	0.92
Ambient Temperature 1 (-10-+13°C)	16.85	3.16	0.96	0.98	0.99
Ambient Temperature 2 (+13-+36°C)	8.01	2.11	0.98	0.99	0.99
Wind Speed 1 (0-3m/s)	11.15	2.46	0.97	0.99	0.98
Wind Speed 2 (3-6m/s)	11.41	2.29	0.97	0.98	0.99
Wind Speed 3 (6-9m/s)	17.52	4.24	0.94	0.97	0.98
AOI 1 (0-45°)	13.54	2.76	0.96	0.98	0.98
AOI 2 (45-60°)	11.59	2.01	0.97	0.98	0.98
AOI 3 (60-70°)	5.57	1.53	0.99	1.00	0.99

Table 17 Independent parameter variation analysis for whole array, power: RMSE, MAD, R^2, $R_{pearson}$, $R_{spearman}$ (own table)

7.7 Analysis of effects of cross-dependent variation of bin ranges

This chapter analyses the interaction (cross-dependence) of the observed bin ranges (data samples) and thus effects caused by the (co-)variation of each of the above mentioned parameters irradiance, ambient temperature, wind speed and angle of incidence – which allows in total 54 combinations. As above, effects are analyzed via residual analysis. Therefore, residuals – differences between modeled and measured values – are plotted over the corresponding parameters of interest. Furthermore, plots include information about RMSE and R^2 values related to the corresponding ranges. As above, the following analysis at first focuses on effects on the temperature model of Faiman (2008) and then on effects on the modeled PV module output power according to IEC 61853-3 draft's calculation procedures.

Temperature - Modeled versus measured

The following figures illustrate the analysis of residuals, depending on the combined variation of irradiance, ambient temperature, wind speed and angle of incidence – in total 54 combinations. They include information about RMSE variation for each observed range (red y-axis on the right side and red dashed line inside each graph) as well as information about the coefficient of determination R^2 (written along the x-axis for each bin range).

Each figure represents one range of angles of incidence (AOI range 1, range 2, range 3). Plots inside one figure illustrate changes in ambient temperature (horizontal, from left to right) and wind speed (vertical, from top to bottom). Residuals are plotted over increasing irradiance values along the x-axis.

Normally distributed data samples of temperature residuals that have a minimum sample size of 42 data points are considered to be within a margin of error MOE of ±1 °C deviation of the data sample (bin range) mean to the entire data set population's mean – with a confidence level of 95%.

Angle of incidence range 1 – 0° to 45°

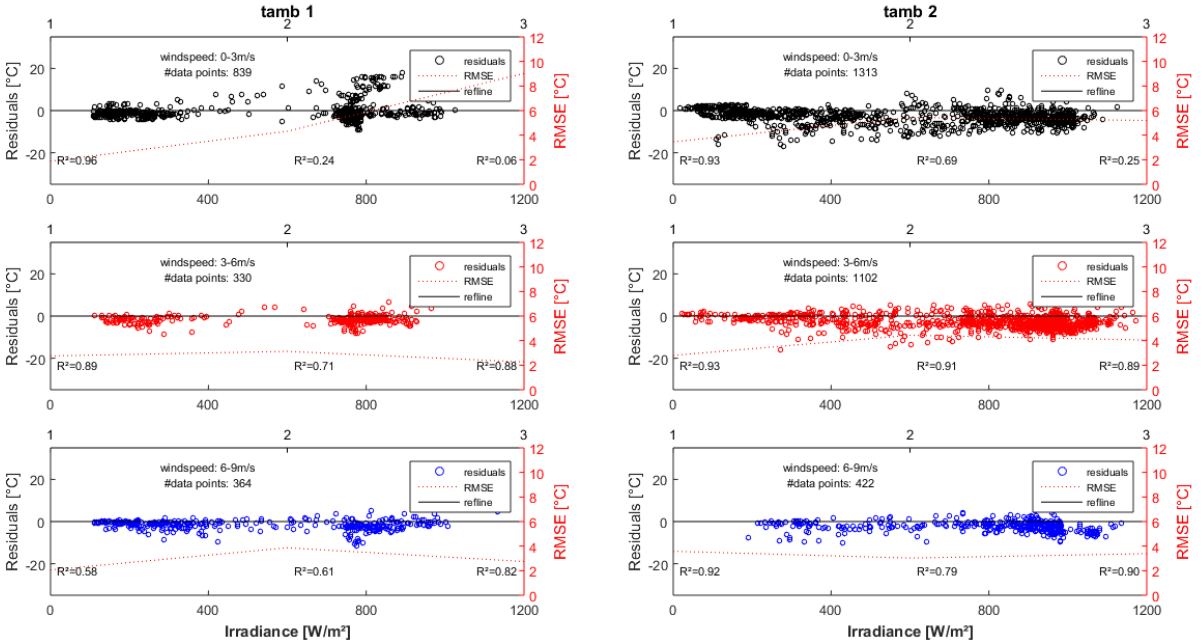

Figure 44 Parameter variation analysis of residuals for the modeled temperature, AOI1 (own figure)

All of the observed data samples at these range of AOI between 0° and 45° (AOI range 1) are above the expected minimum sample size of 42 – except samples at low ambient temperature ranges between -10 and +13°C, wind speeds ranging from 0 to 6 m/s and irradiances from 400 to 800 W/m².

The figure above shows the tendency of increased RMSE of about 9 °C and increased change in variance of residuals for increasing irradiances at low wind speeds between 0 and 3 m/s and low ambient temperatures between -10 and +13 °C (tamb1) – also reflected in significant decrease of R^2 below 0.1. The influence of the irradiance on the PV module temperature prediction changes with increasing wind speeds between 3 and 9 m/s and/or increased ambient temperatures between +13 and +35 °C – leading to slightly lower values in RMSE ranging from about 2 to 5 °C and better values of R^2 around 1.

Best values in RMSE and R^2 at these ranges of AOI are reached for irradiances between 0 and 400 W/m² – with values of RMSE of about 2 °C and R^2 of 0.96. Worst values in RMSE and R^2 can be found for high irradiance values and low wind speeds leading to values in RMSE of about 9 °C and values of R^2 below 0.1.

Angle of incidence range 2 – 45° to 60°

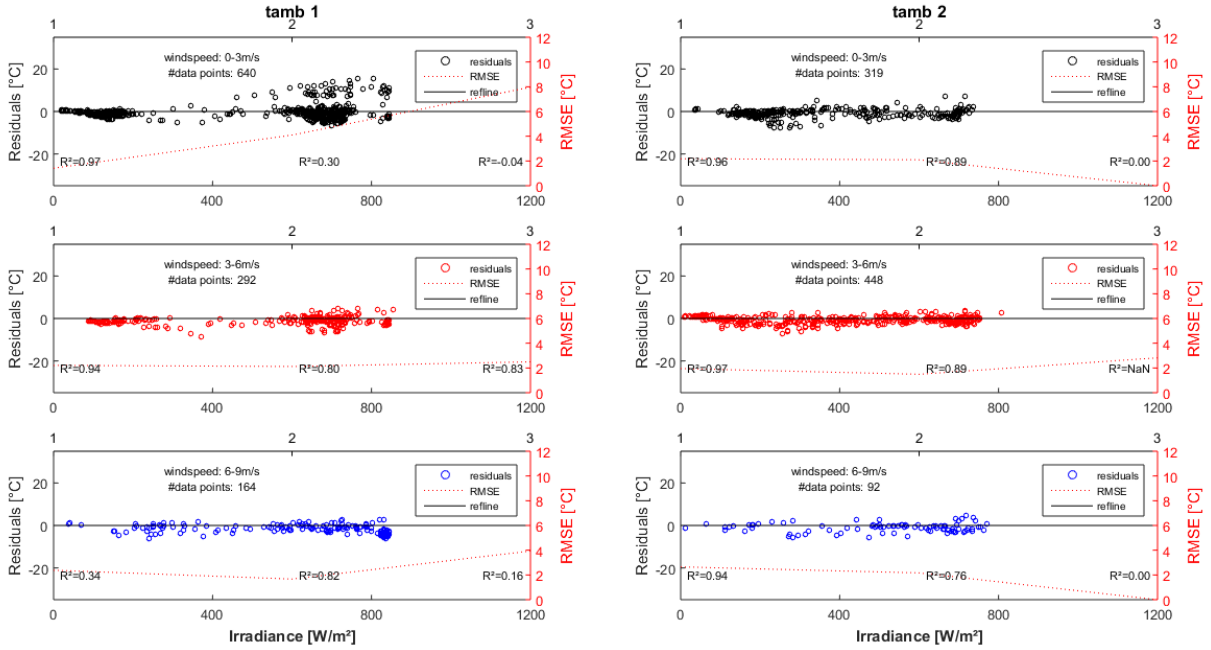

Figure 45 Parameter variation analysis of residuals for the modeled temperature, AOI2 (own figure)

For ranges of AOI between 45° and 60° (AOI range 2) the expected minimum sample size of 42 data points can not be achieved for irradiance values above 800 W/m².

It can be seen that changes of irradiance have their strongest influence at low ambient temperatures between -10 and +13 °C and low wind speeds between 0 and 3 m/s. As observed above, an increase of wind speed and/or ambient temperature leads to less influence of the irradiance on the modeling error.

Best values in RMSE and R² at this range of AOI are achieved at low wind speeds between 0 and 3 m/s, low ambient temperatures between -10 and +13 °C and irradiances between 0 and 400 W/m² – with values of RMSE of 1.4 °C and with R² of 0.97. Worst values in RMS and R² can be seen for low wind speeds between 0 and 3 m/s, low ambient temperatures between -10 and 13 °C and high irradiances between 400 and 800 W/m² – with values of RMSE of about 4 °C and R² below 0.3.

Angle of incidence range 3 – 60° to 70°

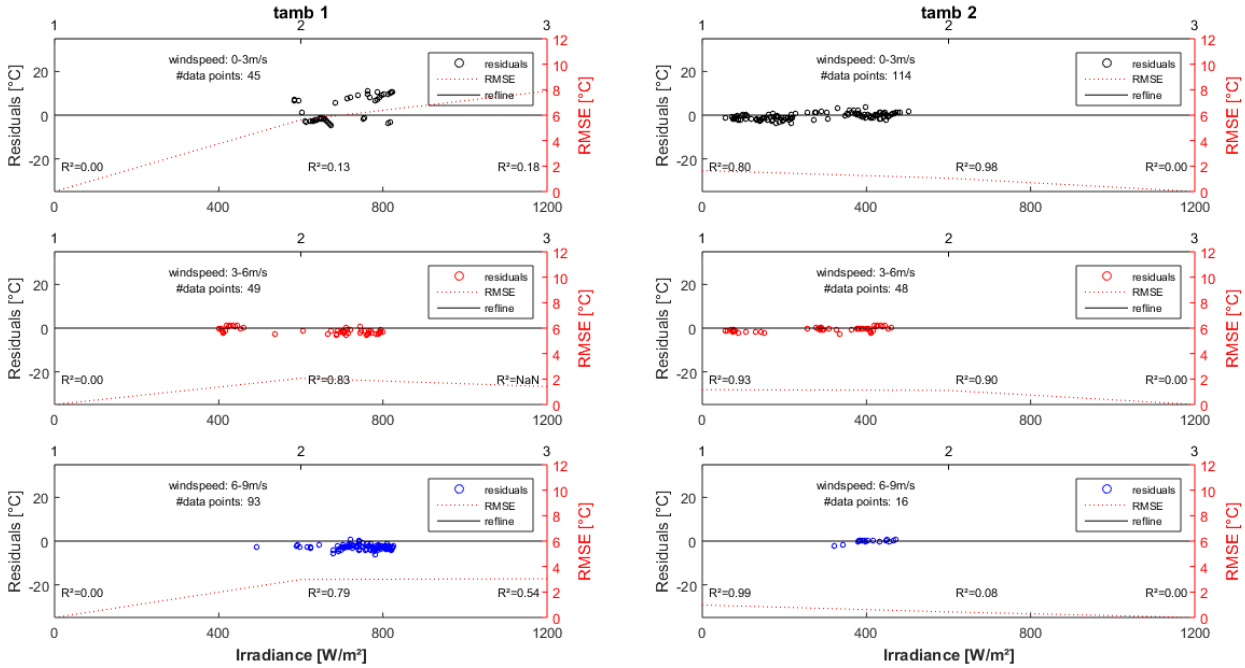

Figure 46 Parameter variation analysis of residuals for the modeled temperature, AOI3 (own figure)

The minimum required sample size of 42 data points can only be achieved for low ambient temperatures and irradiances between 400 and 800 W/m² as well as for high ambient temperatures, irradiances between 0 and 400 W/m² and wind speeds from 0 to 6 m/s. Thus, the observed data set does not allow a full comparison of parameter variation at this range of angle of incidence between 60 and 70°.

However, it is visible that residuals differ significantly at lower wind speeds, lower ambient temperatures and irradiances between 400 and 800 W/m², showing a slightly bigger difference to the zero reference line with more positive values – i.e. overprediction of the model.

Tables, including information about RMSE and R^2 as well as the median absolute deviation (MAD), $R_{pearson}$ and $R_{spearman}$ confirm the above described findings and can be found in the Appendix E of this work. The following table shows the results of the three best and the three worst combinations of the above described combinations of bin ranges according to their values in RMSE of samples that show a close to normal distribution of their residuals and meet the minimum sample size of 42 data points:

Range combination		RMSE [°C]	MAD [°C]	R^2 [-]	$R_{pearson}$ [-]	$R_{spearman}$ [-]
Best	AOI3/Wind3/Tamb2/Irr.1	0.98	0.37	0.99	1.00	0.79
	AOI3/Wind1/Tamb2/Irr.2	1.04	0.76	0.98	0.99	0.85
	AOI3/Wind2/Tamb2/Irr.2	1.11	0.92	0.90	0.95	0.68
Worst	AOI1/Wind1/Tamb2/Irr.2	5.44	2.58	0.69	0.83	0.82
	AOI1/Wind2/Tamb2/Irr.2	4.44	1.90	0.91	0.95	0.95
	AOI1/Wind2/Tamb2/Irr.3	4.04	1.62	0.89	0.94	0.92

Table 18 Three best and worst cases parameter variation analysis for whole array, temperature: RMSE, MAD, R^2, $R_{pearson}$, $R_{spearman}$ (own table)

In order to assure that the observed sample means are within the desired MOE to the population mean, at a confidence level of 95 %, residuals need to be (roughly) normally distributed. Therefore, normal distribution of the temperature residuals of all the of the above mentioned and observed 54 data samples (bin ranges) can be verified via normal probability plots and/or frequency range histograms of residuals listed in the Appendix F. Data samples that do not show a normal distribution indicate behavior that is not accounted for by the applied model.

Power - Modeled versus measured

The following figures also illustrate the analysis of residuals, depending on the combined variation of irradiance, ambient temperature, wind speed and angle of incidence – in total 54 combinations. They include information about RMSE variation for each observed range (red y-axis on the right side and red dashed line) as well as information about the coefficient of determination R^2 (written along the x-axis for each bin range).

As above, each figure represents one range of angles of incidence (AOI range 1, range 2, range 3). Plots inside one figure illustrate changes in ambient temperature (horizontal, from left to right) and wind speed (vertical, from top to bottom). Residuals are plotted over increasing irradiance values along the x-axis.

Normally distributed data samples of temperature residuals that have a minimum sample size of 138 data points are considered to be within a margin of error MOE of ±2 W deviation of the data sample (bin range) mean to the mean of the entire data set population's mean – with a confidence level of 95%.

Angle of incidence range 1 – 0° to 45°

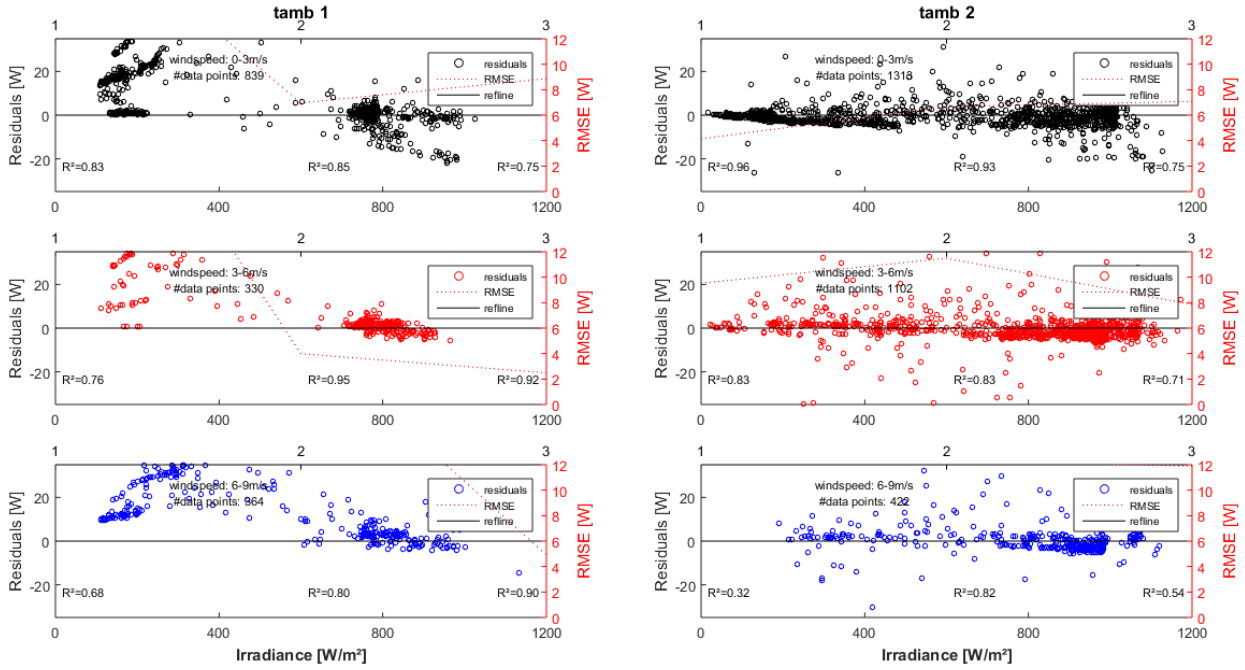

Figure 47 Parameter variation analysis of residuals for the modeled power, AOI1 (own figure)

The minimum required sample size of 138 data points can be achieved for all ranges – except for samples at low ambient temperatures, wind speeds between 3 and 9 m/s and irradiances from 400 to 800 W/m².

Results show that increasing wind speeds and/or ambient temperatures influence the effect of the irradiance on the modeling error significantly, as also observed above. Thus, higher wind speeds and/or ambient temperatures allow better power estimations at high irradiances. Samples at low irradiances between 0 and 400 W/m² and low ambient temperatures between -10 and +13°C show significant deviation of residuals from zero at all wind speed ranges – represented as significant overpredictions. This can be related to magnified errors through linear inter-/extrapolation and non-linearities of the PV performance at these ranges of irradiance and temperature – discussed in the following sections.

Best values in RMSE and R^2 at these ranges of AOI are achieved for high irradiances between 800 and 1200 W/m², high wind speeds between 6 and 9 m/s and low ambient temperatures between -10 and +13 °C – with RMSE of about 2.5 W and R^2 of 0.9. Worst values in RMSE and R^2 can be seen for low irradiances between 0 and 400 W/m², high wind speeds between 6 and 9 m/s and low ambient temperatures between -10 and +13 °C, with RMSE of about 33 W and R^2 of about 0.8, as well as for irradiances between 0 and 400 W/m², low wind speeds between 0 and 3 m/s and low ambient temperatures between -10 and +13 °C with RMSE of about 23 W and R^2 of about 0.8.

Angle of incidence range 2 – 45° to 60°

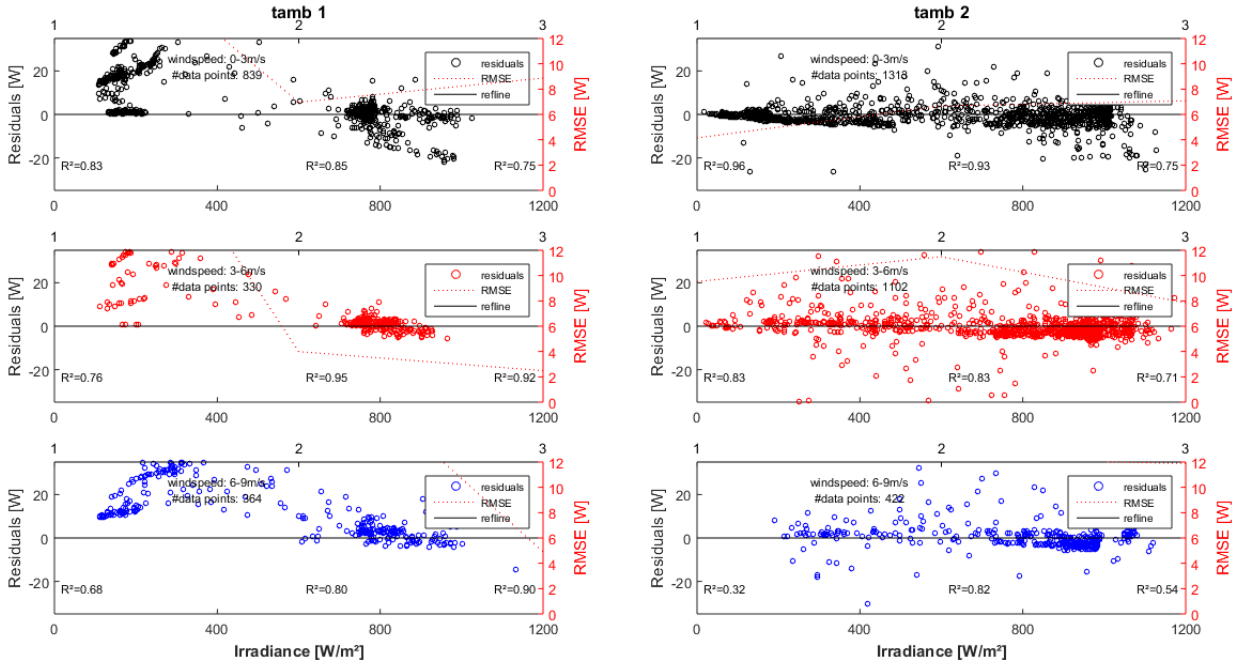

Figure 48 Parameter variation analysis of residuals for the modeled power, AOI2 (own figure)

The minimum required sample size of 138 data points cannot be achieved for samples with low ambient temperatures between -10 and +13 °C, wind speeds between 3 and 9 m/s and irradiances from 400 to 800 W/m².

As above, results show that high ranges of wind speeds and/or ambient temperature influence the effect of the irradiance on the modeling error significantly – leading to lower errors with increased irradiance. Also, increased modeling error at low irradiances between 0 and 400 W/m² and low ambient temperatures between -10 and +13 °C and all wind speed ranges is visible – as above represented as strong overpredictions. This indicates difficulties through linear inter-/extrapolation approach and non-linearities of the PV performance at these ranges of irradiance and temperature – discussed in the following sections.

Best values in RMSE and R^2 at this ranges of AOI are achieved for high wind speeds between 6 and 9 m/s and, high irradiances between 800 and 1200 W/m² and low ambient temperatures between -10 and +13 °C, with RMSE of about 1.7 W and R^2 0.9. Worst values in RMSE and R^2 can be found for low ambient temperatures and irradiances between 0 and 400 W/m², leading to RMSE ranging between 20 W to 33 W and R^2 of 0.8.

Angle of incidence range 3 – 45° to 75°

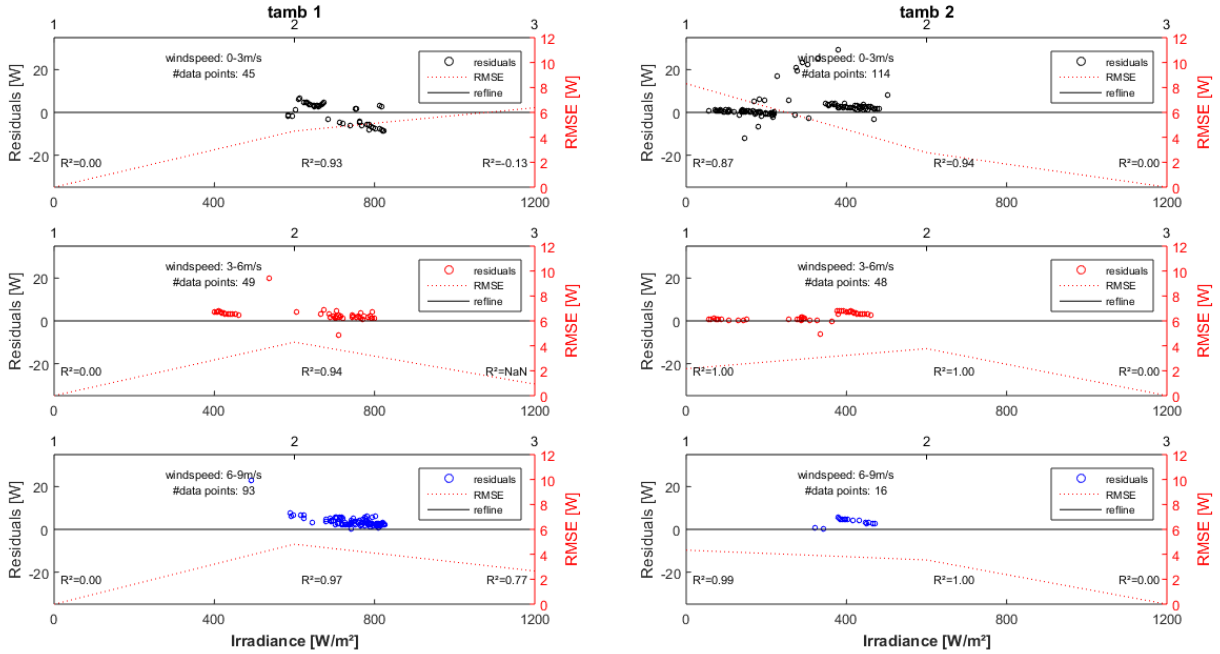

Figure 49 Parameter variation analysis of residuals for the modeled power, AOI3 (own figure)

The minimum sample size of 138 data points cannot be achieved for any of the observed data samples at these ranges of AOI between 60° and 75° (AOI range 3). Therefore, a conclusive interpretation of power estimation errors for the above shown data sample variation at AOI range 3 is not possible.

Tables, including information about RMSE and R^2 as well as the median absolute deviation (MAD), $R_{pearson}$ and $R_{spearman}$ confirm the above described findings and can be found in the Appendix G of this thesis. To exemplary illustrate the range of the results, the following table shows the three best and the three worst combinations of the above described combinations of bin ranges according to RMSE that show a normal distribution of their residuals and meet the minimum sample size of 138 data points:

Ranges		RMSE [W]	MAD [W]	R^2 [-]	$R_{pearson}$ [-]	$R_{spearman}$ [-]
Best	AOI2/Wind2/Tamb1/Irr.3	1.656	0.776	0.876	0.939	0.946
	AOI3/Wind2/Tamb2/Irr.1	2.163	0.386	0.995	0.998	0.991
	AOI1/Wind2/Tamb1/Irr.3	2.486	1.929	0.918	0.958	0.920
Worst	AOI1/Wind2/Tamb1/Irr.1	33.208	9.512	0.765	0.876	0.904
	AOI1/Wind3/Tamb1/Irr.1	33.134	11.163	0.682	0.827	0.824
	AOI2/Wind2/Tamb1/Irr.1	27.969	10.710	0.838	0.916	0.904

Table 19 Three best and worst cases parameter variation analysis for whole array, power: RMSE, MAD, R^2, $R_{pearson}$, $R_{spearman}$ (own table)

In order to assure that the observed sample means are within the desired MOE to the population mean, at a confidence level of 95 %, residuals need to be (roughly) normally distributed. Therefore, normal distribution of the power residuals of all the of the above mentioned and observed 54 data samples (bin ranges) can be verified via normal probability plots and/or frequency range histograms of residuals listed in the Appendix H. Data samples that do not show a normal distribution indicate behavior that is not accounted for by the applied model.

7.8 Summary and discussion of results – Evaluation of modeling algorithms

The observed data set population of about 7000 data points of 1-minute averages of weather and PV operational measurements taken at NIST – measured over a data set of 21 days with characteristic weather conditions – allowed a wide-ranging evaluation of the modeling algorithms used by the IEC 61853-3 committee draft. Evaluation results are summarized and interpreted in the following sub-sections.

Correction procedures and evaluation of entire data set population

As for the correction procedures for AOI and spectral effects, the AOI correction of Martin and Ruiz (2000) showed the most significant effect on the measured irradiance with a mean difference between measured and corrected values of about 50 W/m². The approach for spectral correction through the model developed by Lee and Panchula (2016), leads to smaller changes in the measured irradiance of about 1 W/m² mean difference to the AOI-corrected irradiance.

The analysis of the residuals of the entire data set population of all observed days shows normally distributed residuals with relatively small errors in PV module temperature and power prediction over the entire data set – represented by RMSE values of about 4 °C for the temperature prediction and 13 W for the power prediction as shown in the following table.

Power Prediction Error		**Temperature Prediction Error**	
RMSE [W]	$\mu_{power,\ res.}$ [W]	RMSE [°C]	$\mu_{temperature,\ res.}$ [°C]
12.7	-4.2	3.7	1.5

Table 20 RMSE for power and temperature prediction over entire data set population (own table)

Evaluation of days with characteristic weather conditions

The analysis of each day of the data set population individually allowed to conclude general tendencies of the model with respect to the particular weather conditions on the specific days. Here, RMSE for power prediction ranges from about 2 to 37 W. RMSE for temperature prediction ranges from about 1 to 7 °C. Days with lower daily average irradiance tendentially showed lower errors expressed by RMSE and MAD than days with higher daily average irradiances, especially for temperature estimations. The evaluated model also demonstrated difficulties in estimation of temperature for days with significant fluctuation of measured data (e.g., caused by cloudy days). This could indicate the need for averaging data over longer time periods and/or a better consideration of thermal mass of the PV module in the modeling equations. However, as tendencies are not clearly visible in the analysis of individual days of measurement – especially for the power prediction –, a more comprehensive understanding of the behavior of the model is provided through the analysis of bin ranges

(i.e. data samples) of the entire data set population – via examining variation of ranges independently and cross-dependently.

Evaluation of independent variation of bin ranges (data set population)

The independent variation of the observed 11 bin ranges for irradiance, ambient temperature, wind speed and angle of incidence shows clear tendencies. Modeling errors range from 6 to 18 W RMSE for the power prediction and 3 to 5 °C for the temperature prediction.

It can be seen that for the temperature prediction, modeling errors increase with increasing irradiance. Whereas increasing irradiance causes a decrease of modeling error for the power prediction.

Increasing ambient temperature causes a slight increase in modeling error for the temperature prediction and a clearly visible decrease in modeling error for the power prediction.

The effect of increasing wind speed leads to an increase in modeling error for the power prediction and a decrease in modeling error for the temperature prediction. Whereas these changes are mostly visible for wind speeds above 6 m/s for the power prediction.

Changes in AOI seem to lead to slightly lower modeling errors at higher AOI for the temperature and power prediction. The influence of AOI on the temperature prediction is rather minimal, whereas the influence of AOI on power prediction leads to significant changes.

The following table sums up values of RMSE of the analysis of the independent variation of observed bins for the power and temperature prediction at high/low irradiance, temperature, wind speed and AOI ranges.

Ranges of Parameters	**Power Prediction Error**	**Temperature Prediction Error**
[-]	RMSE [W]	RMSE [°C]
High Irradiance	7.8	4.6
Low Irradiance	18.1	2.5
High Temperature	8.0	3.7
Low Temperature	16.9	3.5
High Wind speed	17.5	3.0
Low Wind speed	11.2	4.2
High AOI	5.6	3.1
Low AOI	13.5	4.1

Table 21 RMSE for power and temperature prediction for high and low observed bin ranges (own table)

Evaluation of cross-dependent variation of bin ranges (data set samples)

The analysis of the interaction (cross-dependence) between all the 11 observed bin ranges through data samples – which allows in total the comparison of 54 combinations of bins – agrees with the findings above and allows a better understanding of the dependencies of the modeling error behavior for certain bin ranges. In the following, cross-dependencies between the individual parameter ranges are analyzed and interpreted.

- **Cooling mechanisms and overprediction at low irradiances**

  The observed data shows significant correlation between irradiance and wind speed variation at all ranges of AOI. The figure below illustrates ranges of AOI between 0 and 45°. It can be seen that at lower wind speeds between 0 and 3 m/s (blue dots), an increase in irradiance causes also an increase in modeling error – visible as power underprediction (negative residuals) and temperature overprediction (positive residuals), especially pronounced at irradiances above approximately 800 W/m². With increased wind speeds above 3 m/s (red and yellow dots), the prediction error decreases considerably – also represented as a decrease in slope of T_{meas} - T_{amb} as a function of irradiance and wind speed.

  This effect might be related to neglecting natural convection at low wind speeds and high irradiance ranges in the temperature model – also discussed by Koehl et al. (2011). Neglecting natural convective cooling at high irradiances and low wind speeds leads to an overprediction of the module temperature (shown as positive residuals), causing also visible underprediction of power (shown as negative residuals). This effect is illustrated in the figure below.

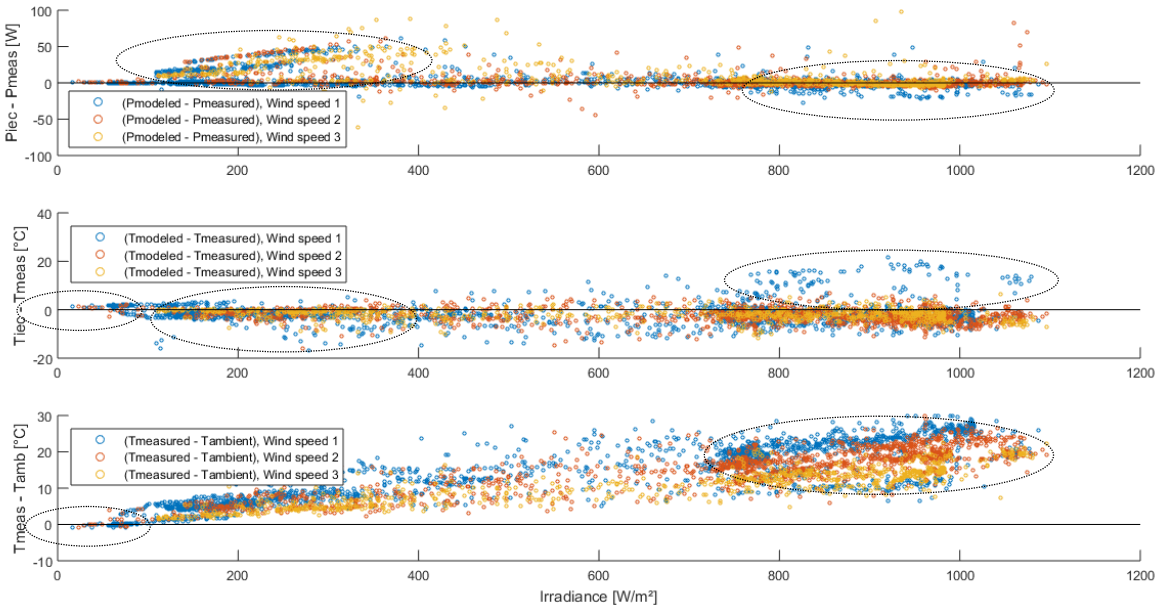

Figure 50 Cooling mechanisms and overprediction at low irradiances – AOI range 1 (own figure)

Next to neglecting natural convection at low wind speeds and high irradiances, Koehl et al. (2011) also discuss neglecting of radiation cooling for low wind speeds and low irradiances – causing negative differences between module and ambient temperature. The effect of radiation is minimally visible, leading to slight temperature overprediction (positive residuals) causing also minimally visible underprediction (negative residuals) of power at all observed ranges of AOI. However, the influences of radiation cooling on the prediction error at the observed ranges are small, as radiation cooling mostly occurs at very low irradiances and/or during night times. At AOI between 45 and 75°, the correlation between wind speed and irradiance is similar and shown in the figure below.

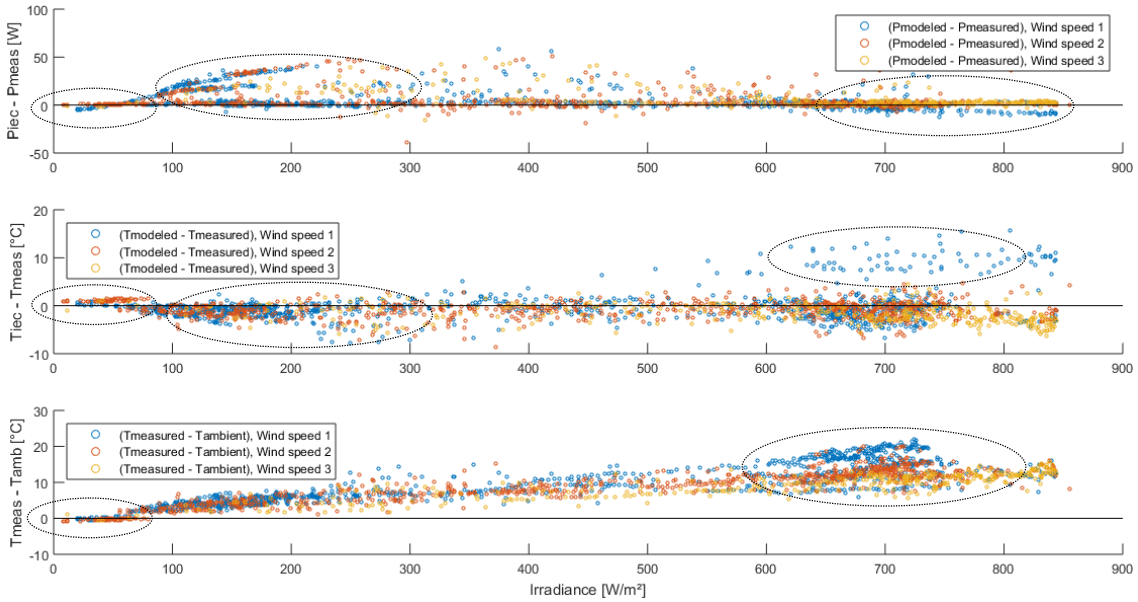

Figure 51 Cooling mechanisms and overprediction at low irradiances, AOI range 2 and 3 (own figure)

Next to the observed cooling mechanisms, both figures above also show strong deviation of residuals at irradiance values between 100 and 300 W/m² - also seen in Figure 47 to 49 at low ambient temperature ranges between -10 and +13 °C. These errors – represented as strong overpredictions (positive residuals) in power and visible underprediction (negative residuals) in module temperature – are most probably related to difficulties of the linear inter-/extrapolation method of the IEC's modeling algorithms to accurately predict power for lower ranges of irradiance and lower ranges of module temperature. Also, the visible underprediction of module temperature possibly contributes to a stronger overprediction in power – as also discussed and pointed out in the following sub-section.

- **Influence of ambient temperature and angle of incidence**

  The figure below shows the residuals of module temperature and power prediction, as well as measured PV module temperature plotted over the ambient temperature for different ranges of AOI (shown in blue and red). It can be seen that the influence of the ambient temperature on the modeling error seems to be most significant at high ranges of AOI between 45° and 75° (red dots). At these ranges of AOI, higher ambient temperatures lead to lower modeling errors for both, temperature and power prediction. At low ranges of AOI between 0° and 45° (blue dots), increased ambient temperatures seem to have significant impact on the temperature estimation – causing strong underprediction of the module temperature and visible variation of residuals for the power prediction.

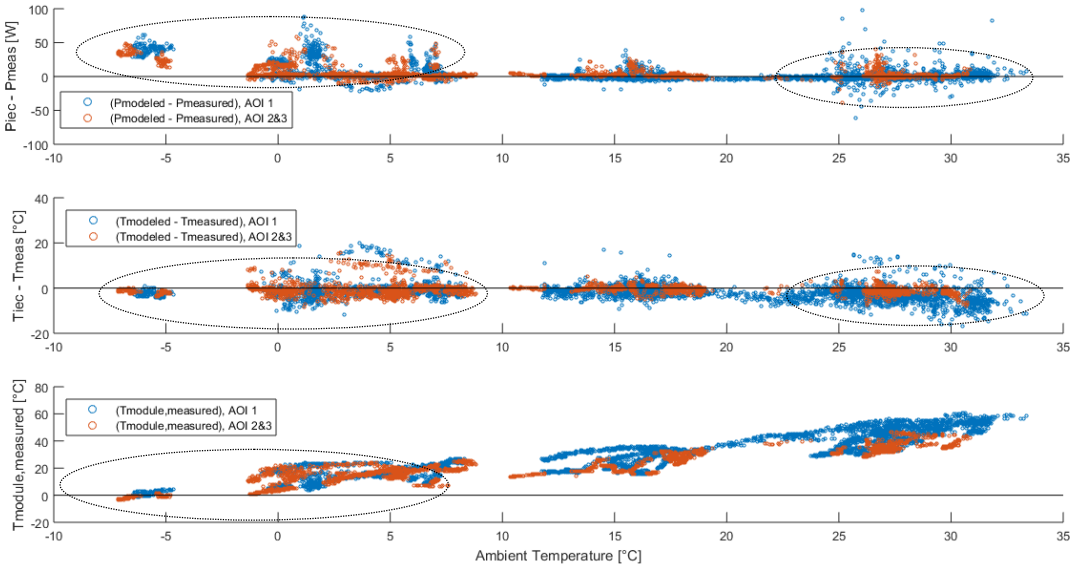

Figure 52 Influence of ambient temperature and AOI on temperature and power prediction (own figure)

These effects can also be related to the higher influence of the irradiance on the module temperature at lower ranges of AOI. The following figure shows temperature and power prediction residuals plotted over the ambient temperature for the different observed ranges of irradiance (shown in blue, red and yellow). It can be seen that at low ambient temperatures below 10 °C and low irradiances between 0 and 400 W/m², the prediction of PV module power leads to high estimation errors – as mentioned above. Most of the visible data points at these ranges show PV module temperatures that are significantly below 15 °C – i.e. outside the range of the available performance matrix used for the interpolation method for power prediction.

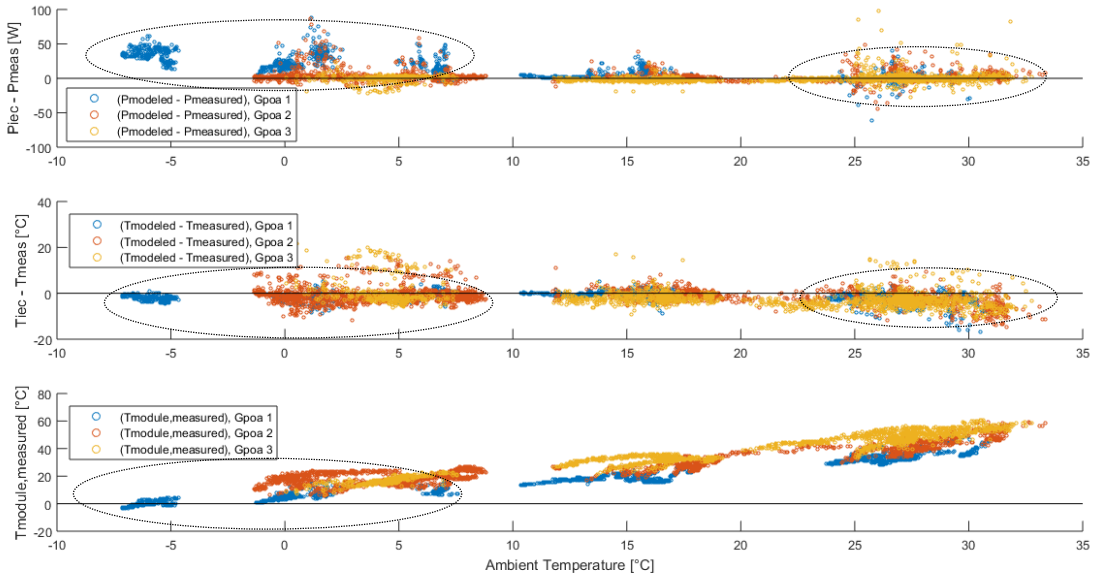

Figure 53 Influence of ambient temperature and irradiance on temperature and power prediction (own figure)

Therefore, in order to predict the PV module power for these lower module temperatures, the performance matrix is linearly extrapolated to applicable ranges – as suggested by the IEC 61853-3 draft. This possibly leads to irregularities introduced through magnifying errors in the performance matrix through linear extrapolation, as well as possible non-linearities in PV performance at lower irradiances and/or module temperatures – also discussed by Whitaker and Newmiller (1998). Thus, linear extrapolation of the available performance matrix to lower PV module temperature ranges, especially for lower irradiance ranges, introduces significantly visible irregularities in prediction of PV module power.

Taking a look at the figure below, it can be seen that these errors in power prediction mostly occur for AOI between 30° and 50° – also observed in Figure 43. At the same time, increasing AOI causes lower errors and less negative residuals in temperature prediction – i.e. a tendentially lower influence of the irradiance on the module temperature – also visible in a decrease of difference between measured module temperature and ambient temperature.

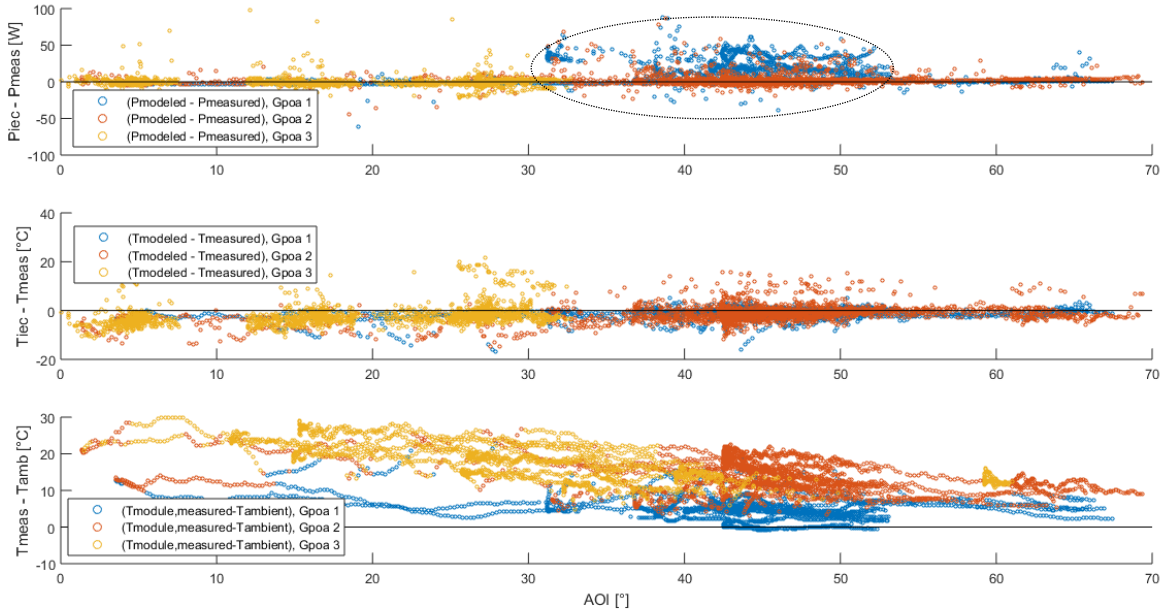

Figure 54 Influence of AOI on temperature and power prediction (own figure)

Summarizing the main findings of this section, the evaluated IEC 61853-3 committee draft modeling algorithms present increased modeling errors at low irradiance ranges between 100 and 300 W/m² and low ambient temperature ranges below 10 °C – leading to PV module temperatures below 15 °C that lie outside the ranges of the available performance matrix provided by IEC 61853-1. These prediction errors are shown as strong overpredictions – mostly independent of wind speed and occurring mainly at high AOI between 30 and 50° – and are possibly caused by errors introduced/magnified through linear extrapolation of the performance matrix to lower PV module temperature ranges, as well as non-linearities of PV module performance at lower irradiances and module temperatures – not taken into account by the linear inter-/extrapolation method.

Furthermore, errors at these ranges of low irradiance, low ambient temperature and high AOI can partly be related to increased angular losses, caused for example through soiling/dust deposition not sufficiently considered through the angular loss coefficient a_r in the model of Martin and Ruiz (2000) – also illustrated in Figure 7.

Also, not accurately considering the PV module's thermal mass, natural convection and radiation cooling by the temperature model leads to visible deviation of residuals for the temperature and power prediction.

The following table gives an overview of the modeling error RMSE for each of the observed bin ranges. It is important to mention that not all of the listed bin ranges in the table meet the required minimum sample size and/or show normally distributed residuals. A table with bin ranges that meet these requirements can be found in the Appendix I.

RMSE [°C]	RMSE [W]	Irradiance [W/m²]	Ambient Temp. [°C]	Wind speed [m/s]	AOI [°]
1,877	23,164	Irr. 1	tamb 1	Wind speed 1	AOI 1
4,317	6,963	Irr. 2			
9,030	8,870	Irr. 3			
3,457	4,145	Irr. 1		Wind speed 2	
5,440	6,667	Irr. 2			
5,196	7,077	Irr. 3			
2,754	33,208	Irr. 1		Wind speed 3	
3,123	3,992	Irr. 2			
2,266	2,486	Irr. 3			
2,794	9,525	Irr. 1	tamb 2	Wind speed 1	
4,437	11,491	Irr. 2			
4,044	7,848	Irr. 3			
2,064	33,134	Irr. 1		Wind speed 2	
3,864	22,248	Irr. 2			
2,746	4,907	Irr. 3			
3,583	16,938	Irr. 1		Wind speed 3	
3,029	12,221	Irr. 2			
3,385	11,897	Irr. 3			
1,415	19,189	Irr. 1	tamb 1	Wind speed 1	AOI 2
4,096	6,722	Irr. 2			
7,965	6,519	Irr. 3			
2,180	3,828	Irr. 1		Wind speed 2	
2,096	7,052	Irr. 2			
		Irr. 3			
2,210	27,969	Irr. 1		Wind speed 3	
2,120	7,804	Irr. 2			
2,494	1,656	Irr. 3			
1,951	6,798	Irr. 1	tamb 2	Wind speed 1	
1,490	7,012	Irr. 2			
		Irr. 1		Wind speed 2	
2,381	25,484	Irr. 2			
1,668	10,763	Irr. 3			
3,935	3,083	Irr. 1		Wind speed 3	
2,651	14,230	Irr. 2			
2,165	7,513	Irr. 3			
		Irr. 1	tamb 1	Wind speed 1	AOI 3
		Irr. 2			
5,629	4,503	Irr. 3			

7,883	6,374	Irr. 1		Wind speed 2	
1,644	8,308	Irr. 2			
1,044	2,776	Irr. 3			
		Irr. 1		Wind speed 3	
		Irr. 2			
2,062	4,295	Irr. 3			
		Irr. 1	tamb 2	Wind speed 1	
1,164	2,163	Irr. 2			
1,107	3,774	Irr. 3			
		Irr. 1		Wind speed 2	
		Irr. 2			
2,983	4,812	Irr. 3			
3,040	2,660	Irr. 1		Wind speed 3	
0,977	4,331	Irr. 2			
0,439	3,546	Irr. 3			

Table 22 RMSE for power and temperature prediction for all possible combinations of bin ranges, (own table, color code: high = red to low = green, empty cells represent ranges with no data points)

8 Spatial PV array performance analysis

The analysis above compares modeled and measured values of power and temperature via the analysis of residuals. Temperature measurements refer to the PV module temperature measured at the backside of a PV module located in the middle of the PV ground array – as described in section 1.4. Power measurements refer to the mean of all the 96 traced PV modules inside the observed PV array – as also described in section 1.4.
This chapter focuses on the comparison of modeled and measured PV module output power pointing out differences between the 96 individually traced PV modules mounted within each string of the observed PV ground array at NIST. As module temperature is not monitored for each of the observed, traced PV modules, a direct comparison of measured and modeled PV module temperature for each PV module is not taken into account within the scope of this work. However, tendencies for local irradiance and temperature differences between the observed PV modules inside the array are represented through the IV curve parameters Isc and Voc – as explained in section 3 of this work.
The analysis of local position differences between traced modules inside the array is done through the graphical illustration of residuals of power (difference between modeled and measured values) as well as differences in the measured Voc and Isc for the following data sets – as also in the evaluation above:

1. Entire data set population of all observed days
2. Independent bin range variation
3. Cross-dependence and interaction of bin ranges

The visualization of results in this part of the analysis is done through boxplots in which the traced module parameters are grouped according to their position inside the PV array – according to section 3.4. To graphically support the boxplots and to represent a better spatial illustration of position effects of traced modules within the PV array, boxplots are shown in combination with heat maps of the 96 traced PV modules. Results of independent and cross-dependent bin range variation are summed up within this chapter and can be found in the tables of Appendix J.

8.1 Analysis of entire data set population

In the following, the analysis of position differences between traced PV modules inside the observed PV ground array represents the entire observed data set population.

Differences between modeled and measured PV module output power

The figure below shows differences between IEC 61853-3 CD modeled and on-site measured PV module output power for each position group (boxplot) and the median of the power difference between modeled and measured values for each individually traced PV module (heat map) inside the PV array – for the entire data set population.

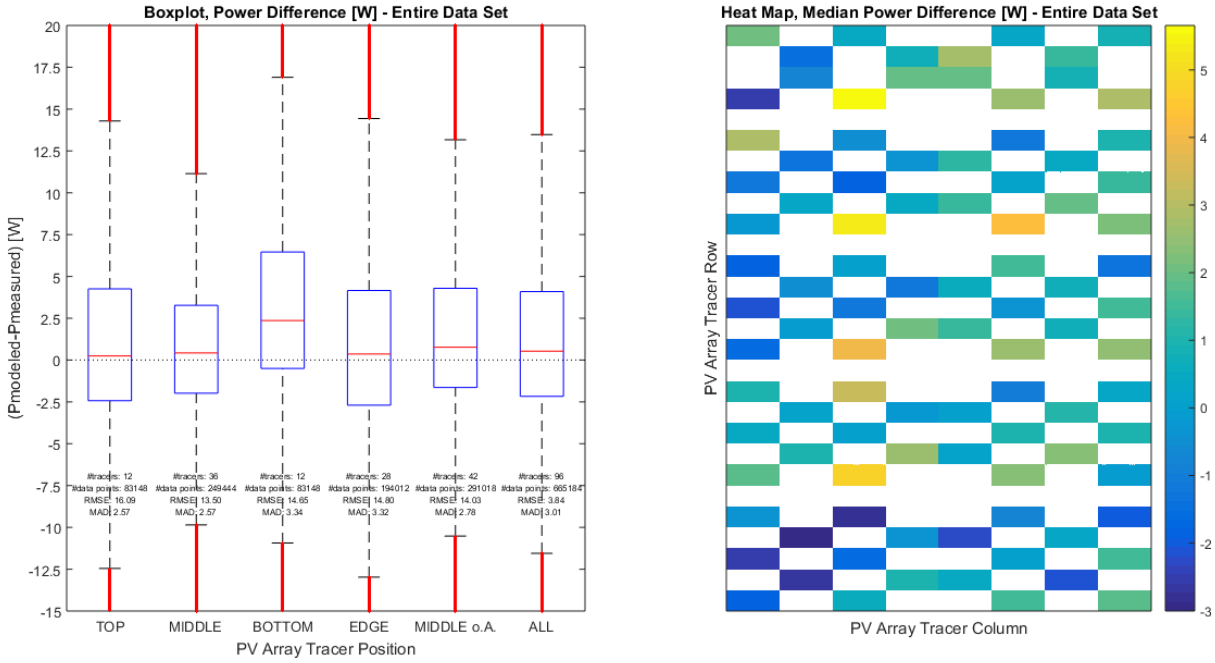

Figure 55 Boxplot and heat map, power difference, entire data set population (own figure)[11]

The boxplot of Figure 55 shows that the median of the differences between modeled and measured PV module output power for PV modules in bottom rows of the array is significantly higher compared to other position groups. This means that for the observed data set population, PV modules located in the bottom rows show a clear tendency of being overestimated by the applied modeling algorithms. Furthermore, the heat map in the figure above shows a tendency of lower median power differences towards the south/southwest side of the PV array (bottom left and left part of heat map) – showing an approximate difference in median power difference of about 2 to 4 W to modules on the north/northwest side. The observed effects can be related and explained by further analyzing IV curve parameters, such as Voc and Isc.

[11] The observed heat maps show all PV array rows, but do not show all 48 PV array columns, only those with tracers. Sheds and locations with no tracers are separated through white spaces (NaN).

Measured open circuit voltage (Voc)

The figure below shows the boxplot of the measured Voc depending on the position of the traced PV modules inside the ground array of the entire data set population. The heat map illustrates the median of measured Voc values of the entire data set population for each traced PV module inside the array.

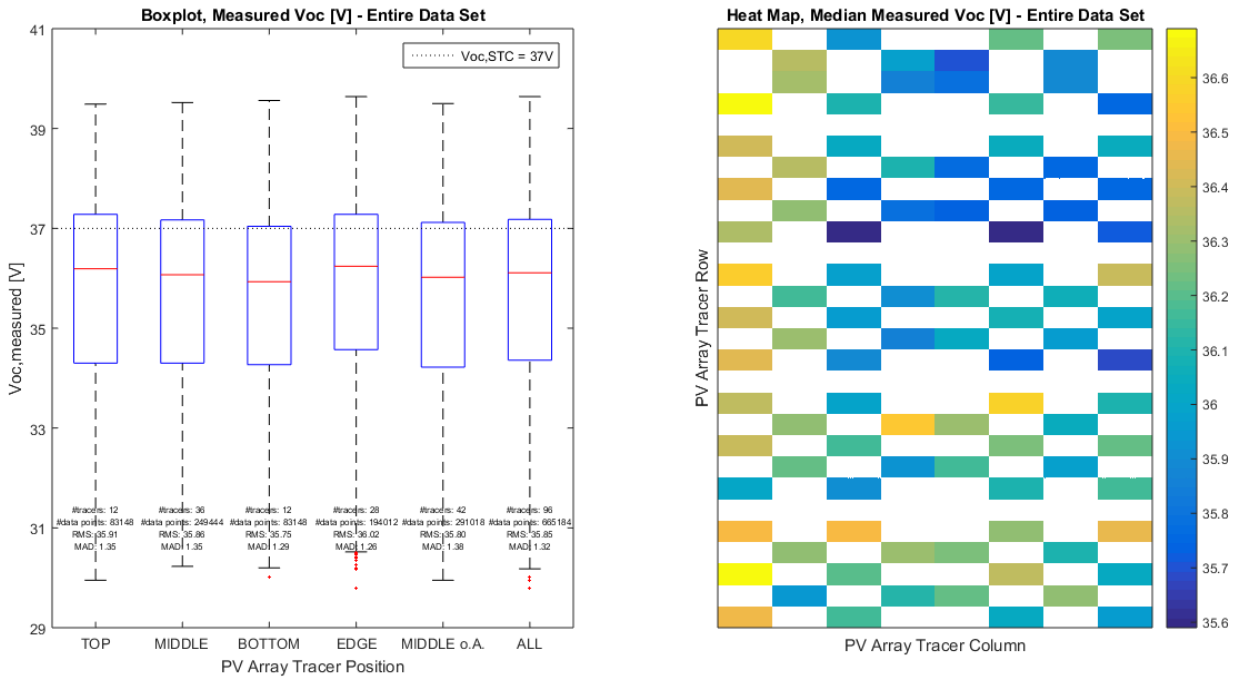

Figure 45 Boxplot and heat map, measured Voc, entire data set population (own figure)

The boxplot of the figure above shows clear variation of measured Voc between the positions of traced PV modules inside the PV array for the entire data set population. It can be seen that the median of the measured Voc values of PV modules in top rows of the array is slightly higher compared to PV modules mounted in middle or bottom rows. Also, modules mounted at the edge of the array show higher median measured Voc compared to modules located in the middle of the array. This can be related to less convective cooling for PV modules in bottom rows and for modules located in the middle of the array, as modules in these positions might not be as exposed to wind as in modules in top rows and at the edge of the array. The decrease of heat loss through convection can cause locally increased temperatures, and thus decreased values in Voc. Furthermore, the heat map of the figure above shows slightly higher medians in measured Voc for PV modules mounted at the south/southwest side (bottom left and left part of heat map) of the PV array, compared to modules mounted at the north/northeast side (upper right part of heat map) – showing an approximate difference of median measured Voc of about 0.2 to 1 V between these positions. This finding correlates with differences in power prediction, shown before.

Measured short circuit current (Isc)

The figure below shows the boxplot of the measured Isc depending on the position of the traced PV modules inside the ground array of the entire data set population. The heat map illustrates the median of measured Isc values of the entire data set population for each traced PV module inside the array.

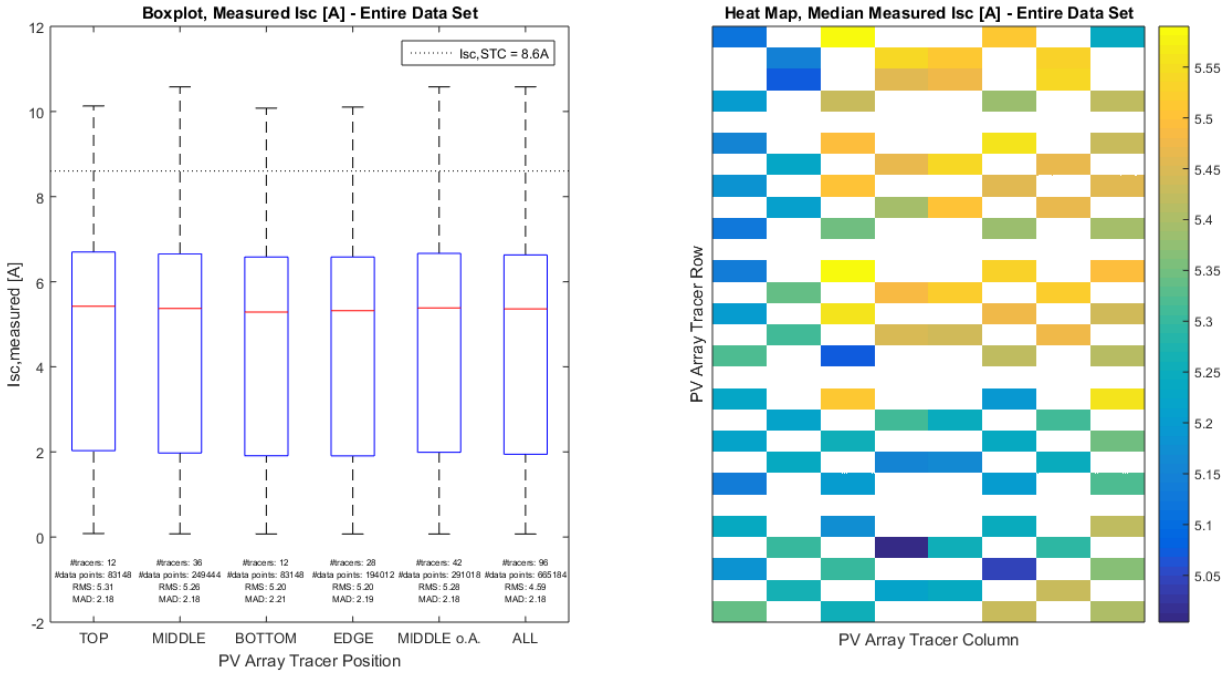

Figure 46 Boxplot and heat map, measured Isc, entire data set population (own figure)

The figure above shows clear differences in Isc across the whole PV array for the entire observed data set population. Furthermore, it can be seen that the median of measured Isc values for PV modules at top rows of the array shows slightly higher values for the entire data set population, when compared to middle and bottom positions of the array. The heat map of the median of measured Isc values for all the traced PV modules shows a clear tendency to lower values in Isc for PV modules mounted at the south/southwest side (bottom left and left part of heat map) of the PV array – confirming the tendency related to the median of modeled versus measured power difference and median measured Voc, mentioned above – showing an approximate difference in median measured Isc of about 0.2 to 0.5 A. The affected PV modules seem to show slightly increased Isc possibly due to a positive temperature coefficient, correlating to decreased Voc in the same area of the array due to a negative temperature coefficient. Another possible reason for this difference in median values of Isc across the spatial distribution of PV modules can for example be related to stronger dust deposition or soiling and thus increased reflection losses on the south and southwest side of the array or higher reflection of surroundings on the north and northeast side of the array. Due to the pattern of Isc differences across the array, as well as the relatively young age of the PV array, degradation effects are assumed to be unlikely.

8.2 Analysis of independent and cross-dependent variation of bin ranges

In the following, the effects of the independent and cross-dependent variation of the observed bin ranges are analyzed according to their impact on performance differences between the observed positions within the PV array. An overview of the results is provided through tables in Appendix J, containing the median power difference between modeled and measured power as well as tables showing the median measured Voc and Isc for each position group and observed bin range.

Differences between modeled and measured PV module output power

The spatial PV array analysis of the power prediction error related to the position of the traced modules within the array in general confirms the findings above. Results show that while PV modules in the top rows of the array show a tendency to be more often underpredicted by the IEC modeling algorithms, modules mounted in bottom rows show the tendency to be more often overpredicted. The following table shows the counts of ranges with the median power prediction error below and above zero for all observed weather ranges and positions of the array.

Variation type	Ranges with median power prediction error	Top	Middle	Bottom	Edge	Middle o. A.	All
Independent variation (11 ranges)	<0 (underprediction)	4	3	0	4	2	3
	>0 (overprediction)	7	8	11	7	9	8
Cross-dependent variation (54 ranges)	<0 (underprediction)	14	12	5	12	11	11
	>0 (overprediction)	31	33	40	33	34	34

Table 23 Counts of median power prediction error for all weather ranges and PV array positions[12] (own table)

[12] Numbers of underprediction and overprediction add up to 11 for the independent variation and to 45 for the cross-dependent variation of observed weather ranges. This is, because not all the observed 54 ranges show sufficient measurement points for a complete analysis of the entire array.

Tables in Appendix J show that overprediction occurs most significantly at low irradiances and low ambient temperatures (as observed above), leading to median power prediction errors up to about 30 W. While underprediction is most significant at high irradiances, high ranges of AOI, low wind speeds and low ambient temperatures, leading to median power prediction errors ranging down to about -7 W. This can be confirmed with the following observations:

The figure below illustrates power prediction differences for each observed position and tracer across the PV array at high wind speeds, low ambient temperatures and high irradiances, showing clearly visible differences between east and west side of the PV array – with lower prediction errors on the west side. Furthermore, it can be seen that tracers mounted in bottom positions of the PV array show a strong tendency of power overprediction.

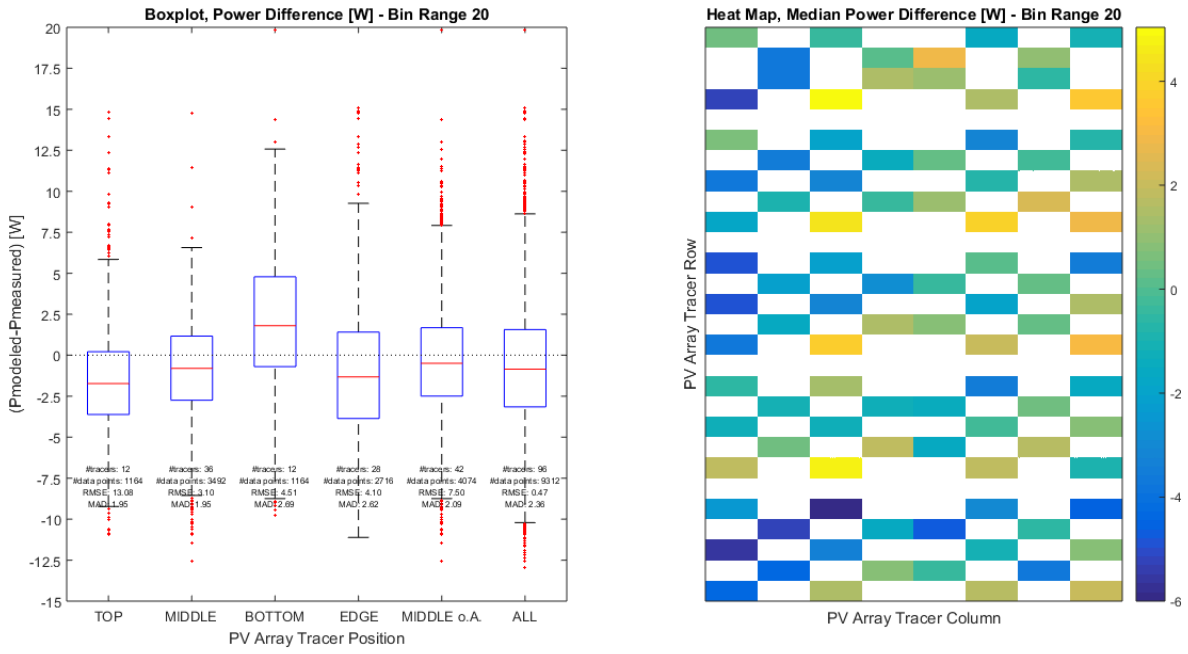

Figure 56 Differences in measured Voc across the array at high wind speeds, low ambient temperatures and high irradiances (own figure)

Inconsistencies in power prediction error across the PV array become slightly more pronounced at increased ambient temperatures – as illustrated in the figure below.

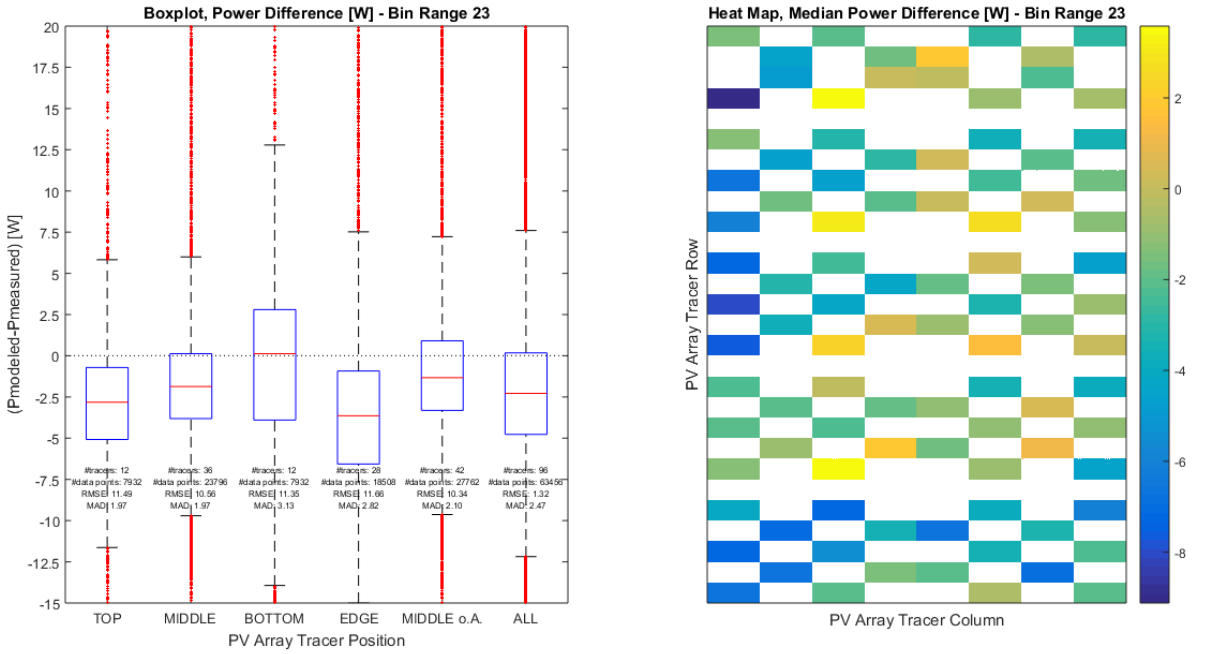

Figure 57 Differences in measured Voc across the array at high wind speeds, high ambient temperatures and high irradiances (own figure)

These differences across the PV array almost disappear at low wind speeds, low ambient temperatures and low irradiances, also showing significant tendency of overprediction for all the observed module positions and tracers, as observed above – shown in the figure below.

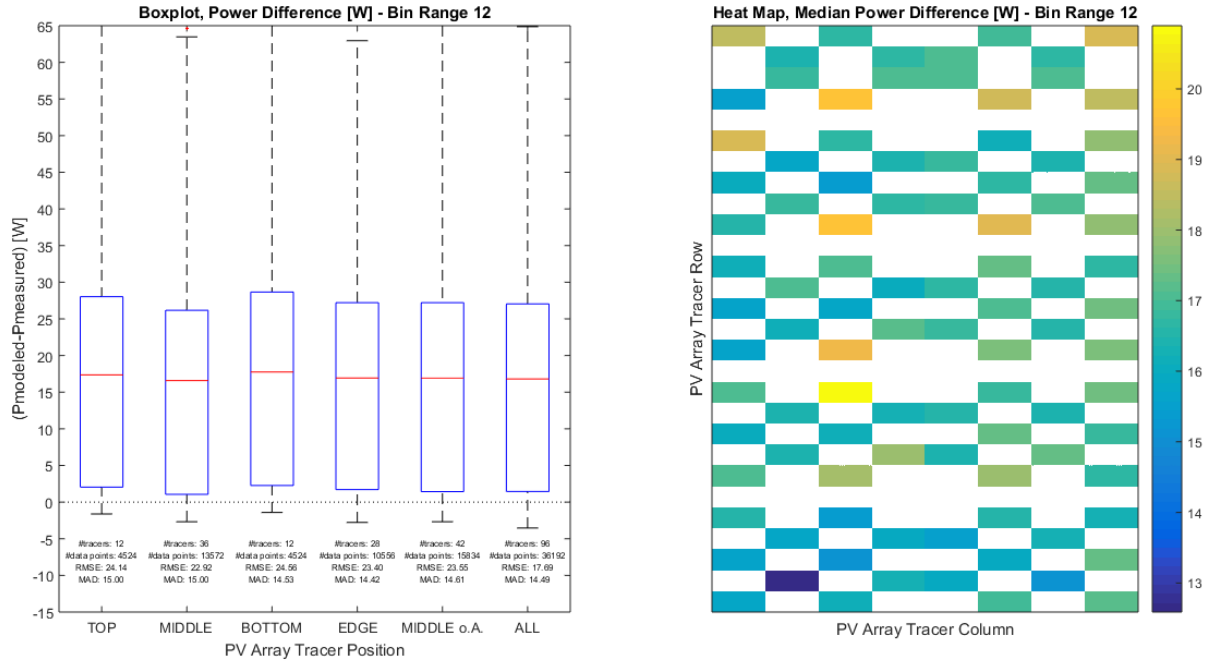

Figure 58 Differences in measured Voc across the array at high wind speeds, high ambient temperatures and high irradiances (own figure)

Thus, the observed weather conditions show significant variability in power prediction error across the PV array for high irradiances and/or ambient temperatures, being also dependent on wind speed. Inconsistencies across the PV array are lowest at low ranges of irradiance and/or ambient temperature. These findings can be confirmed through the analysis of the IV-curve parameters Voc and Isc:

Analysis of measured open circuit voltage (Voc)

The spatial analysis of measured Voc for all observed bin ranges shows that modules mounted in the bottom rows of the array have the tendency to lower measured median Voc, compared to the other positions – confirming the findings above. Differences between median measured Voc are for example visible at high irradiances, high wind speeds and low ambient temperatures – shown in the figure below.

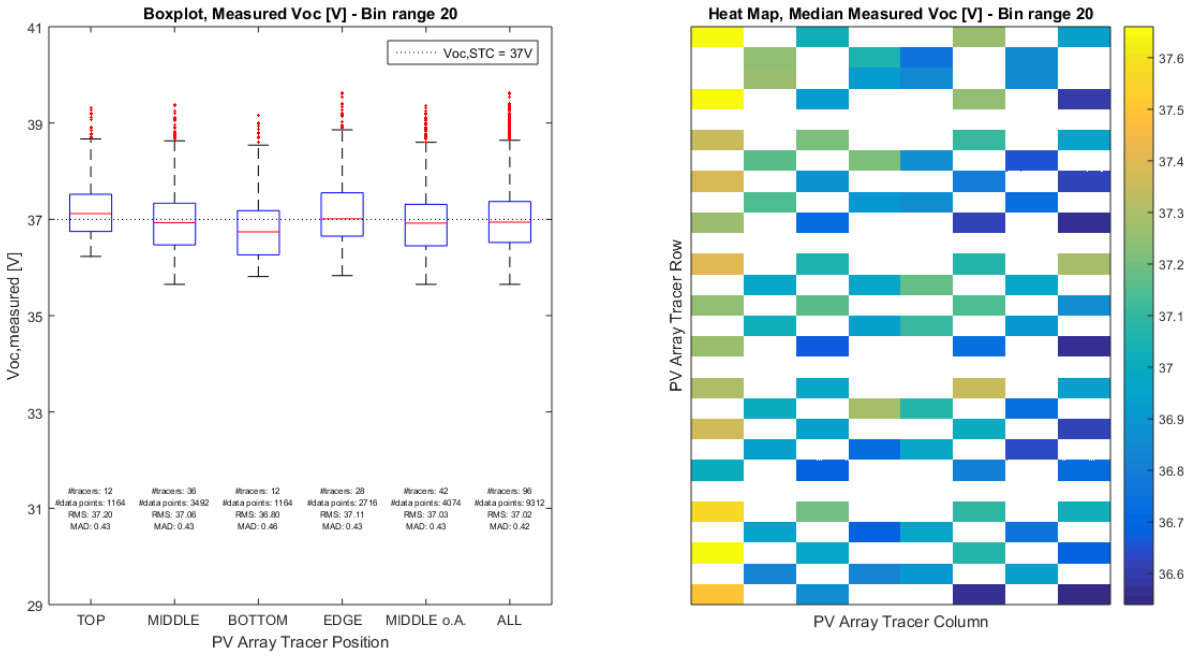

Figure 59 Differences in measured Voc across the array at high wind speeds, low ambient temperatures and high irradiances (own figure)

At these weather conditions, a spatial difference in median measured Voc between east and west side of the PV array becomes clearly visible. These inconsistencies across the array become more with increasing ambient temperatures at high wind speeds and high irradiances, leading to the observed tendency of higher Voc at the south/southwest side of the array – shown in the figure below.

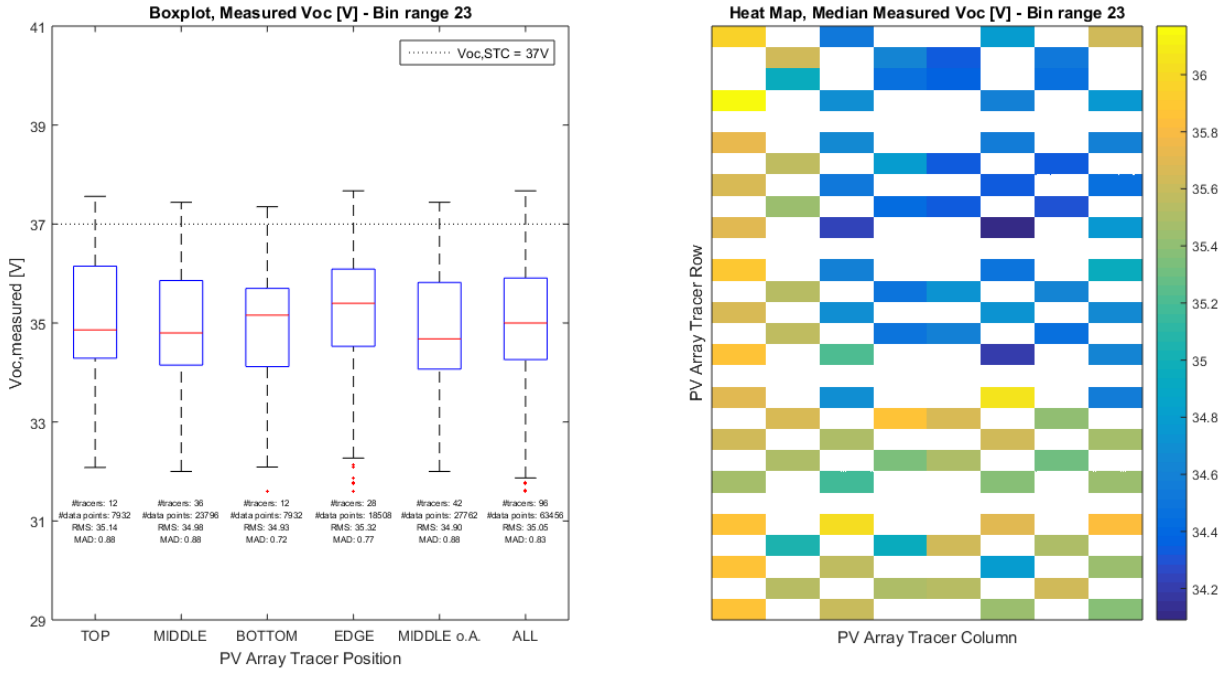

Figure 60 Differences in measured Voc across the array at high wind speeds, high ambient temperatures and high irradiances (own figure)

The observed differences between measured Voc almost disappear entirely at low wind speeds, low ambient temperatures and low irradiances – as shown in the figure below.

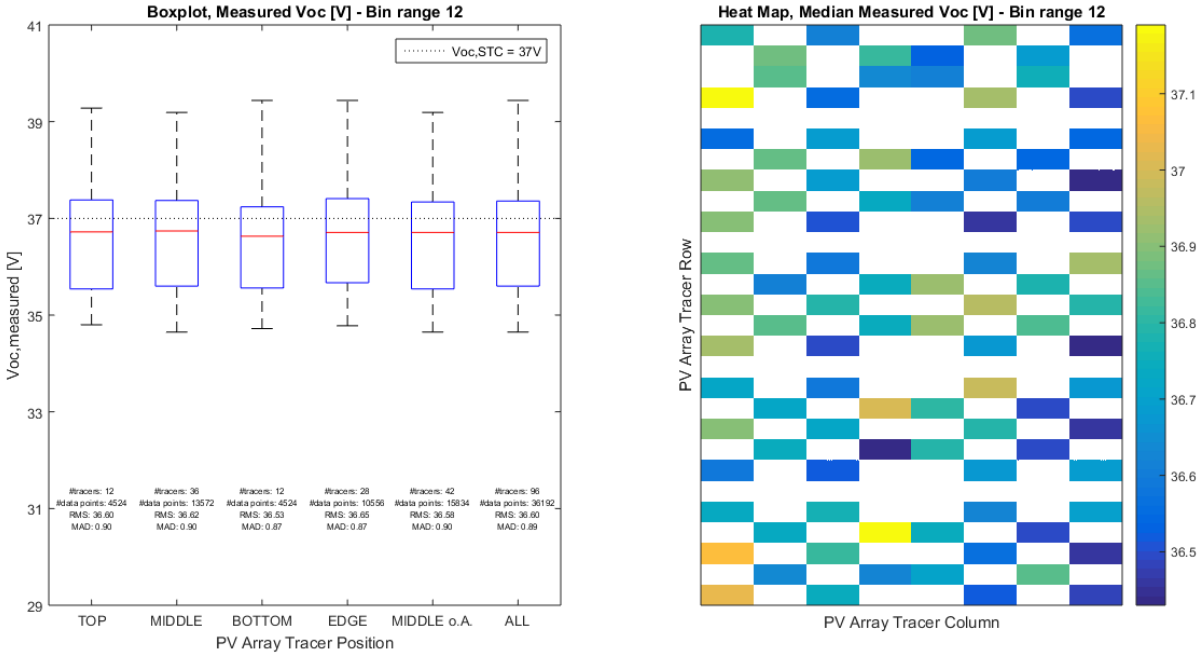

Figure 61 Differences in measured Voc across the array at low wind speeds, low ambient temperatures and low irradiances (own figure)

Thus, the spatial analysis of Voc measurements for the observed PV array shows a strong dependence on ambient temperature and/or irradiance and wind speed. Higher ranges of ambient temperature and/or irradiance and wind speed cause significantly visible inconsistencies in median measured Voc across the array, indicating local temperature differences – with the tendency to higher temperatures at the north/northeast part of the array and lower temperatures at the south/southeast part. The observed differences also seem to be strongly dependent on wind speed (and possibly also wind direction – not considered).
A table showing the median measured Voc for all positions at all observed weather ranges can be found in Appendix J.

Analysis of measured short circuit current (Isc)

The spatial analysis of measured Isc for all observed bin ranges confirms the findings above and illustrates that PV modules mounted at the south and southwest side of the array show significantly lower median in measured Isc, compared to other positions of the array. As seen above, this effect especially is pronounced for higher irradiances and/or temperature ranges and wind speeds, leading to slightly higher median measured Isc in the north/northeast part of the array.

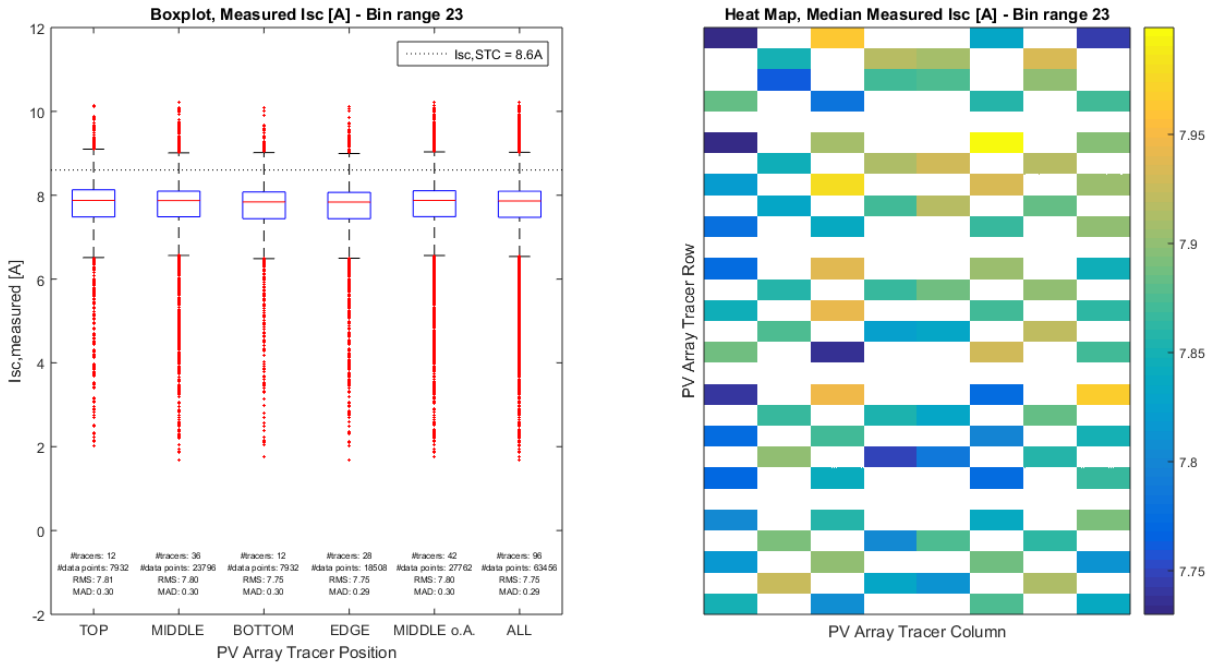

Figure 62 Differences in measured Isc across the array at high wind speeds, high ambient temperatures and high irradiances (own figure)

As shown before, these observed inconsistencies disappear almost completely at lower wind speeds, lower ambient temperatures and lower irradiances, as can be seen in the figure below.

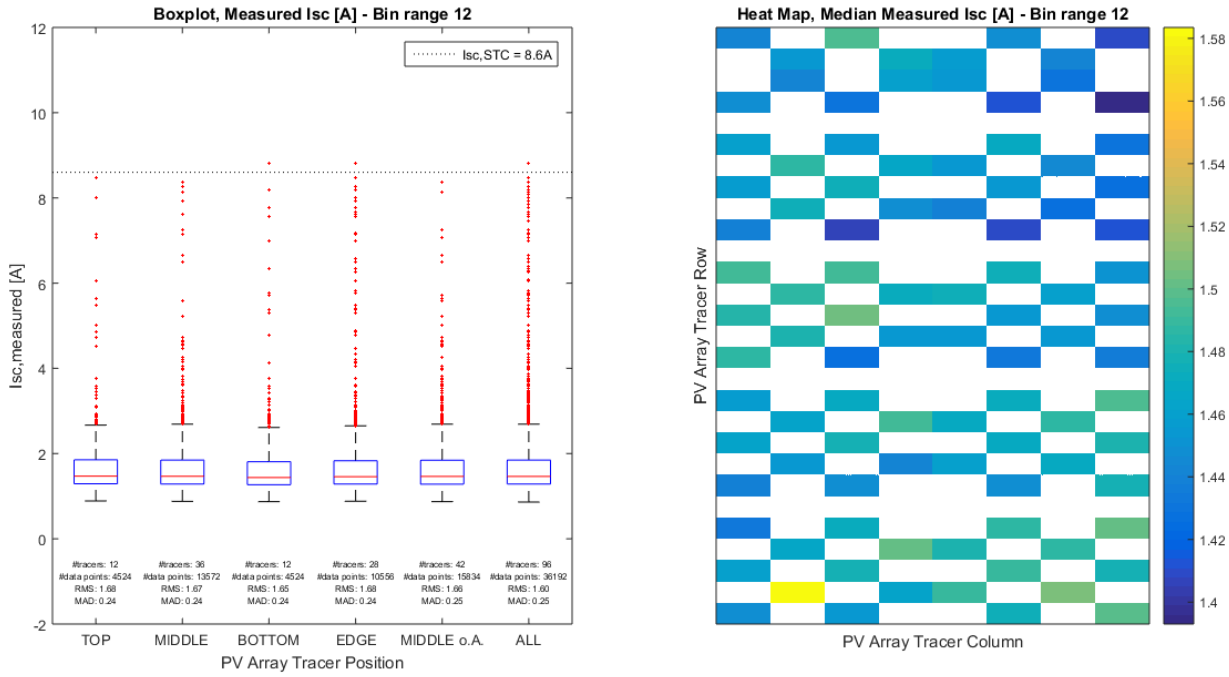

Figure 63 Differences in measured Isc across the array at low wind speeds, low ambient temperatures and low irradiances (own figure)

Thus, the spatial analysis of Isc measurements for the observed PV array confirms the findings above, showing a strong dependence on ambient temperature and/or irradiance and wind speed. Higher ranges of ambient temperature and/or irradiance and wind speed cause significantly visible inconsistencies in median measured Isc across the array, indicating local temperature differences across the array – with the tendency to higher temperatures at the north/northeast part of the array and lower temperatures at the south/southeast part. The observed differences also seem to be strongly dependent on wind speed (and possibly wind direction – not considered).

A table showing the median measured Voc for all positions at all observed weather ranges can be found in Appendix J.

8.3 Summary and discussion of results – Spatial PV array performance analysis

The analysis of local differences between the modules mounted in the observed PV array agrees with findings of the evaluation of modeled and measured power for various ranges of weather conditions, and further allowed the illustration of spatial performance differences across the array.

The comparison of power residuals for the observed 6 PV module position groups shows a tendentially higher overprediction of PV modules located in bottom rows of the array – which corresponds to differences in IV-curve parameters Voc and Isc. Furthermore, a clear tendency of lower median power prediction error to the south and southwest of the PV array can be seen – differing from the rest of the array with about 2 to 4 W for the entire data set population, with the same tendencies also visible in Voc and Isc measurements.

The comparison of measured Voc for the observed 6 PV module positions groups shows lower median measured value in Voc for PV modules located in bottom rows and in the middle of the array – which can be related to increased local temperatures at these positions. Furthermore, a clear difference between median measured Voc of modules located on the south and southwest side of the array can be observed – showing differences of about 0.2 to 1 V higher median measured Voc compared to PV modules located at the north/northeast part of the array – for the entire data set population.

Differences can also be seen for measured Isc. PV modules located in the bottom rows show slightly lower values in Isc, when compared to other positions. Furthermore, a tendency of lower median measured Isc towards the south and southwest part of the PV array can be observed with differences up to 0.5 A – compared to PV modules located at the north/northeast part of the array, for the entire data set population.

The observed differences in Voc and Isc (and consequently power) might be related to local temperature inconsistencies across the array caused through the influence of ambient temperature and/or irradiance combined with changes in wind speed. It is assumed that modules located at the south/southwest side of the PV array are more exposed to wind, and thus convective cooling, than modules located at the north/northeast side. The observations correlate with each other, as increased temperature influences Isc positively (positive temperature coefficient) and Voc as well as power negatively (negative temperature coefficient). However, a verification of these findings would require more granular module temperature and the consideration of wind speed and wind direction measurements across the array, which is not part of the scope of this research. Furthermore, the effect of exposure to different surroundings across the PV array can also contribute to the observed inconsistencies, leading for example to different degree of soiling/dust deposition on the surface of PV modules.

Although the described tendencies of Voc and Isc differences between the observed positions of PV modules inside the array are clearly visible, they do not influence the power prediction variability as strongly as expected. However, in order to enable a more accurate spatial prediction of PV module output power for entire PV arrays through the observed modeling algorithms, this research allows to conclude that the following two considerations are of high importance:

1- Mounting location of modules within the array:
   For the observed array and data set, especially modules that are mounted in bottom rows and in the middle of the array are found to show significant differences in power prediction error. These difference might be related to temperature and/or irradiance differences across the array. Furthermore, the wind speed and possibly the wind direction, as well as the degree of exposition of the modules to wind appear to be influential – as described above. Thus, mounting location of PV modules within an array plays a crucial role for performance predictions. The verification of these assumptions would require a more granular monitoring of module temperature and wind speed and/or wind direction across the PV array.

2- Surroundings of array and ground conditions:
   It is assumed that the observed inconsistencies across the array are related to temperature and/or irradiance differences combined with the influence of wind speed and/or wind direction on the module temperature. However, also the exposure to different surroundings on each side of the PV array might be influential. For example, spatial differences in dust deposition and/or reflection of irradiance by surroundings can also lead to differences of the module performance across the array and therefore should be considered in potential performance predictions of PV arrays. Thus, surroundings of PV modules mounted inside PV arrays are also of high importance for performance predictions. The effects of the surrounding environment on PV arrays are also discussed by Maghami et al. (2016) and Fairbrother (2017).

9 Conclusion and outlook

The quantification of PV system operation reliability under outdoor conditions earns high attention, as it is strongly related to the operation costs throughout the life-time of PV systems. PV reliability, next to other market drivers, therefore also strongly influences the continuing growth of the installed PV capacity worldwide. Quantifying PV system reliability requires the understanding of occurring effects at real life outdoor operation conditions. An existing method to quantify and predict these effects present the modeling algorithms suggested by the international standard IEC 61853-3 – which is currently under development and available as committee draft. This standard aims to provide an energy rating method for PV modules at different climatic conditions around the world. Thus, it provides an approach for the quantification of performance parameters of PV systems mounted outdoors at different places over the world – also aiding the understanding of climate sensitivity of PV systems. International standardization processes in this context are also seen as key support of open markets, free trade and interoperability, and thus further supporting a continuing growth of PV globally – as also discussed in ANEC (2010).

The effort of this research is to evaluate sub-models, applied by the IEC 61853-3, via using granular intra-array PV module measurements as well as weather parameters measured at the campus of NIST in Gaithersburg, Maryland (USA). The research focus lies in the comparison of instantaneously measured PV module temperature and power with predictions of the IEC algorithms, based on weather data inputs. Measurements and predictions are compared for various weather conditions, comparing the (cross-) dependent variation of bins of irradiance, ambient temperature, wind speed and angle of incidence. Additionally, a spatial analysis of performance variability within the observed PV array aims to provide better understanding of inconsistencies occurring at different positions within the array. With this, it is aimed to aid potential efforts for the performance modeling of entire PV arrays. The observed data set population consists of 21 days of measurements, measured at different days with characteristic weather conditions. Monitoring data consists of 1-minute averages of weather data parameters, as well as 1-minute averages of traced PV operational data measured at 96 field deployed PV modules – each of them mounted within one series string of the observed PV array. Additionally, IV curve traces of all of the 96 traced modules are taken in 5-minute intervals, allowing also the analysis of IV curve parameters.

Results show that the IEC 61853-3 modeling algorithms allow the prediction of temperature in the range between 1 and 9 °C RMSE, and power prediction in the range between 2 and 33 W RMSE – for the observed data set population. Best results are shown for days with little fluctuation in monitoring data, e.g. caused at cloudy days. This could indicate the need for longer averaging periods of monitoring data and/or the better consideration of the PV module’s thermal mass in the temperature model. Evaluations of the variation of the observed bin ranges (data samples) of weather conditions show a strong dependence of the

modeling errors on irradiance, wind speed and ambient temperature. For the observed data set population, biggest errors up to about 33 W RMSE occur at low irradiances between 100 and 300 W/m² and low ambient temperatures below 10 °C, mostly independent from wind speed and occurring at AOI between 30 and 50°. These prediction errors are shown as significant overpredictions, most certainly related to error magnification caused by linear extrapolation of the available performance matrix to PV module temperature ranges below 15 °C, as well as possible non-linearities of PV module performance at lower irradiances and module temperatures – not taken into account by the linear inter-/extrapolation method. A similar effect is also discussed by Whitaker and Newmiller (1998). Also, as the observed increased prediction errors are found at higher ranges of AOI between 30 and 50°, possible errors in consideration of reflection losses through increased angular losses (caused for example through dust deposition) could add to the observed prediction error. Furthermore, neglecting natural convection and radiation cooling effects by the temperature model – also discussed by Koehl et al. (2011) – lead to visible deviation of residuals for temperature and power prediction, showing errors between 5 and 10 °C RMSE for module temperature prediction, and errors between 7 and 10 W RMSE for power prediction. Errors caused by natural convection decrease with increasing wind speeds between 3 and 9 m/s to about 2 °C RMSE for temperature and 2 to 4 W RMSE for power prediction. Furthermore, prediction errors decrease with higher ambient temperatures between 13 and 35 °C and high ranges of AOI between 45 and 75° - leading to prediction errors between 0.5 and 3 °C RMSE for the module temperature and between 3 and 5 W RMSE for the module power.
Based on these observations, possible improvements for evaluated IEC 61853-3 CD modeling algorithms could be a better consideration of thermal mass and effects such as natural convection and radiation in the thermal model, as well as improvements related to the linear inter-/extrapolation method in combination with the performance matrix of IEC 61853-1. One approach for the improvement of the inter-/extrapolation method could be the expansion of required measurement points for the performance matrix, enabling to cover all ranges of observed irradiances and module temperatures at certain climates – thus, decreasing the probability of errors introduced via linear inter-/extrapolation.

The spatial analysis of performance parameters and power prediction errors at different locations of the PV array shows a strong dependence of inconsistencies across the array on irradiance and/or ambient temperature, as well as changes in wind speed. Especially PV modules located in the bottom rows of the array and in the middle of the array show a significant tendency of overprediction by the IEC modeling algorithms. Also, the south/southwest part of the PV array shows a strong tendency of performance prediction differences, compared to other positions of the array – with differences ranging between 2 and 4 W median error difference for the power prediction. The analysis of the IV curve parameters, Voc and Isc, reveals that observed differences are possibly also related to local temperature differences across the PV array – reflected by median differences in Voc

ranging between 0.2 and 1 V and median differences in Isc ranging up to 0.5 A for the affected positions compared to not affected regions of the PV array.
However, results of the spatial array analysis are seen as first indicators of inconsistencies occurring across the PV array. A verification of the assumptions would require the analysis of more granular measurement of PV module temperature and wind speed (and possibly wind direction) across the array. Also, the effect of different surroundings across the array, that could as well influence the PV module performance significantly, needs to be taken into consideration, e.g. via more granular irradiance and/or ground reflection measurements and a more accurate consideration of soiling and dust deposition for each PV module inside the array – also discussed by Maghami et al. (2016) and Fairbrother (2017).

All in all it can be concluded that the IEC 61853-3 committee draft calculation procedures allowed remarkable prediction of temperature and power of the observed field deployed PV modules mounted inside the ground array at the campus of NIST, by using 1-minute averages of instantaneous monitoring weather and PV operational data. Findings related to the behavior of the modeling algorithms at various ranges of weather conditions can indicate possible strengths and weaknesses of the IEC's prediction algorithms for different climatic conditions. This is of high interest, as the standard ultimately aims to provide an energy rating method for different climate zones around the world. However, the findings of this work primarily serve as a practical application example of the IEC 61853-3 sub-models and mainly refer to and are limited by the observed ranges of measured data at the PV array installation location at NIST in Gaithersburg, Maryland (USA).

References

ALONSO-ABELLA, M., CHENLO, F., NOFUENTES, G. & TORRES-RAMÃ-REZ, M. 2014. Analysis of spectral effects on the energy yield of different PV (photovoltaic) technologies: The case of four specific sites. *Energy,* 67**,** 435-443.

ANEC 2010. Standardization for a competitive and innovative Europe: a vision for 2020. *Report of the expert panel for the review of the european standardization system.* EXP 384 final ed.: European Association for the Co-ordination of Consumer Representation in Standardisation

ASHRAE 1977. ASHRAE IAM Model Standard 93-77. New York: American Society of Heating, Refrigerating and Air-Conditioning Engineers.

BOYD, M. T. 2013. Analytical model for solar irradiance near a planar vertical diffuse reflector – Formulation, validation, and simulations. Gaithersburg, MD, USA: NIST.

BOYD, M. T. 2015. High-Speed Monitoring of Multiple Grid-Connected Photovoltaic Array Configurations. *NIST Technical Note 1896.* NIST - Energy and Environment Division - Engineering Laboratory.

BOYD, M. T. 2016a. Broadband Outdoor Radiometer Calibration Shortwave. Gaithersburg, MD, USA: NIST.

BOYD, M. T. 2016b. NIST Weather Station for Photovoltaic and Building System Research. *NIST Technical Note 1913.* NIST - Energy and Environment Division - Engineering Laboratory

CFV 2016. IEC 61853 Test Report. Albuquerque: CFV Solar Test Laboratory.

CTR. 2017. *Infinity Project - Climate Sensitive Photovoltaics* [Online]. Available: http://www.ctr.at/en/collaboration/ffg-programmes/infinity.html [Accessed 06/22/2017.

DALIENTO, S., CHOUDER, A., GUERRIERO, P., PAVAN, A. M., MELLIT, A., MOEINI, R. & TRICOLI, P. 2017. Monitoring, Diagnosis, and Power Forecasting for Photovoltaic Fields: A Review. *International Journal of Photoenergy,* 2017.

DE SOTO, W., KLEIN, S. A. & BECKMAN, W. A. 2006. Improvement and validation of a model for photovoltaic array performance. *Solar Energy,* 80**,** 78-88.

DIRNBERGER, D., BLACKBURN, G., MÃ¼LLER, B. R. & REISE, C. 2015. On the impact of solar spectral irradiance on the yield of different PV technologies. *Solar Energy Materials and Solar Cells,* 132**,** 431-442.

FAIMAN, D. 2008. Assessing the Outdoor Operating Temperature of Photovoltaic Modules. *Progress in Photovoltaics: Research and Applications*.

FAIRBROTHER, A. 2017. Photovoltaic backsheet degradation and gradient exposure conditions due to array design. Gaithersburg, MD: National Institute of Standards and Technology - NIST.

GUEYMARD, C. 1995. *SMARTS2: a simple model of the atmospheric radiative transfer of sunshine: algorithms and performance assessment*, Florida Solar Energy Center Cocoa, FL.

HULD, T. & AMILLO, A. 2015. Estimating PV Module Performance over Large Geographical Regions: The Role of Irradiance, Air Temperature, Wind Speed and Solar Spectrum. *Energies,* 8**,** 5159-5181.

HULD, T., AMILLO, A., VOURLIOTI, P., MÜLLER, R. & NORTON, M. 2015. Application of Satellite-Based Spectrally-Resolved Solar Radiation Data to PV Performance Studies. *Energies***,** 34.

HULD, T., FRIESEN, G., SKOCZEK, A., KENNY, R. P., SAMPLE, T., FIELD, M. & DUNLOP, E. D. 2011. A power-rating model for crystalline silicon PV modules. *Solar Energy Materials and Solar Cells,* 95**,** 3359-3369.

IEA 2014a. Analytical Monitoring of Grid-connected Photovoltaic Systems - Good Practices for Monitoring and Performance Analysis. Report IEA-PVPS T13-03:2014 ed. Brussels, Belgium: IEA PVPS Task 13, Subtask 2.

IEA 2014b. Review of Failures of Photovoltaic Modules. Report IEA-PVPS T13-01:2014 ed. Brussels, Belgium: IEA PVPS Task 13, Subtask 3.2.

IEA 2015. Technology Roadmap - Nuclear Energy. 2015 edition ed. Brussels, Belgium: International Energy Agency, Nuclear Energy Agency.

IEA 2016. Trends 2016 in Photovoltaic Applications. *Report IEA PVPS T1-30:2016.* 21st Edition 2016 ed. Brussels, Belgium: International Energy Agency - Photovoltaic Power Systems Programme.

IEA 2017a. 2016 - Snapshot of Global Photovoltaic Markets. *Report IEA PVPS T1-31:2017.* Brussels, Belgium: International Energy Agency - Photovoltaic Power Systems Programme.

IEA. 2017b. *IEA PVPS Task 13* [Online]. Available: http://www.iea-pvps.org/index.php?id=57 [Accessed 06/22/2017.

IEA 2017c. PV Performance Modeling Methods and Practices - Results from the 4th PV Performance Modeling Collaborative Workshop. Report IEA-PVPS T13-06:2017 ed. Brussels, Belgium: IEA PVPS Task 13, Subtask 2.

IEC 2009. IEC 60891:2009 - Photovoltaic devices - Procedures for temperature and irradiance corrections to measured I-V characteristics. *TC 82 - Solar photovoltaic energy systems.* IEC Central Office: Geneva.

IEC 2011. IEC 61853-1:2011 - Photovoltaic (PV) module performance testing and energy rating - Part 1: Irradiance and temperature performance measurements and power rating. *TC 82 - Solar photovoltaic energy systems.* IEC Central Office: Geneva.

IEC 2016a. IEC 61853-2:2016 - Photovoltaic (PV) module performance testing and energy rating - Part 2: Spectral responsivity, incidence angle and module operating temperature measurements. *TC 82 - Solar photovoltaic energy systems.* IEC Central Office: Geneva.

IEC 2016b. IEC 61853-3 ED1 - 82/1066/CD - Photovoltaic (PV) module performance testing and energy rating - Part 3: Energy Rating of PV Modules. IEC Central Office: Geneva.

IEC 2016c. IEC 61853-4 ED1 - 82/1067/CD - Photovoltaic (PV) module performance testing and energy rating - Part 4: Standard reference climatic profiles. IEC Central Office: Geneva.

JORDAN, D., C., KURTZ, S., R. 2012. Photovoltaic Degradation Rates - An Analytical Review NREL.

KEOGH, W. M. & BLAKERS, A. W. 2004. Accurate Measurement, Using Natural Sunlight, of Silicon Solar Cells. *Progress in Photovoltaics: Research and Applications*.

KING, D. L., KRATOCHVIL, J. A. & BOYSON, W. E. Measuring solar spectral and angle-of-incidence effects on photovoltaic modules and solar irradiance sensors. Photovoltaic Specialists Conference, 1997., Conference Record of the Twenty-Sixth IEEE, 1997. IEEE, 1113-1116.

KING, D. L., KRATOCHVIL, J. A. & BOYSON, W. E. 2004. *Photovoltaic array performance model*, United States. Department of Energy. Sandia National Laboratories.

KOEHL, M., HECK, M., WIESMEIER, S. & WIRTH, J. 2011. Modeling of the nominal operating cell temperature based on outdoor weathering. *Solar Energy Materials and Solar Cells,* 95**,** 1638-1646.

LAUKAMP, H., SCHOEN, T. & RUOSS, D. 2002. Reliability Study of Grid Connected PV Systems, Field Experience and Recommended Design Practice. *IEA Int. Agency, Paris, France, Tech. Rep. IEA-PVPS T7-08*.

LEE, M. & PANCHULA, A. 2016. Spectral Correction for Photovoltaic Module Performance Based on Air Mass and Precipitable Water. San Francisco, CA, 94105, USA: First Solar.

MAGHAMI, M. R., HIZAM, H., GOMES, C., RADZI, M. A., REZADAD, M. I. & HAJIGHORBANI, S. 2016. Power loss due to soiling on solar panel: A review. *Renewable and Sustainable Energy Reviews,* 59**,** 1307-1316.

MARTIN, N. & RUIZ, J. M. 2000. Calculation of the PV modules angular losses under field conditions by means of an analytical model. *Solar Energy Materials and Solar Cells***,** 14.

MATHWORKS. 2017a. *Documentation - Coefficient of Determination (R-Squared)* [Online]. Available: https://de.mathworks.com/help/stats/coefficient-of-determination-r-squared.html [Accessed 08/03/2017.

MATHWORKS. 2017b. *Documentation - Linear Regression* [Online]. Available: https://de.mathworks.com/help/stats/linear-regression-model-workflow.html#btcpwno [Accessed 05/23/2017.

MOLINA, M. G. 2016. Modelling and Control of Grid-connected Solar Photovoltaic Systems. INTECH.

NIST/SEMATECH 2012. NIST/SEMATECH e-Handbook of Statistical Methods.

NREL 2000. NREL's SOLPOS 2.0: Documentation. National Renewable Energy Laboratory Center for Renewable Energy Resources Renewable Resource Data Center

NREL 2011. System Voltage Potential-Induced Degradation Mechanisms in PV Modules and Methods for Test. NREL/CP-5200-50716 ed. 37th IEEE Photovoltaic Specialists Conference (PVSC 37) Seattle, Washington.

NREL 2012. Understanding Light-Induced Degradation of c-Si Solar Cells. NREL/CP-5200-54200 ed. 2012 IEEE Photovoltaic Specialists Conference Austin, Texas.

PVEDUCATION. 2017a. *Properties of Sunlight - Air Mass* [Online]. Available: http://www.pveducation.org/pvcdrom/2-properties-sunlight/air-mass#footnoteref3_733fmn1 [Accessed 05/22/2017.

PVEDUCATION. 2017b. *Solar Cell Operation - Effect of Temperature* [Online]. Available: http://www.pveducation.org/pvcdrom/effect-of-temperature [Accessed 05/22/2017.

PVEDUCATION. 2017c. *Solar Cell Operation - Spectral Response* [Online]. Available: http://www.pveducation.org/pvcdrom/spectral-response 05/22/2017].

PVPMC. 2017. *Photovoltaic Performance Modeling Collaborative* [Online]. National Technology and Engineering Solutions of Sandia, LLC. Available: https://pvpmc.sandia.gov/ [Accessed 05/20/2017 2017].

SKOPLAKI, E. & PALYVOS, J. 2009. Operating temperature of photovoltaic modules: A survey of pertinent correlations. *Renewable Energy,* 34**,** 23-29.

SPATARU, S., SERA, D., KEREKES, T. & TEODORESCU, R. 2015. Diagnostic method for photovoltaic systems based on light I–V measurements. *Solar Energy,* 119**,** 29-44.

STRATASENSE, L. 2013. Stratasense Wireless IV Curve Tracer - Brochure.

WHITAKER, C. & NEWMILLER, J. 1998. Photovoltaic module energy rating procedure. Final subcontract report. National Renewable Energy Lab., Golden, CO (United States); Endecon Engineering (United States).

YAHYAOUI, I. & SEGATTO, M. E. V. 2017. A practical technique for on-line monitoring of a photovoltaic plant connected to a single-phase grid. *Energy Conversion and Management,* 132**,** 198-206.

Figures

Tables

Equations

Appendix A – PV array monitoring system components

Monitoring data set	Parameter	Abbreviation	Measurement equipment	Model of equipment
Weather data	ambient temperature	T_{amb}	RTD probe in a multi-plate passively ventilated radiation shield	R.M. Young 41342LC in an R.M. Young 41003
	wind speed	v	ultrasonic wind sensor	Vaisala WMT52
	global horizontal irradiance	GHI	thermopile pyranometer	Eppley PSP
	direct normal irradiance	DNI	thermopile pyrheliometer	Kipp & Zonen CHP 1
	global in-plane irradiance	G_{poa}	thermopile pyranometer	Kipp & Zonen CMP 11
PV module operational data	module backside temperature	$T_{mod,meas}$	RTD	Unknown, Pt1000
	operational current	I_{op}	wireless IV curve tracer	Stratasense
	operational voltage	V_{op}	wireless IV curve tracer	Stratasense
	IV curve traces	-	wireless IV curve tracer	Stratasense
Camera pictures	entire array	-	network camera	Axis Q6032-E PTZ
	middle third	-	network camera	Axis Q6032-E PTZ
	north third	-	network camera	Axis Q6032-E PTZ
	south third	-	network camera	Axis Q6032-E PTZ
	sky camera	-	fisheye lens network camera	Axis M3027-PVE with a Fujinon FE185C046HA-1
	sky camera	-	fisheye lens network camera	Alcor System OMEA-2.0M-HCA with a Fujinon FE185C046HA-1

Table 24 Field deployed PV array monitoring system components (own table)

Figure 64 PV ground array strings and array fence dimensions (Boyd, 2015)

235 WATT

NU-U235F2

NEC 2008 Compliant
Module output cables: 12 AWG PV Wire

ELECTRICAL CHARACTERISTICS	
Maximum Power (Pmax)*	235 W
Tolerance of Pmax	+10%/-5%
Type of Cell	Monocrystalline silicon
Cell Configuration	60 in series
Open Circuit Voltage (Voc)	37.0 V
Maximum Power Voltage (Vpm)	30.0 V
Short Circuit Current (Isc)	8.60 A
Maximum Power Current (Ipm)	7.84 A
Module Efficiency (%)	14.4%
Maximum System (DC) Voltage	600 V
Series Fuse Rating	15 A
NOCT	47.5°C
Temperature Coefficient (Pmax)	-0.485%/°C
Temperature Coefficient (Voc)	-0.351%/°C
Temperature Coefficient (Isc)	0.053%/°C

*Illumination of 1 kW/m² (1 sun) at spectral distribution of AM 1.5 (ASTM E892 global spectral irradiance) at a cell temperature of 25°C.

MECHANICAL CHARACTERISTICS	
Dimensions (A x B x C below)	39.1" x 64.6" x 1.8"/994 x 1640 x 46 mm
Cable Length (G)	43.3"/1100 mm
Output Interconnect Cable**	12 AWG with MC4 Locking Connector
Weight	41.9 lbs / 19.0 kg
Max Load	50 psf (2400 Pascals)
Operating Temperature (cell)	-40 to 194°F / -40 to 90°C

**A safety lock clip (Multi Contact part number PV-SSH4) may be required in readily accessible locations per NEC 2008 690.33 (C)
**PV Wire per UL Subject 4703

QUALIFICATIONS	
UL Listed	UL 1703
Fire Rating	Class C

WARRANTY

25-year limited warranty on power output
Contact Sharp for complete warranty information

DIMENSIONS

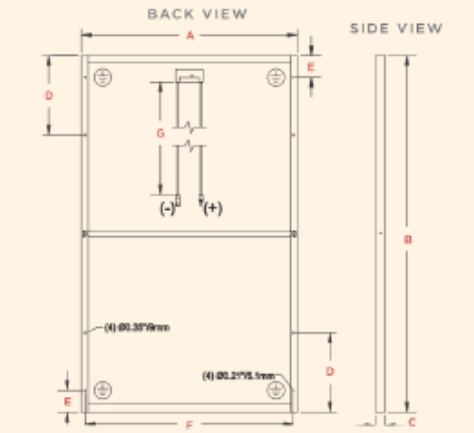

A	B	C	D	E	F	G
39.1"/994 mm	64.6"/1640 mm	1.8"/46 mm	14.4"/365 mm	3.9"/100 mm	37.7"/958 mm	43.3"/1100 mm

Contact Sharp for tolerance specifications

"BUY AMERICAN"

Sharp solar modules are manufactured in the United States and Japan, and qualify as "American" goods under the "Buy American" clause of the American Recovery and Reinvestment Act (ARRA).

SHARP

SHARP ELECTRONICS CORPORATION
5901 Bolsa Avenue, Huntington Beach, CA 92647
1-800-SOLAR-06 • Email: sharpsolar@sharpusa.com
www.sharpusa.com/solar

10L-080 • PC-11-10

Figure 65 Manufacturer data sheet for PV module at ground mounted PV array

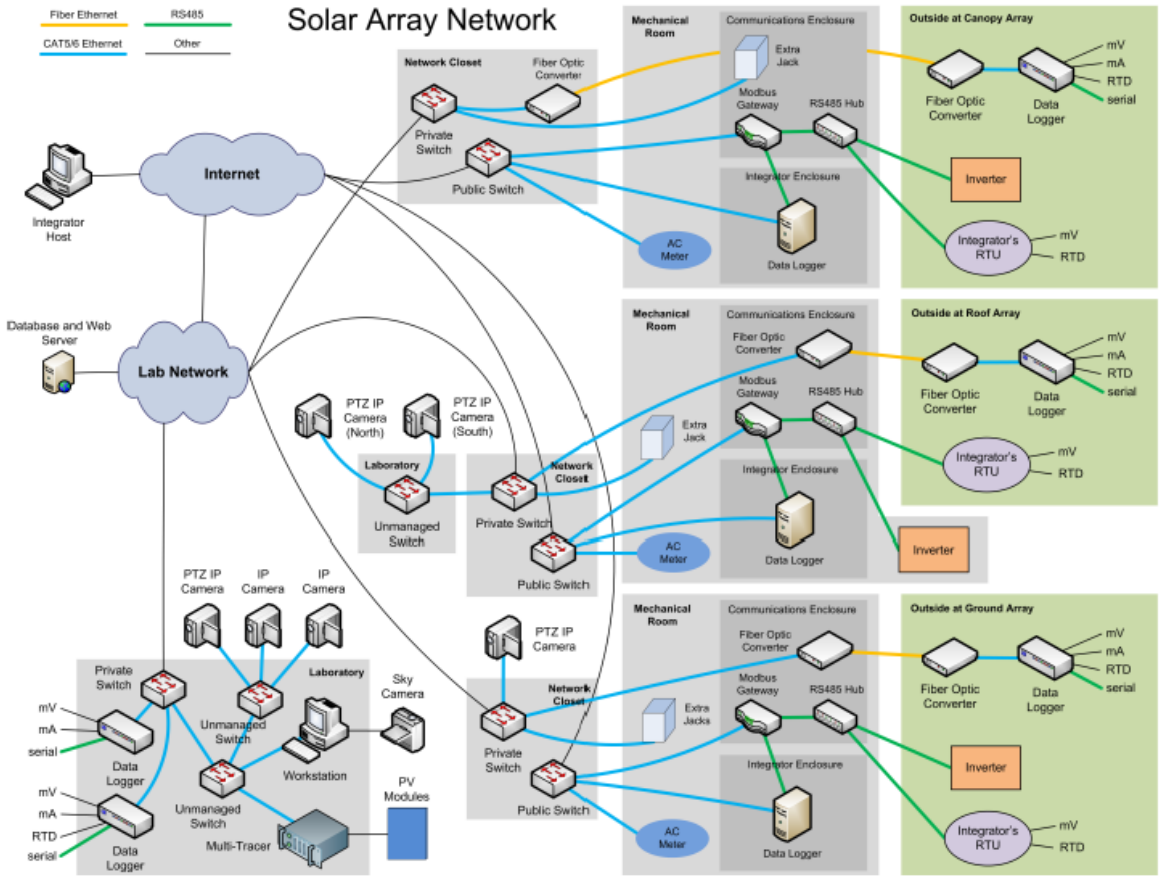

Figure 66 Schematical figure of the communication network for data acquisition (Boyd, 2015)

Appendix B – Performance matrix

Test Sequence	Module ID	Date Tested	Tested By	Reference Device	Spectral MM Factor	Temperature [°C]	Irradiance [W/m2]	Isc [A]	Voc [V]	Imp [A]	Vmp [V]	Pmp [W]	FF [%]	Eff [%]	Ix [A]	Ixx [A]
Matrix	Average	22.09.2016	KL/DCZ	CAL271 Out	1,0000	15	100	0,85	34,9	0,80	29,7	23,7	80,0	14,5	0,84	0,64
Matrix	Average	22.09.2016	KL/DCZ	CAL271 Out	1,0000	15	200	1,69	36,1	1,60	30,6	48,8	80,0	15,0	1,69	1,26
Matrix	Average	22.09.2016	KL/DCZ	CAL271 Out	1,0000	15	400	3,38	37,2	3,19	31,1	99,3	79,1	15,2	3,36	2,45
Matrix	Average	22.09.2016	KL/DCZ	CAL271 Out	1,0000	15	500	4,22	37,5	3,98	31,2	124,3	78,4	15,2	4,20	3,02
Matrix	Average	22.09.2016	KL/DCZ	CAL271 Out	1,0000	15	600	5,06	37,8	4,77	31,2	148,9	77,7	15,2	5,05	3,57
Matrix	Average	22.09.2016	KL/DCZ	CAL271 Out	1,0000	15	800	6,76	38,3	6,34	31,2	197,7	76,4	15,2	6,73	4,63
Matrix	Average	22.09.2016	KL/DCZ	CAL271 Out	1,0000	15	1000	8,46	38,6	7,91	31,0	245,3	75,1	15,0	8,42	5,64
Matrix	Average	22.09.2016	KL/DCZ	CAL271 Out	1,0000	25	100	0,85	33,6	0,80	28,4	22,7	79,1	13,9	0,85	0,63
Matrix	Average	22.09.2016	KL/DCZ	CAL271 Out	1,0000	25	200	1,70	34,8	1,60	29,2	46,7	78,9	14,3	1,69	1,25
Matrix	Average	22.09.2016	KL/DCZ	CAL271 Out	1,0000	25	400	3,39	36,0	3,18	29,8	94,9	77,8	14,6	3,37	2,43
Matrix	Average	22.09.2016	KL/DCZ	CAL271 Out	1,0000	25	600	5,08	36,6	4,75	29,9	142,2	76,4	14,5	5,06	3,53
Matrix	Average	22.09.2016	KL/DCZ	CAL271 Out	1,0000	25	800	6,78	37,1	6,33	29,9	189,2	75,3	14,5	6,75	4,59
Matrix	Average	22.09.2016	KL/DCZ	CAL271 Out	1,0000	25	1000	8,48	37,4	7,89	29,7	234,5	73,8	14,4	8,44	5,58
Matrix	Average	22.09.2016	KL/DCZ	CAL271 Out	1,0000	25	1100	9,33	37,6	8,67	29,6	256,6	73,2	14,3	9,29	6,06
Matrix	Average	22.09.2016	KL/DCZ	CAL271 Out	1,0000	50	100	0,86	30,3	0,79	24,9	19,8	76,0	12,1	0,85	0,62
Matrix	Average	22.09.2016	KL/DCZ	CAL271 Out	1,0000	50	200	1,71	31,5	1,58	25,8	40,9	75,9	12,5	1,70	1,21
Matrix	Average	22.09.2016	KL/DCZ	CAL271 Out	1,0000	50	400	3,42	32,8	3,16	26,5	83,8	74,6	12,8	3,40	2,36
Matrix	Average	22.09.2016	KL/DCZ	CAL271 Out	1,0000	50	600	5,12	33,5	4,72	26,7	125,9	73,5	12,9	5,09	3,43
Matrix	Average	22.09.2016	KL/DCZ	CAL271 Out	1,0000	50	800	6,82	34,0	6,27	26,6	167,1	72,1	12,8	6,79	4,44
Matrix	Average	22.09.2016	KL/DCZ	CAL271 Out	1,0000	50	1000	8,53	34,4	7,81	26,5	206,9	70,6	12,7	8,48	5,40
Matrix	Average	22.09.2016	KL/DCZ	CAL271 Out	1,0000	50	1100	9,37	34,5	8,57	26,4	226,0	69,8	12,6	9,32	5,87
Matrix	Average	22.09.2016	KL/DCZ	CAL271 Out	1,0000	75	100	0,86	26,8	0,79	21,5	16,9	73,0	10,4	0,86	0,60
Matrix	Average	22.09.2016	KL/DCZ	CAL271 Out	1,0000	75	200	1,72	28,2	1,57	22,5	35,3	72,8	10,8	1,71	1,18
Matrix	Average	22.09.2016	KL/DCZ	CAL271 Out	1,0000	75	400	3,43	29,6	3,12	23,3	72,5	71,5	11,1	3,41	2,27
Matrix	Average	22.09.2016	KL/DCZ	CAL271 Out	1,0000	75	600	5,14	30,3	4,65	23,5	109,1	70,0	11,2	5,10	3,30
Matrix	Average	22.09.2016	KL/DCZ	CAL271 Out	1,0000	75	800	6,85	30,9	6,18	23,5	145,0	68,5	11,1	6,81	4,27
Matrix	Average	22.09.2016	KL/DCZ	CAL271 Out	1,0000	75	1000	8,57	31,3	7,69	23,3	179,2	66,8	11,0	8,49	5,18
Matrix	Average	22.09.2016	KL/DCZ	CAL271 Out	1,0000	75	1100	9,41	31,5	8,44	23,2	196,0	66,2	10,9	9,33	5,63

Table 25 Performance matrix, not extrapolated (CFV, 2016)

Test Sequence	Module ID	Date Tested	Tested By	Reference Device	Spectral MM Factor	Temperature [°C]	Irradiance [W/m2]	Isc [A]	Voc [V]	Imp [A]	Vmp [V]	Pmp [W]	FF [%]	Eff [%]	Ix [A]	Ixx [A]
Matrix	**Average**	**22.09.2016**	**KL/DCZ**	**CAL271 Out**	**1,0000**	**-5**	**50**	**0,4**	**38,4**	**0,4**	**33,3**	**12,5**	**82,4**	**16,2**	**0,4**	**0,3**
Matrix	Average	22.09.2016	KL/DCZ	CAL271 Out	1,0000	**-5**	100	**3,8**	**43,0**	**3,6**	**36,8**	**113,0**	**82,3**	**17,9**	**3,8**	**2,8**
Matrix	Average	22.09.2016	KL/DCZ	CAL271 Out	1,0000	**-5**	200	**7,2**	**47,5**	**6,8**	**40,2**	**215,7**	**82,7**	**19,7**	**7,2**	**5,3**
Matrix	Average	22.09.2016	KL/DCZ	CAL271 Out	1,0000	**-5**	400	**14,3**	**47,6**	**13,5**	**38,2**	**434,7**	**75,9**	**18,5**	**14,2**	**10,2**
Matrix	Average	22.09.2016	KL/DCZ	CAL271 Out	1,0000	**-5**	500	**8,4**	**42,5**	**7,9**	**35,4**	**264,0**	**78,8**	**17,2**	**8,4**	**5,9**
Matrix	Average	22.09.2016	KL/DCZ	CAL271 Out	1,0000	**-5**	600	**5,0**	**41,6**	**4,8**	**35,2**	**169,0**	**81,6**	**17,3**	**5,0**	**3,7**
Matrix	Average	22.09.2016	KL/DCZ	CAL271 Out	1,0000	**-5**	800	**6,7**	**41,9**	**6,4**	**35,1**	**223,3**	**79,9**	**17,1**	**6,7**	**4,8**
Matrix	Average	22.09.2016	KL/DCZ	CAL271 Out	1,0000	**-5**	1000	**8,4**	**42,2**	**8,0**	**34,9**	**277,7**	**78,7**	**17,0**	**8,4**	**5,8**
Matrix	**Average**	**22.09.2016**	**KL/DCZ**	**CAL271 Out**	**1,0000**	**0**	**50**	**0,4**	**37,1**	**0,4**	**32,0**	**12,1**	**81,6**	**15,5**	**0,4**	**0,3**
Matrix	Average	22.09.2016	KL/DCZ	CAL271 Out	1,0000	**0**	100	**2,1**	**39,4**	**2,0**	**33,7**	**62,3**	**81,6**	**16,4**	**2,1**	**1,6**
Matrix	Average	22.09.2016	KL/DCZ	CAL271 Out	1,0000	**0**	200	**4,2**	**42,2**	**4,0**	**35,9**	**126,2**	**81,7**	**17,5**	**4,2**	**3,1**
Matrix	Average	22.09.2016	KL/DCZ	CAL271 Out	1,0000	**0**	400	**8,4**	**43,1**	**8,0**	**35,5**	**254,8**	**78,4**	**17,3**	**8,4**	**6,1**
Matrix	Average	22.09.2016	KL/DCZ	CAL271 Out	1,0000	**0**	500	**6,7**	**41,1**	**6,4**	**34,2**	**207,9**	**79,0**	**16,6**	**6,7**	**4,8**
Matrix	Average	22.09.2016	KL/DCZ	CAL271 Out	1,0000	**0**	600	**5,0**	**40,3**	**4,8**	**33,9**	**162,3**	**80,3**	**16,6**	**5,0**	**3,7**
Matrix	Average	22.09.2016	KL/DCZ	CAL271 Out	1,0000	**0**	800	**6,7**	**40,7**	**6,4**	**33,8**	**214,7**	**78,8**	**16,5**	**6,7**	**4,7**
Matrix	Average	22.09.2016	KL/DCZ	CAL271 Out	1,0000	**0**	1000	**8,4**	**41,0**	**8,0**	**33,6**	**266,9**	**77,5**	**16,4**	**8,4**	**5,8**
Matrix	**Average**	**22.09.2016**	**KL/DCZ**	**CAL271 Out**	**1,0000**	**5**	**50**	**0,4**	**35,7**	**0,4**	**30,6**	**11,6**	**80,8**	**14,9**	**0,4**	**0,3**
Matrix	Average	22.09.2016	KL/DCZ	CAL271 Out	1,0000	**5**	100	**1,3**	**36,9**	**1,2**	**31,5**	**36,7**	**80,8**	**15,4**	**1,3**	**1,0**
Matrix	Average	22.09.2016	KL/DCZ	CAL271 Out	1,0000	**5**	200	**2,5**	**38,6**	**2,4**	**32,8**	**75,0**	**80,9**	**16,0**	**2,5**	**1,9**
Matrix	Average	22.09.2016	KL/DCZ	CAL271 Out	1,0000	**5**	400	**5,1**	**39,6**	**4,8**	**33,0**	**151,8**	**79,2**	**16,1**	**5,0**	**3,7**
Matrix	Average	22.09.2016	KL/DCZ	CAL271 Out	1,0000	**5**	500	**5,0**	**39,1**	**4,8**	**32,7**	**153,6**	**79,0**	**15,9**	**5,0**	**3,6**
Matrix	Average	22.09.2016	KL/DCZ	CAL271 Out	1,0000	**5**	600	**5,0**	**39,1**	**4,8**	**32,6**	**155,6**	**79,0**	**15,9**	**5,0**	**3,6**
Matrix	Average	22.09.2016	KL/DCZ	CAL271 Out	1,0000	**5**	800	**6,7**	**39,5**	**6,3**	**32,5**	**206,2**	**77,6**	**15,8**	**6,7**	**4,7**
Matrix	Average	22.09.2016	KL/DCZ	CAL271 Out	1,0000	**5**	1000	**8,4**	**39,8**	**7,9**	**32,3**	**256,1**	**76,3**	**15,7**	**8,4**	**5,7**
Matrix	**Average**	**22.09.2016**	**KL/DCZ**	**CAL271 Out**	**1,0000**	**15**	**50**	**0,4**	**34,4**	**0,4**	**29,3**	**11,2**	**80,0**	**14,3**	**0,4**	**0,3**
Matrix	Average	22.09.2016	KL/DCZ	CAL271 Out	1,0000	15	100	0,85	34,9	0,80	29,7	23,7	80,0	14,5	0,84	0,64
Matrix	Average	22.09.2016	KL/DCZ	CAL271 Out	1,0000	15	200	1,69	36,1	1,60	30,6	48,8	80,0	15,0	1,69	1,26
Matrix	Average	22.09.2016	KL/DCZ	CAL271 Out	1,0000	15	400	3,38	37,2	3,19	31,1	99,3	79,1	15,2	3,36	2,45
Matrix	Average	22.09.2016	KL/DCZ	CAL271 Out	1,0000	15	500	4,22	37,5	3,98	31,2	124,3	78,4	15,2	4,20	3,02
Matrix	Average	22.09.2016	KL/DCZ	CAL271 Out	1,0000	15	600	5,06	37,8	4,77	31,2	148,9	77,7	15,2	5,05	3,57
Matrix	Average	22.09.2016	KL/DCZ	CAL271 Out	1,0000	15	800	6,76	38,3	6,34	31,2	197,7	76,4	15,2	6,73	4,63
Matrix	Average	22.09.2016	KL/DCZ	CAL271 Out	1,0000	15	1000	8,46	38,6	7,91	31,0	245,3	75,1	15,0	8,42	5,64
Matrix	**Average**	**22.09.2016**	**KL/DCZ**	**CAL271 Out**	**1,0000**	**25**	**50**	**0,4**	**33,0**	**0,4**	**27,9**	**10,7**	**79,2**	**13,7**	**0,4**	**0,3**
Matrix	Average	22.09.2016	KL/DCZ	CAL271 Out	1,0000	25	100	0,85	33,6	0,80	28,4	22,7	79,1	13,9	0,85	0,63
Matrix	Average	22.09.2016	KL/DCZ	CAL271 Out	1,0000	25	200	1,70	34,8	1,60	29,2	46,7	78,9	14,3	1,69	1,25
Matrix	Average	22.09.2016	KL/DCZ	CAL271 Out	1,0000	25	400	3,39	36,0	3,18	29,8	94,9	77,8	14,6	3,37	2,43
Matrix	Average	23.09.2016	KL/DCZ	CAL271 Out	1,0000	25	500	4,24	36,4	3,97	29,9	118,7	77,0	14,6	4,21	3,01
Matrix	Average	22.09.2016	KL/DCZ	CAL271 Out	1,0000	25	600	5,08	36,6	4,75	29,9	142,2	76,4	14,5	5,06	3,53
Matrix	Average	22.09.2016	KL/DCZ	CAL271 Out	1,0000	25	800	6,78	37,1	6,33	29,9	189,2	75,3	14,5	6,75	4,59
Matrix	Average	22.09.2016	KL/DCZ	CAL271 Out	1,0000	25	1000	8,48	37,4	7,89	29,7	234,5	73,8	14,4	8,44	5,58
Matrix	Average	22.09.2016	KL/DCZ	CAL271 Out	1,0000	25	1100	9,33	37,6	8,67	29,6	256,6	73,2	14,3	9,29	6,06
Matrix	**Average**	**22.09.2016**	**KL/DCZ**	**CAL271 Out**	**1,0000**	**50**	**50**	**0,4**	**29,6**	**0,4**	**24,5**	**9,2**	**76,1**	**11,9**	**0,4**	**0,3**
Matrix	Average	22.09.2016	KL/DCZ	CAL271 Out	1,0000	50	100	0,86	30,3	0,79	24,9	19,8	76,0	12,1	0,85	0,62
Matrix	Average	22.09.2016	KL/DCZ	CAL271 Out	1,0000	50	200	1,71	31,5	1,58	25,8	40,9	75,9	12,5	1,70	1,21
Matrix	Average	22.09.2016	KL/DCZ	CAL271 Out	1,0000	50	400	3,42	32,8	3,16	26,5	83,8	74,6	12,8	3,40	2,36
Matrix	Average	23.09.2016	KL/DCZ	CAL271 Out	1,0000	50	500	4,26	33,3	3,94	26,7	105,3	74,2	12,9	4,25	2,92
Matrix	Average	22.09.2016	KL/DCZ	CAL271 Out	1,0000	50	600	5,12	33,5	4,72	26,7	125,9	73,5	12,9	5,09	3,43
Matrix	Average	22.09.2016	KL/DCZ	CAL271 Out	1,0000	50	800	6,82	34,0	6,27	26,6	167,1	72,1	12,8	6,79	4,44
Matrix	Average	22.09.2016	KL/DCZ	CAL271 Out	1,0000	50	1000	8,53	34,4	7,81	26,5	206,9	70,6	12,7	8,48	5,40
Matrix	Average	22.09.2016	KL/DCZ	CAL271 Out	1,0000	50	1100	9,37	34,5	8,57	26,4	226,0	69,8	12,6	9,32	5,87
Matrix	**Average**	**22.09.2016**	**KL/DCZ**	**CAL271 Out**	**1,0000**	**75**	**50**	**0,4**	**26,1**	**0,4**	**21,0**	**7,7**	**73,0**	**10,1**	**0,4**	**0,3**
Matrix	Average	22.09.2016	KL/DCZ	CAL271 Out	1,0000	75	100	0,86	26,8	0,79	21,5	16,9	73,0	10,4	0,86	0,60
Matrix	Average	22.09.2016	KL/DCZ	CAL271 Out	1,0000	75	200	1,72	28,2	1,57	22,5	35,3	72,8	10,8	1,71	1,18
Matrix	Average	22.09.2016	KL/DCZ	CAL271 Out	1,0000	75	400	3,43	29,6	3,12	23,3	72,5	71,5	11,1	3,41	2,27
Matrix	Average	23.09.2016	KL/DCZ	CAL271 Out	1,0000	75	500	4,28	30,0	3,89	23,4	91,1	70,8	11,2	4,25	2,81
Matrix	Average	22.09.2016	KL/DCZ	CAL271 Out	1,0000	75	600	5,14	30,3	4,65	23,5	109,1	70,0	11,2	5,10	3,30
Matrix	Average	22.09.2016	KL/DCZ	CAL271 Out	1,0000	75	800	6,85	30,9	6,18	23,5	145,0	68,5	11,1	6,81	4,27
Matrix	Average	22.09.2016	KL/DCZ	CAL271 Out	1,0000	75	1000	8,57	31,3	7,69	23,3	179,2	66,8	11,0	8,49	5,18
Matrix	Average	22.09.2016	KL/DCZ	CAL271 Out	1,0000	75	1100	9,41	31,5	8,44	23,2	196,0	66,2	10,9	9,33	5,63

Table 26 Extrapolated performance matrix (CFV, 2016)

Appendix C – Daylight times of observed days

Month	Zenith angle <= 90°	Day of evaluation	Chosen daylight times*
August	05:18	07.08.2016	8:30 - 17:30
September	05:44	05.09.2016	8:45 - 17:00
October	06:12	05.10.2016	9:00 - 16:00
November	06:45	05.11.2016	9:00 - 15:00
December	07:27	20.12.2016	10:00 - 14:00
January	07:31	08.01.2017	10:00 - 14:30
February	07:15	04.02.2017	9:30 - 15:30
March	06:37	05.03.2017	9:00 - 16:00
April	05:44	08.04.2017	8:45 - 17:00

Table 27 Daylight times of observed days (own table)

*conservatively chosen daylight times at times without shading of the array and no snow deposition on top of the field deployed PV modules and measurement equipment; not considered: last rainfall (i.e. cleaning of dust deposition)

Appendix D – Observed combinations of bin ranges

AOI range	Wind speed ranges	Ambient temperature range	Irradiance range	Number of bin range	Type of observation
-	-	-	1	**1**	**Independent variation of bin 11 bin ranges**
-	-	-	2	**2**	
-	-	-	3	**3**	
-	-	1	-	**4**	
-	-	2	-	**5**	
-	1	-	-	**6**	
-	2	-	-	**7**	
-	3	-	-	**8**	
1	-	-	-	**9**	
2	-	-	-	**10**	
3	-	-	-	**11**	
1	1	1	1	**12**	**Cross-dependent variation of bin 54 bin ranges (data samples)**
1	1	1	2	**13**	
1	1	1	3	**14**	
1	1	2	1	**15**	
1	1	2	2	**16**	
1	1	2	3	**17**	
1	2	1	1	**18**	
1	2	1	2	**19**	
1	2	1	3	**20**	
1	2	2	1	**21**	
1	2	2	2	**22**	
1	2	2	3	**23**	
1	3	1	1	**24**	
1	3	1	2	**25**	
1	3	1	3	**26**	
1	3	2	1	**27**	
1	3	2	2	**28**	
1	3	2	3	**29**	
2	1	1	1	**30**	
2	1	1	2	**31**	
2	1	1	3	**32**	
2	1	2	1	**33**	
2	1	2	2	**34**	
2	1	2	3	**35**	

2	2	1	1	**36**	
2	2	1	2	**37**	
2	2	1	3	**38**	
2	2	2	1	**39**	
2	2	2	2	**40**	
2	2	2	3	**41**	
2	3	1	1	**42**	
2	3	1	2	**43**	
2	3	1	3	**44**	
2	3	2	1	**45**	
2	3	2	2	**46**	
2	3	2	3	**47**	
3	1	1	1	**48**	
3	1	1	2	**49**	
3	1	1	3	**50**	
3	1	2	1	**51**	
3	1	2	2	**52**	
3	1	2	3	**53**	
3	2	1	1	**54**	
3	2	1	2	**55**	
3	2	1	3	**56**	
3	2	2	1	**57**	
3	2	2	2	**58**	
3	2	2	3	**59**	
3	3	1	1	**60**	
3	3	1	2	**61**	
3	3	1	3	**62**	
3	3	2	1	**63**	
3	3	2	2	**64**	
3	3	2	3	**65**	

Table 28 Observed combinations of bin ranges (own table)

Appendix E – Temperature prediction results

Nr.	RMSE [°C]	MAD [°C]	R^2 [-]	Rpearson [-]	Rspearman [-]	Irradiance [W/m²]	Ambient Temp. [°C]	Wind speed [m/s]	AOI [°]
12	1,877	0,601	0,961	0,980	0,957	Irr. 1			
13	4,317	1,435	0,242	0,494	0,564	Irr. 2		Wind speed 1	
14	9,030	1,793	0,057	0,255	0,335	Irr. 3			
15	3,457	1,389	0,932	0,966	0,938	Irr. 1			
16	5,440	2,576	0,693	0,833	0,823	Irr. 2	tamb 1	Wind speed 2	
17	5,196	1,645	0,251	0,502	0,504	Irr. 3			
18	2,754	1,149	0,894	0,946	0,932	Irr. 1			
19	3,123	0,958	0,705	0,841	0,874	Irr. 2		Wind speed 3	
20	2,266	1,088	0,884	0,941	0,922	Irr. 3			AOI 1
21	2,794	1,130	0,927	0,963	0,924	Irr. 1			
22	4,437	1,904	0,907	0,952	0,953	Irr. 2		Wind speed 1	
23	4,044	1,618	0,889	0,943	0,921	Irr. 3			
24	2,064	0,609	0,575	0,760	0,774	Irr. 1			
25	3,864	1,359	0,614	0,786	0,760	Irr. 2	tamb 2	Wind speed 2	
26	2,746	1,446	0,817	0,905	0,845	Irr. 3			
27	3,583	1,073	0,917	0,958	0,956	Irr. 1			
28	3,029	1,129	0,785	0,887	0,898	Irr. 2		Wind speed 3	
29	3,385	1,379	0,903	0,950	0,853	Irr. 3			
30	1,415	0,635	0,972	0,986	0,980	Irr. 1			
31	4,096	1,402	0,300	0,550	0,603	Irr. 2		Wind speed 1	
32	7,965	4,482	-0,039	0,050	0,283	Irr. 3			
33	2,180	0,869	0,959	0,980	0,944	Irr. 1			
34	2,096	1,364	0,889	0,943	0,874	Irr. 2	tamb 1	Wind speed 2	
35						Irr. 3			
36	2,210	0,558	0,939	0,970	0,982	Irr. 1			
37	2,120	1,003	0,795	0,892	0,890	Irr. 2		Wind speed 3	
38	2,494	1,001	0,832	0,917	0,835	Irr. 3			AOI 2
39	1,951	1,359	0,973	0,987	0,856	Irr. 1			
40	1,490	0,825	0,894	0,946	0,941	Irr. 2		Wind speed 1	
41						Irr. 3			
42	2,381	1,506	0,337	0,596	0,303	Irr. 1			
43	1,668	0,892	0,816	0,904	0,868	Irr. 2	tamb 2	Wind speed 2	
44	3,935	1,083	0,157	0,421	0,460	Irr. 3			
45	2,651	1,533	0,943	0,972	0,684	Irr. 1			
46	2,165	1,060	0,762	0,875	0,878	Irr. 2		Wind speed 3	
47						Irr. 3			
48						Irr. 1			
49	5,629	2,541	0,133	0,398	0,390	Irr. 2		Wind speed 1	
50	7,883	1,229	0,182	-0,534	-0,083	Irr. 3			
51	1,644	0,990	0,799	0,895	0,886	Irr. 1			
52	1,044	0,760	0,975	0,988	0,847	Irr. 2	tamb 1	Wind speed 2	
53						Irr. 3			
54						Irr. 1			
55	2,062	0,671	0,826	0,912	0,857	Irr. 2		Wind speed 3	
56						Irr. 3			AOI 3
57	1,164	0,540	0,930	0,966	0,984	Irr. 1			
58	1,107	0,917	0,897	0,951	0,675	Irr. 2		Wind speed 1	
59						Irr. 3			
60						Irr. 1			
61	2,983	0,539	0,790	0,891	0,884	Irr. 2	tamb 2	Wind speed 2	
62	3,040	0,527	0,544	0,753	0,742	Irr. 3			
63	0,977	0,369	0,994	0,998	0,786	Irr. 1			
64	0,439	0,325	0,082	0,461	0,143	Irr. 2		Wind speed 3	
65						Irr. 3			

Table 29 Statistical parameters for temperature prediction, ranges 12 to 65 (own table)

Appendix F – Distribution of temperature residuals

(Samples that reach the minimum required sample size of 42 data points, own figures)

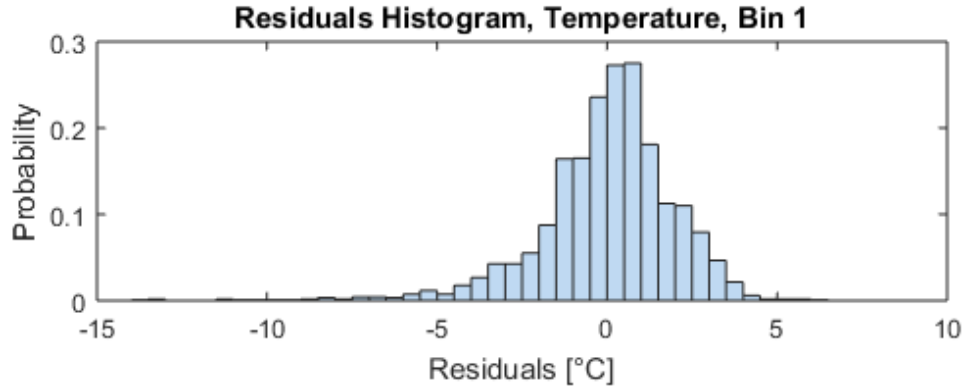

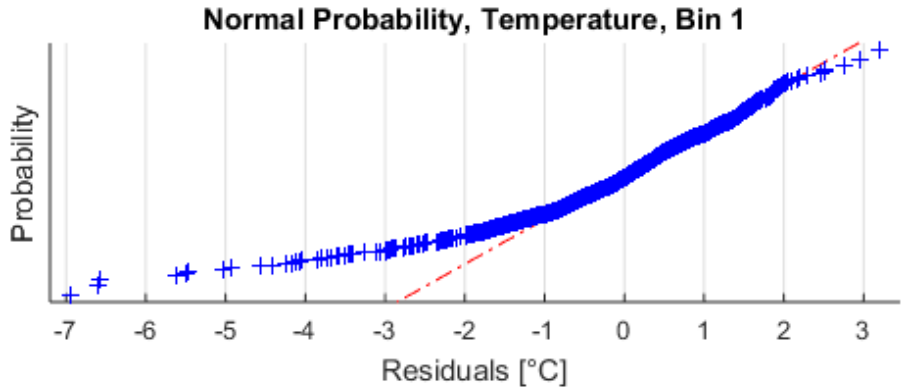

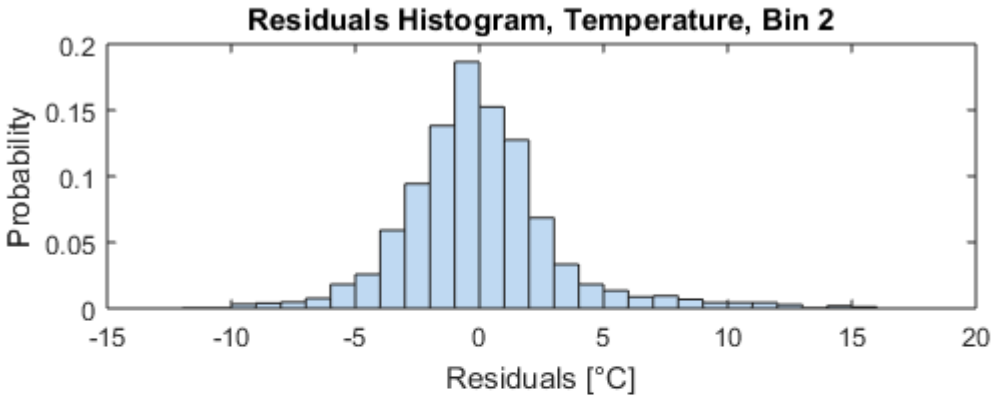

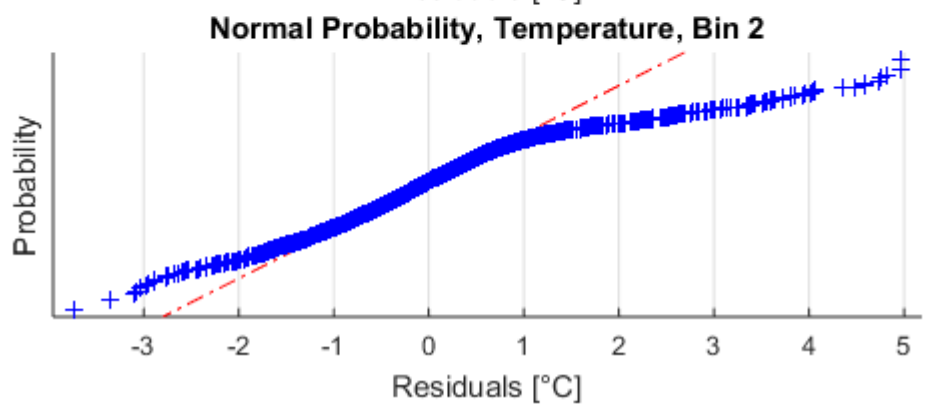

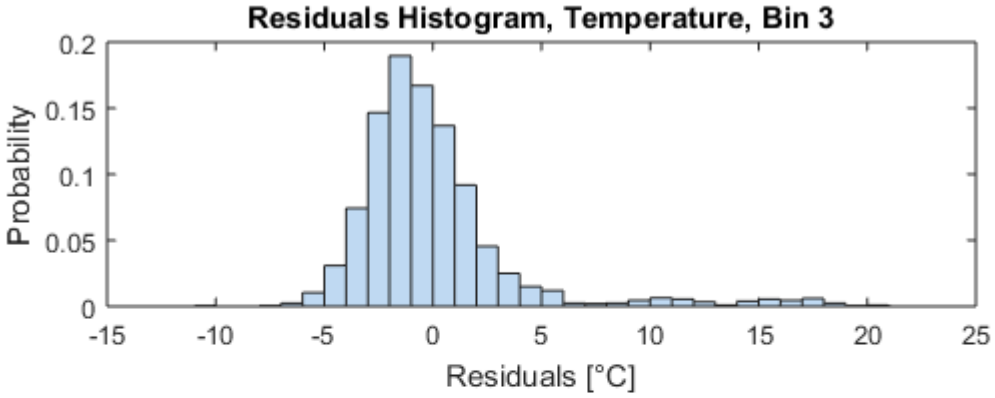
Residuals Histogram, Temperature, Bin 3
Probability
0.2
0.15
0.1
0.05
0
-15
-10
-5
0
5
10
15
20
25
Residuals [°C]

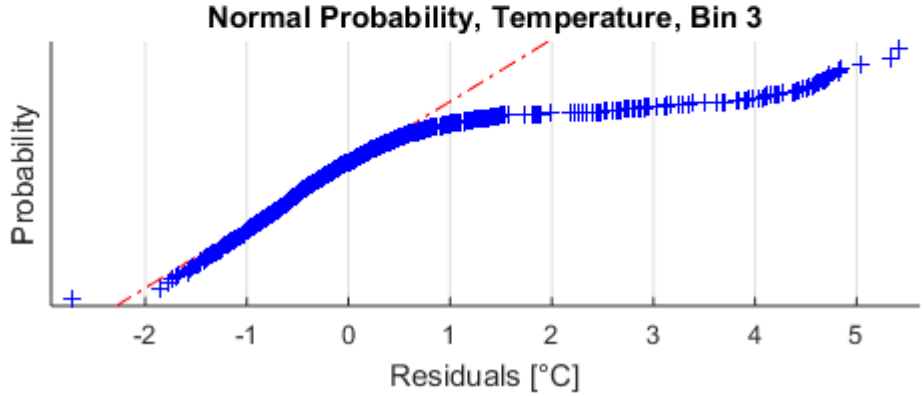
Normal Probability, Temperature, Bin 3
Probability
-2
-1
0
1
2
3
4
5
Residuals [°C]

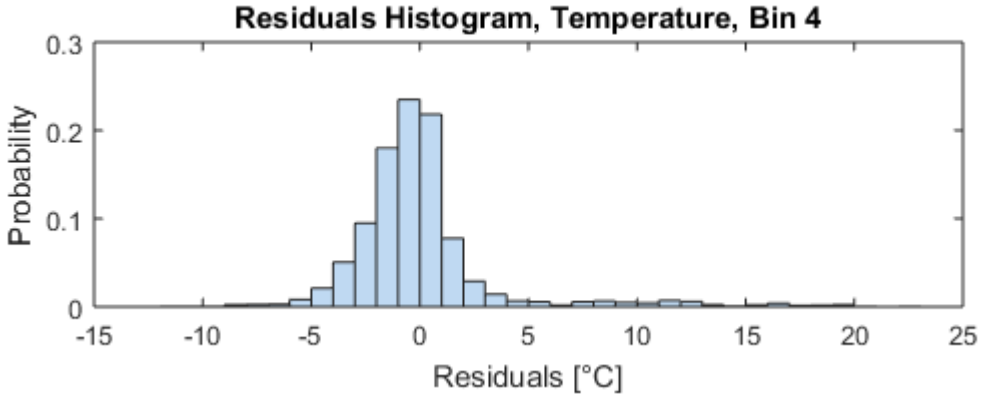
Residuals Histogram, Temperature, Bin 4
Probability
0.3
0.2
0.1
0
-15
-10
-5
0
5
10
15
20
25
Residuals [°C]

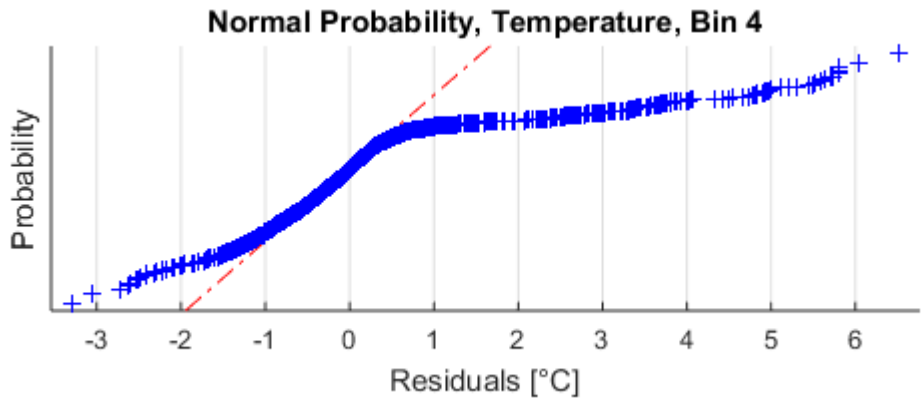
Normal Probability, Temperature, Bin 4
Probability
-3
-2
-1
0
1
2
3
4
5
6
Residuals [°C]

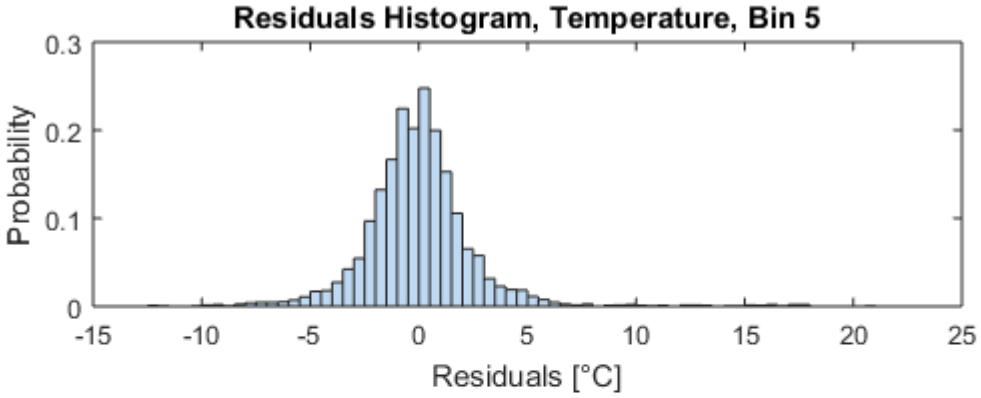
Residuals Histogram, Temperature, Bin 5
Probability
0.3
0.2
0.1
0
-15
-10
-5
0
5
10
15
20
25
Residuals [°C]

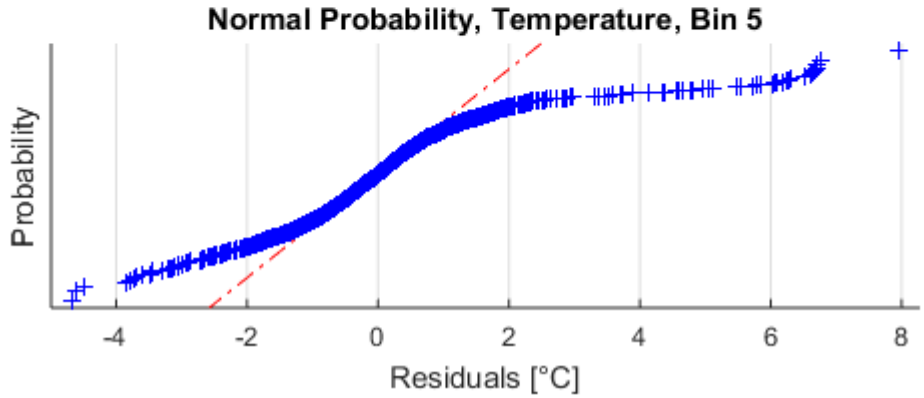
Normal Probability, Temperature, Bin 5
Probability
-4
-2
0
2
4
6
8
Residuals [°C]

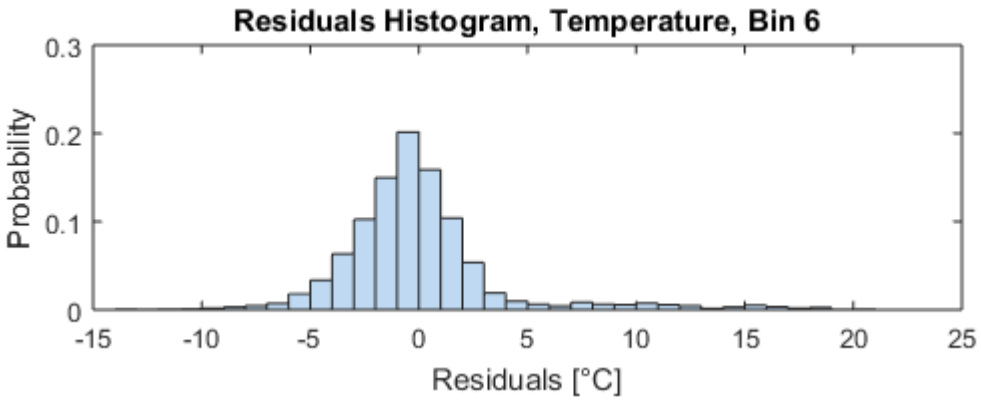
Residuals Histogram, Temperature, Bin 6
Probability
0.3
0.2
0.1
0
-15
-10
-5
0
5
10
15
20
25
Residuals [°C]

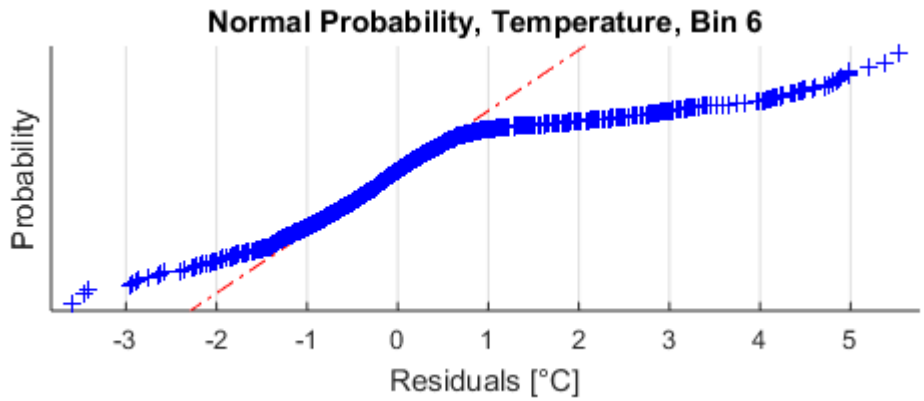
Normal Probability, Temperature, Bin 6
Probability
-3
-2
-1
0
1
2
3
4
5
Residuals [°C]

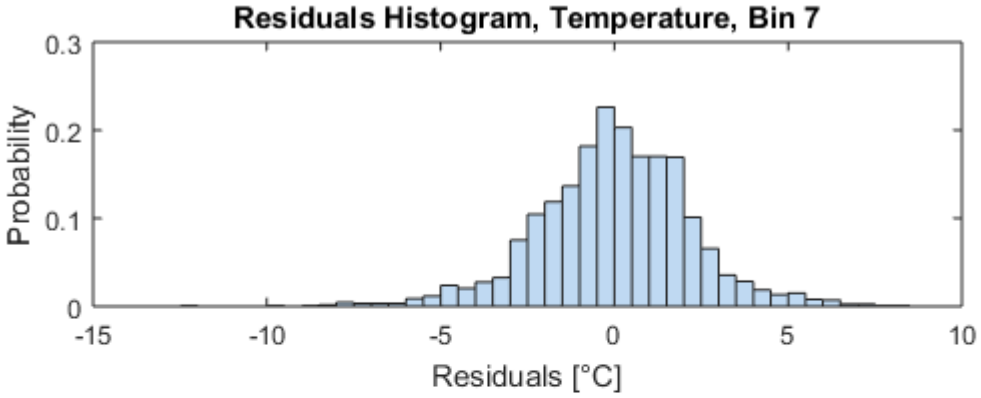
Residuals Histogram, Temperature, Bin 7
Probability
0.3
0.2
0.1
0
-15
-10
-5
0
5
10
Residuals [°C]

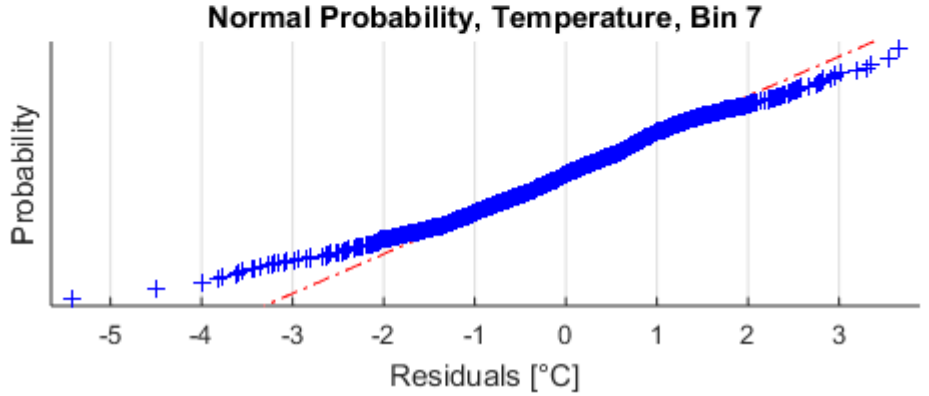
Normal Probability, Temperature, Bin 7
Probability
-5
-4
-3
-2
-1
0
1
2
3
Residuals [°C]

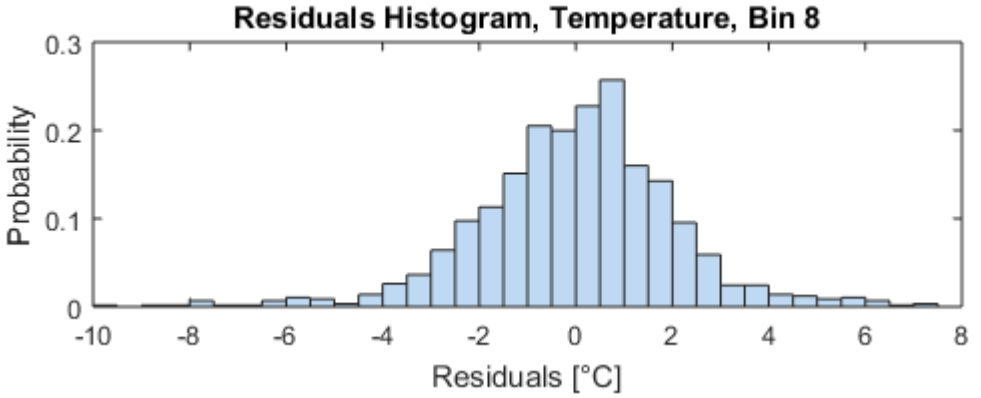
Residuals Histogram, Temperature, Bin 8
Probability
0.3
0.2
0.1
0
-10
-8
-6
-4
-2
0
2
4
6
8
Residuals [°C]

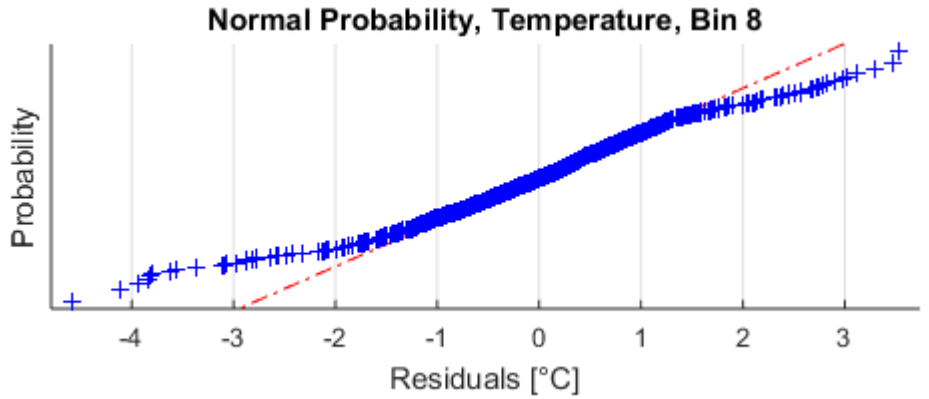
Normal Probability, Temperature, Bin 8
Probability
-4
-3
-2
-1
0
1
2
3
Residuals [°C]

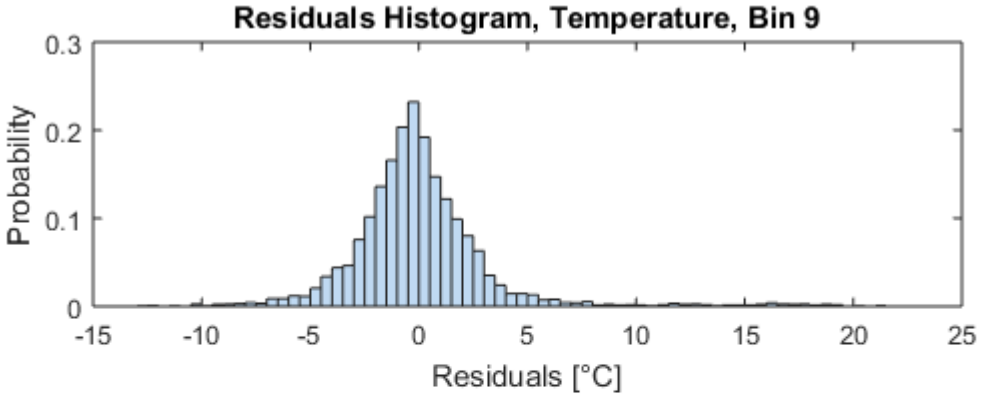
Residuals Histogram, Temperature, Bin 9
Probability
0.3
0.2
0.1
0
-15
-10
-5
0
5
10
15
20
25
Residuals [°C]

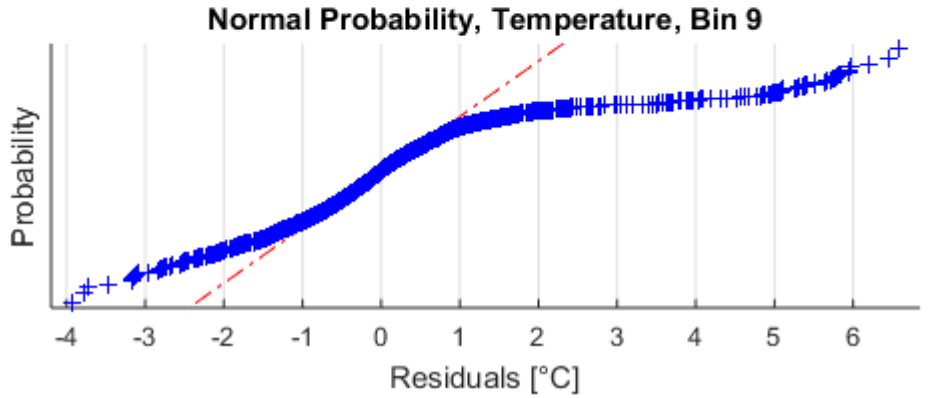
Normal Probability, Temperature, Bin 9
Probability
-4
-3
-2
-1
0
1
2
3
4
5
6
Residuals [°C]

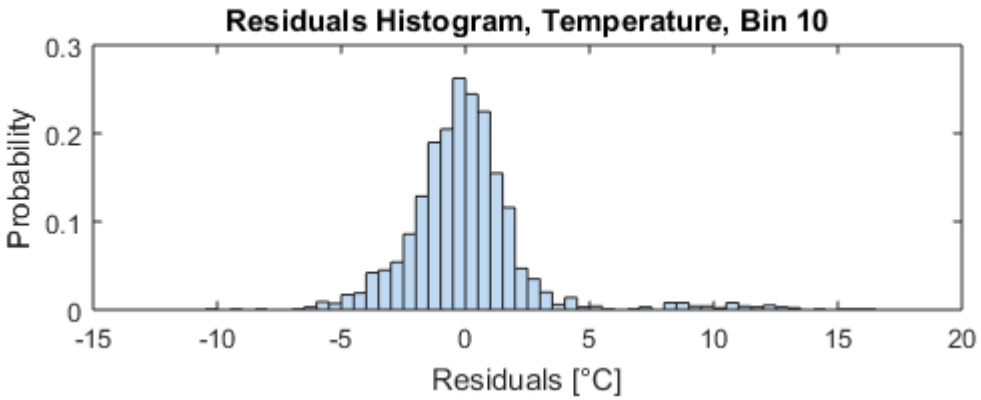
Residuals Histogram, Temperature, Bin 10
Probability
0.3
0.2
0.1
0
-15
-10
-5
0
5
10
15
20
Residuals [°C]

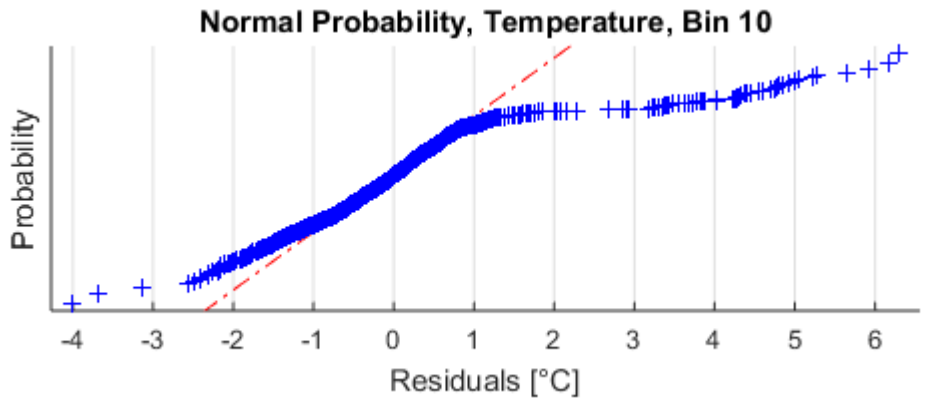
Normal Probability, Temperature, Bin 10
Probability
-4
-3
-2
-1
0
1
2
3
4
5
6
Residuals [°C]

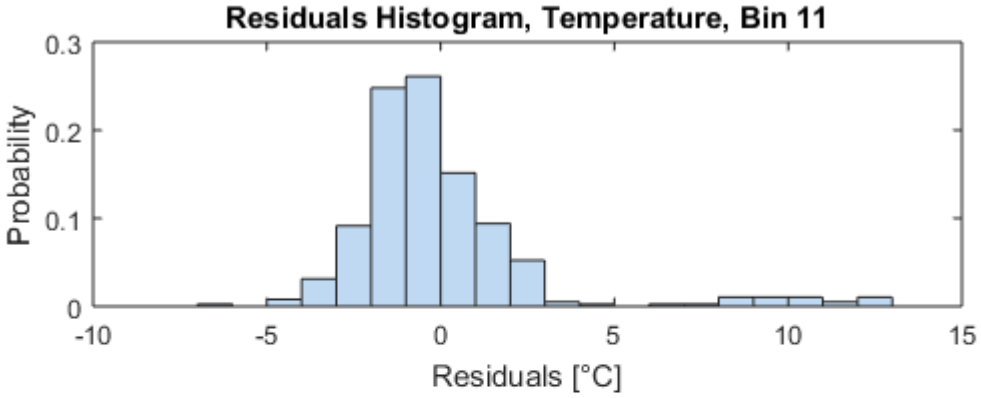
Residuals Histogram, Temperature, Bin 11
Probability
0.3
0.2
0.1
0
-10
-5
0
5
10
15
Residuals [°C]

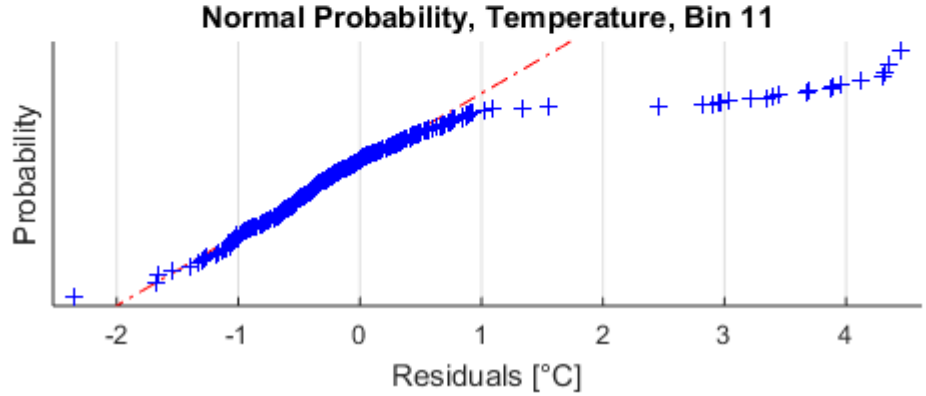
Normal Probability, Temperature, Bin 11
Probability
-2
-1
0
1
2
3
4
Residuals [°C]

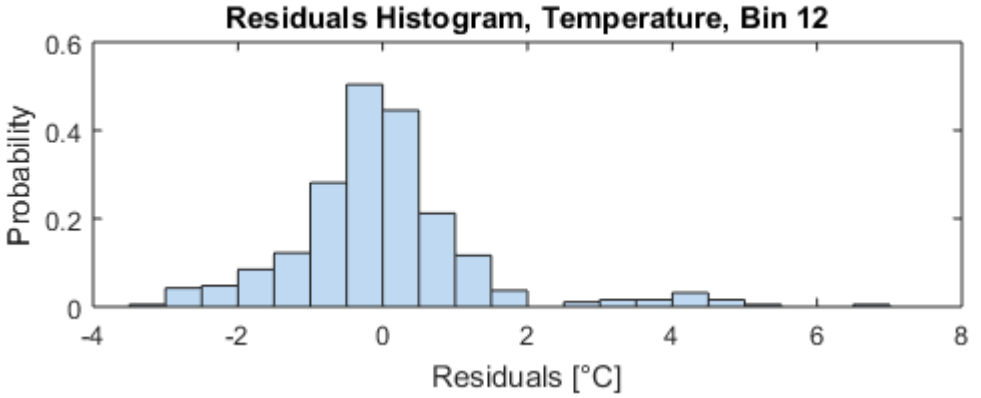
Residuals Histogram, Temperature, Bin 12
Probability
0.6
0.4
0.2
0
-4
-2
0
2
4
6
8
Residuals [°C]

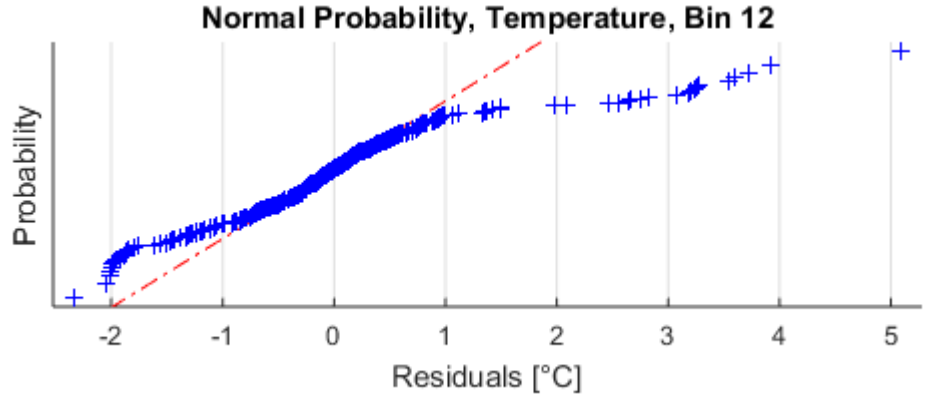
Normal Probability, Temperature, Bin 12
Probability
-2
-1
0
1
2
3
4
5
Residuals [°C]

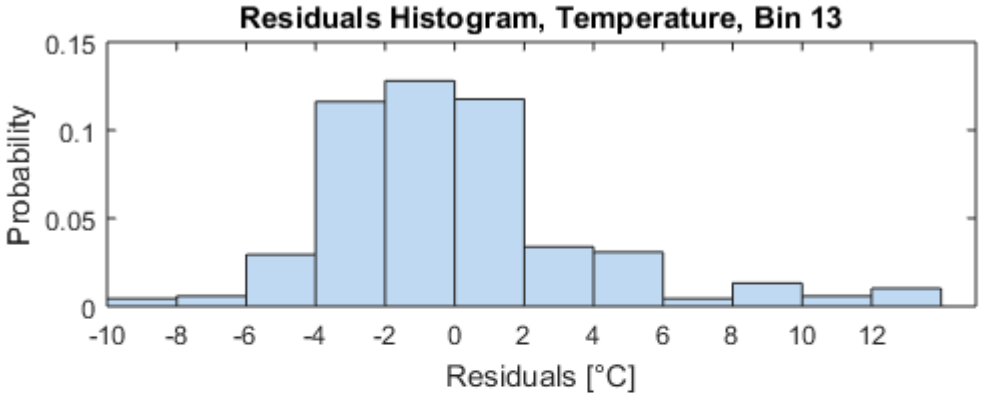
Residuals Histogram, Temperature, Bin 13
Probability
0.15
0.1
0.05
0
-10
-8
-6
-4
-2
0
2
4
6
8
10
12
Residuals [°C]

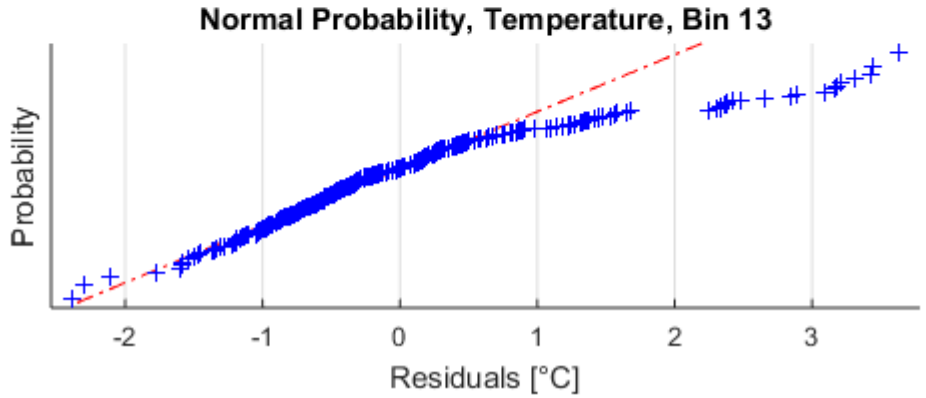
Normal Probability, Temperature, Bin 13
Probability
-2
-1
0
1
2
3
Residuals [°C]

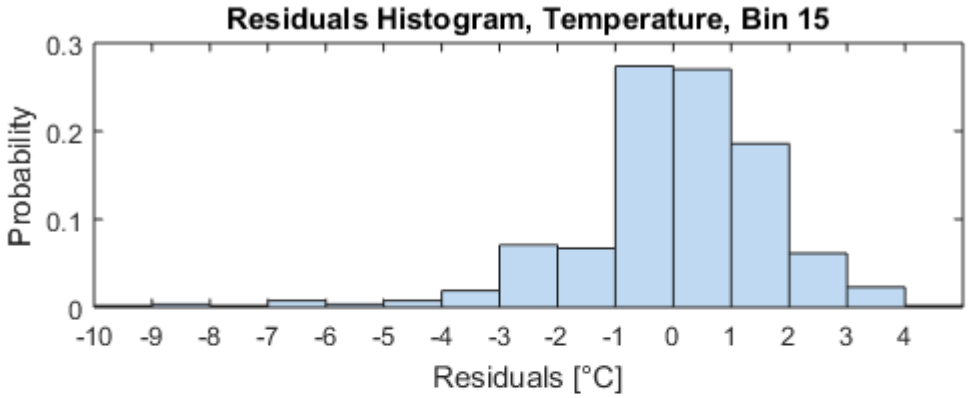
Residuals Histogram, Temperature, Bin 15
Probability
0.3
0.2
0.1
0
-10
-9
-8
-7
-6
-5
-4
-3
-2
-1
0
1
2
3
4
Residuals [°C]

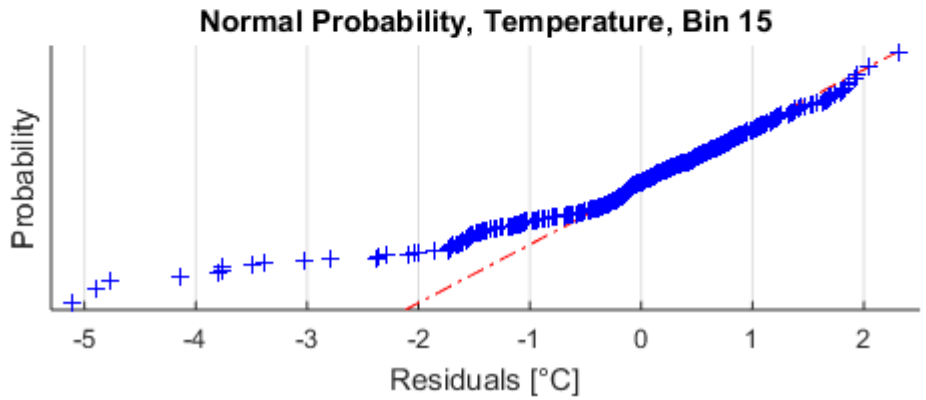
Normal Probability, Temperature, Bin 15
Probability
-5
-4
-3
-2
-1
0
1
2
Residuals [°C]

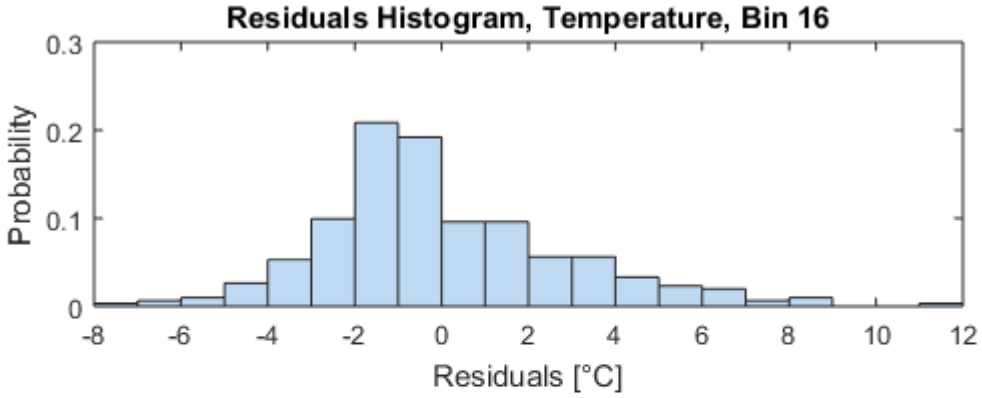
Residuals Histogram, Temperature, Bin 16
Probability
0.3
0.2
0.1
0
-8
-6
-4
-2
0
2
4
6
8
10
12
Residuals [°C]

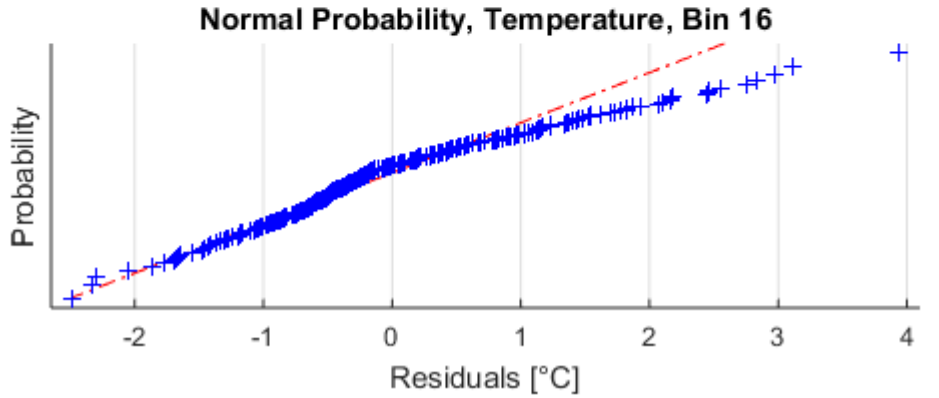
Normal Probability, Temperature, Bin 16
Probability
-2
-1
0
1
2
3
4
Residuals [°C]

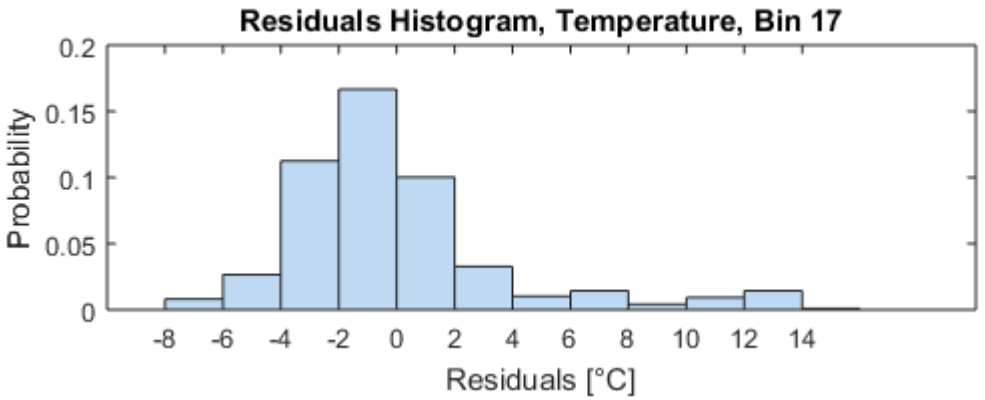
Residuals Histogram, Temperature, Bin 17
Probability
0.2
0.15
0.1
0.05
0
-8
-6
-4
-2
0
2
4
6
8
10
12
14
Residuals [°C]

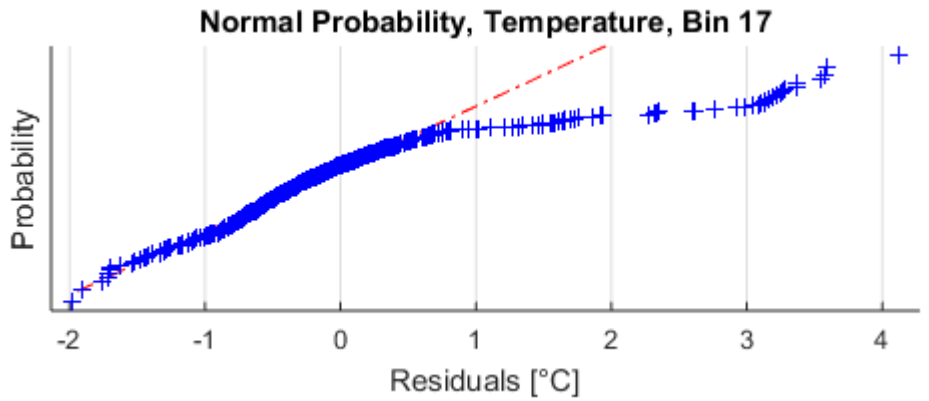
Normal Probability, Temperature, Bin 17
Probability
-2
-1
0
1
2
3
4
Residuals [°C]

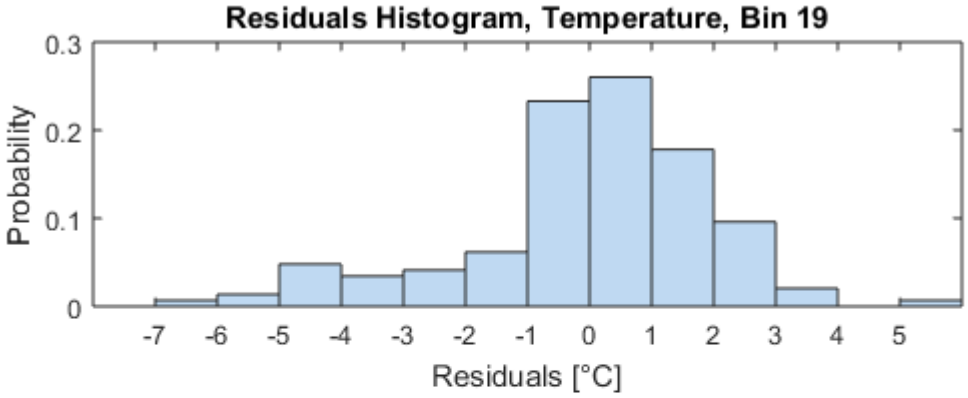
Residuals Histogram, Temperature, Bin 19
Probability
0.3
0.2
0.1
0
-7 -6 -5 -4 -3 -2 -1 0 1 2 3 4 5
Residuals [°C]

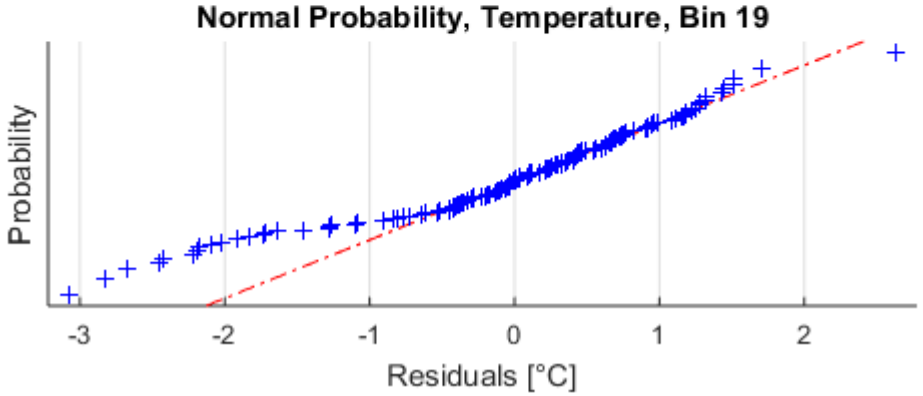
Normal Probability, Temperature, Bin 19
Probability
-3 -2 -1 0 1 2
Residuals [°C]

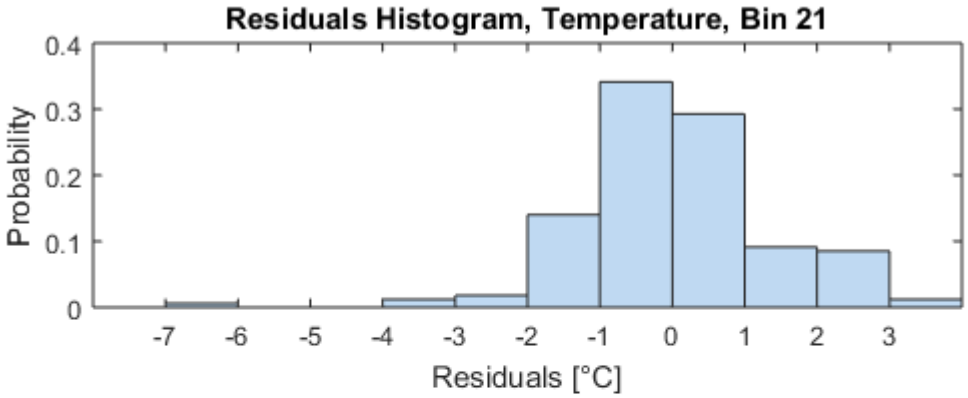
Residuals Histogram, Temperature, Bin 21
Probability
0.4
0.3
0.2
0.1
0
-7 -6 -5 -4 -3 -2 -1 0 1 2 3
Residuals [°C]

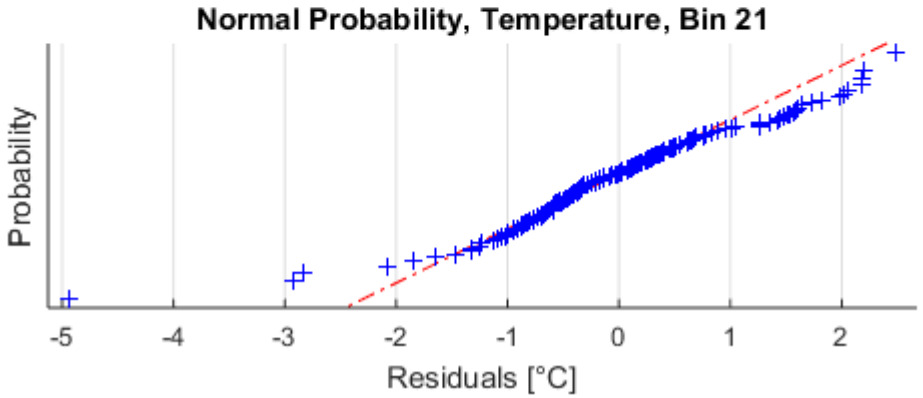
Normal Probability, Temperature, Bin 21
Probability
-5 -4 -3 -2 -1 0 1 2
Residuals [°C]

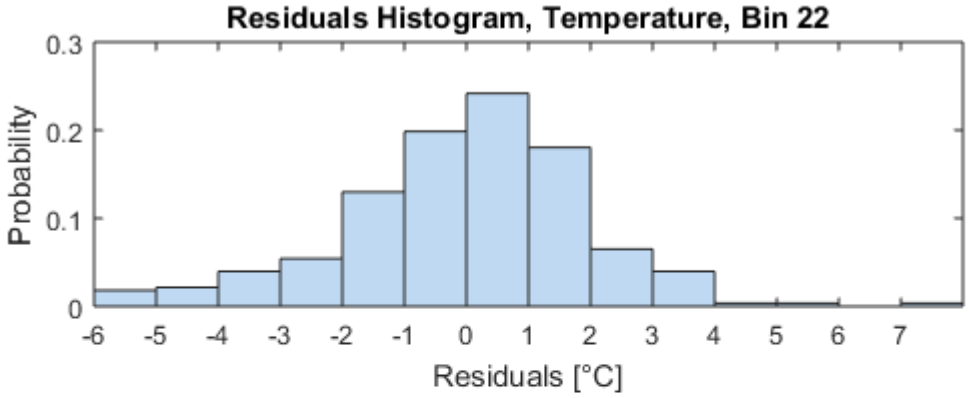
Residuals Histogram, Temperature, Bin 22
Probability
0.3
0.2
0.1
0
-6 -5 -4 -3 -2 -1 0 1 2 3 4 5 6 7
Residuals [°C]

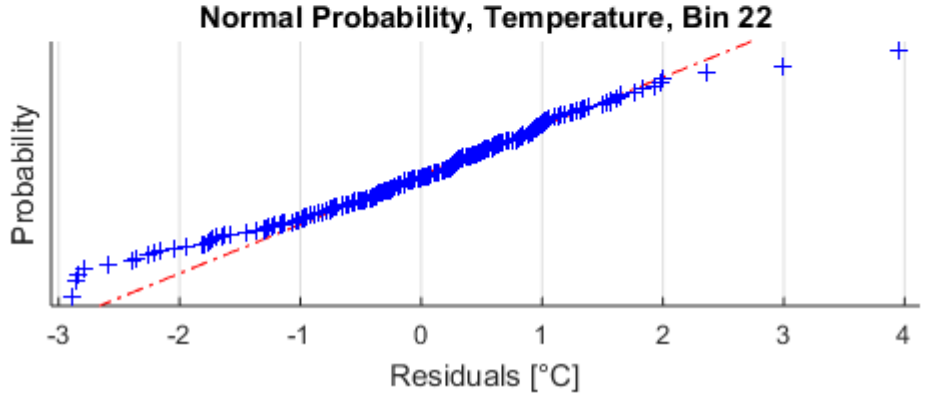
Normal Probability, Temperature, Bin 22
Probability
-3 -2 -1 0 1 2 3 4
Residuals [°C]

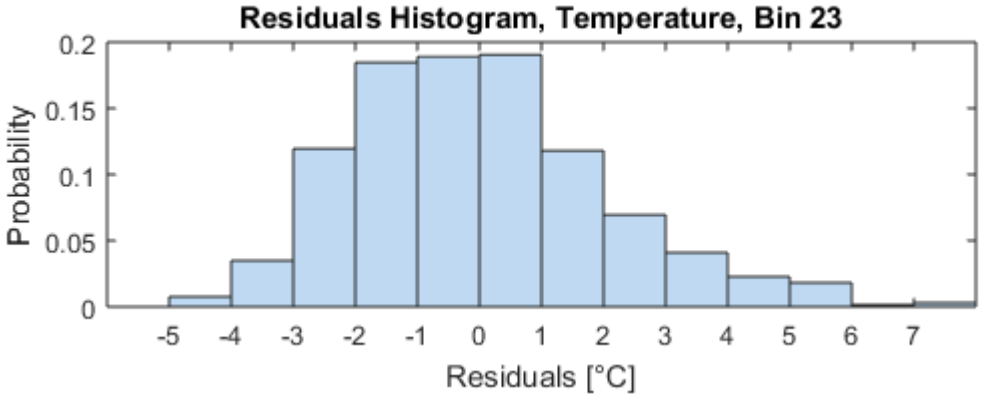
Residuals Histogram, Temperature, Bin 23
Probability
0.2
0.15
0.1
0.05
0
-5 -4 -3 -2 -1 0 1 2 3 4 5 6 7
Residuals [°C]

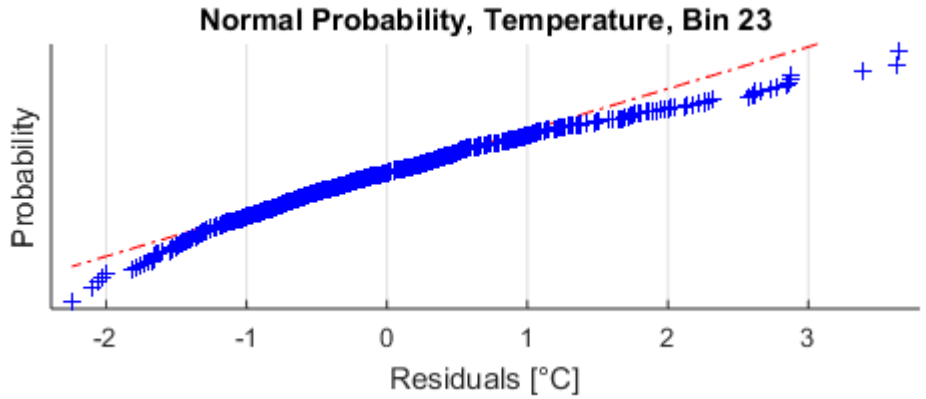
Normal Probability, Temperature, Bin 23
Probability
-2 -1 0 1 2 3
Residuals [°C]

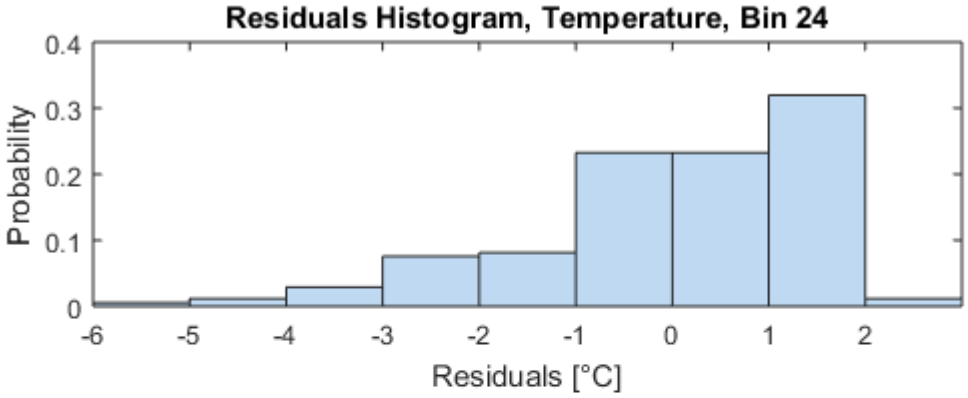
Residuals Histogram, Temperature, Bin 24
Probability
0.4
0.3
0.2
0.1
0
-6
-5
-4
-3
-2
-1
0
1
2
Residuals [°C]

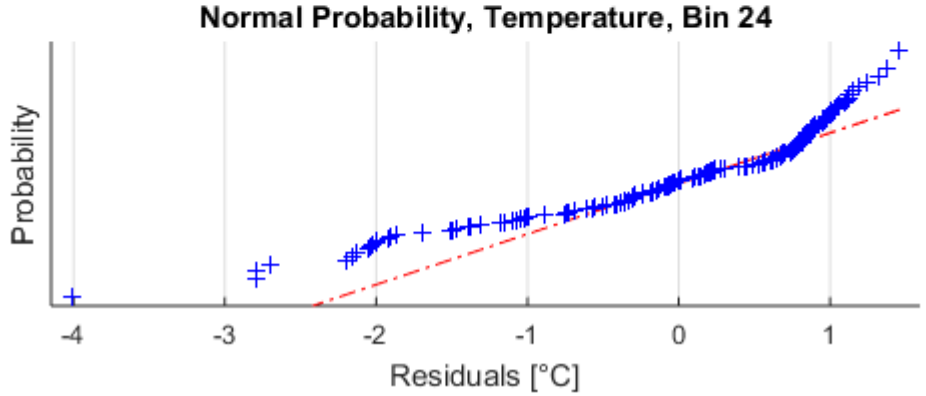
Normal Probability, Temperature, Bin 24
Probability
-4
-3
-2
-1
0
1
Residuals [°C]

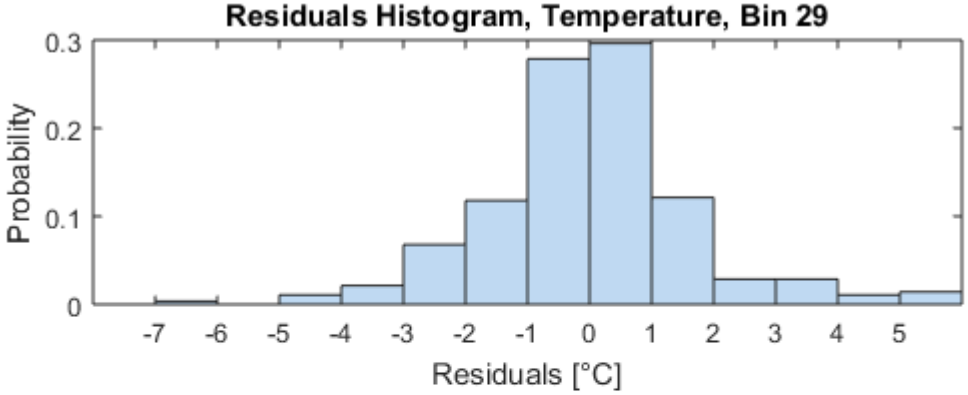
Residuals Histogram, Temperature, Bin 29
Probability
0.3
0.2
0.1
0
-7
-6
-5
-4
-3
-2
-1
0
1
2
3
4
5
Residuals [°C]

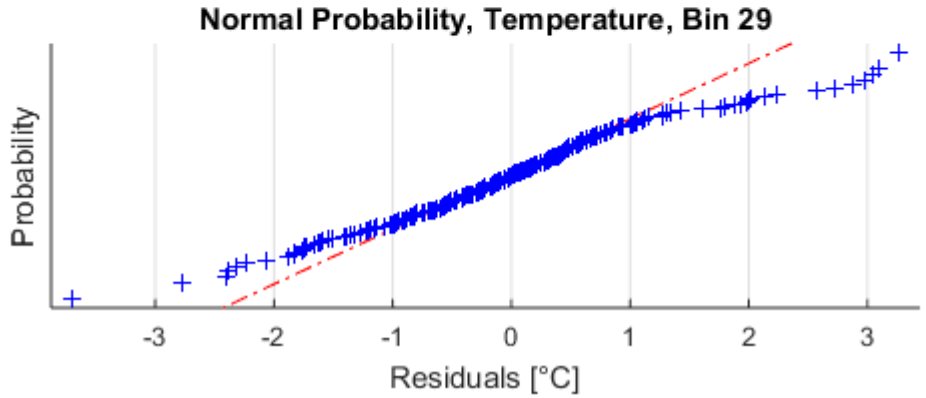
Normal Probability, Temperature, Bin 29
Probability
-3
-2
-1
0
1
2
3
Residuals [°C]

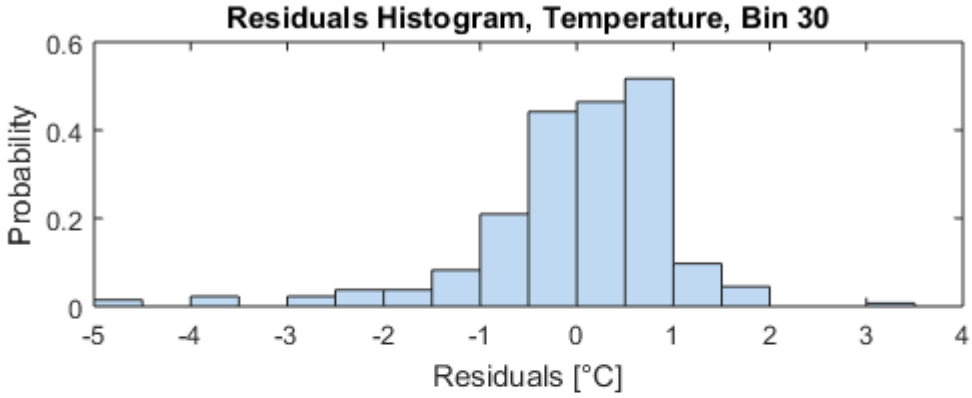
Residuals Histogram, Temperature, Bin 30
Probability
0.6
0.4
0.2
0
-5
-4
-3
-2
-1
0
1
2
3
4
Residuals [°C]

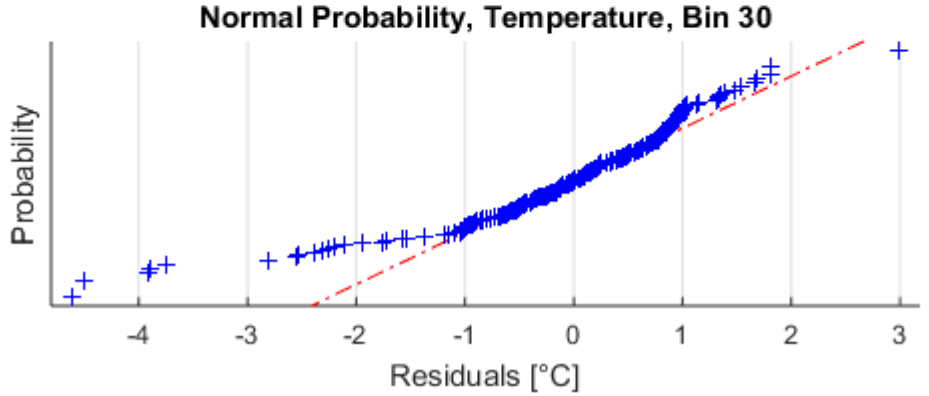
Normal Probability, Temperature, Bin 30
Probability
-4
-3
-2
-1
0
1
2
3
Residuals [°C]

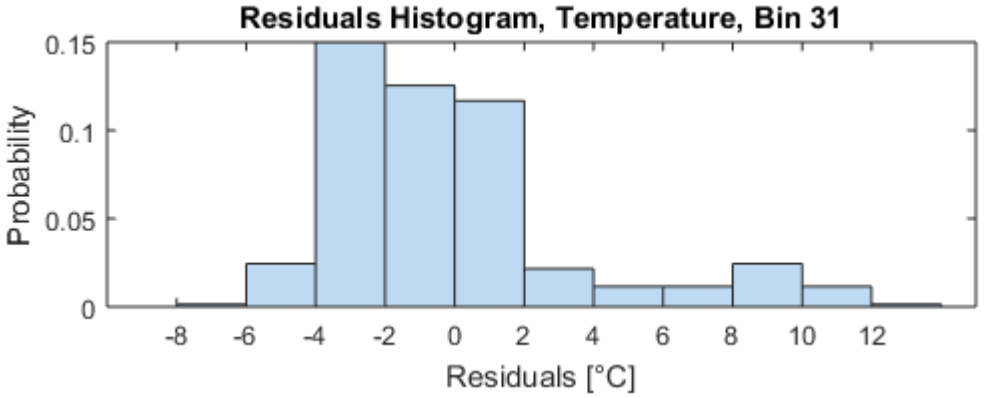
Residuals Histogram, Temperature, Bin 31
Probability
0.15
0.1
0.05
0
-8
-6
-4
-2
0
2
4
6
8
10
12
Residuals [°C]

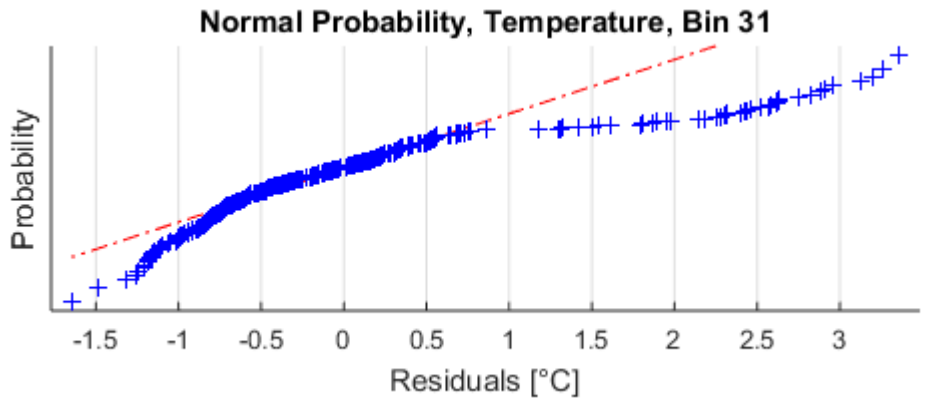
Normal Probability, Temperature, Bin 31
Probability
-1.5
-1
-0.5
0
0.5
1
1.5
2
2.5
3
Residuals [°C]

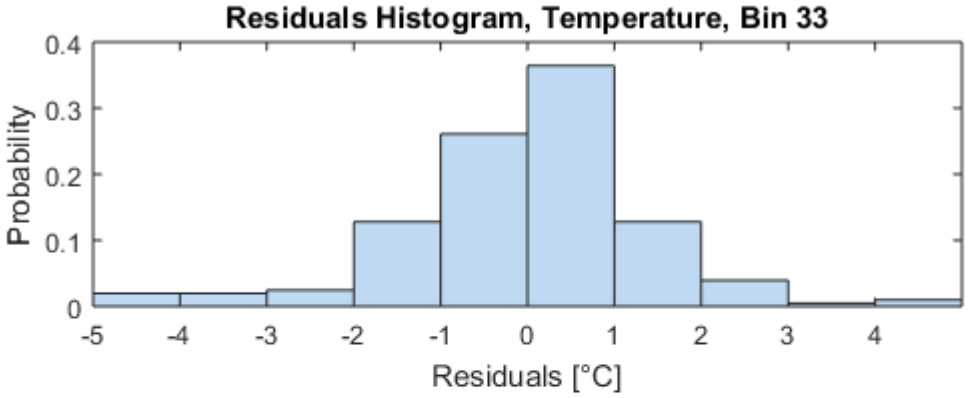
Residuals Histogram, Temperature, Bin 33
Probability
0.4
0.3
0.2
0.1
0
-5
-4
-3
-2
-1
0
1
2
3
4
Residuals [°C]

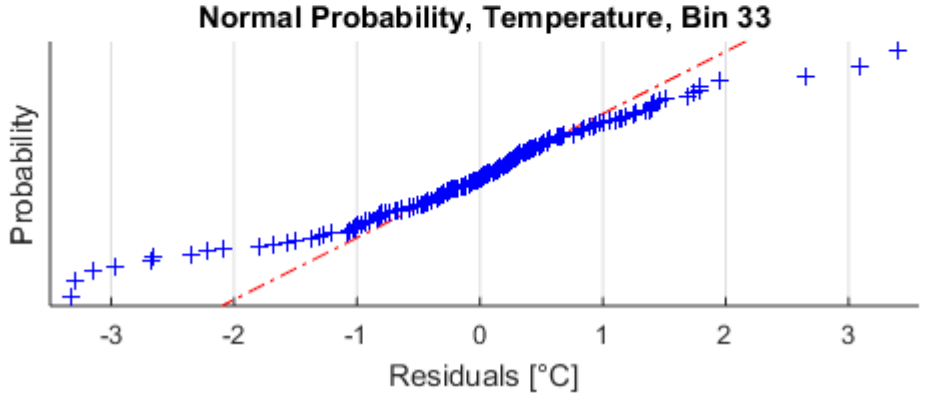
Normal Probability, Temperature, Bin 33
Probability
-3
-2
-1
0
1
2
3
Residuals [°C]

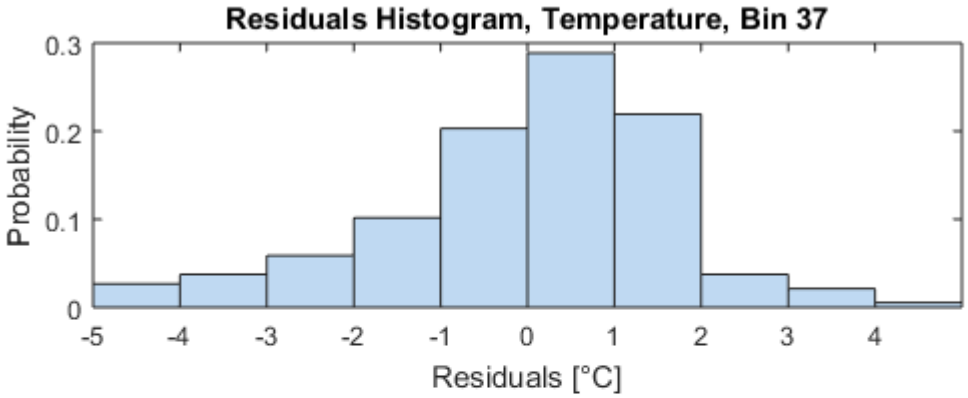
Residuals Histogram, Temperature, Bin 37
Probability
0.3
0.2
0.1
0
-5
-4
-3
-2
-1
0
1
2
3
4
Residuals [°C]

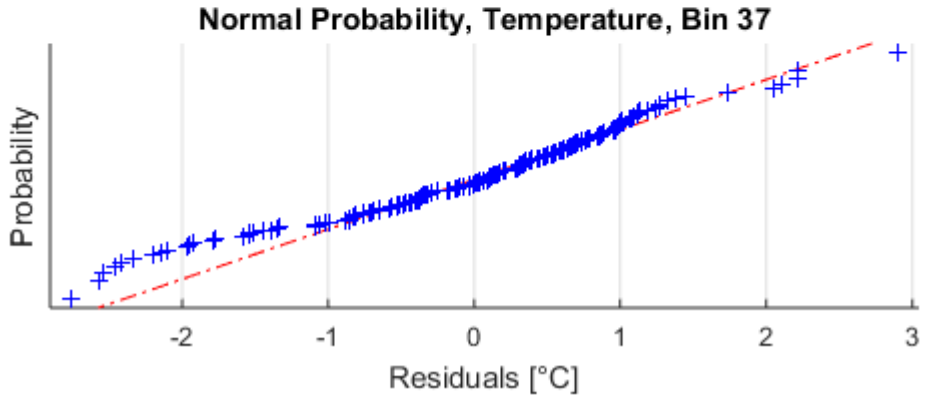
Normal Probability, Temperature, Bin 37
Probability
-2
-1
0
1
2
3
Residuals [°C]

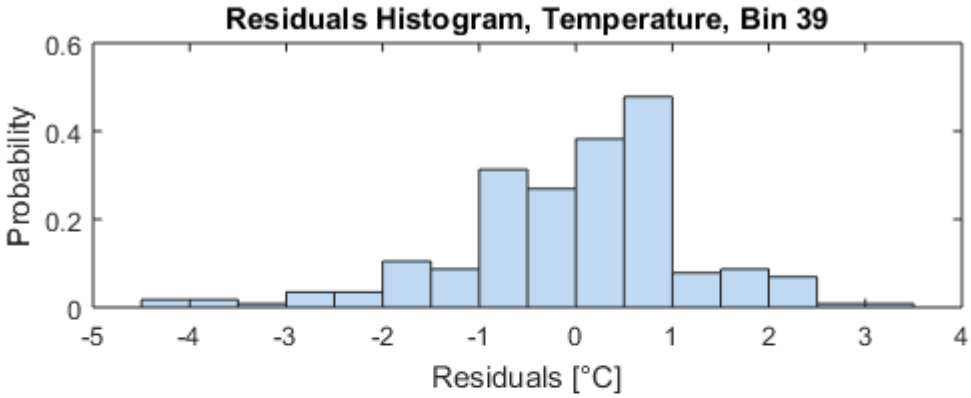
Residuals Histogram, Temperature, Bin 39
Probability
0.6
0.4
0.2
0
-5
-4
-3
-2
-1
0
1
2
3
4
Residuals [°C]

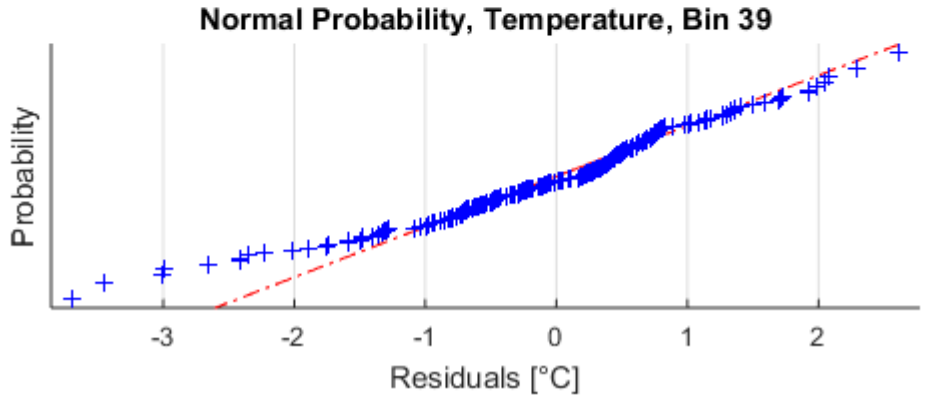
Normal Probability, Temperature, Bin 39
Probability
-3
-2
-1
0
1
2
Residuals [°C]

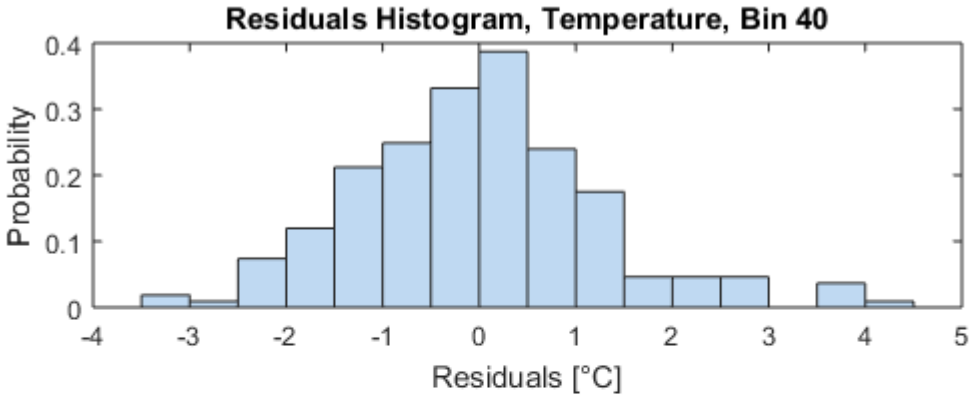
Residuals Histogram, Temperature, Bin 40
Probability
0.4
0.3
0.2
0.1
0
-4
-3
-2
-1
0
1
2
3
4
5
Residuals [°C]

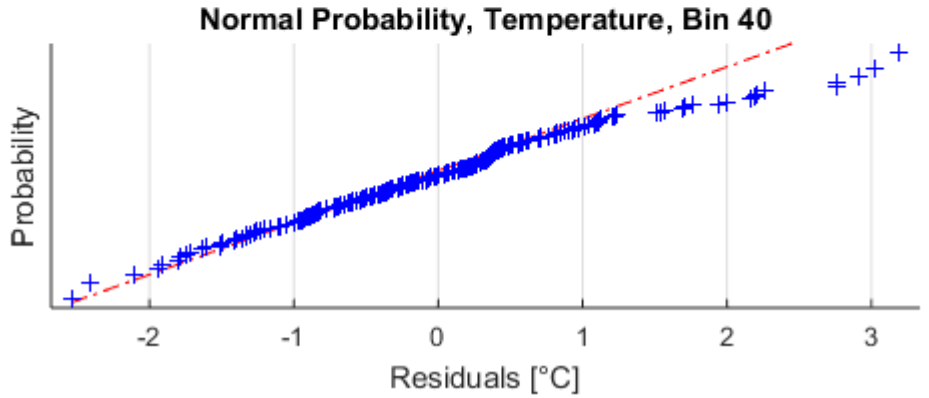
Normal Probability, Temperature, Bin 40
Probability
-2
-1
0
1
2
3
Residuals [°C]

Appendix G – Power prediction results

Nr.	RMSE [W]	MAD [W]	R^2 [-]	Rpearson [-]	Rspearman [-]	Irradiance [W/m²]	Ambient Temp. [°C]	Wind speed [m/s]	AOI [°]
12	23,164	15,661	0,828	0,910	0,812	Irr. 1			
13	6,963	1,404	0,845	0,920	0,818	Irr. 2		Wind speed 1	
14	8,870	3,275	0,754	0,869	0,840	Irr. 3			
15	4,145	1,287	0,958	0,979	0,976	Irr. 1			
16	6,667	2,821	0,935	0,967	0,969	Irr. 2	tamb 1	Wind speed 2	
17	7,077	2,645	0,753	0,868	0,908	Irr. 3			
18	33,208	9,512	0,765	0,876	0,904	Irr. 1			
19	3,992	1,084	0,946	0,973	0,929	Irr. 2		Wind speed 3	
20	2,486	1,929	0,918	0,958	0,920	Irr. 3			AOI 1
21	9,525	1,293	0,831	0,912	0,905	Irr. 1			
22	11,491	2,369	0,834	0,914	0,921	Irr. 2		Wind speed 1	
23	7,848	1,913	0,712	0,844	0,903	Irr. 3			
24	33,134	11,163	0,682	0,827	0,824	Irr. 1			
25	22,248	3,962	0,801	0,896	0,929	Irr. 2	tamb 2	Wind speed 2	
26	4,907	2,420	0,900	0,949	0,956	Irr. 3			
27	16,938	1,178	0,323	0,581	0,820	Irr. 1			
28	12,221	3,411	0,818	0,906	0,914	Irr. 2		Wind speed 3	
29	11,897	1,995	0,538	0,734	0,895	Irr. 3			
30	19,189	8,706	0,794	0,892	0,796	Irr. 1			
31	6,722	1,372	0,836	0,915	0,942	Irr. 2		Wind speed 1	
32	6,519	3,697	0,140	0,418	0,616	Irr. 3			
33	3,828	1,315	0,954	0,977	0,988	Irr. 1			
34	7,052	1,792	0,910	0,954	0,953	Irr. 2	tamb 1	Wind speed 2	
35						Irr. 3			
36	27,969	10,710	0,838	0,916	0,904	Irr. 1			
37	7,804	0,980	0,821	0,906	0,978	Irr. 2		Wind speed 3	
38	1,656	0,776	0,876	0,939	0,946	Irr. 3			AOI 2
39	6,798	0,614	0,935	0,967	0,983	Irr. 1			
40	7,012	1,155	0,924	0,962	0,970	Irr. 2		Wind speed 1	
41						Irr. 3			
42	25,484	6,909	0,774	0,883	0,761	Irr. 1			
43	10,763	1,719	0,917	0,958	0,980	Irr. 2	tamb 2	Wind speed 2	
44	3,083	0,819	0,381	0,629	0,787	Irr. 3			
45	14,230	7,396	0,772	0,884	0,888	Irr. 1			
46	7,513	1,214	0,881	0,940	0,934	Irr. 2		Wind speed 3	
47						Irr. 3			
48						Irr. 1			
49	4,503	2,403	0,929	0,965	0,977	Irr. 2		Wind speed 1	
50	6,374	1,010	-0,127	0,117	0,283	Irr. 3			
51	8,308	0,978	0,873	0,935	0,954	Irr. 1			
52	2,776	0,499	0,936	0,968	0,973	Irr. 2	tamb 1	Wind speed 2	
53						Irr. 3			
54						Irr. 1			
55	4,295	0,744	0,940	0,970	0,987	Irr. 2		Wind speed 3	
56						Irr. 3			AOI 3
57	2,163	0,386	0,995	0,998	0,991	Irr. 1			
58	3,774	0,470	0,997	0,999	1,000	Irr. 2		Wind speed 1	
59						Irr. 3			
60						Irr. 1			
61	4,812	0,976	0,972	0,986	0,987	Irr. 2	tamb 2	Wind speed 2	
62	2,660	0,441	0,767	0,882	0,916	Irr. 3			
63	4,331	0,172	0,986	0,994	1,000	Irr. 1			
64	3,546	0,597	0,999	1,000	1,000	Irr. 2		Wind speed 3	
65						Irr. 3			

Table 30 Statistical parameters for power prediction, ranges 12 to 65 (own table)

Appendix H – Distribution of power residuals

(Samples that reach the minimum required sample size of 138 data points, own figures)

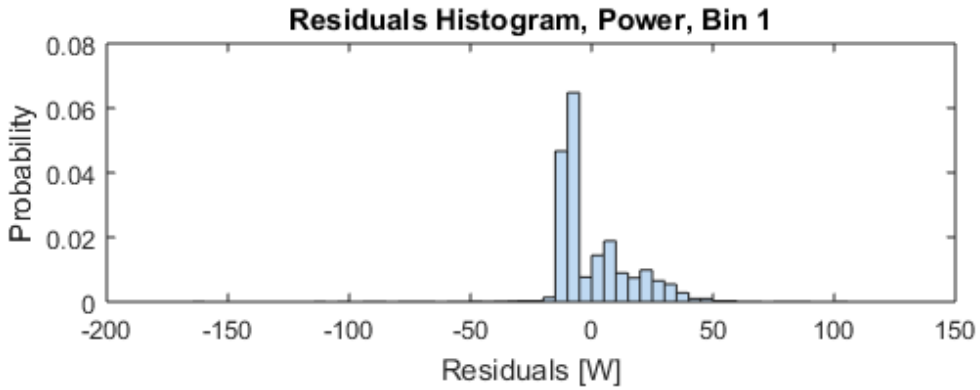

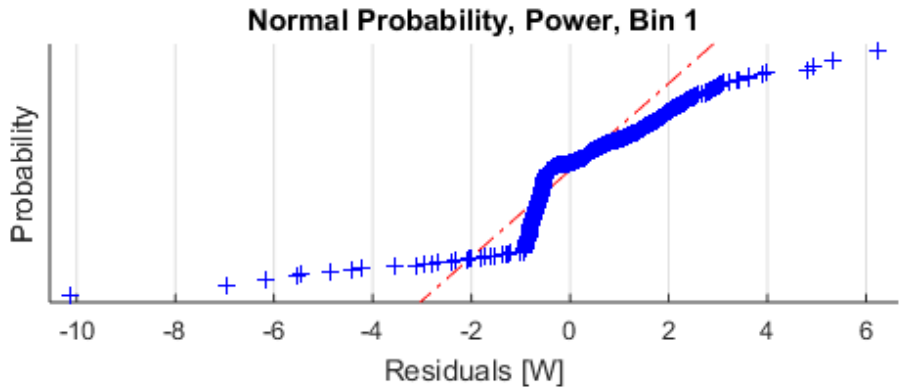

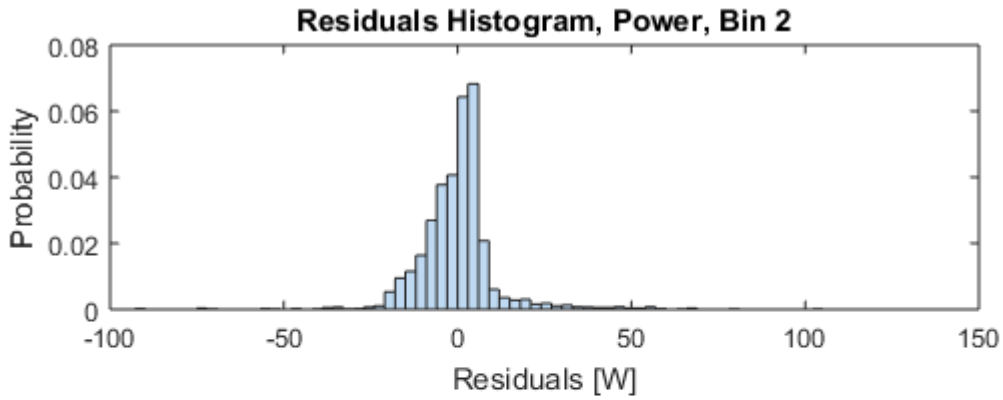

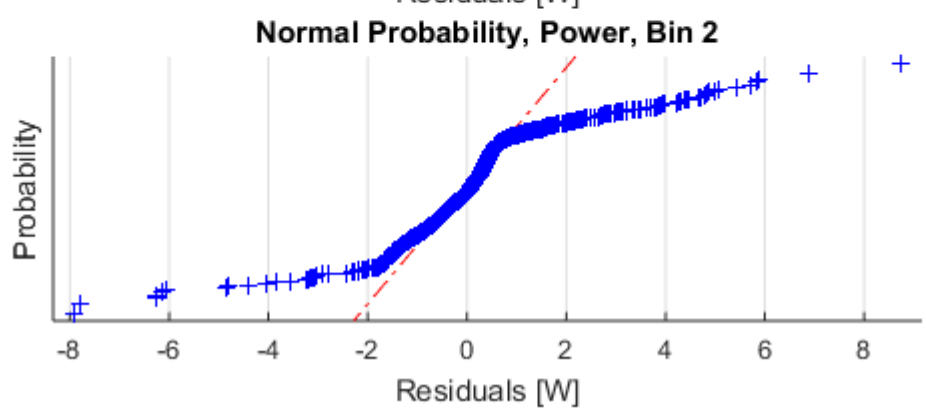

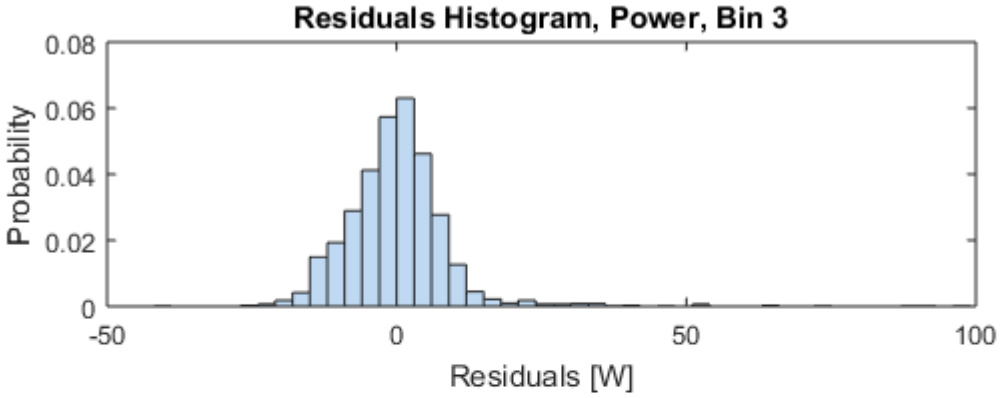
Residuals Histogram, Power, Bin 3
Probability
0.08
0.06
0.04
0.02
0
-50
0
50
100
Residuals [W]

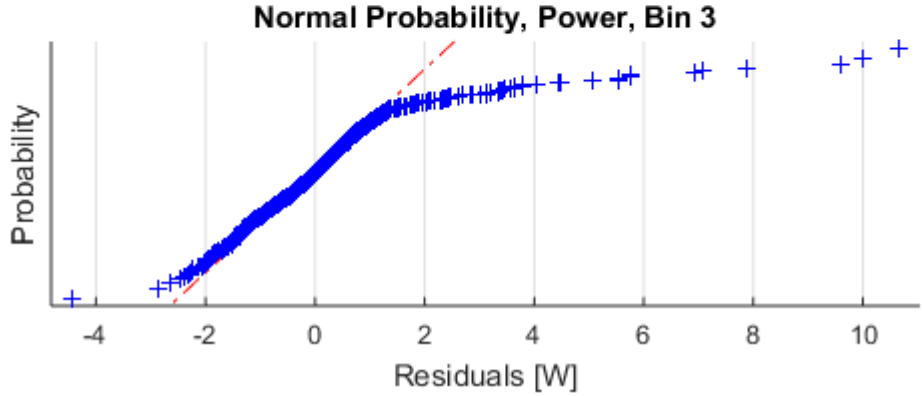
Normal Probability, Power, Bin 3
Probability
-4
-2
0
2
4
6
8
10
Residuals [W]

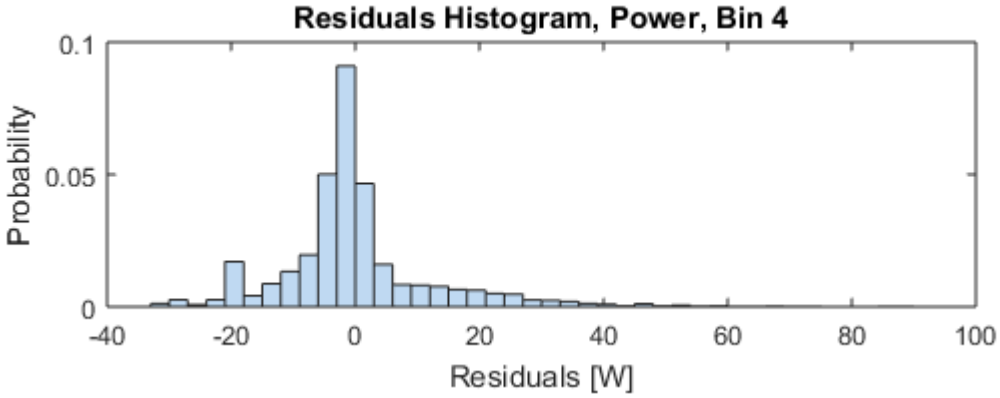
Residuals Histogram, Power, Bin 4
Probability
0.1
0.05
0
-40
-20
0
20
40
60
80
100
Residuals [W]

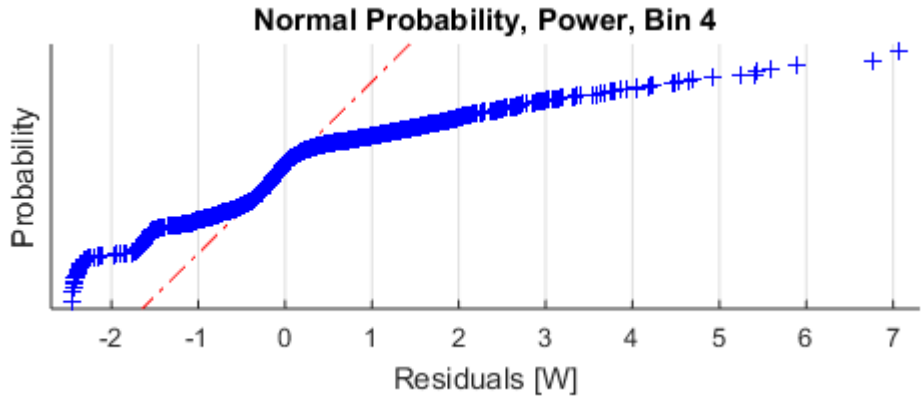
Normal Probability, Power, Bin 4
Probability
-2
-1
0
1
2
3
4
5
6
7
Residuals [W]

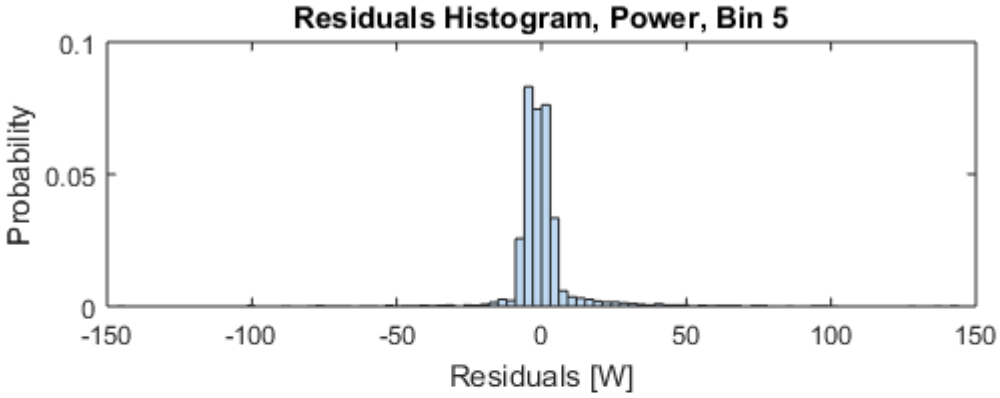
Residuals Histogram, Power, Bin 5
Probability
0.1
0.05
0
-150
-100
-50
0
50
100
150
Residuals [W]

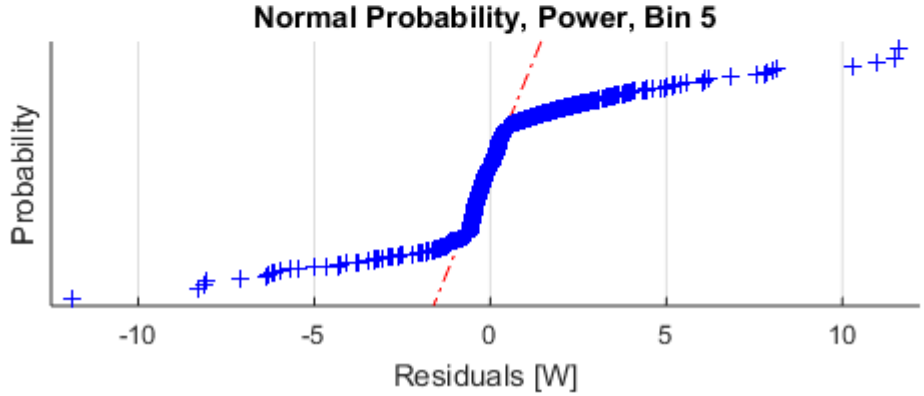
Normal Probability, Power, Bin 5
Probability
-10
-5
0
5
10
Residuals [W]

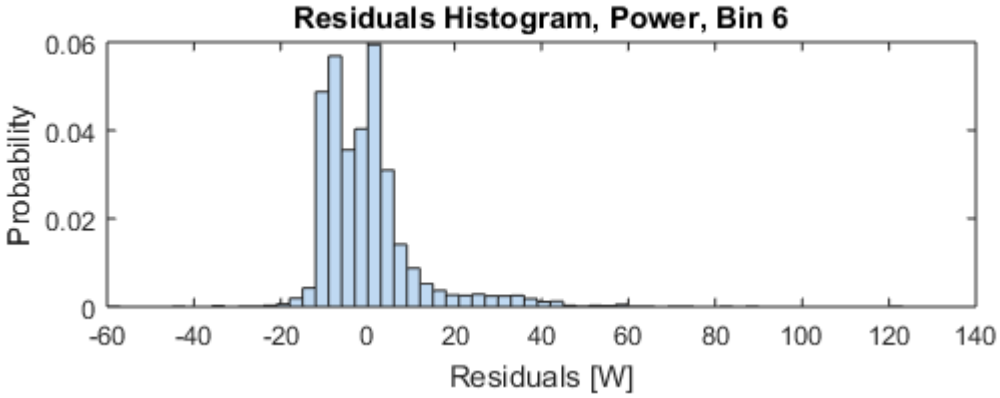
Residuals Histogram, Power, Bin 6
Probability
0.06
0.04
0.02
0
-60
-40
-20
0
20
40
60
80
100
120
140
Residuals [W]

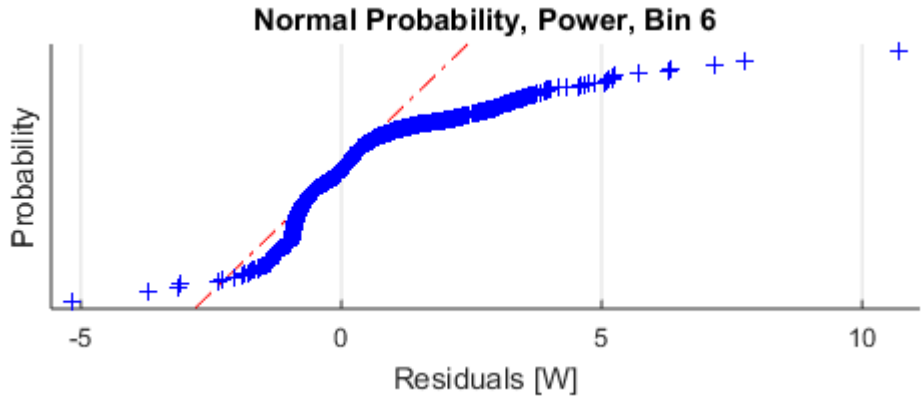
Normal Probability, Power, Bin 6
Probability
-5
0
5
10
Residuals [W]

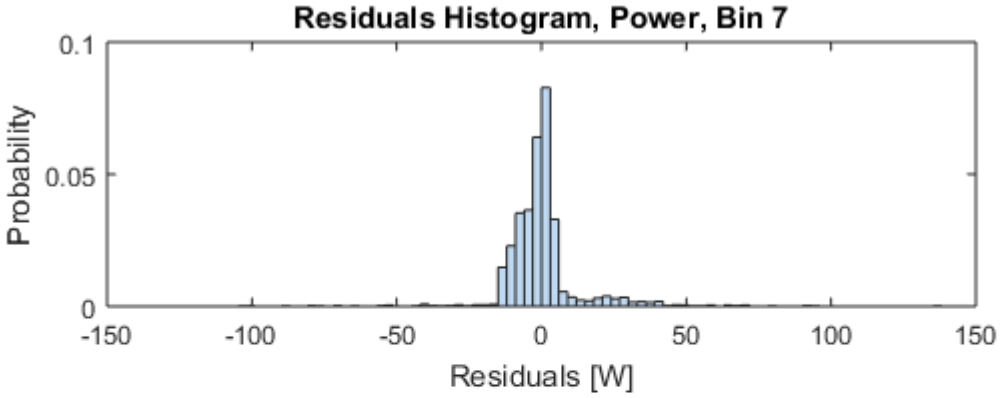
Residuals Histogram, Power, Bin 7
Probability
0.1
0.05
0
-150
-100
-50
0
50
100
150
Residuals [W]

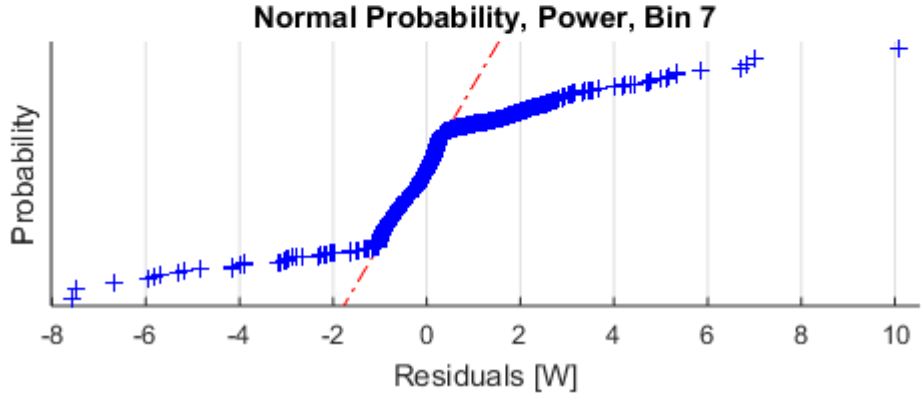
Normal Probability, Power, Bin 7
Probability
-8
-6
-4
-2
0
2
4
6
8
10
Residuals [W]

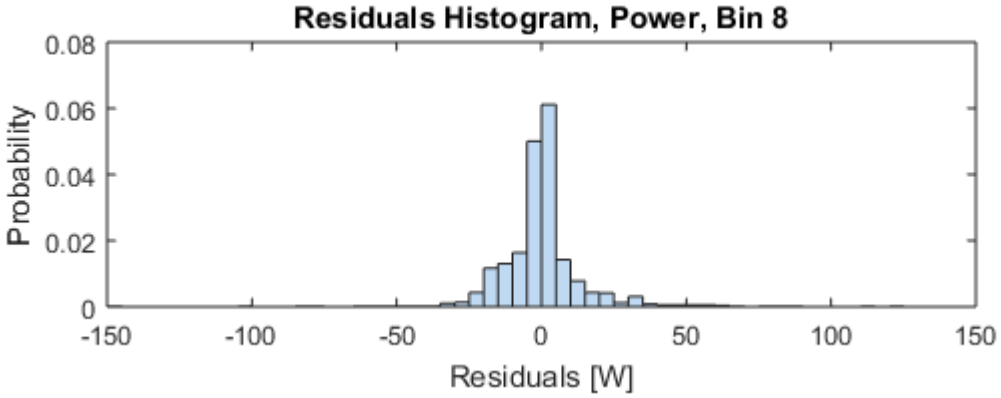
Residuals Histogram, Power, Bin 8
Probability
0.08
0.06
0.04
0.02
0
-150
-100
-50
0
50
100
150
Residuals [W]

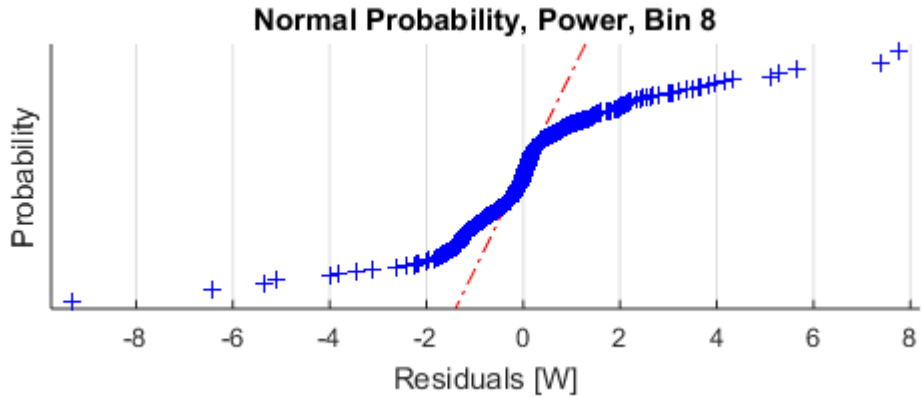
Normal Probability, Power, Bin 8
Probability
-8
-6
-4
-2
0
2
4
6
8
Residuals [W]

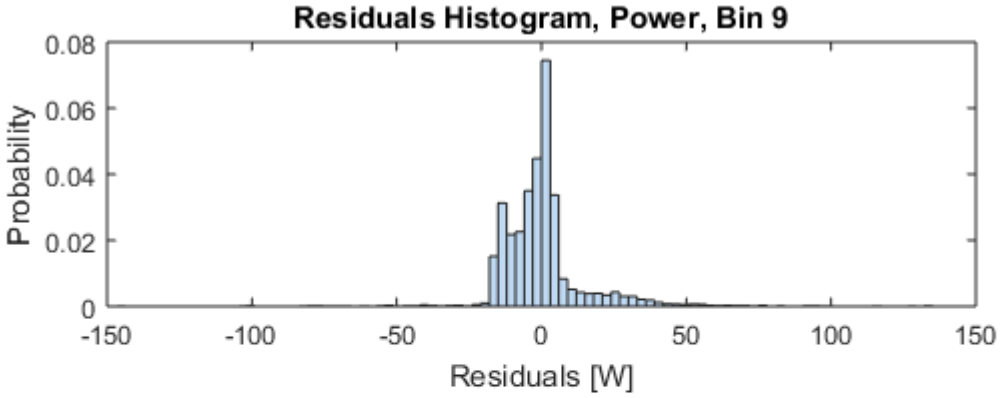
Residuals Histogram, Power, Bin 9
Probability
0.08
0.06
0.04
0.02
0
-150
-100
-50
0
50
100
150
Residuals [W]

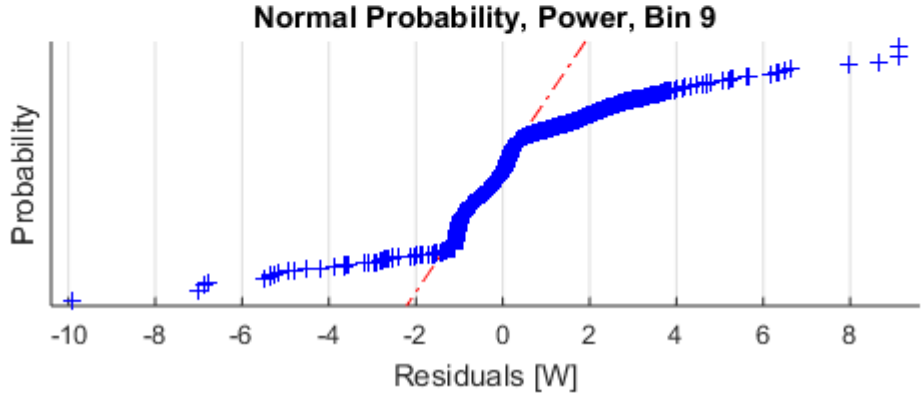
Normal Probability, Power, Bin 9
Probability
-10
-8
-6
-4
-2
0
2
4
6
8
Residuals [W]

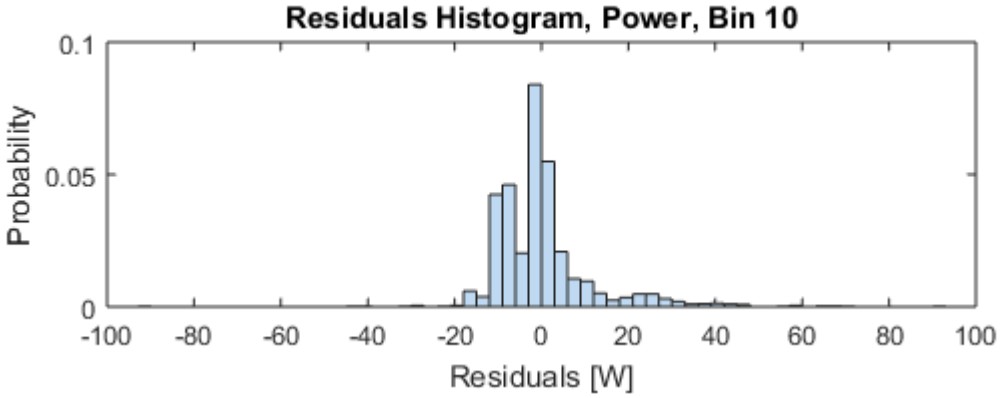
Residuals Histogram, Power, Bin 10
Probability
0.1
0.05
0
-100
-80
-60
-40
-20
0
20
40
60
80
100
Residuals [W]

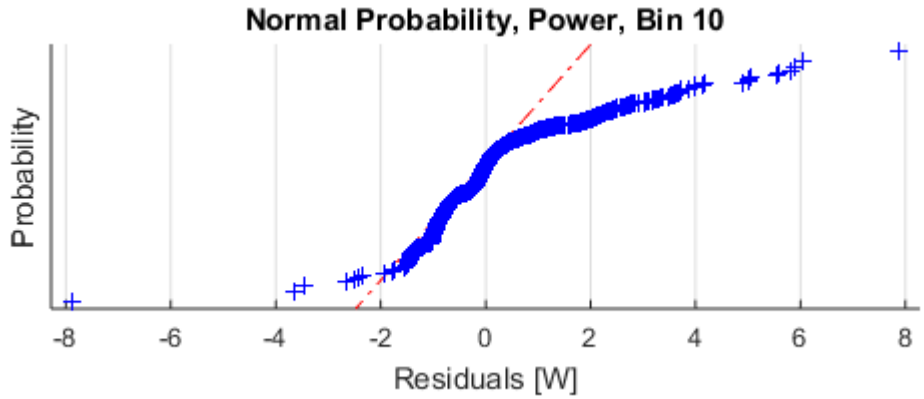
Normal Probability, Power, Bin 10
Probability
-8
-6
-4
-2
0
2
4
6
8
Residuals [W]

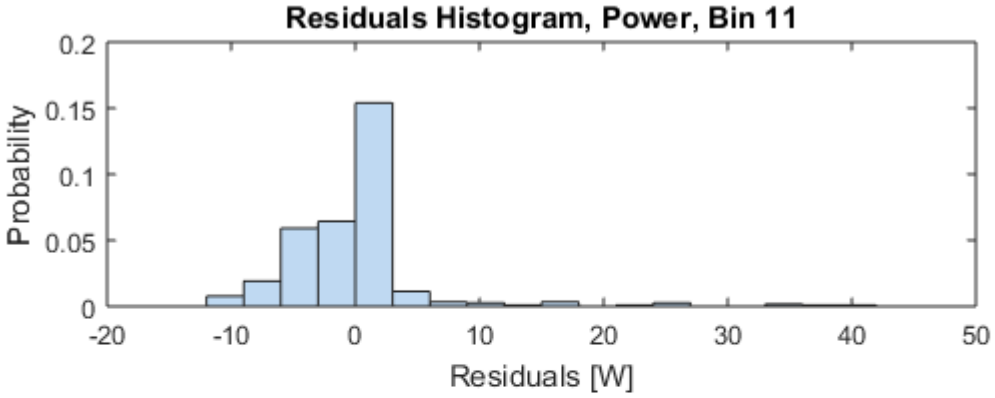
Residuals Histogram, Power, Bin 11
Probability
0.2
0.15
0.1
0.05
0
-20
-10
0
10
20
30
40
50
Residuals [W]

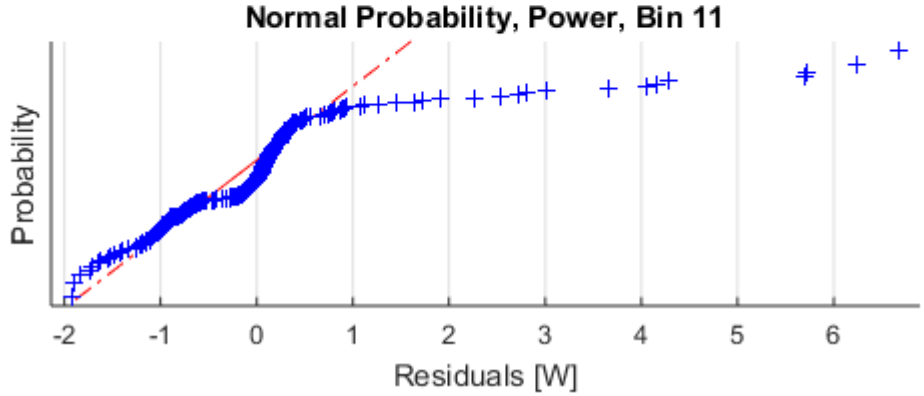
Normal Probability, Power, Bin 11
Probability
-2
-1
0
1
2
3
4
5
6
Residuals [W]

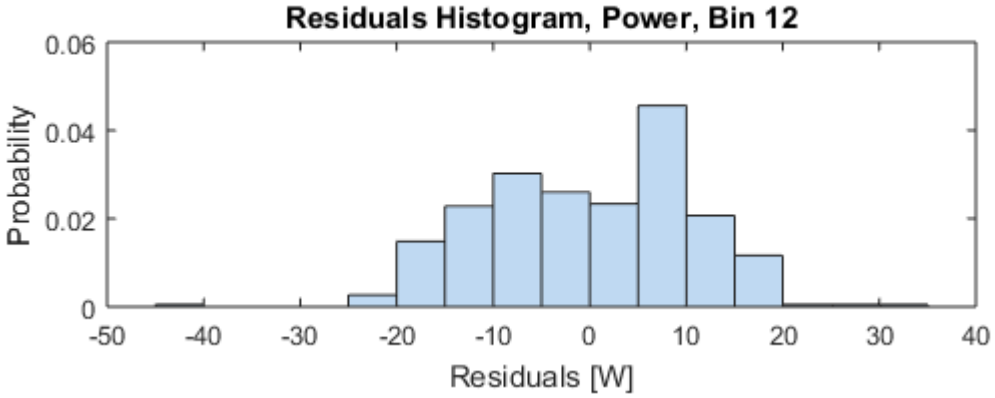
Residuals Histogram, Power, Bin 12
Probability
0.06
0.04
0.02
0
-50
-40
-30
-20
-10
0
10
20
30
40
Residuals [W]

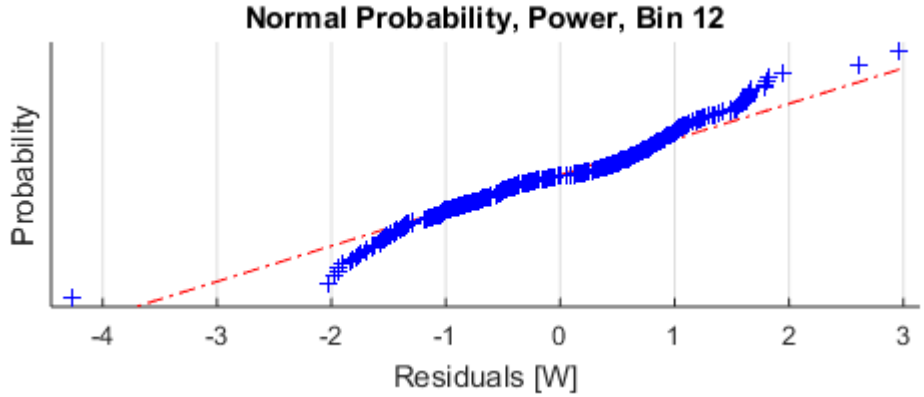
Normal Probability, Power, Bin 12
Probability
-4
-3
-2
-1
0
1
2
3
Residuals [W]

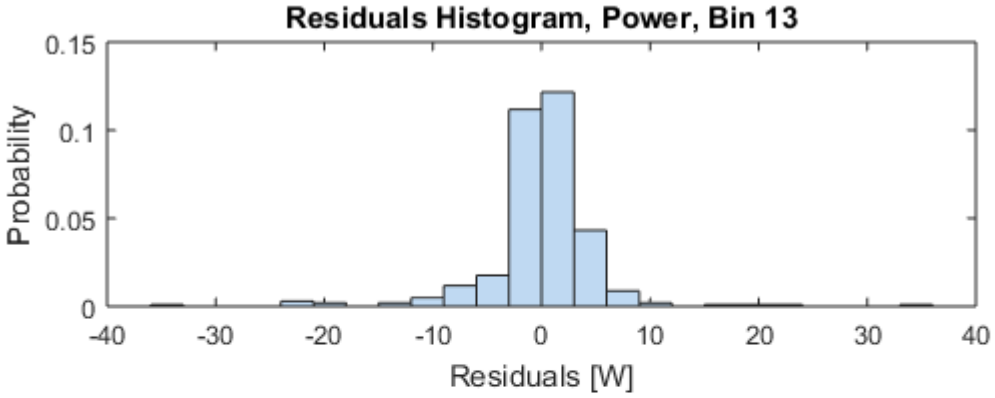
Residuals Histogram, Power, Bin 13
Probability
0.15
0.1
0.05
0
-40
-30
-20
-10
0
10
20
30
40
Residuals [W]

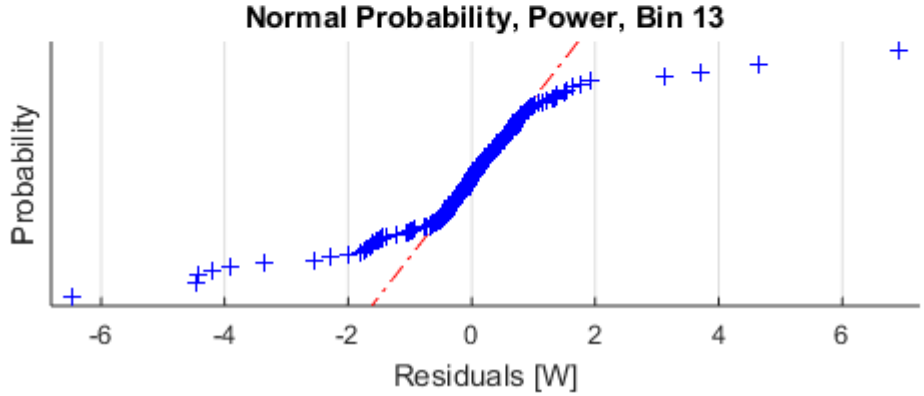
Normal Probability, Power, Bin 13
Probability
-6
-4
-2
0
2
4
6
Residuals [W]

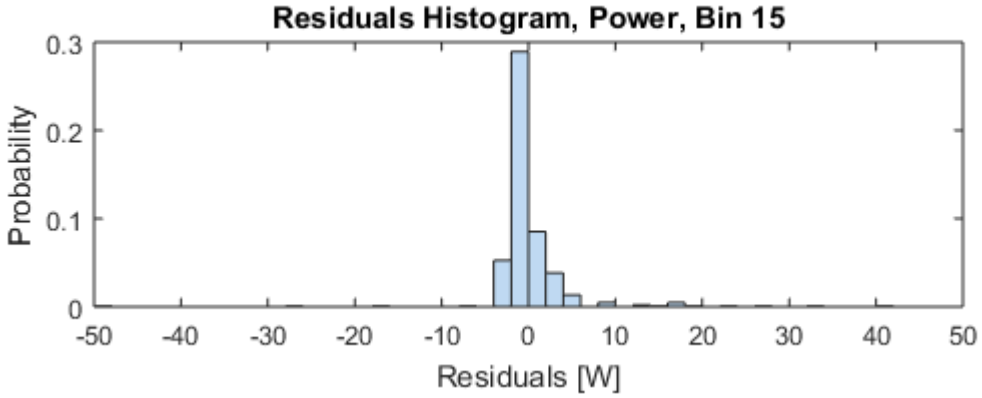
Residuals Histogram, Power, Bin 15
Probability
0.3
0.2
0.1
0
-50
-40
-30
-20
-10
0
10
20
30
40
50
Residuals [W]

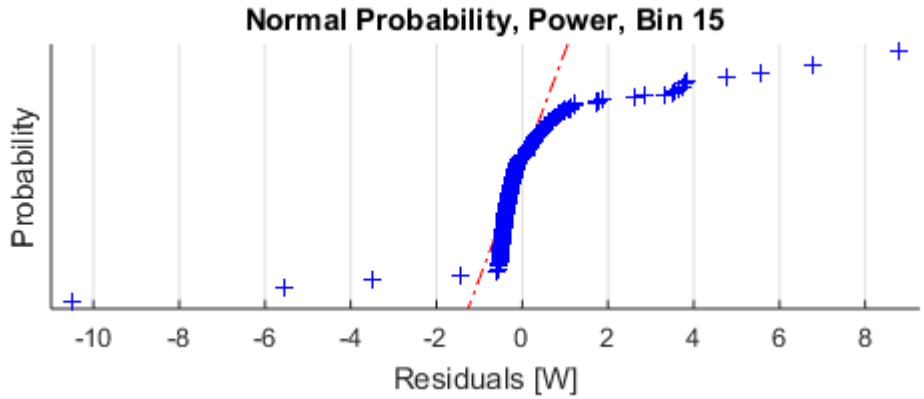
Normal Probability, Power, Bin 15
Probability
-10
-8
-6
-4
-2
0
2
4
6
8
Residuals [W]

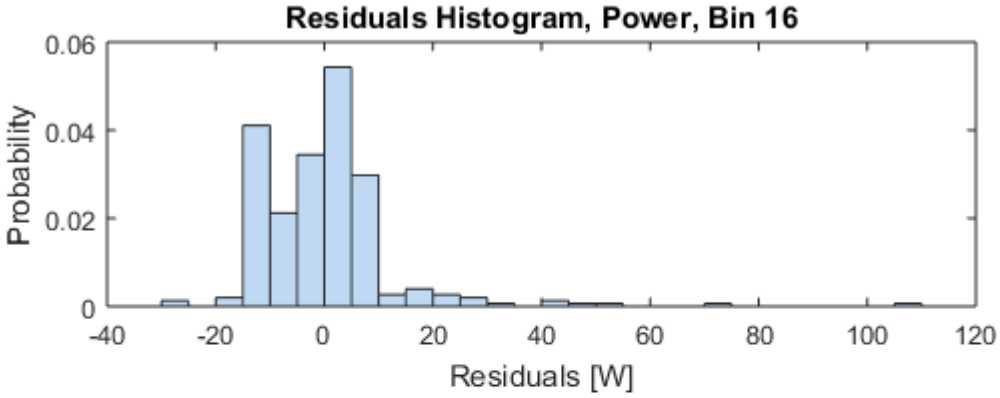
Residuals Histogram, Power, Bin 16
Probability
0.06
0.04
0.02
0
-40
-20
0
20
40
60
80
100
120
Residuals [W]

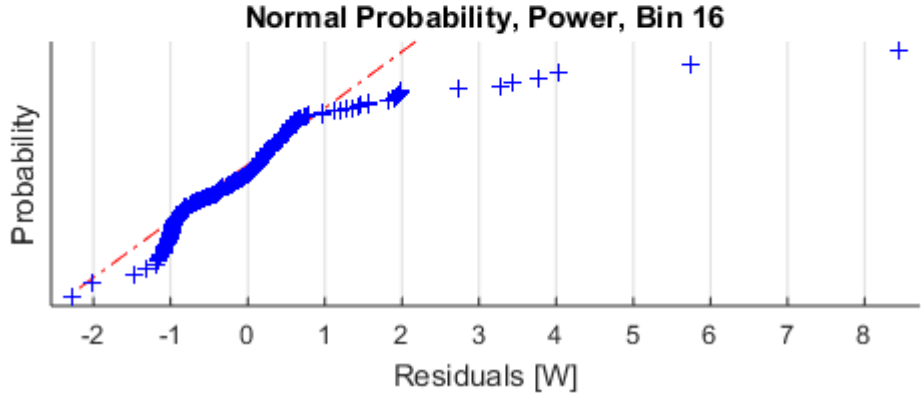
Normal Probability, Power, Bin 16
Probability
-2
-1
0
1
2
3
4
5
6
7
8
Residuals [W]

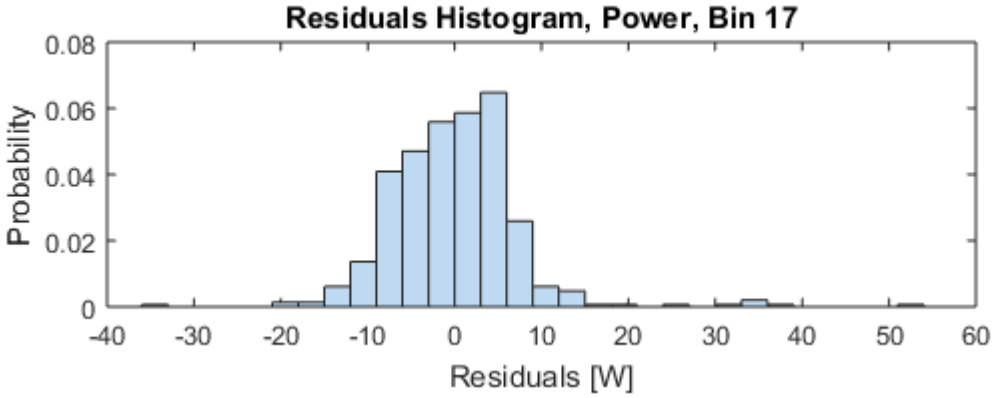
Residuals Histogram, Power, Bin 17
Probability
0.08
0.06
0.04
0.02
0
-40
-30
-20
-10
0
10
20
30
40
50
60
Residuals [W]

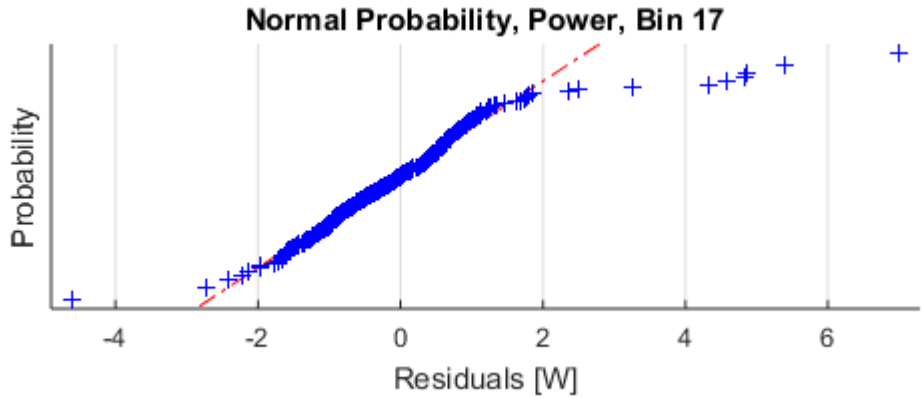
Normal Probability, Power, Bin 17
Probability
-4
-2
0
2
4
6
Residuals [W]

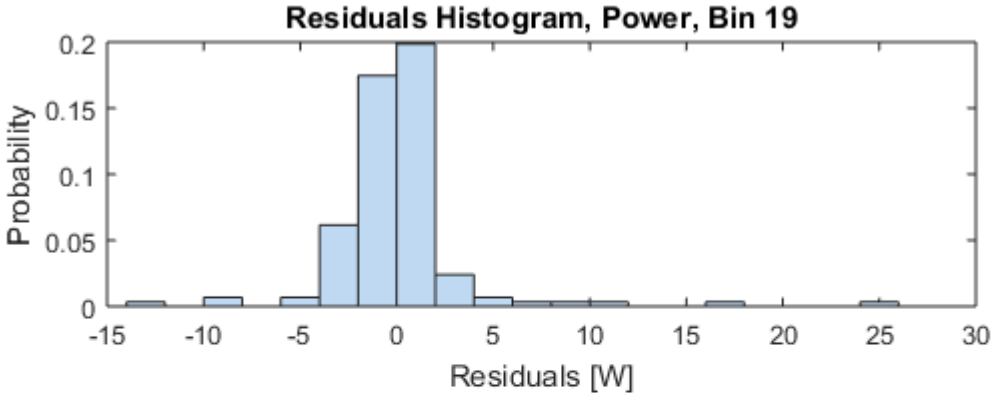
Residuals Histogram, Power, Bin 19
Probability
0.2
0.15
0.1
0.05
0
-15
-10
-5
0
5
10
15
20
25
30
Residuals [W]

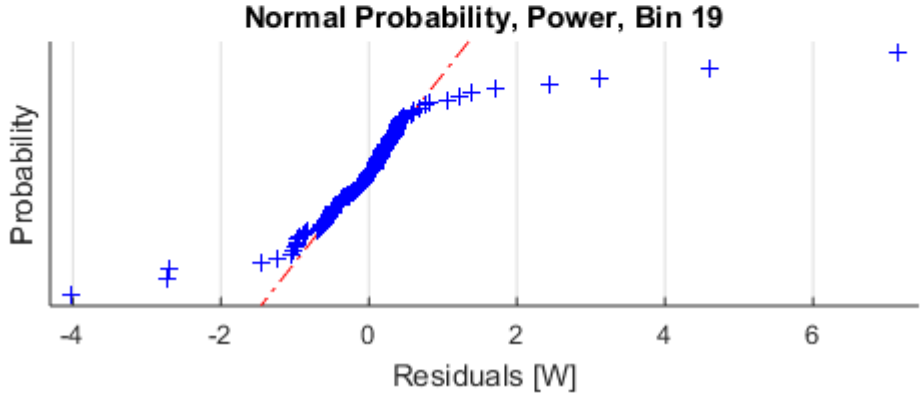
Normal Probability, Power, Bin 19
Probability
-4
-2
0
2
4
6
Residuals [W]

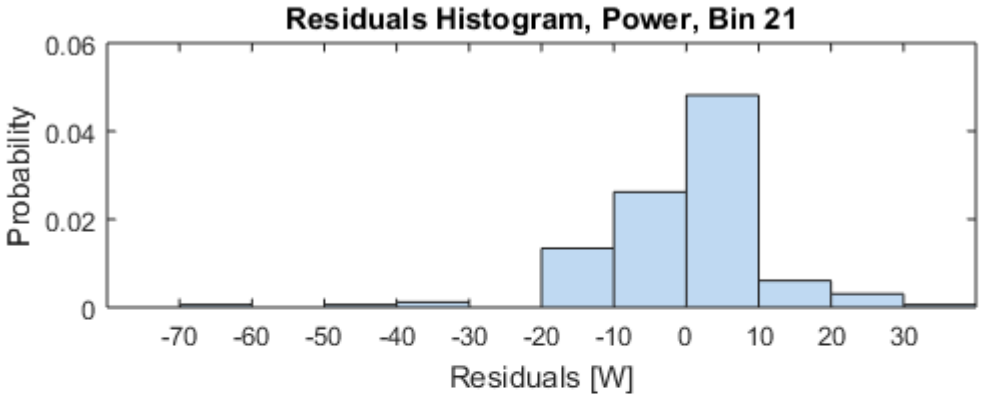
Residuals Histogram, Power, Bin 21
Probability
0.06
0.04
0.02
0
-70
-60
-50
-40
-30
-20
-10
0
10
20
30
Residuals [W]

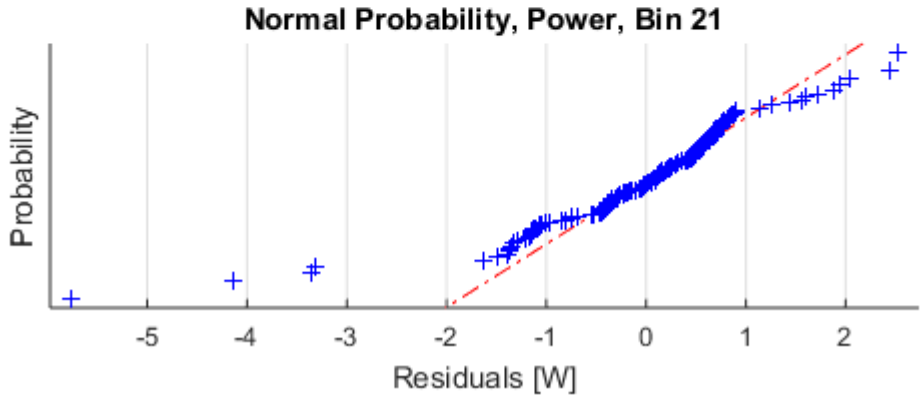
Normal Probability, Power, Bin 21
Probability
-5
-4
-3
-2
-1
0
1
2
Residuals [W]

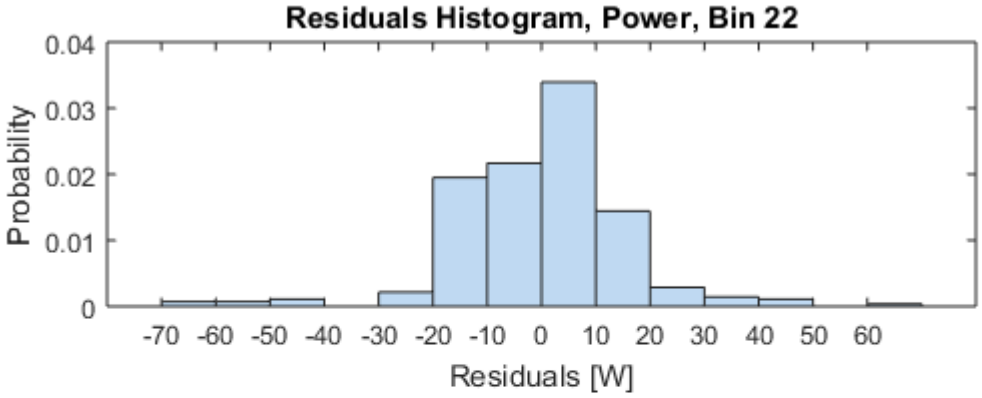
Residuals Histogram, Power, Bin 22
Probability
0.04
0.03
0.02
0.01
0
-70 -60 -50 -40 -30 -20 -10 0 10 20 30 40 50 60
Residuals [W]

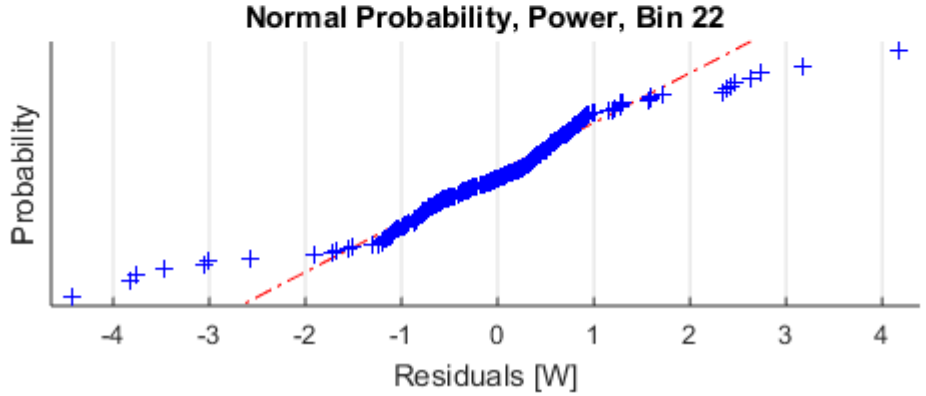
Normal Probability, Power, Bin 22
Probability
-4 -3 -2 -1 0 1 2 3 4
Residuals [W]

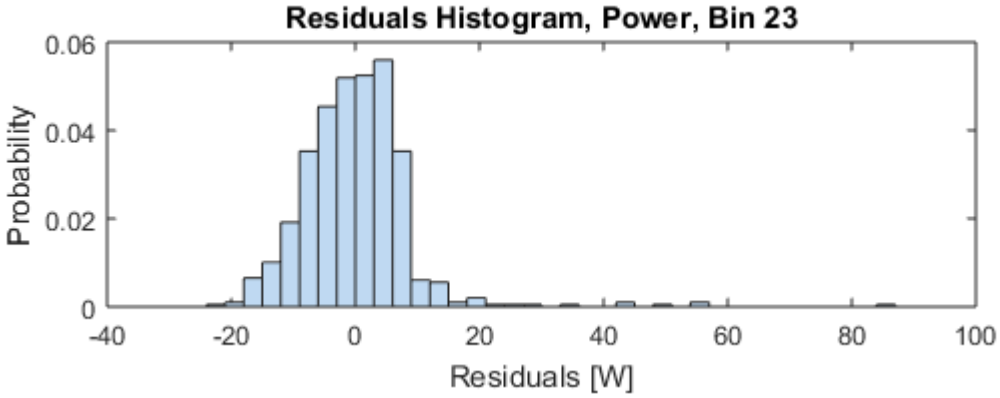
Residuals Histogram, Power, Bin 23
Probability
0.06
0.04
0.02
0
-40 -20 0 20 40 60 80 100
Residuals [W]

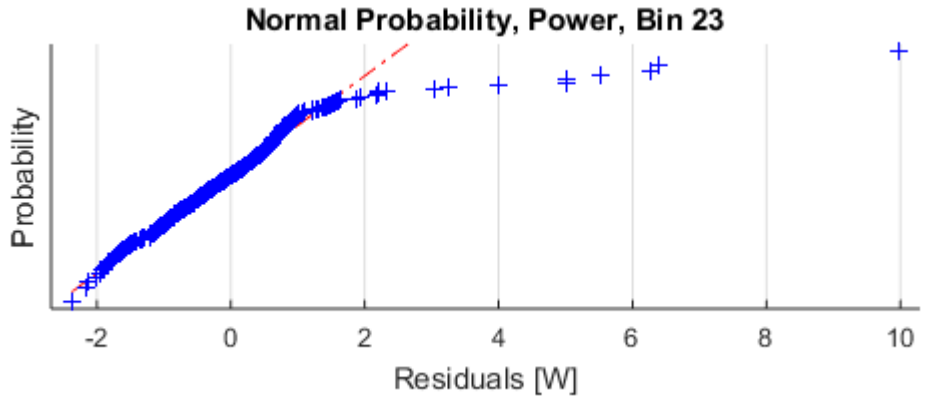
Normal Probability, Power, Bin 23
Probability
-2 0 2 4 6 8 10
Residuals [W]

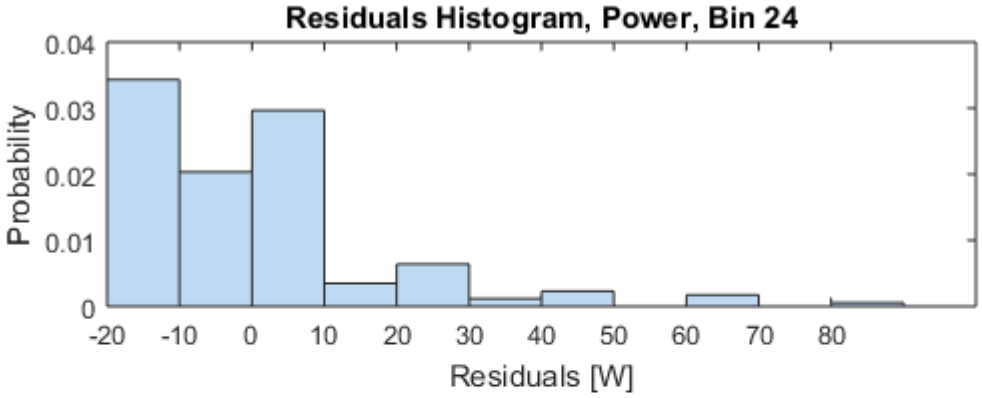
Residuals Histogram, Power, Bin 24
Probability
0.04
0.03
0.02
0.01
0
-20 -10 0 10 20 30 40 50 60 70 80
Residuals [W]

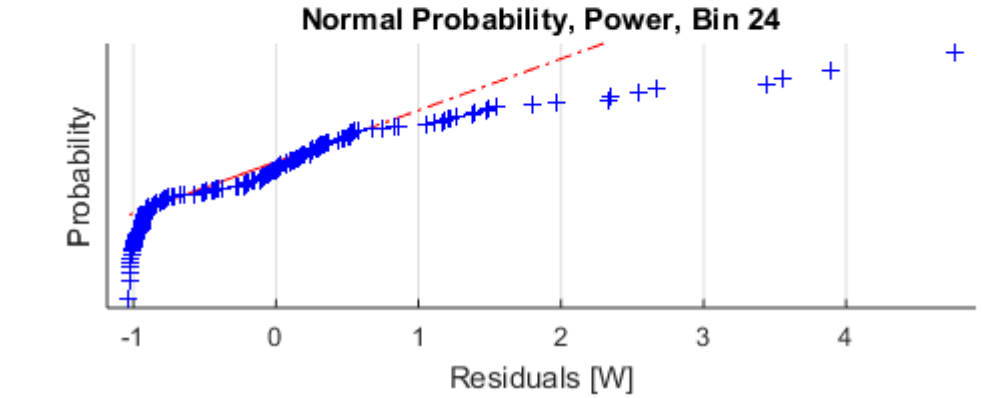
Normal Probability, Power, Bin 24
Probability
-1 0 1 2 3 4
Residuals [W]

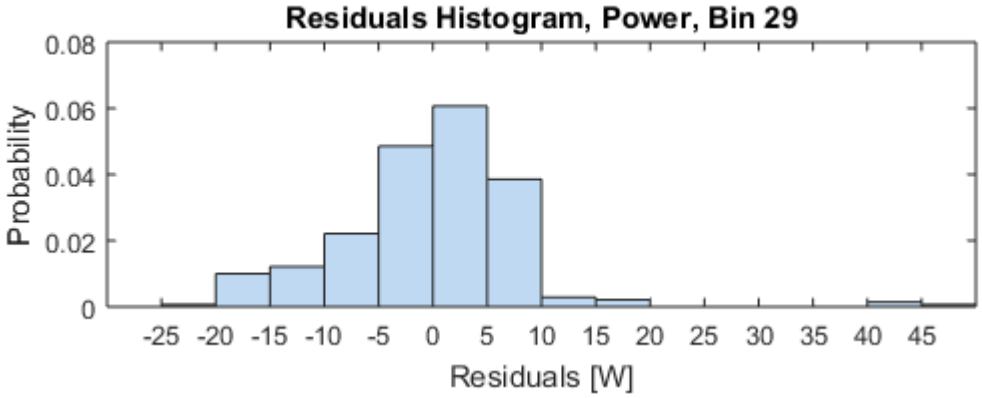
Residuals Histogram, Power, Bin 29
Probability
0.08
0.06
0.04
0.02
0
-25 -20 -15 -10 -5 0 5 10 15 20 25 30 35 40 45
Residuals [W]

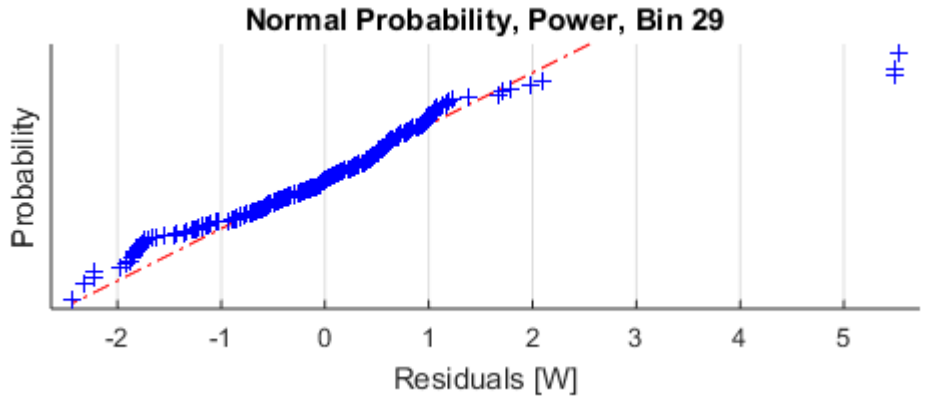
Normal Probability, Power, Bin 29
Probability
-2 -1 0 1 2 3 4 5
Residuals [W]

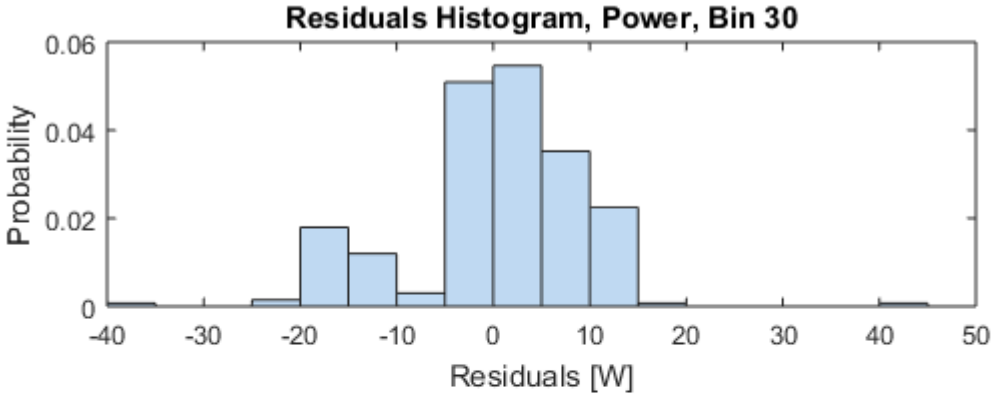
Residuals Histogram, Power, Bin 30
Probability
0.06
0.04
0.02
0
-40
-30
-20
-10
0
10
20
30
40
50
Residuals [W]

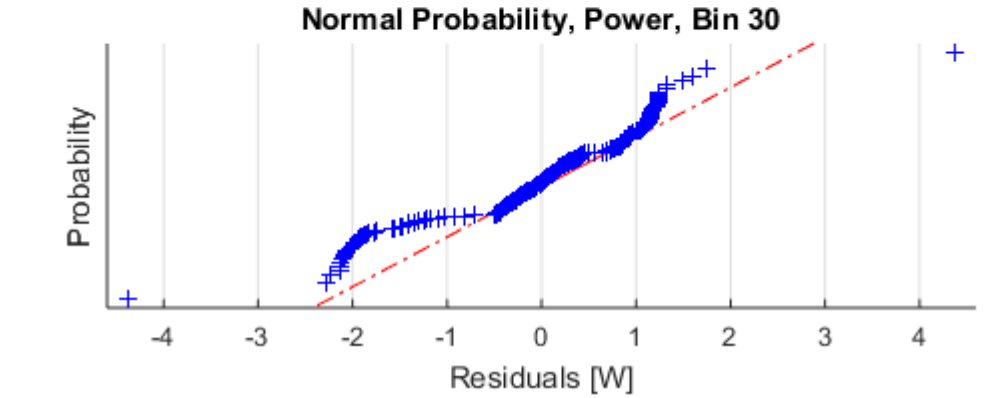
Normal Probability, Power, Bin 30
Probability
-4
-3
-2
-1
0
1
2
3
4
Residuals [W]

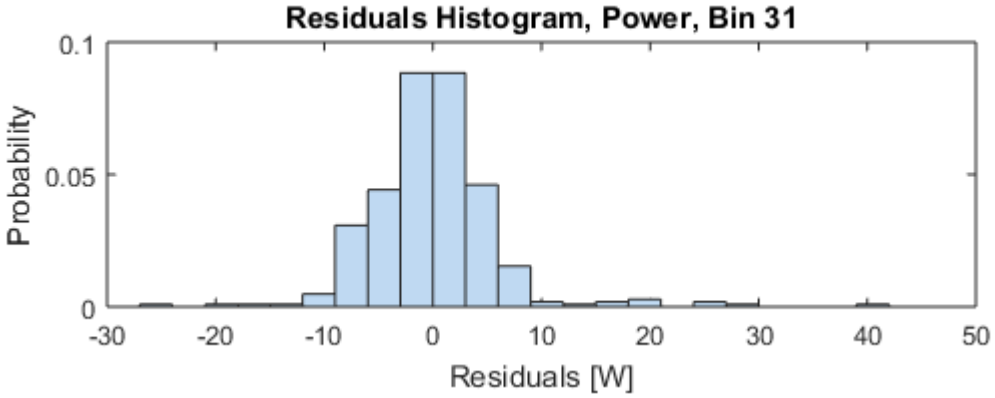
Residuals Histogram, Power, Bin 31
Probability
0.1
0.05
0
-30
-20
-10
0
10
20
30
40
50
Residuals [W]

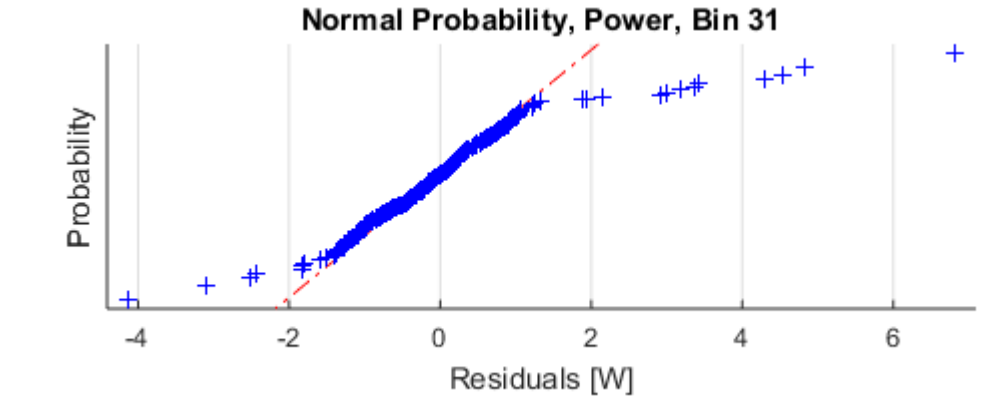
Normal Probability, Power, Bin 31
Probability
-4
-2
0
2
4
6
Residuals [W]

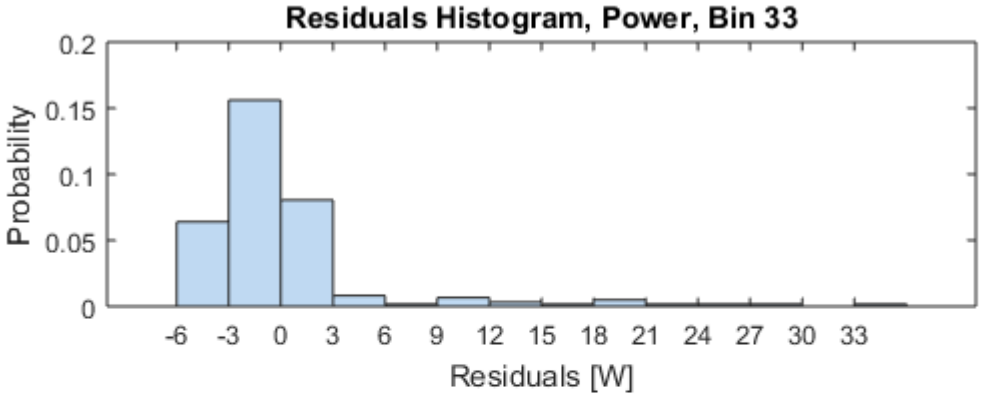
Residuals Histogram, Power, Bin 33
Probability
0.2
0.15
0.1
0.05
0
-6 -3 0 3 6 9 12 15 18 21 24 27 30 33
Residuals [W]

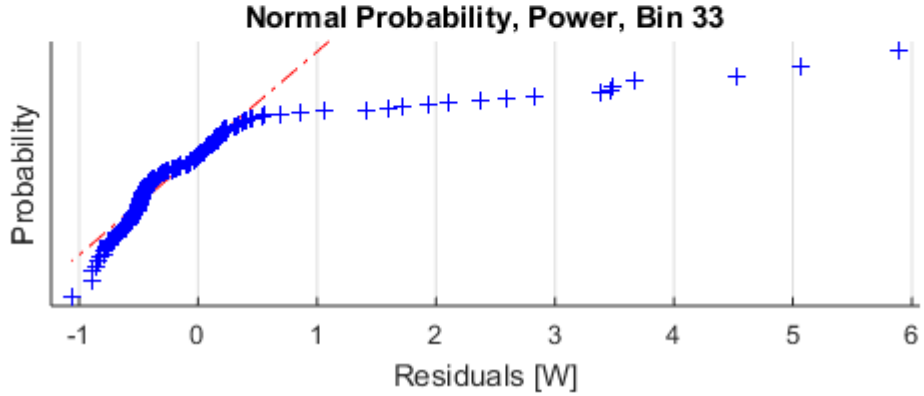
Normal Probability, Power, Bin 33
Probability
-1 0 1 2 3 4 5 6
Residuals [W]

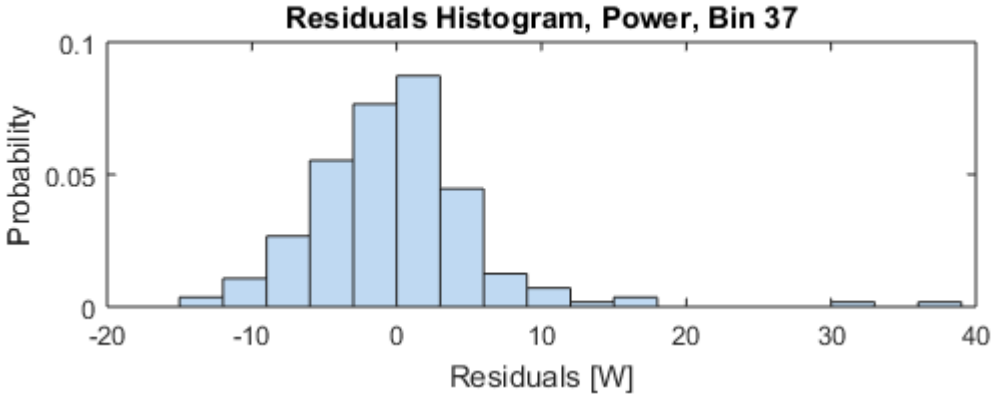
Residuals Histogram, Power, Bin 37
Probability
0.1
0.05
0
-20 -10 0 10 20 30 40
Residuals [W]

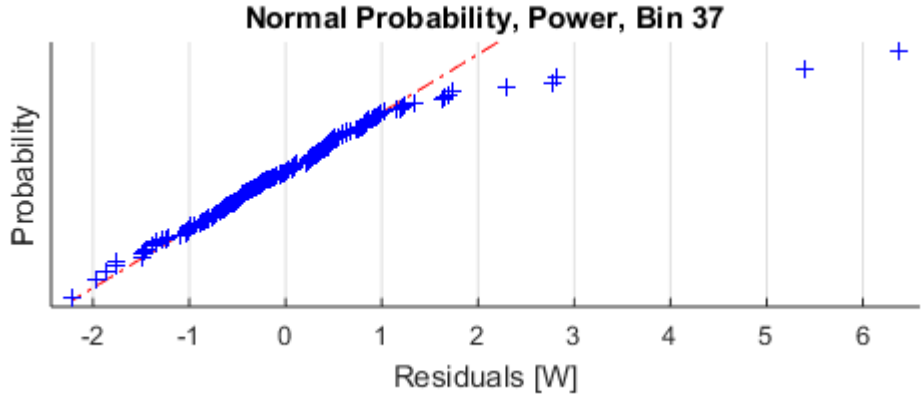
Normal Probability, Power, Bin 37
Probability
-2 -1 0 1 2 3 4 5 6
Residuals [W]

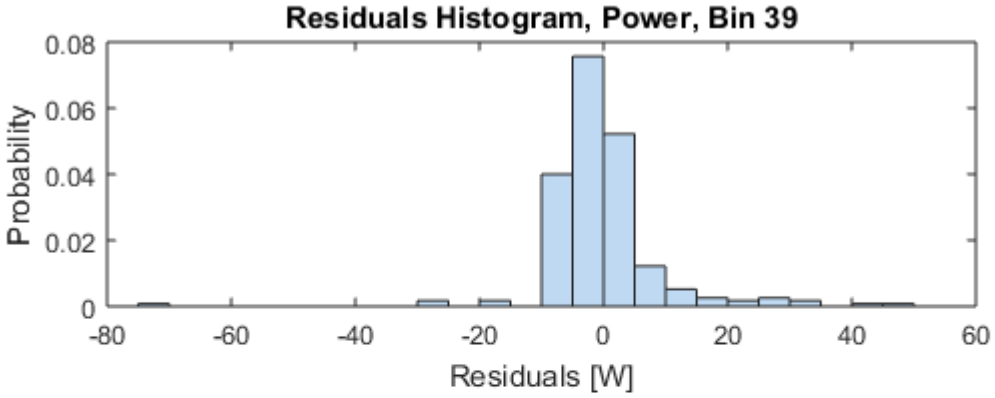
Residuals Histogram, Power, Bin 39
Probability
0.08
0.06
0.04
0.02
0
-80
-60
-40
-20
0
20
40
60
Residuals [W]

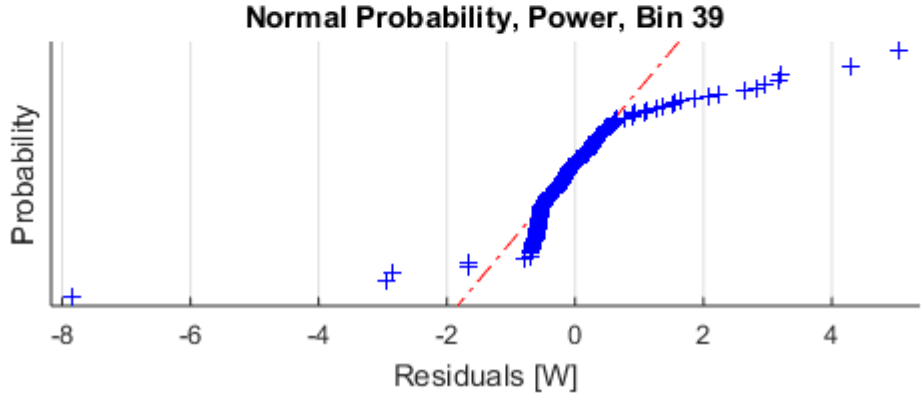
Normal Probability, Power, Bin 39
Probability
-8
-6
-4
-2
0
2
4
Residuals [W]

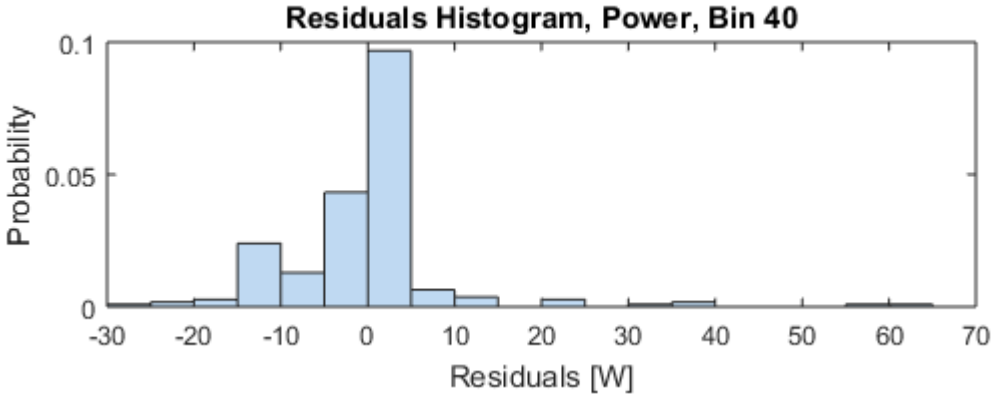
Residuals Histogram, Power, Bin 40
Probability
0.1
0.05
0
-30
-20
-10
0
10
20
30
40
50
60
70
Residuals [W]

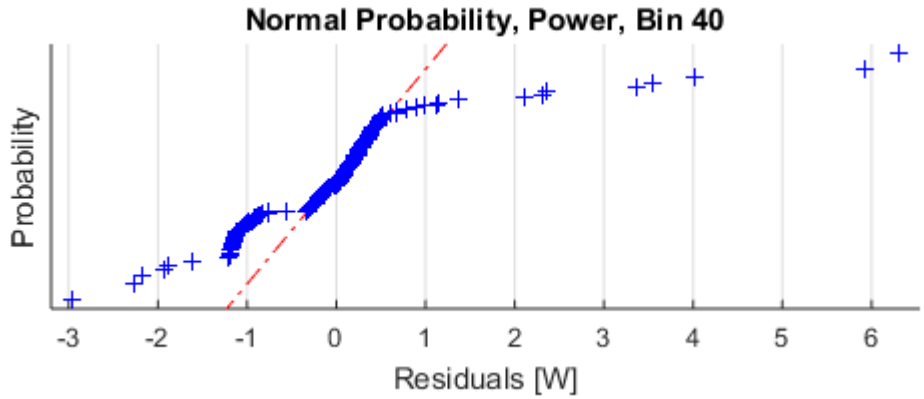
Normal Probability, Power, Bin 40
Probability
-3
-2
-1
0
1
2
3
4
5
6
Residuals [W]

Appendix I – Bin ranges with minimum sample size and (roughly) normal distribution

Nr.	RMSE [°C]	RMSE [W]	Irradiance [W/m²]	Ambient Temp. [°C]	Wind speed [m/s]	AOI [°]
12	1,877	23,164	Irr. 1			
13	4,317	6,963	Irr. 2		Wind speed 1	
14			Irr. 3			
15	3,457	4,145	Irr. 1			
16	5,440	6,667	Irr. 2	tamb 1	Wind speed 2	
17	5,196	7,077	Irr. 3			
18			Irr. 1			
19	3,123	3,992	Irr. 2		Wind speed 3	
20			Irr. 3			
21	2,794	9,525	Irr. 1			
22	4,437	11,491	Irr. 2		Wind speed 1	
23	4,044	7,848	Irr. 3			
24	2,064	33,134	Irr. 1			
25			Irr. 2	tamb 2	Wind speed 2	
26			Irr. 3			
27			Irr. 1			
28			Irr. 2		Wind speed 3	
29	3,385	11,897	Irr. 3			AOI 1
30	1,415	19,189	Irr. 1			
31	4,096	6,722	Irr. 2		Wind speed 1	
32			Irr. 3			
33	2,180	3,828	Irr. 1			
34			Irr. 2	tamb 1	Wind speed 2	
35			Irr. 3			
36			Irr. 1			
37	2,120	7,804	Irr. 2		Wind speed 3	
38			Irr. 3			
39	1,951	6,798	Irr. 1			
40	1,490	7,012	Irr. 2		Wind speed 1	
41						
42			Irr. 1			
43			Irr. 2	tamb 2	Wind speed 2	
44			Irr. 3			
45			Irr. 1			
46			Irr. 2		Wind speed 3	
47			Irr. 3			AOI 2
48			Irr. 1			
49			Irr. 2		Wind speed 1	
50			Irr. 3			
51			Irr. 1			
52			Irr. 2	tamb 1	Wind speed 2	
53			Irr. 3			
54			Irr. 1			
55			Irr. 2		Wind speed 3	
56			Irr. 3			
57			Irr. 1			
58			Irr. 2		Wind speed 1	
59			Irr. 3			
60			Irr. 1			
61			Irr. 2	tamb 2	Wind speed 2	
62			Irr. 3			
63			Irr. 1			
64			Irr. 2		Wind speed 3	
65			Irr. 3			AOI 3

Table 31 Data samples with the achieved minimum sample size (own table)

Appendix J – Position analysis for all combinations of bin ranges

Bin Nr.	Median power difference [W] - Bin ranges 1 to 11					
-	Top	Middle	Bottom	Edge	Middle o.A.	All
1	2,71	1,91	4,10	2,63	2,52	2,46
2	0,20	0,59	3,06	0,49	0,98	0,71
3	-2,33	-1,61	0,46	-2,68	-1,18	-1,84
4	2,36	2,18	5,12	2,60	2,84	2,65
5	-0,94	-0,73	0,96	-0,95	-0,31	-0,64
6	0,04	0,02	1,51	0,00	0,35	0,14
7	-0,07	0,34	2,40	0,11	0,68	0,39
8	1,73	2,05	4,86	2,42	2,47	2,34
9	-0,60	-0,27	1,75	-0,51	0,16	-0,21
10	1,25	1,22	3,36	1,39	1,61	1,45
11	1,42	1,55	3,38	1,73	1,85	1,84

Table 32 Median power prediction error for each array position, bin range 1 to 11 (own table)

Bin Nr.	Median measured Voc [Voc] - Bin ranges 1 to 11					
-	Top	Middle	Bottom	Edge	Middle o.A.	All
1	35,32	35,38	35,30	35,44	35,33	35,37
2	36,80	36,69	36,48	36,83	36,63	36,72
3	36,18	35,95	35,81	36,25	35,88	36,01
4	37,37	37,23	37,09	37,31	37,20	37,24
5	34,43	34,41	34,41	34,67	34,35	34,47
6	35,33	35,49	35,42	35,69	35,38	35,52
7	35,92	35,75	35,59	35,91	35,71	35,78
8	36,81	36,69	36,56	36,81	36,65	36,72
9	36,04	35,90	35,78	36,09	35,85	35,95
10	36,56	36,50	36,34	36,58	36,45	36,51
11	37,45	37,26	37,09	37,30	37,22	37,26

Table 33 Median measured Voc for each array position, bin range 1 to 11 (own table)

Bin Nr.	Median measured Isc [A] - Bin ranges 1 to 11					
-	Top	Middle	Bottom	Edge	Middle o.A.	All
1	1,55	1,55	1,52	1,53	1,55	1,54
2	5,71	5,72	5,66	5,71	5,71	5,72
3	7,56	7,54	7,49	7,49	7,55	7,52
4	5,54	5,54	5,48	5,54	5,53	5,54
5	5,12	4,89	4,69	4,58	4,97	4,81
6	3,82	3,66	3,48	3,43	3,73	3,60
7	5,80	5,79	5,72	5,75	5,79	5,77
8	6,03	6,02	5,97	6,00	6,02	6,02
9	6,18	6,15	6,08	6,11	6,15	6,14
10	4,29	4,29	4,22	4,25	4,28	4,29
11	5,13	5,28	5,27	5,39	5,20	5,31

Table 34 Median measured Isc for each array position, bin range 1 to 11 (own table)

Bin Nr.	Median power difference [W] - Bin ranges 12 to 65					
-	Top	Middle	Bottom	Edge	Middle o.A.	All
12	17,37	16,59	17,75	16,94	16,92	16,80
13	0,05	0,61	3,33	0,09	1,05	0,62
14	-3,33	-2,72	-0,23	-3,33	-2,41	-2,96
15	-1,16	-1,38	-0,37	-1,05	-1,03	-1,11
16	-2,10	-2,24	0,19	-2,24	-1,71	-2,08
17	-3,06	-2,81	-1,48	-3,89	-2,33	-3,00
18	32,93	31,87	33,60	32,57	32,35	32,18
19	0,41	1,38	4,75	1,09	1,78	1,45
20	-1,73	-0,80	1,80	-1,32	-0,49	-0,85
21	1,50	1,53	4,29	2,04	1,81	1,74
22	-1,13	-0,98	1,86	-1,37	-0,45	-0,91
23	-2,82	-1,87	0,12	-3,64	-1,33	-2,28
24	30,21	28,94	30,73	29,37	29,56	29,16
25	5,17	4,20	8,13	5,32	5,12	4,95
26	-0,45	0,15	2,44	0,14	0,47	0,13
27	2,65	1,96	5,24	2,98	2,42	2,43
28	0,93	0,98	4,83	1,57	1,46	1,28
29	-2,40	-1,31	0,90	-2,01	-0,93	-1,43
30	16,13	15,58	16,45	15,84	15,83	15,74
31	0,39	0,70	3,23	0,43	1,09	0,74
32	-4,04	-6,86	-4,13	-5,95	-5,55	-5,88
33	0,69	0,54	1,68	0,77	0,82	0,71
34	-1,36	-1,26	0,74	-1,04	-0,86	-0,83
35	NaN	NaN	NaN	NaN	NaN	NaN
36	21,80	21,36	22,68	20,87	21,88	21,55
37	1,16	1,66	4,64	1,77	2,04	1,85
38	0,08	0,34	2,79	0,52	0,59	0,49
39	1,10	0,82	1,76	1,00	1,02	0,93
40	-0,52	-0,09	2,02	-0,18	0,22	0,01
41	NaN	NaN	NaN	NaN	NaN	NaN
42	19,99	19,30	21,02	18,87	19,86	19,42
43	2,13	2,29	5,02	2,82	2,68	2,63
44	1,33	1,85	4,15	1,55	2,11	1,94
45	11,44	8,30	10,09	10,33	9,21	8,56
46	0,69	0,85	2,63	0,98	1,17	0,99
47	NaN	NaN	NaN	NaN	NaN	NaN
48	NaN	NaN	NaN	NaN	NaN	NaN
49	0,61	0,99	2,14	0,39	1,33	0,67
50	-3,87	-7,01	-4,34	-6,13	-5,88	-6,09
51	0,73	0,49	1,50	1,04	0,73	0,84
52	1,54	2,09	3,43	2,24	2,28	2,40

53	NaN	NaN	NaN	NaN	NaN	NaN
54	NaN	NaN	NaN	NaN	NaN	NaN
55	0,81	1,02	3,07	1,04	1,28	1,17
56	-0,44	0,26	2,37	0,11	0,36	0,28
57	0,81	0,76	1,73	0,97	0,86	0,84
58	3,60	3,59	4,87	3,60	3,84	3,72
59	NaN	NaN	NaN	NaN	NaN	NaN
60	NaN	NaN	NaN	NaN	NaN	NaN
61	1,98	1,99	4,21	2,24	2,26	2,24
62	1,13	1,54	3,72	1,49	1,76	1,73
63	4,28	4,71	5,65	4,54	4,77	4,62
64	3,53	3,46	4,79	3,47	3,76	3,59
65	NaN	NaN	NaN	NaN	NaN	NaN

Table 35 Median power prediction error for each array position, bin ranges 12 to 65 (own table)

Bin Nr.	Median measured Voc [V] - Bin ranges 12 to 65					
-	Top	Middle	Bottom	Edge	Middle o.A.	All
12	37,45	37,26	37,09	37,30	37,22	37,26
13	36,72	36,74	36,63	36,71	36,71	36,71
14	37,08	36,93	36,80	37,10	36,88	36,95
15	38,13	37,92	37,73	37,99	37,90	37,94
16	33,93	33,98	33,94	34,08	33,91	33,99
17	33,76	33,73	33,69	33,95	33,66	33,75
18	33,64	33,56	33,49	33,77	33,51	33,59
19	37,50	37,52	37,38	37,50	37,50	37,49
20	37,18	36,93	36,73	37,10	36,92	36,98
21	37,12	36,93	36,74	37,01	36,92	36,94
22	35,29	35,30	35,20	35,36	35,26	35,28
23	34,74	34,75	34,89	35,04	34,63	34,86
24	34,86	34,80	35,16	35,40	34,68	35,00
25	37,13	37,05	36,91	37,06	37,04	37,04
26	37,61	37,44	37,25	37,54	37,44	37,48
27	37,85	37,61	37,50	37,71	37,61	37,65
28	35,95	35,90	35,72	35,92	35,88	35,89
29	36,23	36,08	35,90	36,17	36,05	36,09
30	36,32	36,08	35,91	36,31	36,05	36,12
31	36,72	36,77	36,62	36,73	36,73	36,73
32	37,29	37,19	37,14	37,35	37,14	37,22
33	37,83	37,61	37,42	37,76	37,59	37,63
34	34,03	34,10	33,99	34,19	34,04	34,11
35	34,27	34,32	34,34	34,57	34,22	34,37
36	NaN	NaN	NaN	NaN	NaN	NaN
37	36,96	36,90	36,81	36,93	36,90	36,91
38	37,55	37,36	37,24	37,43	37,34	37,38
39	37,68	37,46	37,29	37,64	37,45	37,48
40	34,04	34,05	33,92	34,04	34,02	34,03
41	NaN	NaN	NaN	NaN	NaN	NaN
42	35,26	35,35	34,53	35,15	34,80	34,52
43	36,81	36,83	36,67	36,81	36,80	36,81
44	37,87	37,69	37,49	37,72	37,68	37,69
45	37,78	37,55	37,34	37,72	37,53	37,57
46	34,66	34,63	34,45	34,68	34,61	34,63
47	36,15	35,99	35,85	36,09	35,97	36,01
48	NaN	NaN	NaN	NaN	NaN	NaN
49	NaN	NaN	NaN	NaN	NaN	NaN
50	37,64	37,48	37,25	37,60	37,46	37,48
51	37,77	37,62	37,44	37,76	37,62	37,63
52	33,16	33,12	32,94	33,08	33,11	33,09

53	35,62	35,54	35,33	35,62	35,47	35,54
54	NaN	NaN	NaN	NaN	NaN	NaN
55	NaN	NaN	NaN	NaN	NaN	NaN
56	37,64	37,45	37,22	37,56	37,43	37,47
57	37,70	37,54	37,32	37,68	37,51	37,52
58	33,99	33,90	33,87	33,94	33,88	33,87
59	35,87	35,73	35,61	35,79	35,73	35,74
60	NaN	NaN	NaN	NaN	NaN	NaN
61	NaN	NaN	NaN	NaN	NaN	NaN
62	37,88	37,69	37,53	37,74	37,67	37,71
63	37,86	37,66	37,46	37,78	37,65	37,68
64	35,87	35,84	35,62	35,80	35,75	35,80
65	36,06	36,01	35,80	36,03	35,97	36,00

Table 36 Median measured Voc for each array position, bin ranges 12 to 65 (own table)

Bin Nr.	Median measured Isc [A] - Bin ranges 12 to 65					
-	Top	Middle	Bottom	Edge	Middle o.A.	All
12	1,47	1,47	1,44	1,46	1,47	1,47
13	6,20	6,20	6,15	6,19	6,20	6,20
14	7,23	7,21	7,15	7,23	7,20	7,22
15	1,62	1,62	1,59	1,61	1,62	1,61
16	5,21	5,09	4,81	4,83	5,16	5,04
17	7,76	7,72	7,64	7,64	7,73	7,69
18	1,79	1,80	1,76	1,78	1,80	1,81
19	6,19	6,18	6,13	6,18	6,18	6,18
20	6,77	6,77	6,71	6,76	6,77	6,77
21	2,14	2,12	2,03	2,10	2,12	2,11
22	5,54	5,45	5,30	5,41	5,48	5,49
23	7,88	7,87	7,84	7,84	7,88	7,86
24	2,03	2,00	1,94	1,99	1,98	1,99
25	6,12	6,13	6,07	6,10	6,12	6,12
26	6,92	6,92	6,87	6,91	6,91	6,92
27	2,53	2,55	2,47	2,49	2,55	2,50
28	5,55	5,55	5,39	5,59	5,53	5,58
29	7,71	7,71	7,68	7,68	7,72	7,71
30	1,10	1,10	1,08	1,08	1,10	1,09
31	5,53	5,52	5,47	5,51	5,51	5,52
32	6,74	6,76	6,74	6,75	6,75	6,75
33	1,73	1,73	1,68	1,71	1,72	1,72
34	5,03	4,91	4,90	4,90	4,92	4,92
35	NaN	NaN	NaN	NaN	NaN	NaN
36	1,31	1,30	1,27	1,29	1,30	1,29
37	5,48	5,46	5,41	5,45	5,45	5,46
38	6,74	6,76	6,74	6,75	6,76	6,76
39	1,12	1,11	1,09	1,10	1,12	1,11
40	5,21	5,28	5,25	5,29	5,22	5,29
41	NaN	NaN	NaN	NaN	NaN	NaN
42	2,15	2,14	2,12	2,13	2,14	2,14
43	5,64	5,65	5,58	5,63	5,63	5,63
44	6,71	6,73	6,70	6,72	6,72	6,72
45	1,21	1,21	1,15	1,19	1,21	1,20
46	5,20	5,16	5,17	5,19	5,16	5,17
47	NaN	NaN	NaN	NaN	NaN	NaN
48	NaN	NaN	NaN	NaN	NaN	NaN
49	5,31	5,32	5,30	5,31	5,31	5,32
50	6,57	6,59	6,56	6,58	6,59	6,59
51	1,44	1,39	1,35	1,33	1,43	1,38
52	3,50	3,49	3,46	3,53	3,48	3,50

53	NaN	NaN	NaN	NaN	NaN	NaN
54	NaN	NaN	NaN	NaN	NaN	NaN
55	5,99	6,03	6,00	6,01	6,02	6,02
56	6,46	6,48	6,46	6,48	6,47	6,47
57	2,29	2,30	2,26	2,27	2,27	2,24
58	3,34	3,35	3,33	3,34	3,35	3,34
59	NaN	NaN	NaN	NaN	NaN	NaN
60	NaN	NaN	NaN	NaN	NaN	NaN
61	5,96	5,98	5,93	5,96	5,97	5,97
62	6,55	6,56	6,53	6,55	6,56	6,56
63	2,99	3,00	2,98	2,98	3,00	3,00
64	3,52	3,54	3,52	3,52	3,54	3,54
65						

Table 37 Median measured Isc for each array position, bin ranges 12 to 65 (own table)